Universidade de Aveiro Departamento de Física
2009

Sónia de Sousa Nobre

Híbridos Orgânicos/Inorgânicos Nanoestruturados Fotoluminescentes

Photoluminescent Nanostructured Organic/Inorganic Hybrids

Universidade de Aveiro Departamento de Física
2009

Sónia de Sousa Nobre

Híbridos Orgânicos/Inorgânicos Nanoestruturados Fotoluminescentes

Photoluminescent Nanostructured Organic/Inorganic Hybrids

Dissertação apresentada à Universidade de Aveiro para cumprimento dos requisitos necessários à obtenção do grau de Doutor em Física, realizada sob a orientação científica do Doutor Luís António Ferreira Martins Dias Carlos, Professor Catedrático do Departamento de Física da Universidade de Aveiro, da Doutora Maria Rute de Amorim Sá Ferreira André, Investigadora Auxiliar do Laboratório Associado CICECO e Professora Auxiliar Convidada do Departamento de Física da Universidade de Aveiro e do Doutor Michel Wong Chi Man, Directeur de Recherche do Laboratoire d' Architectures Moléculaires et Matériaux Nanostructurés, Institut Charles Gerhardt, École Nationale Supérieure de Chimie de Montpellier.

Apoio financeiro da FCT e do FSE no âmbito do III Quadro Comunitário de Apoio.

À memória de meu pai,
À minha mãe,
A meu irmão.

o júri

presidente

Prof. Doutor Domingos Moreira Cardoso
Professor catedrático da Universidade de Aveiro

Prof. Doutor Rui Almeida
Professor catedrático do Instituto Superior Técnico Lisboa

Doutor Rachid Mahiou
Directeur de Recherches CNRS da Université Blaise Pascal Clermont Ferrand

Prof. Doutora Verónica de Zea Bermudez
Professora associada com agregação da Universidade de Trás-os-Montes e Alto Douro, Vila-Real

Doutor Clément Sanchez
Directeur de recherches CNRS da Université Pierre et Marie Curie, Paris

Prof. Doutor Jean-Louis Bantignies
Professor da Université Montpellier II

Prof. Doutora Maria Rute de Amorim Sá Ferreira
Investigadora Auxiliar do Laboratório Associado CICECO e Professora Auxiliar Convidada do Departamento de Física da Universidade de Aveiro

Prof. Doutor Luís António Ferreira Martins Dias Carlos
Professor catedrático da Universidade de Aveiro

Doutor Michel Wong Chi Man
Directeur de Recherche CNRS do Institut Charles Gerhardt, École Nationale Supérieure de Chimie de Montpellier

agradecimentos

O trabalho apresentado nesta tese é resultado da participação e colaboração de algumas pessoas e instituições. Gostaria de em primeiro lugar agradecer aos meus orientadores Professor Doutor Luís Dias Carlos, Professora Doutora Maria Rute Ferreira e Doutor Michel Wong Chi Man por me terem dado a oportunidade de doutoramento, pela formação científica que me proporcionaram, pelo seu constante apoio e palavras de incentivo.

Ao Professor Doutor Leite Videira por me ter acompanhado ao longo das destes últimos anos, pelos seus conselhos e amizade.

À Professora Doutora Verónica Bermudez por toda sua ajuda nas diferentes etapas do trabalho, em particular nas discussões de FT-IR, pela sua disponibilidade e colaboração pessoal.

Ao Professor Doutor João Rocha, Doutor Luís Mafra, Doutor Uwe Pischel, Professor Doutor Oscar Malta pelas discussões em diferentes pontos do trabalho.

Aos técnicos Marta Ferro, Isabel Martins, Rosário Soares, Celeste Azevedo, Lina Carvalho, Didier Cot, ao Doutor Philippe Dieudonné e à Andreia Macedo pelas diferentes medidas de caracterização estrutural.

Ao Doutor Xavier Cattöen pela sua contribuição nos vários pontos do trabalho, em particular neste último ano, pela sua amizade e compreensão.

À Doutora Patrícia Pereira Lima por toda ajuda nas diferentes etapas, pela sua disponibilidade, pelas discussões e pela sua amizade.

Aos colegas e amigos que de uma ou de outra forma contribuíram para que esta tese chegasse a bom porto, Édison Percorado, Soma Das, Mariana Fernandes, Sofia Benyahya, Montserrat Trilla, Sébastien Richard, Celeste Maçarico.

À minha família por ter estado sempre presente e tanto me ter apoiado.

Enfim, a todos os que me acompanharam, quer nos bons ou maus momentos, deixo aqui o mais sincero agradecimento.

palavras-chave

Híbridos orgânicos/inorgânicos, nanoestruturação, fotoluminescência, transferência de energia, auto-organização, lantanídeos, sol-gel.

resumo

O presente trabalho propõe-se caracterizar a estrutura e as propriedades de fotoluminescência de materiais híbridos orgânicos/inorgânicos.

A origem química e fotofísica subjacente à emissão de luz branca dos di-ureiasils, híbridos compostos por uma rede siliciosa ligada covalentemente por pontes ureia a cadeias poliméricas, foi estudada fazendo uso de dois compostos modelo que reproduzem, selectivamente, as componentes orgânica e inorgânica daquela rede híbrida. A emissão nos di-ureiasils resulta da convolução de uma componente originada nos grupos ureia com uma outra proveniente dos domínios siliciosos. A comparação entre os tempos de vida das emissões dos compostos modelo com as do híbrido, a dependência do tempo de vida destas emissões com a temperatura e a variação da curva de decaimento associada à emissão dos grupos ureia com o tempo de atraso entre o final da excitação e o início da medida, suportam a ocorrência de transferência de energia entre a componente originada nos domínios siliciosos e a proveniente dos grupos ureia. A taxa de transferência de energia foi quantitativamente estimada considerando os mecanismos de troca (3.7×10^{8} s^{-1}) e dipolo-dipolo (1.3×10^{9} s^{-1}). Esta taxa foi, também, calculada para um di-ureiasil incorporando um complexo de Eu^{3+} tendo-se verificado que o canal mais eficiente para a luminescência é: (S_0) Híbrido → (T) Híbrido → (T) Ligando → ($^5D_1$, $^5D_0$) → $^7F_{0-4}$.

Um precursor híbrido com cadeias alquílicas e grupos ureia (P12), preparado por catálise àcida ou nucleofílica, deu origem, respectivamente, a uma estrutura lamelar cristalina (L12) e a um material amorfo (A12). Iões Eu3+ foram incorporados nos dois sistemas. Para os híbridos obtidos por catálise nucleofílica, demonstrou-se que a sua morfologia é fortemente determinada pela presença e modos de coordenação dos iões Eu^{3+}. Todos os híbridos são emissores de luz branca. A incorporação de iões Eu^{3+} diminui o rendimento quântico da rede híbrida, o que indica a existência de transferência de energia rede-iões Eu^{3+}.

Um precursor incorporando bipiridina e grupos ureia foi preparado pelo método sol-gel através de catálise nucleofílica, dando origem a híbridos amorfos. Estes híbridos são caracterizados por uma emissão de banda larga atribuída à sobreposição de três componentes: i) estado tripleto da bipridina, recombinações electrão-lacuna originadas ii) nos grupos ureia e iii) nos domínios siliciosos. Valores de 0.18-0.22 foram obtidos para o rendimento quântico, para excitação no UV/azul. Foi demonstrado que os híbridos podem ser excitados com um LED de INGaN comercial, tornando-os materiais promissores para aplicações em fontes de luz de estado sólido. Os híbridos foram também preparados incorporando iões Eu^{3+}, Gd^{3+}, Tb^{3+} e Eu^{3+}/Tb^{3+}. Os materiais resultantes são emissores de luz branca onde a emissão intra 4-f dos iões lantanídeo se sobrepõe à emissão da rede híbrida.

keywords

Organic/inorganic hybrids, nanostrcturing, photoluminescence, energy transfer, self-assembly, lanthanides, sol-gel

abstract

The present work focuses on the characterization of the structural and photoluminescence (PL) properties of a series of organic/inorganic hybrids. The photophysical and chemical origin behind the white-light photoluminescent features of amide-functionalized hybrids lacking metal activators (di-ureasils) was studied making use of two model compounds that selectively reproduced the organic and inorganic counterpart parts. The comparison between the lifetimes of the two emissions of the inorganic and organic model compounds with those of the hybrids, the Arrhenius dependence with temperature of the siliceous-related lifetime in the hybrids, and the nonexponential behavior of the decay curve of the siliceous-related emission under lower excitation wavelengths are experimental evidence supporting the occurrence of energy transfer in the hybrids. This energy transfer rate is quantitatively estimated for a di-ureasil, generalizing the ideas proposed by Malta, considering the exchange (3.7×10^{8} s^{-1}) and dipole–dipole mechanisms (1.3×10^{9} s^{-1}). The energy transfer rates were also calculated for a di-ureasil incorporating a Eu^{3+} complex and it was found that the most efficient luminescence channel is (S_0)Hybrid → (T)Hybrid → (T)Ligand → ($^5D_1$, $^5D_0$) → $^7F_{0-4}$.

A di-urea cross-linked alkylsilane precursor prepared using HCl induced the formation of a crystalline lamellar structure (L12); when prepared with NH_4F an amorphous material (A12) was obtained. Eu^{3+} ions were incorporated in the two systems and the unique role played by the Eu^{3+} ions in the modulation of the morphology of Eu@A12 hybrids was for the first time demonstrated via inhibition of the growth of the siloxane network formed through sol-gel reactions and urea-mediated supramolecular self-assembly. All the hybrids are room temperature multi-wavelength emitters and the incorporation of Eu^{3+} into the L12 and A12 hybrids induces a decrease in the absolute emission quantum yield values, supporting the existence of hybrid-to-Eu^{3+} energy transfer.

A di-urea cross-linked bipyridine (bpy) precursor prepared by sol-gel synthesis under nucleophilic catalysis, by TBAF and NH_4F, gave rise to amorphous hybrids (termed as H and M). They are characterized by emission spectra that consist of a broad band unequivocally ascribed to a superposition of three distinct components: i) bpy triplet state, ii) electron-hole recombinations originated in the NH/C=O groups of the urea cross-linkages and iii) siliceous nanoclusters. Quantum yield values of 0.22-0.18 were measured under excitation in the long-wavelength UV and blue spectral regions. It was demonstrated that H can be efficiently excited using a commercial LED, placing bpy-hybrids as promising materials for photonics and solid state lighting. M was also prepared in the presence of Eu^{3+}, Gd^{3+}, Tb^{3+}, and Eu^{3+}/Tb^{3+} and formed hybrids that are room temperature multi-wavelength emitters. This is due to the convolution of the emission arising from the hybrid's emitting centres and the Ln^{3+} intra-4f transitions. The emission colour is tuned across the CIE diagram depending on the Ln^{3+} ions and the excitation wavelength.

Index

Chapter 1 - Introduction

1.1 Context and state of the art

1.2 Objectives and organization of the thesis

1.3 References

1.1 Context and state of the art

The term organic/inorganic hybrid materials is used for many different systems combining organic and inorganic units, such as amorphous or crystalline coordination compounds, independently of the interaction between the inorganic and organic counterpart units.[1] The most wide-ranging definition is the following: an organic/inorganic hybrid material includes two moieties blended on the molecular scale. A more detailed definition distinguishes between the possible interactions connecting the inorganic and organic entities. Class I hybrids are those that display weaker interactions between the two phases, such as Van der Waals, hydrogen bonding or weak electrostatic interaction. Class II hybrids are those that show stronger chemical interactions, such as covalent bonds between the components.[2]

The choice of the organic units, essentially polymers, is usually guided mainly by their mechanical and thermal behaviour. Moreover, other properties such as hydrophobic/hydrophilic balance, chemical stability, bio-compatibility, optical and/or electronic properties and chemical functionalities (*i.e.* solvation, wettability, templating effect) are also considered. The organic counterpart in many cases also allows easy shaping and better processing of the materials. The inorganic components (*e.g.* silica, transition metal oxides, metallic phosphates, nanoclays, nanometals, metal chalcogenides) provide mechanical and thermal stability, besides new functionalities, depending on its chemical nature, structure, size, and crystallinity. Indeed, the inorganic component can implement or improve electronic, optical, magnetic and redox properties, density and the refraction index, for instance. The organic/inorganic hybrids success relies on the possibility of exploiting the synergy (defined as cooperative effects that are produced by two or more particles elements, parts, or organisms, that are not otherwise attainable) between the organic and inorganic components, so that the properties of these hybrids are then not just the sum of the individual contributions of both organic and inorganic phases.[1,3]

The sol–gel process, which is mainly based on inorganic polymerization reactions, is a chemical synthesis method initially used for the preparation of inorganic materials such as glasses and ceramics. Its unique low temperature processing characteristic provides unique opportunities to make organic/inorganic hybrid materials of well-controlled composition through the incorporation of low molecular weight or oligomeric/polymeric

organic molecules with appropriate inorganic moieties at temperatures under which the organics can survive. It has also proven to be a very promising and smooth method to design hybrid organic/inorganic materials with tunable properties.[4-6]

Nanostructuring and control over morphology in hybrids are of great interest for the design of multifunctional materials. In the past ten years, the organization or the texturing of hybrid networks has been templated by organic structure-directing agents, especially surfactants.[7-9] The success of this strategy is clearly related to the ability to control and tune hybrid interfaces. Structured hybrids may also be obtained by direct sol–gel synthesis without using any external template. The controlled hydrolysis of organic/inorganic hybrid precursors bearing pendant long alkylene chains allowed the synthesis of newly designed periodic porous structures.[10,11] In the case of hybrids with bridging organic units (*e*.g. bridged silsesquioxanes), much effort was devoted to improve the structural ordering of the resulting composite through intermolecular interactions and through the shape and structure that the organic fragments may adopt during the formation of the solid.[12,13] Birefringent hybrid solids with anisotropic organization and a lamellar character were obtained favouring van der Waals and/or π–π interactions.[14] Structural ordering was also studied as a function of the chemical nature and geometry of the organic unit (rigid,[14] twisted,[15] planar,[16] or tetrahedral[17] organic units). Highly crystalline solids were obtained using hybrid precursors with flexible hexylene or octylene chains as organic bridging units with van der Waals interactions between alkyl chains.[18] The intermolecular interactions between the organic fragments with urea groups and/or with long alkylene chains offered a nice route to self-direct the structuring of bridged silsesquioxanes.[19] Presumably the ability of molecular precursors to self-assemble via the hydrogen bonds of the urea groups or via weak van der Waals interactions during the hydrolysis–condensation process favours the structuring of the solid materials leading to helical[20] and lamellar structures.[21-23]

The huge amount of possible combinations between the organic and inorganic components made the organic/inorganic hybrids spawn a wide domain of applications[1,2] such as electronics,[24,25] catalysts,[26-28] sensors,[29,30] biomedical devices (controlled drug release[31], development of artificial bone[32]), membranes,[33,34] optics,[3,35-42] materials with high refractive index[43] in the areas of ophthalmic lenses, filters, optical adhesives, highly reflective and antireflection coatings[44]). In the past few years, the synthesis strategy has been increasingly adopted for the development of low cost siloxane-based matrices with

attractive photonic features (*e.g.*, optical switching and data storage,[45] high laser efficiency and photostability,[46] photo-pattern wave-guiding for integrated optics,[47-51] fiber-optic sensors[52,53]).

Silicon, the mainstay semiconductor in microelectronic circuitry, was considered unsuitable for optoelectronic applications owing to its indirect electronic band gap (which limits its efficiency as a light emitter) but since the publication of Canham's paper[54] in 1990, demonstrating efficient tuneable room temperature emission from porous silicon the interest in light-emitting silicon devices has tremendously increased. The development of an optically efficient silicon-compatible material permitting optical and electronic devices to be completely integrated would cause a pronounced impact on displays, communications, computers and related technologies. The siloxane-based organic/inorganic hybrids could allow such integration between optics and electronics.

Recently, a set of review articles about photonic applications of hybrids based on siloxanes were published.[3,35,42,55] Several stable and efficient white-light photoluminescent amine- and amide-functionalized hybrids lacking metal activator ions have been introduced, such as those obtained from 3-aminopropyltriethoxysilane (APTES) and 3-glycidyloxypropyltrimethoxysilane (GPTES),[56-61] urea [NHC(=O)NH], urethane [NHC(=O)O], and amide [NHC(=O)] crosslinked precursors, classed as di-ureasils,[38,62-66] di-urethanesils,[67,68] and di-amidosils,[69] respectively. The APTES hybrid including formic acid is one of the most efficient phosphors known among those not containing metal activator ions, with an external photoluminescence quantum yield of 0.35 ± 0.10.[56] The APTES acetic acid analog exhibits two distinct emissions with quantum yields between 0.12 and 0.20 [57] and similar values were reported for the di-ureasils, di-urethanesils and di-amidosils.[65,66,68,69] The potential technological relevance of these amine- or amide-functionalized hybrids for the fabrication of several nanostructured systems, such as efficient white-light room-temperature emitters,[38,62-70] was demonstrated. The efficient photoluminescence (quantum yields higher than those reported for amorphous porous silicon[71] and similar to the typical values of the most efficient conjugated polymers[72]) results from a convolution of the emission originated in the NH/C=O groups of the urea, urethane, or amide bridges with electron-hole recombination's occurring in the siloxane nanoclusters.[65,66]

Lanthanide ions, particularly the trivalent ones, Ln^{3+}, are special in photonics because of their unique photo-physical properties,[73] especially with respect to their application in phosphors,[73-75] generation and amplification of light in lasers (*e.g.*, Nd^{3+} in yttrium aluminum garnet, YAG[76]), and optical amplifiers (*e.g.*, Er^{3+} -doped fiber amplifiers, EDFA's[77,78]). The parity and spin-forbidden 4*f*–4*f* transitions of these ions are observed, with low molar absorption coefficients, ε (or absorption cross-sections, σ_{ABS}), typically $\varepsilon < 10 L.mol^{-1}.cm^{-1}$ (or $\sigma_{ABS} < 4 \times 10^{-20} cm^2$), in comparison with the values 10 times larger for 3*d*–3*d* transitions or 10^2 times larger for ligand-to-metal charge-transfer (LMCT) transitions. High luminescence quantum yields may be obtained for essentially narrow bandwidth, long-lived emission bands, lying from the ultra-violet (UV) to the near infrared (NIR) spectral regions. Furthermore, the 4*f*–4*f* transitions are ultrasensitive both in vitro and in vivo bioassays,[74,75,79] and the relatively low toxicity of Ln^{3+} ions (compared with that of heavy metals), especially in the complexed state,[80] and their high magnetic susceptibility allow the use of Ln^{3+}-bearing systems in multimodality resonance imaging and radionuclide anticancer therapies.[81,82] The sensitivity of the 4*f* transitions used to obtain information about the local environment around the metal ions[3,82] is particularly evident for Eu^{3+}, which is a powerful local ion probe (as detailed in chapter 2).

As already noticed, the direct Ln^{3+} photo-excitation is not very efficient, limiting the light output. However, this can be improved with the consequent increase of the Ln^{3+} luminescence intensity through the design of Ln^{3+} complexes, in which the ligands incorporate organic chromophores covalently bonded to the 4*f* metal centre. These molecules can also shield the metal ion from deleterious quenching interactions (*e.g.*, with water molecules or OH groups). These chromophores typically present effective absorption cross sections 10^4–10^5 times higher and over a much broader spectral range than the Ln^{3+} corresponding ones, and the energy they absorb can be transferred to nearby Ln^{3+} ions, which in turn undergo a radiative emitting process. In analogy to light harvesting molecules found in natural photosynthetic systems, this process is called Ln^{3+} luminescence sensitization, or antenna effect,[83] and such complexes may be seen as efficient light-conversion molecular devices.[84,85] Ln^{3+} ions form complexes with various organic molecules, such as aromatic carboxylic acids, β-diketonates, calixarenes, cryptands, podands, and heterocyclic ligands, emitting efficiently in the near-UV (Ce^{3+} and Gd^{3+}), visible (blue, Tm^{3+}; green, Tb^{3+} and Er^{3+}; yellow, Dy^{3+}; orange, Sm^{3+}; and red,

Eu^{3+}), and NIR (Nd^{3+}, Er^{3+}, Tm^{3+} and Yb^{3+}) spectral regions. These materials are of great interest for a wide range of photonic applications, such as tunable lasers, amplifiers for optical communications, components of the emitter layers in multilayer organic light-emitting diodes (OLEDs), luminescent labels in advanced time-resolved fluoro-immunoassays, light concentrators for photovoltaic devices, and antenna in photosensitive bioinorganic compounds.[75,81,82,86,87] Important issues concern the somewhat low thermal and photochemical stability that together with poor mechanical properties represent relevant disadvantages concerning the technological applicability of Ln^{3+} complexes, namely in lighting, sensing, and displays. Moreover, most of them are usually isolated as hydrates, in which two or three water molecules are included in the first coordination sphere of the central ion, quenching the emission due to the activation of non-radiative decay paths. The degradation of most Ln^{3+} based complexes (*e.g.*, β-diketonate chelates[88,89]) under UV irradiation (in certain cases, in only a few hours) is often attributed to photo-bleaching or photon-induced chemical damage, and has not yet been completely elucidated.

In order to simultaneously overcome these drawbacks and to improve their thermal stability, mechanical features and light-emission properties (*e.g.*, quantum yield, lifetime, and UV photostability), Ln^{3+} complexes have been encapsulated into polymers,[90] liquid crystals,[91] and sol-gel derived organic/inorganic hybrids,[88,92-96] mostly siloxane-based ones, such as the ones presented in this thesis. The interest in the photoluminescence of Ln^{3+}-based organic/inorganic hybrids has thus grown considerably during the last decade, with the concomitant design of materials with tunable attributes and offering modulated properties, opening up exciting directions in materials science and related technologies, with significant implications in the nano-technological processing (*e.g.*, integration, miniaturization, and multi-functionalisation) of devices. Promising applications are therefore expected, such as light-emitting and quantum-dot devices, active waveguides in the vis-NIR spectral regions, active coatings, and bioanalytical and biomedical actuators and sensors.[79]

1.2 Objectives and organization of the thesis

The major objective of this thesis is to develop hierarchically ordered functional organic/inorganic hybrids with potential applications in photonics. Other objectives of the project is to address the mechanism of self-organization in order materials, the relationship between the ordered nanostructures and the corresponding emission properties and the energy transfer mechanisms within the non doped hybrid host and between the hybrid host and the Ln^{3+} ions.

This thesis is divided in six chapters. In the first chapter, the state of the art, the context of the work and the main aims of the thesis are described. The second chapter deals with the background concepts that will be used along the thesis such as the Ln^{3+} emission features, the energy transfer properties and the sol-gel method. Chapter three focuses on the origin and energy transfer processes behind the emission features of organic/inorganic hybrids, namely di-ureasils, that were well studied and characterized in previous works,[37,63] in order to have a theoretical scheme that might be useful in guiding the interpretation of experimental data and in the design of new organic/inorganic hybrids. In chapter 3, the origin and mechanisms of white-light emission in amine-functionalized hybrids lacking metal activator and energy transfer processes occurring in these hybrids and also in the same hybrids incorporating Eu^{3+} ions (as salt or complexes) are thus discussed. The following step of the thesis consisted in the synthesis of new hybrids with the purpose of studying the influence of both the organization and the organic unit in the photoluminescence features. In both cases the pristine and Ln^{3+} -containing hybrids were studied. This work is presented in chapter four and five on two different kinds of hybrids. In the fourth chapter, the structural and photoluminescence features of hybrids obtained from the same precursor (designated **P12**) using acidic or nucleophilic catalysis, in the presence of Eu^{3+} ions is described. The fifth chapter is devoted to a new bipyridine hybrid: the structural and photoluminescence features of the non doped host and the host incorporating Ln^{3+} ions (Eu^{3+},Tb^{3+} and Gd^{3+}) are presented. Finally, in chapter six the general conclusions and future perspectives are presented. In Appendix A, the description of the experimental techniques and the general conditions used are detailed, giving special emphases to photoluminescence which is the experimental key technique of this work. In Appendix B is given a resume of the thesis in French.

Main Results

- Quantitative discussion of the energy transfer mechanisms behind the white-light emission (which results from a convolution of the emission originated in the NH/C=O groups of the organic/inorganic cross-links with electron-hole recombinations occurring in the siloxane nanoclusters, both emissions typical of D-A pairs) of sol-gel derived amine- and amide-functionalized hybrids. The dipole-dipole energy transfer rate between the two emitting centres (3×10^{9} s^{-1}) is larger than the value estimated for the transfer rate mediated by the exchange mechanism (3.7×10^{8} s^{-1})

- Quantitative discussion of energy transfer occurring in sol-gel derived organic/inorganic di-ureasil hybrids incorporating either $[Eu(btfa)_3(4,4'\text{-bpy})(EtOH)]$ (btfa=benzoyltrifluoroacetonate, 4,4'-bpy=4,4'-bipyridine) or $Eu(CF_3SO_3)_3$. Host-to-Eu^{3+} energy transfer occurs either via ligand singlet and triplet excited states or directly from the hybrid emitting centres through the dipole-dipole, dipole-2^{λ} pole (λ = 2, 4 and 6) and exchange mechanisms. The ligand-to-Eu^{3+} energy transfer rate is typically one order of magnitude larger than the value estimated for direct hybrid-to-Eu^{3+} transfer (3.75×10^{10} and 3.26×10^{9} s^{-1}, respectively to the $^5D_1$ level). The most efficient luminescence channel is $(S_0)_{Hybrid} \rightarrow (T)_{Hybrid} \rightarrow (T)_{Ligand} \rightarrow (^5D_1, ^5D_0) \rightarrow {}^7F_{0\text{-}6}$.

- For the first time, a family of ordered Ln^{3+} doped organic/inorganic hybrids was introduced. In order to establish a relationship between the long range organisation of the hybrid materials and their physical properties, the photoluminescence features of the lamellar materials (the pristine form **L12** and the ones doped with Eu^{3+} ions **Eu@L12**) were compared with the ones of the corresponding amorphous hybrids (the pristine form **A12** and the ones doped with Eu^{3+} ions **Eu@A12**) derived from the same precursor. Hybrids with approximately the same Eu^{3+} concentration (~1 %) but with different morphologies (**L12@Eu-1** and **A12@Eu-1**) were synthesised starting from the same precursor. This family of hierarchical structured bridged silsesquioxanes gave a unique example in which the effect of the morphology in the photoluminescence features could be addressed in detail.

- Two amorphous bipyridine (bpy)-based materials were synthesized exhibiting high stability over time and the highest emission quantum yield values (0.22±0.02 and 0.18±0.02, respectively) reported so far in hybrid materials for excitation in the long UV/blue regions, stability over time using a commercial light emitting diode (LED). The origin of the emission was ascribed to three distinct components: i) bpy triplet state; ii) electron-hole recombinations originated in the ii) NH/C=O groups of the urea cross-linkages and iii) siliceous nanoclusters.

- Urea/bpy-based hybrids incorporating Eu^{3+}, Gd^{3+}, and/or Tb^{3+} ions were also synthesized and the key role played by the light emitted by the hybrid host in the luminescence of the corresponding Ln^{3+}-based hybrids was demonstrated.

Publications that resulted from the work

1) "Energy Transfer and Emission Quantum Yields of Organic/Inorganic Hybrids Lacking Metal Activator Centers", S. S. Nobre, P. P. Lima, L. Mafra, R. A. S. Ferreira, R. O. Freire, L. Fu, U. Pischel, V. de Zea Bermudez, O. L. Malta, and L. D. Carlos, *J. Phys. Chem. C*, **2007**, 111, 3275-3284.
2) "Energy Transfer Mechanisms in Organic/Inorganic Hybrids Incorporating Europium(III) – A Quantitative Assessment by Light Emission Spectroscopy", P. P. Lima, S. S. Nobre, R. O. Freire, S. A. Júnior, R. A. S. Ferreira, U. Pischel, O. L. Malta, L. D. Carlos, *J. Phys. Chem. C*, **2007**, 111, 17627-17634.
3) "Photoluminescence of Eu(III)-doped lamellar bridged silsesquioxanes self-templated through a hydrogen bonding array", S. S. Nobre, C. D. S. Brites, R. A. S. Ferreira, V. de Zea Bermudez , C. Carcel, J. J. E. Moreau, J. Rocha, M. Wong Chi Man, L. D. Carlos, *J. Mater. Chem.*, **2008**, 18, 4172-4182.
4) "Eu^{3+}- Assisted Short-Range Ordering of Photoluminescent Bridged Silsesquioxanes", S. S. Nobre, X. Cattoën, R. A. S. Ferreira, C. Carcel, V. de Zea Bermudez, M. Wong Chi Man and L. D. Carlos, *submitted.*
5) "Efficient tunable blue and green light emission of bipyridine-based bridged silsesquioxanes for solid-state lighting", S. S. Nobre, X. Cattoën, R. A. S. Ferreira, M. Wong Chi Man and L. D. Carlos, *submitted.*
6) "Lanthanide-containing 2,2-bipyridine bridged urea cross-linked polysilsequioxanes", S. S. Nobre, R. A. S. Ferreira, X. Cattoën, S. Benyahya, M. Taillefer, V. de Zea Bermudez, M. Wong Chi Man and L. D. Carlos, *accepted, Spectroscopy Letters.*

The work behind this thesis was also presented as five oral and fifteen poster presentations in national and international conferences.

1.3 References

1. C. Sanchez, *J. Mater. Chem.*, 2005, **15**, 3557.
2. P. Judeinstein and C. Sanchez, *J. Mater. Chem.*, 1996, **6**, 511.
3. L. D. Carlos, R. A. S. Ferreira, V. de Zea Bermudez and S. J. L. Ribeiro, *Adv. Mater.*, 2009, **21**, 509.
4. L. L. Hench and J. K. West, *Chem. Rev.*, 1990, **90**, 33.
5. J. Y. Wen and G. L. Wilkes, *Chem. Mater.*, 1996, **8**, 1667.
6. C. J. Brinker and G. W. Scherer, in *Sol–Gel Science: the Physics and Chemistry of Sol–Gel Processing*, Academic Press, San Diego, 1990.
7. F. Hoffmann, M. Cornelius, J. Morell and M. Froba, *Angew. Chem. Int. Edit.*, 2006, **45**, 3216.
8. L. Mercier and T. J. Pinnavaia, *Chem. Mater.*, 2000, **12**, 188.
9. D. G. Shchukin, G. B. Sukhorukov and H. Mohwald, *Angew. Chem. Int. Edit.*, 2003, **42**, 4472.
10. A. Shimojima and K. Kuroda, *Angew. Chem. Int. Edit.*, 2003, **42**, 4057.
11. A. Shimojima, Z. Liu, T. Ohsuna, O. Terasaki and K. Kuroda, *J. Am. Chem. Soc.*, 2005, **127**, 14108.
12. R. J. P. Corriu, J. J. E. Moreau, P. Thepot and M. Wong Chi Man, *Chem. Mater.*, 1992, **4**, 1217.
13. K. Shea, D. Loy and O. W. Webster, *Chem. Mater.*, 1989, **1**, 574.
14. B. Boury, R. J. P. Corriu, V. Le Strat, P. Delord and M. Nobili, *Angew. Chem. Int. Edit.*, 1999, **38**, 3172.
15. G. Cerveau, R. J. P. Corriu, E. Framery and F. Lerouge, *Chem. Mater.*, 2004, **16**, 3794.
16. G. Cerveau, R. J. P. Corriu, E. Framery and F. Lerouge, *J. Mater. Chem.*, 2004, **14**, 3019.
17. F. Lerouge, G. Cerveau and R. J. P. Corriu, *New. J. Chem.*, 2006, **30**, 1364.
18. X. F. Zhou, S. Yang, C. Z. Yu, Z. H. Li, X. Yan, Y. Cao and D. Y. Zhao, *Chem. Eur. J.*, 2006, **12**, 8484.
19. J. J. E. Moreau, L. Vellutini, M. Wong Chi Man, C. Bied, J. L. Bantignies, P. Dieudonne and J. L. Sauvajol, *J. Am. Chem. Soc.*, 2001, **123**, 7957.

20. J. J. E. Moreau, L. Vellutini, M. Wong Chi Man and C. Bied, *J. Am. Chem. Soc*., 2001, **123**, 1509.
21. J. J. E. Moreau, L. Vellutini, P. Dieudonne, M. Wong Chi Man, J. L. Bantignies, J. L. Sauvajol and C. Bied, *J. Mater. Chem.*, 2005, **15**, 4943.
22. J. J. E. Moreau, B. P. Pichon, G. Arrachart, C. Bied and M. Wong Chi Man, *New. J. Chem.*, 2005, **29**, 653.
23. J. J. E. Moreau, B. P. Pichon, M. Wong Chi Man, C. Bied, H. Pritzkow, J. L. Bantignies, P. Dieudonne and J. L. Sauvajol, *Angew. Chem. Int. Edit.*, 2004, **43**, 203.
24. Y. J. Zhang, Q. X. Tang, H. X. Li and W. P. Hu, *Appl. Phys. Lett.*, 2009, **94**, 203304.
25. M. Lu, B. H. Xie, J. H. Kang, F. C. Chen, Y. Yang and Z. H. Peng, *Chem. Mater.*, 2005, **17**, 402.
26. M. H. Valkenberg and W. F. Holderich, *Catalysis Reviews*, 2002, **44**, 321.
27. A. P. Wight and M. E. Davis, *Chem. Rev.*, 2002, **102**, 3589.
28. A. Brethon, C. Bied, J. J. E. Moreau and M. Wong Chi Man, *J. Sol-Gel Sci. Techn.*, 2009, **50**, 141.
29. J. W. Grate, S. N. Kaganove, S. J. Patrash, R. Craig and M. Bliss, *Chem. Mater.*, 1997, **9**, 1201.
30. A. Walcarius, *Chem. Mater.*, 2001, **13**, 3351.
31. H. Zhang, D. K. Pan, K. Zou, J. He and X. Duan, *J. Mater. Chem.*, 2009, **19**, 3069.
32. D. Arcos, I. Izquierdo-Barba and M. Vallet-Regi, *J. Mater. Sci: Mater. Med.*, 2009, **20**, 447.
33. M. K. Mistry, N. R. Choudhury, N. K. Dutta, R. Knott, Z. Q. Shi and S. Holdcroft, *Chem. Mater.*, 2008, **20**, 6857.
34. B. Q. Wang, B. Li, Q. Deng and S. J. Dong, *Anal. Chem.*, 1998, **70**, 3170.
35. C. Sanchez, B. Lebeau, F. Chaput and J. P. Boilot, *Adv. Mater.*, 2003, **15**, 1969.
36. V. Bekiari, P. Lianos and P. Judeinstein, *Chem. Phys. Lett.*, 1999, **307**, 310.
37. L. D. Carlos, V. de Zea Bermudez, R. A. S. Ferreira, L. Marques and M. Assunção, *Chem. Mater.*, 1999, **11**, 581.
38. V. de Zea Bermudez, L. D. Carlos, M. C. Duarte, M. M. Silva, C. J. R. Silva, M. J. Smith, M. Assunção and L. Alcacér, *J. Alloy Compd.*, 1998, **277**, 21.

39. P. Escribano, B. Julian-Lopez, J. Planelles-Arago, E. Cordoncillo, B. Viana and C. Sanchez, *J. Mater. Chem.*, 2008, **18**, 23.
40. A. Quach, V. Escax, L. Nicole, P. Goldner, O. Guillot-Noel, P. Aschehoug, P. Hesemann, J. Moreau, D. Gourier and C. Sanchez, *J. Mater. Chem.*, 2007, **17**, 2552.
41. R. Hernandez, A. C. Franville, P. Minoofar, B. Dunn and J. I. Zink, *J. Am. Chem. Soc.*, 2001, **123**, 1248.
42. C. Sanchez and B. Lebeau, *Mrs. Bull.*, 2001, **26**, 377.
43. C. L. Lu and B. Yang, *J. Mater. Chem.*, 2009, **19**, 2884.
44. Y. F. Li, J. H. Zhang, S. J. Zhu, H. P. Dong, Z. H. Wang, Z. Q. Sun, J. R. Guo and B. Yang, *J. Mater. Chem.*, 2009, **19**, 1806.
45. C. Sanchez, F. Ribot and B. Lebeau, *J. Mater. Chem.*, 1999, **9**, 35.
46. M. Faloss, M. Canva, P. Georges, A. Brun, F. Chaput and J. P. Boilot, *Appl. Opt.*, 1997, **36**, 6760.
47. S. Motakef, J. M. Boulton and D. R. Uhlmann, *Opt. Lett.*, 1994, **19**, 1125.
48. R. Buestrich, F. Kahalenberg, M. Popall, P. Dannberg, R.-M. Fiedler and O. Rösch, *J. Sol-Gel Sci. Technol.*, 2001, **20**, 181.
49. E. J. Assar, R. R. Gonçalves, M. Ferrari, Y. Massaddeq and S. J. L. Ribeiro, *J. Alloys Comp.*, 2002, **344**, 221.
50. D. C. Oliveira, A. G. Macedo, N. J. O. Silva, C. Molina, R. A. S. Ferreira, P. S. Andre, K. Dahmouche, V. D. Bermudez, Y. Messaddeq, S. J. L. Ribeiro and L. D. Carlos, *Chem. Mater.* , 2008, **20**, 3696.
51. C. M. S. Vicente, E. Pecoraro, R. A. S. Ferreira, P. S. Andre, R. Nogueira, Y. Messaddeq, S. J. L. Ribeiro and L. D. Carlos, *J. Sol-Gel Sci. Techn.*, 2008, **48**, 80.
52. C. M. McDonagh, A. M. Shileds, A. K. Mcevoy, B. D. MacCraith and F. F. Gouin, *J. Sol-Gel Sci. Technol.*, 1998, **13**, 207.
53. P. Lavin, C. M. McDonagh and B. D. MacCraith, *J. Sol-Gel Sci. Technol.*, 1998, **13**, 641.
54. L. T. Canham, *Appl. Phys. Lett.*, 1990, **57**, 1046.
55. C. Sanchez, B. Julian, P. Belleville and M. Popall, *J. Mater. Chem.*, 2005, **15**, 3559.
56. W. H. Green, K. P. Le, J. Grey, T. T. Au and M. J. Sailor, *Science*, 1997, **276**, 1826.
57. V. Bekiari and P. Lianos, *Langmuir*, 1998, **14**, 3459.

58. Y. Uchida, Y.-I. Nobu, I. Momiji and H. Matsui, *J. Sol-Gel Sci. Technol.*, 2000, **19**, 705.

59. Y. Han, J. Lin and H. Zhang, *J. Mater. Lett.*, 2002, **54**, 389.

60. E. Cordoncillo, F. J. Guaita, P. Escribano, C. Philippe, B. Viana and C. Sanchez, *Opt. Mater.*, 2001, **18**, 309.

61. T. Brankova, V. Bekiari and P. Lianos, *Chem. Mater.*, 2003, **15**, 1855.

62. S. J. L. Ribeiro, K. Dahmouche, C. A. Ribeiro, C. V. Santilli and S. H. Pulcinelli, *J. Sol-Gel Sci. Techn.*, 1998, **13**, 427.

63. V. de Zea Bermudez, L. D. Carlos and L. Alcácer, *Chem. Mater.*, 1999, **11**, 569.

64. E. Stathatos, P. Lianos, U. L. Stangar, B. Orel and P. Judeinstein, *Chem. Mater.*, 2000, **16**, 8672.

65. L. D. Carlos, R. A. S. Ferreira, V. de Zea Bermudez and S. J. L. Ribeiro, *Adv. Funct. Mater.*, 2001, **11**, 111.

66. L. D. Carlos, R. A. S. Ferreira, R. N. Pereira, M. Assunção and V. de Zea Bermudez, *J. Phys. Chem. B*, 2004, **108**, 14924.

67. M. C. Gonçalves, V. de Zea Bermudez, R. A. S. Ferreira, L. D. Carlos, D. Ostrovskii and J. Rocha, *Chem. Mater.*, 2004, **16**, 2530.

68. L. S. Fu, R. A. S. Ferreira, N. J. O. Silva, L. D. Carlos, V. De Zea Bermudez and J. Rocha, *Chem. Mater.*, 2004, **16**, 1507.

69. S. C. Nunes, V. de Zea Bermudez, J. Cybinska, R. A. S. Ferreira, J. Legendziewicz, L. D. Carlos, M. M. Silva, M. J. Smith, D. Ostrovskii and J. Rocha, *J. Mater. Chem.*, 2005, **15**, 3876.

70. V. Bekiari, E. Stathatos, P. Lianos, U. L. Stangar, B. Orel and P. Judeinstein, *Chem. Mater.*, 2000, **12**, 3095.

71. L. Pavesi, L. Dal Negro, C. Mazzoleni, G. Franzó and F. Priolo, *Nature*, 2000, **408**, 440.

72. N. C. Greenham, I. D. W. Samuel, A. B. Holmes and R. H. Friend, *Chem. Phys. Lett.*, 1995, **241**, 89.

73. G. Blasse and B. C. Grabmaier, *Luminescent Materials*, Berlin, Germany, 1994.

74. T. Justel, H. Nikol and C. Ronda, *Angew. Chem. Int. Ed.*, 1998, **37**, 3085.

75. M. H. V. Werts, N. Nerambourg, D. Pelegry, Y. Le Grand and M. Blanchard-Desce, *Photochem. Photobiol. Sci.*, 2005, **4**, 531.

76. J. Marling, *IEEE J. Sel. Top. Quantum Electron*, 1978, **14**, 56.
77. K. Kuriki, K. Y. and Y. Okamoto, *Chem. Rev.*, 2002, **102**, 2347.
78. A. Polman and F. C. J. M. Van Veggel, *J. Opt. Soc. Am. B*, 2004, **21**, 871.
79. S. Comby and J.-C. G. Bünzli, in *Handbook on the Physics and Chemistry of Rare Earths*, eds. K. A. Gschneider, J.-C. G. Bünnzli and V. K. Pecharsky, Elsevier Science, New York, 2007.
80. L. Thunus and R. Lejeune, *Coord. Chem. Rev*, 1999, **184**, 125.
81. D. Parker, R. S. Dickins, H. Puschmann, C. Crossland and J. A. K. Howard, *Chem. Rev.*, 2002, **102**, 1977.
82. J.-C. G. Bünnzli, in *Lanthanide Probes in Life, Chemical and Earth Sciences, Theory and Practice*, eds. G. R. Choppin and J.-C. G. Bünnzli, Elsevier, Amsterdam, Netherlands, 1989.
83. J.-M. Lehn, *Angew. Chem. Int. Edit.*, 1990, **29**, 1304.
84. N. Sabbatini, M. Guardigli and J.-M. Lehn, *Coord. Chem. Rev.*, 1993, **123**, 201.
85. G. F. de Sá, O. L. Malta, C. D. Donegá, A. M. Simas, R. L. Longo, P. A. Santa-Cruz and E. F. da Silva, *Coord. Chem. Rev.*, 2000, **196**, 165.
86. J. Kido and Y. Okamoto, *Chem. Rev.*, 2002, **102**, 2357.
87. J. C. G. Bunzli and C. Piguet, *Chem. Soc. Rev.*, 2005, **34**, 1048.
88. P. P. Lima, R. A. S. Ferreira, R. O. Freire, F. A. A. Paz, L. S. Fu, S. Alves, L. D. Carlos and O. L. Malta, *Chemphyschem*, 2006, **7**, 735.
89. A. C. Franville, D. Zambon, R. Mahiou and Y. Troin, *Chem. Mater.*, 2000, **12**, 428.
90. Q. D. Ling, M. J. Yang, Z. F. Wu, X. M. Zhang, L. H. Wang and W. G. Zhang, *Polymer*, 2001, **42**, 4605.
91. P. Carette, C. Li, J. Boyaval and B. Meziane, 2003, **35**, 909.
92. L. S. Fu, R. A. S. Ferreira, N. J. O. Silva, J. A. Fernandes, P. Ribeiro-Claro, I. S. Goncalves, V. De Zea Bermudez and L. D. Carlos, *J. Mater. Chem.*, 2005, **15**, 3117.
93. K. Binnemans, in *Handbook on the Physics and Chemistry of Rare Earths*, eds. K. A. Gschenieder, J.-C. G. Bünnzli and V. K. Pecharsky, 2005.
94. M. Fernandes, V. de Zea Bermudez, R. A. S. Ferreira, L. D. Carlos, A. Charas, J. Morgado, M. M. Silva and M. J. Smith, *Chem. Mater.*, 2007, **19**, 3892.

95. H. R. Li, J. Lin, H. J. Zhang, L. S. Fu, Q. G. Meng and S. B. Wang, *Chem. Mater.*, 2002, **14**, 3651.

96. M. H. V. Werts, R. T. F. Jukes and J. W. Verhoeven, *Phys. Chem. Chem. Phys.*, 2002, **4**, 1542.

Chapter 2 – Background

2.1 Electronic structure and energy levels of lanthanides

The rare earth elements are characterized by the progressive fulfillment of the 4*f* and 5*f* atomic orbitals and are divided in two groups: lanthanides and actinides. The lanthanides have a base electronic structure common to that of Xenon, $1s^2 2s^2 2p^6 3s^2 3p^6 3d^{10} 4s^2 4p^6 4d^{10} 5s^2 5p^6$ with two or three valence electrons ($6s^2$ or $5d^1 6s^2$) and the progressive fulfilment (with the increase of the atomic number) of the 4*f* orbitals. This group consists of fifteen elements with atomic numbers 57 through 71, from lanthanum to lutetium. In the solid state, these elements originate, in general, ions triply ionized, which involves the variation of the number of valence electrons, *N*, between *N=1* and *N=14*. The first ionization state of lanthanides results from the removal of one electron 6*s*, lutetium being the only exception. The second state of ionization corresponds to the removal of another 6*s* electron. Finally, the third ionization state, which is the general state usually observed for these elements, occurs with the removal of 6*s* and 5*d* electrons and, frequently, also, one 4*f* electron. This electronic structure is responsible for the transitions between states of the $4f^N$ configuration. Among the lanthanides, the Sm^{3+}, Eu^{3+}, Tb^{3+} and Dy^{3+} ions generally exhibit luminescence properties in the visible region, as the difference in energy between the fundamental state and the first excited states is *ca.* 7000-15000 cm^{-1}. In the Pr^{3+}, Nd^{3+}, Ho^{3+}, Er^{3+}, Tm^{3+} and Yb^{3+} cations, due to the higher proximity between the fundamental state and the excited state, the non radiative transitions are favored, relatively to the former case. The Gd^{3+} is not luminescent in the visible spectral region, as the difference between the fundamental state and the first excited state is very high (*ca.* 32000 cm^{-1}) and the La^{3+} and Lu^{3+} ions have the 4*f* shell empty and filled, respectively.[1]

The first emission and excitation spectra of compounds based on triply ionized lanthanides were observed by *Becquerel*, in 1908.[2] At low temperatures, the emission and absorption spectra of compounds with triply ionized lanthanides are, in general, characterized by sharp and well defined lines, in some cases separated by just few cm^{-1}. These lines, comparable to the spectral lines of atoms and free molecules, result from the splitting of the energy levels of the $4f^N$ configuration, by action of the electrostatic field generated by the surrounding ligands. The quasi-atomic nature of the spectra suggests that the interaction between the ion and the ligands is small compared, for instance, with the transition metals. This fact is consistent with the delocalization of the $4f^N$ orbital inside the

$5s^2$ and $5p^6$ orbitals, the $4f^N$ electrons being shielded by those external orbitals. This shielding effect allows treating the local field interaction as a perturbation to the atomic levels energy of the $4f$ orbital. These elements have, accordingly, a small ability to participate in the formation of chemical bonding. The delocalization of the $4f$ shell is known as lanthanidic contraction.[3]

In Table 2.1 are presented, as an example, the energy terms (multiplets) of the $4f^6$ configuration for the Eu^{3+} expressed in the *Russel-Saunders* coupling scheme.[4] In this notation the orbital angular momenta of the individual electrons add to form a resultant orbital angular momentum *L*. Likewise, the individual spin angular momenta are presumed to couple to produce a resultant spin angular momentum *S*. Then *L* and *S* combine to form the total angular momentum *J*, with J_Z being its z component:

$$J = \begin{cases} |S+L|,...,S-L \Leftarrow S > L \\ L+S,...L-S \Leftarrow S \leq L \end{cases} \tag{2.1}$$

In *Russel-Saunders* coupling scheme, the terms *L* and *S* define one of the (2S+1)(2L+1) terms (or multiplets) of the configuration, generic represented by $^{(2S+1)}L_J$, in which (2S+1) indicates the spin multiplicity.

Table 2.1 Multiplets of the configuration $4f^6$.

Configuration	Multiplets	Total number of multiplets
f^6	^{1}S P D F G H I K L M N ^{3}P D F G H I K L M N O **4 6 4 8 4 7 3 4 2 2 6 5 9 7 9 6 6 3 3** ^{5}P D F G H I K L ^{7}F **3 2 3 2 2**	119

The numbers (in bold) under the different terms in Table 2.1 indicate the number of multiplets described by the same values of *L* and *S*, showing that these numbers are not sufficient to individually classify each energy term. The introduction of other quantum numbers is necessary (generally represented by α) in order to allow the classification of the multiplets.[4] By introducing such quantum numbers, the $4f^N$ states are completely defined by the base states $|(4f^N)\alpha SLJJ_Z\rangle$. Each of these energy levels can be represented by a

barycenter corresponding to the average of the energy. This average energy level is represented by the Hamiltonian of the free ion H_{FI}, which describes the interactions between the N electrons of the 4*f* shell, as the other shells are completely filled. To a first approximation the effect of the filled electronic shells (or subshells), which are spherically symmetric, is the same for all the terms of the $4f^N$ configuration. The Hamiltonian H_{FI} is written as:

$$H_{FI} = H_o + H_c + H_{SO} = \left[-\frac{\hbar^2}{2m}\sum_{i=1}^{N}\nabla_i^2 - \sum_{i=1}^{N}\frac{Ze^2}{r_i} \right] + \sum_{i<j}\frac{e^2}{r_{ij}} + \sum_{i=1}^{N}\xi(r_i)\vec{s}_i.\vec{l}_i \qquad (2.2)$$

where Ze^2 represents the effective charge of each nucleus (Z is the atomic number and e the electron charge), r_i and r_{ij} represent the distances of each electron to the nucleus and between the electrons i and j, respectively, $\xi(r_i)$ is the spin-orbit coupling parameter, $\vec{s}_i$ is the spin coordinate and $\vec{l}_i$ the orbital coordinate. The first term (H_0) corresponds to the kinetic energy of the N electrons 4*f*, and like the second term (H_c), relative to the nucleus-electron interaction, has spherical symmetry. These terms are not very important for the analysis of the energy values of the different states of the 4*f* configuration. Since they are purely radial, they contribute in an equal way to all the energetic states, without changing the relative energies of the several states of the configuration. The third term (*Hso*) spin-orbit interaction. The relative magnitude of the different interactions follows the order: $H_o > H_e > H_{SO}$. Being so, in a first approximation, H_{FI} can be written as the sum of the term corresponding to the interaction between the N electrons and the term relative to spin-orbit interaction. The term H_e does not act in the spin coordinate because it is an electrostatic interaction. The term H_{SO} is formed by two tensor operators, one which acts in the spin coordinate $\vec{s}_i$ and the other acts in the orbital coordinate $\vec{l}_i$. In the case of Ln^{3+}, and as we are in the presence of an intermediate coupling scheme (the case where the Coulomb and spin-orbit interaction have a similar contribution), these two terms are approximately of the same order of magnitude.[5] As a consequence, H_e cannot be taken as a perturbation to H_{SO} (as in the case of the *j-j* coupling). The reverse case, in which the spin-orbit term is a perturbation to the repulsive interaction term (*Russel-Saunders* coupling or *L-S*) is also not valid in this coupling scheme. Even though the *L-S* coupling does not fit perfectly with the

experimental data it reveals to be a very good approximation in the case of the fundamental multiplet of Eu^{3+} ions.

Even though the interaction between the 4*f* electrons and the chemical environment is small it is responsible for the optical properties of the Ln^{3+} ions. On placing a Ln^{3+} ion in a given chemical environment (crystal, glass, solution), the spherical symmetry of the free ion is destroyed and each spectroscopic level splits under the influence of the asymmetric electric field produced by the environment. This is termed the crystal, or ligand, field effect. The interaction between the ions and the environment is written in terms of a local-field Hamiltonian, H_{LF}, which translates the breaking of the symmetry levels of the free ion. This symmetry breaking gives rise to the field degeneracy removal, in maximum of (2*J* + 1) components for integer values of *J*. Each component of the local field is characterized by the quantum number J_Z. The breaking of degeneracy by a field generated by the ligands around the ion is called Stark effect, which is dependent on the local symmetry group around the ion in the host, as shown in Table 2.2.

The number of spitted components increases with the decreasing symmetry of the ion surroundings. This happens because the decrease of the symmetry corresponds to a decrease of the number of equivalent directions, or in other words, the charge distribution around the ion becomes less spherical (characteristic of the free ion). Consequently, the interaction between the ion and the charge distribution around will provoke a splitting of the free ion levels.

Table 2.2 Splitting observed in each of the *J* levels (integer *J*) for the 32 groups of symmetry[a].

Crystallographic system	J						
	0	1	2	3	4	5	6
Cubic	1	1	2	3	4	4	6
Hexagonal and trigonal	1	2	3	5	6	7	9
Tetragonal	1	2	4	5	7	8	10
Triclinic, monoclinic and orthorhombic	1	3	5	7	9	11	13

[a] **Cubic:** O_h, O, T_d, T_h, T**; Hexagonal:** D_{6h},D_6,C_{6v},C_{6h},C_6,D_{3h},C_{3h}; **Tetragonal:** D_{4h},D_4,C_{4v},C_{4h},C_6,D_{2d},S_4; **Trigonal:**D_{3d},D_3,C_{3v},C_3,S_6; **Orthorhombic:** D_{2h}, D_2,C_{2v}; **Tetragonal:** C_{2h}, C_2,Cs (or C_{1h}); **Triclinic:** S_2 (or C_i), C_1.

The Hamiltonian for an ion placed in a ligand field is written as:

$$H = H_{FI} + H_{LF} \tag{2.3}$$

This term H_{FI} is responsible for the breaking of the spherical symmetry and the consequent splitting of the energy levels in a number of J_Z components is treated as a perturbation to H_{FI}. This is a consequence of the shielding effect of the $5s^2$ and $5p^6$ shells to the 4*f* one. The delocalization of the 4*f* orbital within the other orbital's implies that the ion is just slightly affected by the field generated by the surroundings. The potential of the surrounding will be a small perturbation to the energetic levels of the free ion, whose degeneracy will be lifted in a maximum of (2*J*+1) components. This potential can be given in terms of the punctual charge model introduced by H. Bethe in 1922, which considers the host as a matrix of punctual charges where the ion will be included.[6] Within this context it is possible to calculate the potential of the surroundings of the ion and the potential energy of the 4*f* ions under its action. Assuming that the host has a charge density of $\rho(\vec{R})$ and that the position of the 4*f* electrons is $\vec{r}_i$, the potential energy of each electron in the host, in a volume $d\tau$, accordingly within the formalism developed by Wybourne[5], is described as:

$$V = -\sum_i \int \frac{e_i \rho(\vec{R})}{\left|\vec{R} - \vec{r}_i\right|} d\tau, \ \vec{R} > \vec{r}_i \tag{2.4}$$

V can be expanded in terms of the spherical harmonic function, if the interaction between pairs of electrons *i* and *j* is described by the Legendre polynomials.[7] In this way, it is possible to separate the angular variables from the radial variable, using the Poisson formula. The coordinates $(r_i, \vartheta_i, \varphi_i)$ define the position of the electron *i* and can be expanded in terms of tensor operators, C_q^k [8]. Finally, *V* can be presented as:

$$V = -\sum_{k,q,i} B_q^k C_q^k(\vartheta_i, \varphi_i) \tag{2.5}$$

where the B_q^k (k=2,4,6) parameters are the so-called ligand field parameters of even rank and $C^{(k)}$ is a Racah tensor operator of rank *k* proportional to the spherical harmonic functions. The values of *k* are restricted by parity and triangularity rules for *f* orbitals,[5] *q* depend on the symmetry of the ligand field around the rare earth ion, and in this expression the index *i* runs over the 4*f* electrons. The local field parameters B_q^k are determined phenomenologically. Because the *V* Hamiltonian describes the break of spherical symmetry of the free ion, responsible for the splitting of each level in a maximum of (2*S*+1) components, the number of B_q^k parameters different from zero depends on the punctual symmetry group around the ion in the host.[9]

The ligand field interaction is also of fundamental importance in the case of 4*f*-4*f* transition intensities. Since we are concerned with optical transitions, two operators can perform the transition: the electric dipole operator (ED) and the magnetic dipole operator (MD). The 4*f*-4*f* transitions are in principle electric dipole forbidden by Laporte's rule which states that electronic transitions conserving either symmetry or asymmetry with respect to an inversion center are forbidden. However, the interaction with the ligand field parameters of odd parity or with vibrational states of the host, also, of odd parity mixes electronic states of different parity into the 4*f* wave function. Moreover, the interaction with the ligand field tensor operator mixes electronic states with different *J* but same *S* and *L*. This is the so-called *J*-mixing.

Fig. 2.1 displays a schematic representation and order of magnitude of the effects of the intra-atomic and ligand field interactions acting on the $4f^N$ configuration, in particular of the Eu^{3+} ion.

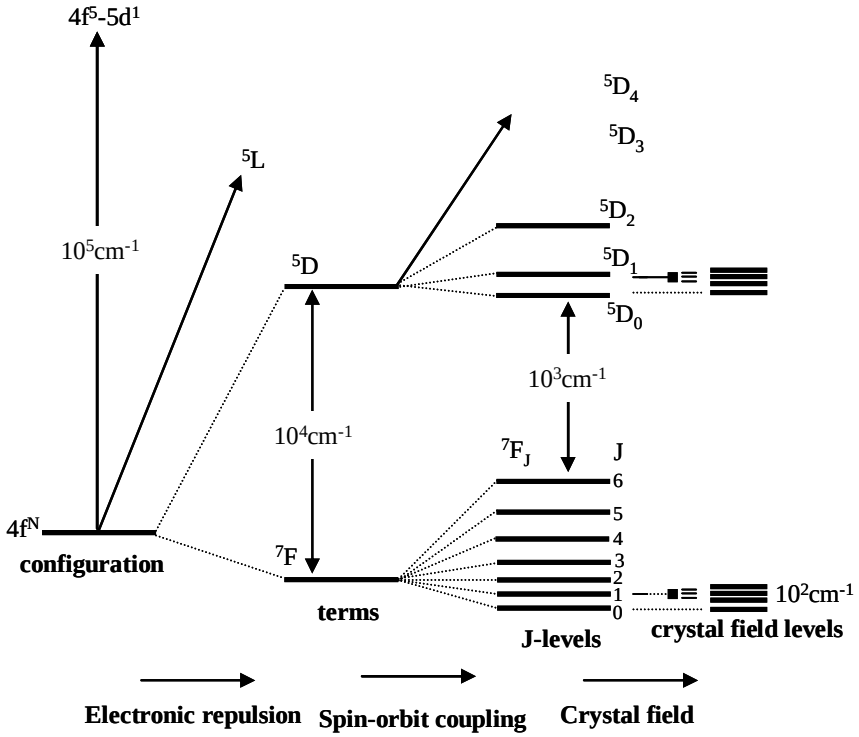

Figure 2.1 Schematic representation and order of magnitude of the effects of the intra-atomic and ligand field interactions acting on the $4f^N$ configuration of the Eu^{3+} ion.[10]

2.2 The 4*f* - 4*f* transitions

The optical properties of Ln^{3+}-containing materials are directly related to the *f–f* transitions in a $4f^N$ electronic configuration.[10-14]

The experimental oscillator strength P_{EXP} is directly proportional to the area under the absorption curve, and is given by:[14,15]

$$P_{EXP} = 4.32\times10^{-9}\frac{1}{\chi}\int \varepsilon(\bar{\nu})d\bar{\nu} \tag{2.6}$$

where $\chi = \frac{(n^2+2)^2}{9n}$ is the local electric field correction factor with the refractive index of the medium *n* and $\bar{\nu}$ is the transition wavenumber. Values of the order of 10^{-6} are observed for P_{EXP}, and both electric- and magnetic-dipole mechanisms are mainly evoked for the reasoning of such experimental intensities.

The Laporte forbidden electric-dipole transitions were treated by Judd[11] and Ofelt[12] in 1962. The calculated oscillator strength, P_{ED}, due to a forced electric-dipole mechanism, *i.e.*, the electric dipole caused by the lack of inversion symmetry, for transitions between f^N states ψJ and $\psi' J'$, was in short given by:[14]

$$P_{ED} = \sum_{\lambda} T_{\lambda}\nu\left|\left\langle f^N \psi J \left\| U^{(\lambda)} \right\| \psi' J' \right\rangle\right|^2 \tag{2.7}$$

where *v* is the transition frequency and $U^{(\lambda)}(\lambda = 2,4,6)$ is the square of the matrix elements of the unit tensor operators of rank λ connecting the initial and final states. The so-called Judd–Ofelt intensity parameters, T_λ, include fundamental constants values, radial wavefunctions of the states, the refractive index correction, and the ligand-field parameters.[14]

Considering Eq. 2.7, the values achieved for the intensity parameters can be compared with experimental ones, determined from a least-squares fit of oscillator-strength values calculated from absorption measurements (phenomenological T_λ parameters). Judd observed underestimated values for the calculated oscillator strengths, suggesting that

other mechanisms probably contributed to the experimental intensities, in addition to the forced electric-dipole one. In an attempt to explain the uncommon intensity variation of some hypersensitive 4*f*–4*f* transitions, Jørgensen and Judd[16] , studied the influence of an additional mechanism, namely dynamic coupling, which could be as operative as the forced electric-dipole mechanism (or, for some transitions, even more relevant).[10] In a simple way, the dynamic coupling mechanism can be described assuming that the electric field of the incident radiation induces the formation of oscillating dipoles on the atoms in the neighbourhood of the Ln^{3+} cations, producing an additional oscillating electric field.[14] Carnall *et al.*[15] kept the same expression for the calculated oscillator strength and removed the *J* dependence of the T_λ values by introducing the τ_λ intensity parameters, in order to facilitate comparison among different lanthanide ions [$\tau_\lambda = T_\lambda(2J+1), (2J+1)$ is the degeneracy of the initial $f^N \psi J$ state of a particular ψJ state of a particular Ln^{3+} ion].[14] Later on, the refractive-index dependence and the fundamental constants were also removed from the intensity parameters, and Judd-Ofelt's equation became:[17]

$$P_{ED} = \chi \frac{8\pi^2 mc\bar{\nu}}{3h(2J+1)} \sum_{\lambda=2,4,6} \Omega_\lambda \left| \left\langle f^N \psi J \left\| U^{(\lambda)} \right\| \psi' J' \right\rangle \right|^2 \tag{2.8}$$

where *h* is Planck's constant, *m* the electron mass, *c* the velocity of light in vacuum and $\sum \Omega_\lambda \left| \left\langle f^N \psi J \left\| U^{(\lambda)} \right\| \psi' J' \right\rangle \right|^2$ is known as the electric-dipole line strength, S_{ED}. The relationship between the original T_λ and Ω_λ is given by:[14]

$$\Omega_\lambda = T_\lambda (2J+1) \left(\frac{8\pi mc\chi}{3h}\right)^{-1} \tag{2.9}$$

The second important mechanism that can be considered for f–f transitions is the magnetic dipole one, which accounts, in a few cases, for the observed absorption intensity (totally or partially). The magnetic-dipole oscillator strength is given by:[14]

$$P_{MD} = \frac{8\pi mc}{3h(2J+1)} \bar{\nu} n \left[-\frac{e}{2mc} \left| \left\langle f^N \psi J \left\| L + 2S \right\| f^N \psi' J' \right\rangle \right|^2 \right] \tag{2.10}$$

where the term between brackets is the magnetic-dipole line strength, S_{MD}, and ($L+2S$) is the spin-orbit operator.[14]

An important issue to be pointed out is that the matrix elements involved in the magnetic-dipole line strength do not depend on the ligand field and, in a good approximation, can be considered constant. The magnetic-dipole oscillator strength can be written as:

$$P_{MD} = P'_{MD}\, n \tag{2.11}$$

where P'_{MD} is the value calculated by Carnall *et al.*[15] for measurements in aqueous solutions. This value is considered in the experimental oscillator strength, in addition to the electric dipole component.[14]

Back to the Judd–Ofelt expression for P_{ED}, since the fundamental work in 1962, the expression became popular and useful, with intensity parameters being obtained, most of the time, by a phenomenological approach. The success was due to the fact that a multi-line absorption spectrum can be accounted with only three intensity parameters, and different host matrices can be compared. Moreover, important parameters difficult to obtain experimentally, such as radiative lifetime values or excited-state absorption coefficients, can easily be calculated with the three intensity parameters.[14]

Since some of the foreseen applications of Ln^{3+}-doped organic/inorganic hybrids consider spontaneous light emission in photonic devices, important parameters to take into account are radiative lifetime values, emission quantum efficiency and quantum yield.[14]

The radiative lifetime (τ_{RAD}) value for a given $f^N\psi' J'$ excited state is obtained as the reciprocal of the total transition radiative probability A_T, which is the sum of all possible radiative decay rates from the J' state towards lower J levels. τ_{RAD} is given by:[14]

$$\tau_{RAD} = \frac{1}{A_T} = \frac{1}{\sum_J A_{J'J}} \tag{2.12}$$

where $A_{J'J}$, is the radiative transition probability (Einstein's spontaneous emission rate), given by:[14]

$$A_{JJ'} = \frac{64\pi^4 e^2 \bar{\nu}^3}{3h(2J+1)}\left[n^2 \chi S_{ED} + n^3 S_{MD}\right] \quad (2.13)$$

where the expressions for S_{ED} and S_{MD} have been described above.

The emission quantum efficiency of a given excited level J' (sometimes called intrinsic quantum yield) is given by the ratio between the radiative decay rate and the total decay rate, which also includes all other processes contributing to the depopulation of the J' level, such as nonradiative decay paths and energy-transfer processes.[14]

Considering the radiative lifetime described above and the experimental lifetime ($\tau_{EXP} = \tau_{RAD} + \tau_{NRAD}$), given by the reciprocal of the total decay rate, the emission quantum efficiency (η) of an excited level is calculated by:[14]

$$\eta = \frac{\tau_{EXP}}{\tau_{RAD}} = \frac{A_{RAD}}{A_{RAD} + A_{NRAD}} \quad (2.14)$$

The emission quantum yield (ϕ) is an experimentally evaluated quantity given by the ratio of number of emitted photons and number of absorbed ones, given by:

$$\phi = \frac{number\ of\ emitted\ photons}{number\ of\ absorved\ photons} \quad (2.15)$$

Considering the UV-excited vis-NIR Ln^{3+} emission in organic/inorganic hybrids, the emission quantum yield includes the absorption efficiency, the intersystem crossing efficiency, connecting ligand and/or host absorbing states with the ligand and/or donor states, the donor–Ln^{3+}, energy-transfer efficiency, the intra-Ln^{3+} nonradiative decay paths efficiency, connecting acceptor and emitting levels, and the J'-level emission quantum efficiency η. We should stress on that according to the above definitions for materials with only one type of emitting species $\eta \geq \phi$.[14]

2.3 The Particular case of the Eu^{3+} ion

In the case of the Eu^{3+} ions the intra-4*f* transitions occur, generally, between the $^5D_0$ and ^7F_J (J=0,1,2,3,4,5,6) levels. All these transitions are essentially of induce electric dipole type, except for the $^5D_0 \rightarrow {}^7F_1$ transition (magnetic). For Eu^{3+} the intensity parameters are difficult to obtain from experimental absorption measurements. In fact few absorption bands are observed with enough intensity in the visible range that could be used in the fitting of Judd's equation as described above. However, the pure magnetic-dipole character of the $^5D_0 \rightarrow {}^7F_1$ transition enables the determination of such intensity parameters from the emission spectrum. Since this transition does not depend on the local ligand field seen by Eu^{3+}, it may be used as reference for the entire spectrum. The $^5D_0 \rightarrow {}^7F_1$ spontaneous decay rate, A_{01}, is given by $A_{01} = A_{01}^{'} n^3$, where $A_{01}^{'} = 14.65\, s^{-1}$ in vacuum.[18] In that way, the intensity of the $^5D_0 \rightarrow {}^7F_{0\text{-}6}$ transitions, I_{0J}, can be expressed in terms of the area of their emission curves, S_{0J}:[14]

$$I_{0J} = hc\bar{\nu}\, A_{0J}\, N(^5D_0) \equiv S_{0J} \tag{2.16}$$

where $N(^5D_0)$ is the population of the $^5D_0$ emitting level; it is possible to write the total radiative decay rate as:[14]

$$A_T = \sum_{J=0}^{6} A_{0J} = \frac{A_{01} hc\nu_{01}}{S_{01}} \times \sum_{J=0}^{6} \frac{S_{0J}}{hc\nu_{0J}} \tag{2.17}$$

Usually, the radiative contribution can be calculated from the relative intensities of the $^5D_0 \rightarrow {}^7F_{0\text{-}4}$ transitions, as the branching ratio for the $^5D_0 \rightarrow {}^7F_{5,6}$ transitions must be neglected, due to their poor relative intensity. As already stated, the ratio between experimental and radiative lifetimes defines the emission quantum efficiency. Furthermore, as shown below, in addition to the radiative path, the number of water molecules in the Eu^{3+} first coordination sphere can be estimated considering that only non-radiative transitions contribute to the $^5D_0$ state depopulation. From Eq. 2.13 the intensity parameters Ω_λ will be given by:

$$\Omega_\lambda = \frac{3h}{64\pi^4 e^2 \bar{\nu}^3} \frac{9}{n(n^2+2)^2} \frac{1}{\left|\left\langle {}^5D_0 \left\| U^{(\lambda)} \right\| {}^7F_J \right\rangle\right|^2} A_{0J} \quad (2.18)$$

with $\lambda=J=2$ and 4. Values for the squared reduced matrix elements are 0.0032 and 0.0023 for $J=2$ and 4, respectively.[19] When the intensity parameters are obtained phenomenological based on the emission spectra it is not possible to distinguish between the induced electric dipole mechanism and the dynamic coupling. The major contribution for the Ω_2 parameter is due to the hyper sensitive $^5D_0 \rightarrow {}^7F_2$ transition. The following correlation was observed: in compounds where a higher degree of covalency would be expected, this value presents a higher value.[20]

Besides the interest in Ln^{3+}-containing materials due to their light-emission properties, the sensitivity of the 4f transitions can also be used to obtain further information about the local environment around the metal ions.[1] This is another important feature particularly evident for Eu^{3+}, which is a powerful local ion probe due to some peculiar spectroscopic characteristics, such as:

- A large energy difference between the $^5D_0$ first excited state and the high-energy $^7F_6$ level of the fundamental septet (*ca.* 12300cm^{-1}). The smaller this gap, the easier is its closing by nonradiative deactivation (*e.g.*, O–H vibrations);
- A non-degenerated first excited state that allows a simpler Stark-effect analysis, with the subsequent correspondence between the observed *J*-splitting degeneracy and the Eu^{3+} local-site symmetry;
- The presence of the ligand-field-independent $^5D_0 \rightarrow {}^7F_1$ magnetic-dipole transition, already discussed above;
- The presence of a single $^5D_0 \rightarrow {}^7F_0$ line permitted for C_s,$C_{1,2,3,4,6}$, and $C_{2v,4v,6v}$ point symmetry groups with a predominantly electric-dipole nature and explained by J-mixing effects.[21-23] The energy of this non-degenerated transition may be directly related to the covalency of the chemical bonds of the first coordination shell in Eu^{3+} (nephelauxetic effect);[24]
- The observation of vibronic lines in a relatively large spectral region of the $^5D_0 \rightarrow {}^7F_2$ excitation transition (24400–21550 cm^{-1}), allowing, in a unique way, the

identification of vibration modes up to *ca.* 3000 cm^{-1}, related to the Ln^{3+} local environment;

- The presence of ligand to metal charge transfer (LMCT) in the UV-vis region of the excitation spectra, ascribed to particular ligand groups.

Thus, changes in the number of Stark components of each intra-4f manifold, variations in the relative intensity between them, differences observed in the energy of particular lines, and the analysis of the excited-state decay curves furnish important information about the metal-ion local coordination, such as the existence of more than one Eu^{3+} local symmetry group, the number of coordinated water molecules, the magnitude of the ligand field, and the importance of the covalency of the Eu^{3+}-ligands bonds.[14]

Generally, in Eu^{3+}-contaning hybrids the large values usually found for the full width at half maximum (fwhm) of the non-degenerated $^5D_0 \rightarrow {}^7F_0$ line, ranging typically from *ca.* 20 to 30 cm^{-1},[25] point out that in organic/inorganic hybrids, the Eu^{3+} ions are accommodated in a continuous distribution of closely similar local sites. Also, in general for Eu^{3+}-contaning hybrids, the number of Stark components observed for the $^7F_{1-4}$ levels corresponds to the $(2J+1)$ maximum local-field splitting (1, 3, 5, 7, and 9, respectively), indicating a low-symmetry local environment (belonging to the orthorhombic, triclinic, or monoclinic crystallographic classes).[23] If the Eu^{3+} local symmetry group does not present a centre of inversion, the Laporte's rule is relaxed due to odd parity terms in the ligand field Hamiltonian,[10] and the emission spectrum is dominated by the $^5D_0 \rightarrow {}^7F_2$ transition.

For Eu^{3+}-containing materials, the number of water molecules (n_w) in the first coordination shell may be obtained by the difference between the decay time values measured in H_2O and D_2O as:[26]

$$n_w = 1.11\left[\frac{1}{\tau(H_2O)} - \frac{1}{\tau(D_2O)} - 0.31\right] \qquad (2.19)$$

where $\tau(H_2O)$ and $\tau(D_2O)$ are the decay times in milliseconds in water and in D_2O, respectively, taken in this latter case as the purely radiative decay. However as stated above, the purely radiative decay may also be calculated from the experimental emission spectrum, and therefore τ_{RAD} can be used in Eq. 2.19 substituting $\tau(D_2O)$. The value

obtained experimentally for the decay τ_{EXP} is also used substituting $\tau(H_2O)$, and Eq. 2.19 can thus be used to calculate n_w in many different media, including Eu^{3+}-containing organic/inorganic hybrids.[14]

The analysis of the $^5D_0 \rightarrow {}^7F_0$ energy allows drawing further conclusions regarding the Eu^{3+} local coordination site. The energy of this transition is related with the so-called nephelauxetic effect, in which the red shift observed for *d-d* and *f-f* energy differences, with respect to the free ion, is associated with a decrease in the values of the Slater integrals F^k and spin-orbit coupling parameter ζ.[23] In fact, a phenomenological equation, expressing the nephelauxetic effect in terms of the red shift observed for the $^5D_0 \rightarrow {}^7F_0$ transition in a large series of Eu^{3+} compounds, has been proposed,[27] and a purely phenomenological parameter, interpreted as a covalency parameter, has been shown to correlate quite well with the nephelauxetic parameter *h* introduced by Jørgensen.[27,28] Therefore, changes occurring in the first Eu^{3+} coordination shell (number, type of coordinated ligands, and/or average radius) induce alterations in the energy of the $^5D_0 \rightarrow {}^7F_0$ transition, in such away that an increase of covalency reflects a shift towards lower energies.[28] An ordinal scale of covalency was recently formalized through a function of the overlap polarizability of a chemical bond (covalent fraction).[24,28] This function depends on the average volume of the overlap region, of the order of 1.5% of the volume of the Ln^{3+}-ligand molecular-like pair.[14]

2.4 Energy transfer

Fluorescence energy transfer is the transfer of the excited state energy from a donor to an acceptor, via a non radiative process, which can be modelled using Förster,[29,30] Dexter[30,31] or Malta[32-34] models.

The Dexter model[30,31] considers short range exchange interactions and the Förster[29,30] model takes multipolar long range interactions into account. The two approaches allow the calculation of the spectral overlap integral between the emission of the donor and the absorption of the acceptor. In the case of the Förster model, besides the overlap integral, it is also possible to calculate the critical radius R_0 for energy transfer, corresponding to the distance of separation for which the *D-A* energy transfer rate is equal to the rate of decay of the excited donor in the absence of acceptor. In the Dexter model,[31] however, the overlap integral is the only quantity that can be calculated directly from empirical spectroscopic

data (the energy transfer rate constants require the knowledge of parameters, which are not related to experimentally determinable quantities).

Malta's model is a more recent one designed to describe the intramolecular energy transfer between singlet (S) and triplet (T) ligand levels and Ln^{3+} ions and between those ligand levels and ligand to metal charge transfer (LMCT) states in lanthanide coordination compounds.[32,33] In this model both the interaction and exchange mechanisms are taken in consideration.

A Dexter energy transfer process[30,31] is a non-radiative energy transfer by exchange interaction (first described in inorganic solids) where a resonant transfer can be obtained between an allowed transition in the sensitizer and a forbidden transition in the activator. In such cases, an acceptor which does not normally respond to a given pumping radiation spectrum can be made to luminesce after energy transfer from the donor. A double electron transfer occurs between the donor and the acceptor. Even though this model involves electron exchange, it is based on resonance theory of energy but does not include any photoconductivity mechanisms. This is a very short range process since it requires the overlap of the wavefunctions of the energy of the two species. According to Dexter, the rate of energy transfer by electron exchange depends exponentially as a function of the separation distance between the donor and the acceptor:

$$W_{DX} = KJ_{DX}e^{-2\frac{R_{DA}}{L}} \tag{2.19}$$

where K is related to specific orbital interactions, J_{DX} is the normalized spectral overlap integral (Eq. 2.20), R_{DA} is the donor-acceptor separation and L is an average *van der Waals* radius for the initial and final molecular orbitals of the donor-acceptor system.

$$J_{DX}=\int_0^\infty f(\tilde{\nu})\varepsilon_A(\tilde{\nu})d\tilde{\nu} \tag{2.20}$$

where $f(\tilde{\nu})$ is the emission spectrum of the donor normalized to unity area and $\varepsilon_A(\tilde{\nu})$ is the absorption spectrum of the acceptor normalized to the unit area, in such a way that $\int_0^\infty \varepsilon_A(\tilde{\nu})d\tilde{\nu}=1$ and $\tilde{\nu}$ is the energy in wavenumbers.

A Förster energy transfer process[29,30] is a non-radiative dipole-dipole interaction mechanism based on a resonance theory of energy transfer, whereby the deactivation of the donor species D*→D, generates an electric field, or transition dipole which stimulates the formation of A* (induction of a dipole oscillation in A by D*). In a Coulombic interaction (dipole-dipole interaction), the energy transfer rate, W_{FT}, is given by:

$$W_{FT} = \frac{1}{\tau_D}\left(\frac{R_0}{R_L}\right)^6 \tag{2.21}$$

with

$$R_0^6 = 8.8\times10^{-25}\,\frac{\kappa^2 \phi_D J_{FT}}{n_0^4} \tag{2.22}$$

where τ_D is the lifetime of the donor in the absence of the acceptor, ϕ_D the quantum yield of the donor in the absence of the acceptor, κ^2 the relative orientation of the donor and acceptor dipoles and n_0 the refractive index of the medium. These equations contain two essential parameters, which are commonly used for the characterization of Förster energy transfer processes: (*i*) the spectral overlap integral J_{FT} of donor emission and acceptor absorption and (*ii*) the critical radius R_0. The spectral overlap integral J_{FT} is given by:

$$J_{FT} = \int_0^\infty f(\tilde{\nu})\varepsilon_A(\tilde{\nu})\tilde{\nu}^{-4}d\tilde{\nu} \tag{2.23}$$

where $f(\tilde{\nu})$ is the emission spectrum of the donor species (hybrid host) normalized to unity area, in such a way that $\int_0^\infty f(\tilde{\nu})d\tilde{\nu}=1$, $\varepsilon_A(\tilde{\nu})$ is the extinction coefficient of the acceptor at the wavenumber $\tilde{\nu}$.

The Malta model was developed to coordination compounds of Ln^{3+} ions, usually trivalent Eu^{3+} and Tb^{3+} ions, with organic ligands.[32,33] The characteristic Ln^{3+} ion luminescence in these compounds is a consequence of the strong absorption in the UV region by one or more ligands, which then transfer energy non-radiatively to the rare earth ion. In this way, the emitting 4*f* level is in general populated much more efficiently than by

direct excitation of the rare earth ion excited levels. Thus, the 4*f*-4*f* luminescence intensity in the visible region is the result of a balance between strong absorption by the ligands, ligand-rare earth ion energy transfer rates, non-radiative decays and radiative emission rates involved.[32,33] Later on the same author described the intermolecular energy transfer between ligand to metal charge transfer states (LMCT) and Ln^{3+} ions and between LMCT and excited ligand states.[34]

i) Energy transfer process in organic/inorganic hybrids lacking metal activator centre

The energy-transfer rate between the donor and acceptor centres due to the exchange mechanism (W_H^{ex}) is given by:[34]

$$W_H^{ex} = \frac{2\pi}{\hbar}\frac{e^4}{R^2}\left\langle \phi^* \middle| \pi^* \right\rangle^2 \left\langle \phi \middle| \pi \right\rangle^2 F \tag{2.24}$$

where π and π^* stand for the molecular orbitals ascribed to the electronic energy levels of the $^{\bullet}$O–O–Si≡(CO_2) oxygen-related defects, ϕ and ϕ^* represent the molecular orbitals ascribed to the electronic energy levels of the NH/C=O-based defects, *R* is the distance though the overlap integrals $\left\langle \phi^* \middle| \pi^* \right\rangle$ and $\left\langle \phi \middle| \pi \right\rangle$ (average distances between the regions of the hybrid where the donor and acceptors states are localized), and *F* is a temperature-dependent factor which contains a sum over Franck-Condon factors and the appropriate energy mismatch conditions, which will be detailed in chapter 3.

The energy-transfer rate between the levels of the oxygen-related defects and those of the NH/C=O-based ones due to the dipole-dipole mechanism (W_H^{dd}) can be given by a Förster-Dexter type expression:[34]

$$W_H^{dd} = \frac{2\pi}{\hbar}\frac{S_{Si}\,S_{NH}}{G_{Si}\,G_{NH}\,R^6}\,F \tag{2.25}$$

where G_{Si} and G_{NH} are the degeneracies of the levels of the $^{\bullet}$O–O–Si≡(CO_2) oxygen-related defects and those of the NH/C=O-based ones, respectively, and S_{Si} and S_{NH} are the dipole strengths of the $\pi \rightarrow \pi^*$ and $\phi \rightarrow \phi^*$ transitions, respectively, in units of (e.s.u.)^2 cm^{-1}.

ii) Energy transfer process in organic/inorganic Eu^{3+} containing hybrids

Three distinct energy-transfer pathways are possible for Ln^{3+}-containing hybrids: 1) the emitting centres of the hybrid host transfer energy to the ligand excited states (hybrid-to-ligand energy transfer) or 2) directly to the Eu^{3+} ions (hybrid-to-Eu^{3+} energy transfer), and 3) the excited ligand states transfer energy to the Eu^{3+} ions (ligand-to-Eu^{3+} energy transfer).

The hybrid-to-ligand energy transfer rate between the donors (hybrid centres) and acceptors (triplet, T, and singlet, S, ligand levels), due to the exchange (W_H^{ex}) and dipole–dipole (W_H^{dd}) mechanisms are calculated using the same expressions as in the case of the organic/inorganic hybrid lacking metal activator centre showed above (Eq. 2.24 and 2.25).

The hybrid-to-Eu^{3+} and the ligand-to-Eu^{3+} energy-transfer rates are calculated based on the theory developed since 1997 by Malta and co-workers[32,33] using the following expressions for the energy transfer rates due to the exchange (W^{ex}) and multipolar (W^m) mechanisms (including the dipole–2^{λ} pole (W^{mp}) and the dipole–dipole (W^{dd}) contributions (λ=2, 4, 6)):

$$W^m = W^{mp} + W^{dd} = \frac{2\pi}{\hbar}\frac{e^2 S}{(2J+1)G} F\left[\sum_{\lambda}\gamma_{\lambda}\left\langle \alpha' J'\left\| U^{(\lambda)}\right\| \alpha J\right\rangle^2 + \frac{2}{R_L^6}\sum_{\lambda}\Omega_{\lambda}^{e.d.}\left\langle \alpha' J'\left\| U^{(\lambda)}\right\| \alpha J\right\rangle^2\right] \quad (2.26)$$

$$W^{ex} = \frac{8\pi}{3\hbar}\frac{e^2(1-\sigma_0)^2}{(2J+1)R_L^4} F\left\langle \alpha' J'\left\| S^{'}\right\| \alpha J\right\rangle^2 \sum_m \left|\left\langle \phi\left|\sum_k \mu_Z(k)\, s_m(k)\right|\phi'\right\rangle\right|^2 \quad (2.27)$$

In the above equations, G is the degeneracy of the donor (ligand or hybrid) initial state, α specifies a given 4*f* spectroscopic term, S is the dipole strength of the hybrid-to-Eu^{3+} or ligand-to-Eu^{3+} transitions, in units of (e.s.u.)^2.cm^2, R_L is the distance between the regions of

the hybrid emitting centres or the ligand molecules in which the donor states are localized, the quantities $\left\langle \alpha' J \left\| U^{(\lambda)} \right\| \alpha J \right\rangle$ are reduced matrix elements of the unit tensor operators *U(λ)*, and $\Omega_{\lambda}^{e.d.}$ represents the forced-electric-dipole contribution to the 4*f*–4*f* intensity parameters. In Eq. 2.27, S' is the total spin operator of Eu^{3+}, μ_Z is the *z* component of the electric-dipole operator, $s_m (m = 0, \pm 1)$ is a spherical component of the spin operator, both for the hybrids or ligand electrons (respectively in the calculus of the W^{ex} hybrid-to-Eu^{3+} or ligand-to-Eu^{3+} energy-transfer rates), and σ_0 is a distance dependent screening factor.

2.5 Calculation of the emission color coordinates

The color coordinates are usually calculated using the system proposed by the *Commission Internationale de l'Éclairage* (CIE) in 1931.[35,36] This procedure is based on the human eye response to the visible light, where there are three cone cells responsible for the color distinction.[37] Each cone cell presents a different sensitivity, designated as $\bar{x}_\lambda$, $\bar{y}_\lambda$ and $\bar{z}_\lambda$, with maximum values at *ca.* 419, 531 and 558 nm, respectively.[37] The sum of the three cone sensitivity functions is called the *photonic response* and displays a maximum sensibility centered at 555 nm, in the green spectral region.[37] The $\bar{x}_\lambda$, $\bar{y}_\lambda$ and $\bar{z}_\lambda$ are called the CIE color-matching functions. Such color matching functions were calculated considering a 2^0 or a 10^0 filed view (defining the 2^0 and the 10^0 standard observers, respectively). In addition, the CIE defined three new primary colors *X*, *Y* and *Z*, needed to match any specific colors. These quantities *X*, *Y* and *Z* are known as tristimulus values. These primary colors have a great advantage, when compared with other color systems, since the color matching functions do not display negative parts. The emission is weighed by the $\bar{x}_\lambda$, $\bar{y}_\lambda$ and $\bar{z}_\lambda$ functions in order to determinate the *X*, *Y* and *Z* primary color though the following set of equations:[35,36]

$$\begin{cases} X = \int \bar{x}_i E_i d\lambda \\ Y = \int \bar{y}_i E_i d\lambda \\ Z = \int \bar{z}_i E_i d\lambda \end{cases} \qquad (2.28)$$

where E stands for the emission spectra intensity and i represents the emission wavelength. To simply the calculus, the spectra can be divided in small wavelength intervals, $\Delta\lambda$ (usually $\Delta\lambda$ =5 or 10 nm), and Eq. (2.28) can be written as:[35,36]

$$\begin{cases} X = \sum_{\lambda=380}^{770} \bar{x}_\lambda . E_\lambda \Delta\lambda \\ Y = \sum_{\lambda=380}^{770} \bar{y}_\lambda . E_\lambda \Delta\lambda \\ Z = \sum_{\lambda=380}^{770} \bar{z}_\lambda . E_\lambda \Delta\lambda \end{cases} \tag{2.29}$$

To make the color perception easier, the tristimulus are converted into a two dimensional system, though a linear transformation. The tristimulus are reformed into chromaticity coordinates (x,y) that are plotted in a two dimensional chromaticity diagram, Fig. 2.2.

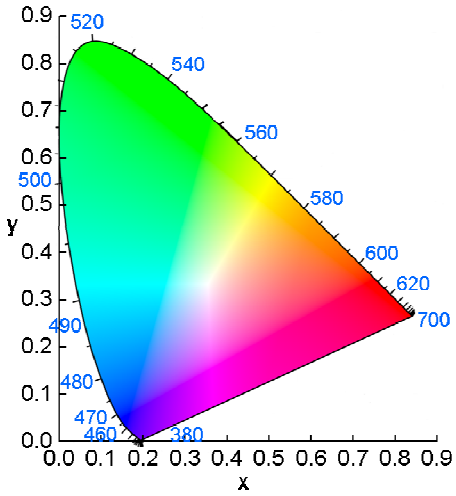

Figure 2.2 The CIE (x,y)-chromaticity diagram.

The chromaticity coordinates are related with X, Y and Z by:[37]

$$\begin{cases} x = \dfrac{X+Y+Z}{X} \\ y = \dfrac{X+Y+Z}{Y} \end{cases} \tag{2.30}$$

The (x,y) chromaticity diagram has particular characteristics, namely:

- The centre of the diagram is taken as the *white point*, whose coordinates are designated as (0.33, 0.33).
- The curve is made of the pure colours from the blue to the red, covering the entire visible spectrum (380-770 nm) and is known as the *spectral locus*;
- The straight line that connects the two extremes of the spectral locus is dominated as *purple boundary*. The colors represented by the purple boundary are not pure colors as they include a mixture of pure red and blue.
- The area circumscribed by the diagram, *spectral locus* and purple boundary, encloses the domain of all colors. The CIE tristimulus X, Y and Z do not belong to the spectral locus, and therefore they do not represent real colors. This is a direct consequence of the postulate that states that any color can be obtained by adding only positive quantities of X, Y and Z.

2.6 Sol-gel process

The present section is devoted to the basic principles of the versatile sol-gel process, the method extensively which has been extensively used in the present work to synthesize luminescent organic/inorganic hybrids in combination with self-assembly processes.

The brief description given as follows will rely entirely on the excellent book by C. J. Brinker and G. W. Scherer,[38] considered to be one of the major references in this field.

2.6.1 Fundamental aspects

The sol-gel process regards the production of inorganic networks through the formation of a colloidal suspension (or sol) and gelation of the sol to form a three dimensional network in a continuous liquid phase (or gel).[38]

A *colloid* is a suspension in which the dispersed phase is so small (~1-1000 nm) that gravitational forces are considered to be negligible and interactions are dominated by short-range forces, such as van der Waals attraction and surface charges.

In the sol-gel process, the starting compounds (usually called precursors) for the preparation of the colloids are compounds in which a metal or metalloid element is surrounded by various *ligands*. The *alkoxide* compounds, which possess organic ligands attached to a metal or metalloid atom and thus belong to the family of *metalorganic* compounds, are the class of precursors most widely used in sol-gel research. The most studied example is silicon tetraethoxide (or tetraethoxysilane, or tetraorthosilicate, TEOS), $Si(OC_2H_5)_4$. As alkoxides possess metal-oxygen-carbon linkages rather than direct metal-carbon bonds they are not organometallic compounds.

Metal alkoxides are popular precursors of the sol-gel method because they react readily with water. During this reaction, called *hydrolysis*, a hydroxyl ion becomes attached to the metal atom:

$$Si(OR)_4 + H_2O \rightarrow HO\text{-}Si(OR)_3 + ROH \qquad (2.31)$$

The R in Eq. 2.31 represents a proton or another ligand (if R is an alkyl, then •OR is an alkoxy group), and therefore ROH is an alcohol. Depending on the amount of water and catalyst added, hydrolysis may go to completion yielding a tetrahydroxysilane:

$$Si(OR)_4 + 4H_2O \rightarrow Si(OH)_4 + 4ROH \quad (2.32)$$

or be incomplete leading to the formation of an alkoxyhydroxysilane, $Si(OR)_{4-n}(OH)_n$.

Two partially hydrolyzed molecules (silanols) may bond to each other through a condensation reaction, with elimination of a siloxane bridging unit:

$$(OR)_3Si\text{-}OH + HO\text{-}Si(OR)_3 \rightarrow (OR)_3Si\text{-}O\text{-}Si(OR)_3 + H_2O \quad (2.33)$$

Or one silanol can condense with an alkoysilane leading to the same siloxane and generation of ROH as alcohol:

$$(OR)_3Si\text{-}OR + HO\text{-}Si(OR)_3 \rightarrow (OR)_3Si\text{-}O\text{-}Si(OR)_3 + ROH \quad (2.34)$$

Since tetra-alkoxysilane is a poly-funcional compound (four alkoxy groups), the hydrolysis-condensation sol-gel process can continue to build larger and larger silicon containing molecules leading to a polymer. A polymer is a huge molecule (or macromolecule) composed of hundreds of individual units (monomers) able to establish at least two bonds. Monomers may be bifunctional, trifuncional or tetrafuncional (i.e., f = 1, 2, 3 or 4, respectively, where f is the *functionality*) when they are able to form two, three or four bonds, respectively. When a monomer with $f > 2$ forms bonds at random fractal structures are usually obtained. A mass fractal differs from a conventional Euclidean object by the fact that, unlike the latter the mass (m) does not change with its radius (r) as $m \propto r^3$, but in the following way:

$$m \propto r^{df} \quad (2.35)$$

where d_f is the mass fractal dimension of the object. Therefore in the case of a fractal $d_f \langle 3$, meaning that its density decreases as the object gets bigger ($\rho \propto m / r^3$).

A monomer with $f > 2$ may reach macroscopic dimensions, extend throughout the solution and become a *gel*. The *gel point* corresponds to the time at which the last bond of the macromolecule is formed. A gel may be defined as a giant molecule including continuous solid skeleton entraps a continuous liquid phase. Gelation can occur after a sol is cast into a mold, making the processability of the final materials into different shapes easy.

Bond formation continues beyond the gel point. The term *aging* corresponds to the changes undergone by the materials in terms of structure and properties after *gelation*. Aging may involve further condensation, dissolution and precipitation of monomers or oligomers, or even phase transformations within the solid or liquid phases. Some gels shrink spontaneously. During this process called *syneresis* the formation of bonds or the attraction between particles induces contraction of the network and the expulsion of the solvents from the pores. Shrinkage of a gel, either during the *syneresis* or as liquid evaporates during *drying*, results in the deformation of the network and percolation of liquid though the pores. Drying by evaporation under normal conditions gives rise to capillarity pressure that causes shrinkage of the gel network. The volume of the resulting dried gel, called *xerogel*, is often reduced by a factor of 5 to 10 compared to the original gel.

2.6.2 Hydrolysis and condensation of silicon alkoxides

Compared with transition metals, silicon is generally less electronegative, its reduced partial positive charge making it comparatively less susceptible to nucleophilic attack. Since N = Z = 4 (where Z is the oxidation state and N is the coordination number), coordination expansion of silicon does not occur spontaneously with nucleophilic reagents. These factors make the kinetics of hydrolysis and condensation relatively slower than observed in transition metals systems.

Silica gels are usually synthesized *via* hydrolysis of monomeric tetrafunctional alkoxide precursors using a mineral acid (*e.g.*, HCl) or a base (NH_3) as a catalyst. Two main types of reactions are generally used to describe the sol-gel process: (1) hydrolysis reactions, Eq. 2.31, during which alkoxides groups (OR) are replaced by hydroxyl groups (OH); (2) condensation reactions in which silanol groups react to produce siloxane bonds (Si-O-Si) plus the by-products alcohol (ROH) (Eq.2.34) or water (Eq. 2.33). In general,

condensation reactions are initiated before the completion of the hydrolysis reactions. Because water and alkoxysilanes are immiscible a mutual solvent such as alcohol is normally used as a homogenizing agent. However gels can be prepared from silicon alkoxides/water mixtures without added solvents, since the alcohol produced as the by-product of the hydrolysis reaction is sufficient to engage the hydrolysis-condensation even in phase separated system. It should be noted that alcohol is not simply a solvent, as it can participate in the *alcoholysis* reactions.

It has been reported that the H_2O : Si molar ratio (r) in Eq. 2.31 has been varied from less than 1 to over 50, and the concentrations of acids or bases have been varied from less than 0.01 to 7 mol.L^{-1}, depending on the desired end product (*e.g.* bulk gels, films, fibers, powders). Because water is one of the by-product of the condensation reactions, an r value of 2 would be in principle enough for complete hydrolysis and condensation to produce anhydrous silica:

$$n\mathrm{Si(OR)_4} + 2n\ \mathrm{H_2O} \rightarrow (\mathrm{SiO_2})_n + 4n\ \mathrm{ROH} \qquad (2.36)$$

In practise, even if $r \rangle\rangle 2$, the reactions usually does not go to completion and a range of intermediate species ($[SiO_x(OH)_y(OR)_z]_n$; where $2x + y + z = 4$) are produced. It has been demonstrated that changes in the various parameters of the synthesis procedure adopted (e.g., value of r, catalyst type and concentration, type of solvent, temperature and pressure) cause modifications on the structure, morphology and consequently on the properties of the resulting silica products.

Typically under acid-catalyzed hydrolysis with low r values weakly branched "polymeric sols" are produced. In contrast base-catalyzed hydrolysis with large r values leads to highly condensed "particulate" sols. The structure of the final silicas materials is the result of successive hydrolysis and condensation reactions, as well as the corresponding reverse reactions.

Hydrolysis

Hydrolysis occurs *via* the nucleophilic attack of the oxygen atom of water molecules on the silicon atom of the alkoxides precursor molecule. Hydrolysis is definitely faster and

more complete in the presence of a catalyst. Although mineral acids or ammonia have been the most widely used catalysts, acid acetic, KOH, KF, HF and amines have also been employed. Generally with understoichiometric conditions (*i.e.*, $r << 2$), the alcohol-producing condensation mechanism dominates. Instead the water-forming condensation reaction is favoured for $r \geq 2$.

Solvents may be classified as *polar* or *nonpolar* and *protic* or *aprotic*. Much polar solvents (*eg.* water, alcohol, or formamide) are normally used for the sol-gel processing of polar, tetrafunctional precursor molecules. Less polar solvents, such as tetrahydrofuran (THF), are appropriate for alkyl-substituted (*i.e.*, incompletely hydrolysable) precursor systems.

Because hydrolysis is catalyzed either by hydroxyl ions (pH>7) or hydronium (pH<7) ions, solvent molecules that hydrogen bond to hydroxyl ions or hydronium ions reduce the catalytic activity under basic or acid conditions, respectively. Consequently, while aprotic solvents that do not hydrogen bond to hydroxyl ions make hydroxyl ions more nucleophilic, protic solvents make hydronium ions more electrophilic.

Under acidic conditions, an alkoxide group will tend to be rapidly protonated. Electron density is withdrawn from silicon, making it more electrophilic and thus more susceptible to react with water molecule. The latter will attack from the rear and will acquire a partial positive charge. The positive charge of the protonated alkoxide will be thus reduced, making the alcohol molecule a better *leaving group*. This process will be accompanied by an inversion of the silicon tetrahedron:

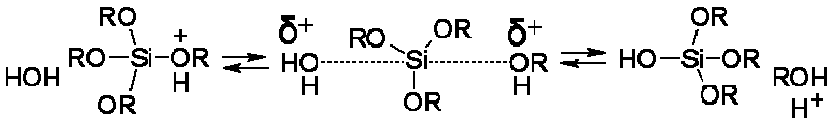

Scheme 2.1 Acid-catalyzed hydrolysis.

Under basic conditions water will first dissociate fast to provide the nucleophilic hydroxyl anions. The hydroxyl anion will then attack the silicon atom.

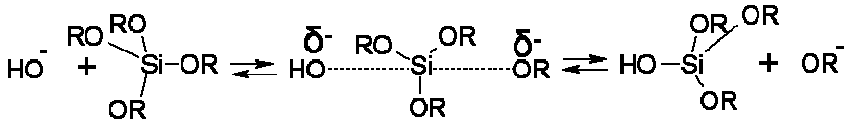

Scheme 2.2 Base-catalyzed hydrolysis.

Condensation

Although in principle condensation of silanols can proceed thermically without the addition of catalysts, their use if beneficial. Mineral acids, ammonia, alkali metals hydroxides, and fluoride anions have been used in this context.

Depending on the pH, either protonated or deprotonated silanols are involved in the condensation mechanism. Because protic solvents form hydrogen bond with nucleophilic deprotonated silanols and aprotic solvents form hydrogen bond with electrophilic protonated silanols, protic solvents retard base-catalyzed condensation and promote acid-catalyzed condensation. Aprotic solvents work in the opposite way.

The most widely accepted mechanism for the condensation reaction involves the attack of a nucleophilic deprotonated silanol on a neutral silicate species:

Scheme 2.3 Base-catalyzed condensation.

This reaction occurs above the isoelectronic point of silica (> pH 2-4.5, depending on the extent of condensation of the silicate species), where surface silanols may be deprotonated depending on their acidity. The acidity of a silanol group depends on the other substituents present on the silicon atom. When basic alkoxy and hydroxy groups are replaced by OSi moieties, the reduced electron density on the Si atom increases the acidity of the protons on the remaining silanol groups. As a consequence reactions between large and highly condensed species incorporating acidic silanol groups, and small, weakly branched species are favoured. As a rule, the condensation rate will be maximized near neutral pH, where significant concentrations of both protonated and deprotonated silanols co-exist, and minimized near the isolectronic point.

2.6.3 Kinetics

As already pointed out above, while hydrolysis is accelerated by acid catalysts, condensation is faster in the presence of base catalysts. In contrast with the situation found with acid catalysts, basic catalysts promote condensation at a relatively early stage. The rate of an acid catalyzed hydrolysis is governed by the concentration of H^+ in the solution. The lower the pH, the faster the reaction. For instance, the hydrolysis of the first OR group on the TEOS molecule is fast, whereas the hydrolysis reactions that follow are slow and depend on steric effects. This implies that monomers are hydrolysed more rapidly than chains, and chains are hydrolysed faster than branches. This type of hydrolysis favours the formation of short linear chains and ultimately to a rather weak polymer network. In the case of base-catalyzed hydrolysis, the reaction rate is a function of the hydroxyl concentration in solution. The hydrolysis reaction is slow and is a rate-determining step, whereas the condensation is relatively fast. This type of condensation favours the formation of highly cross-linked polymers or colloidal particles.

The mechanisms described so far are applicable only when one deals with HCl-*versus* NH_4OH-catalyzed reactions. In fact pH is not the sole factor controlling the hydrolysis and gelation. The nature of the catalyst has a major role as well. A systematic investigation of 6 different catalysts used in the sol-gel process of TEOS in ethanol was carried out while keeping the ratio of other reagents constant (1 mol TEOS: 4 mol water). It was found, that the gelation time increased in the following sequence for the different acids used at the same concentration:

$$HF < CH_3COOH < HCl < HNO_3 < H_2SO_4$$

The pH increased in the order:

$$HCl, HNO_3, H_2SO_4 < HF < CH_3COOH$$

The data led to the conclusion that HF, having an intermediate pH, resulted in the lowest gelation time. The same effect was observed in the presence of CH_3COOH. Thus, the

gelation time does not seem to be directly correlated with the pH value and the specific reaction mechanisms must be taken into account in every particular case.

The influence of the F^- ions on the sol-gel processes of silica is particularly interesting. This ion influences the mechanism of both hydrolysis and condensation, giving new intermediate complexes. Apparently, in the case of condensation, its effectiveness is due to its smaller ionic radius versus that of hydroxyl, which endows it with the same function while temporarily increasing the coordination of silicon. It is known, for instance, that NH_4F allows for an extremely low gelation time. Other anions such as Cl^-, Br^-, I^-, SO_4^{2-}, NO_3- are all larger than hydroxyl (and F-) and hence are much less effective than OH^- (and F^-) in catalyzing the condensation by nucleophilic attack.

2.7 References

1. J.-C. G. Bünnzli, in *Lanthanide Probes in Life, Chemical and Earth Sciences, Theory and Practice*, eds. G. R. Choppin and J.-C. G. Bünnzli, Elsevier, Amsterdam, Netherlands, 1989.
2. J. Becquerel, *Phys. Z*, 1908, **8**, 632.
3. C. K. Jørgensen, *J. Iborg. Nuclear Chem.*, 1955, **1**, 20.
4. S. Hüfner, *Optical Spectra of Transparent Rare Earth*, Academic Press, New York 1978.
5. B. G. Wybourne, *Spectroscopic Properties of Rare Earth Compounds*, Wiley, New York, 1965.
6. H. Bethe, *Ann. Physik.*, 1929, **3**, 133.
7. E. U. Condom and G. H. Shotly, *The theory of Atomic Spectra*, Cambridge, Univerity Press, NewCastle, 1991.
8. I. I. Sobelman, *Atomic Spectra and Radiative Transitions*, McGrawHill, New York, 1964.
9. M. M. F. Cunha, H. F. Brito, L. B. Zinner, G. Vicentini and A. B. Nascimento, *Coord. Chem. Rev.*, 1992, **119**, 1.
10. O. L. Malta and L. D. Carlos, *Quim. Nova*, 2003, **26**, 889.
11. B. R. Judd, *Phys. Rev.*, 1962, **127**, 750.
12. G. S. Ofelt, *J. Chem. Phys*, 1962, **37**, 511.
13. M. F. Reid and B. Ng, *Mol. Phys.*, 1989, **67**, 407.
14. L. D. Carlos, R. A. S. Ferreira, V. de Zea Bermudez and S. J. L. Ribeiro, *Adv. Mater.*, 2009, **21**, 509.
15. W. T. Carnall, P. R. Fields and B. G. Wybourne, *J. Chem. Phys.*, 1965, **42**, 3797.
16. C. K. Jørgensen and B. R. Judd, *Mol. Phys.*, 1964, **8**, 281.
17. R. D. Peacock, *Structure Bonding*, Springer, Berlin, 1975.
18. M. H. V. Werts, R. T. F. Jukes and J. W. Verhoeven, *Phys. Chem. Chem. Phys.*, 2002, **4**, 1542.
19. P. P. Lima, R. A. S. Ferreira, R. O. Freire, F. A. A. Paz, L. S. Fu, S. Alves, L. D. Carlos and O. L. Malta, *Chemphyschem*, 2006, **7**, 735.

20. R. Reisfeld and C. K. Jørgensen, eds. K. A. Gschneidner and L. Eyring, Elsevier Science Publishers 1987.
21. P. Porcher and P. Caro, *J. Lumin.*, 1980, **21**, 207.
22. O. L. Malta, W. M. Azevedo, E. A. Gouveia and G. F. Desa, *J. Lumin.*, 1982, **26**, 337.
23. L. D. Carlos and A. L. L. Videira, *Phys. Rev.*, 1994, **49**, 11721.
24. L. D. Carlos, O. L. Malta and R. Q. Albuquerque, *Chem. Phys. Lett.*, 2005, **416**, 238.
25. L. D. Carlos, R. A. S. Ferreira, V. de Zea Bermudez, C. Molina, L. A. Bueno and S. J. L. Ribeiro, *Phys. Rev. B*, 1999, **60**, 10042.
26. R. M. Supkowski and W. D. Horrocks, *Inorg. Chim. Acta*, 2002, **340**, 44.
27. S. T. Frey and W. D. Horrocks, *Inorg. Chim.*, 1995, **229**, 383.
28. O. L. Malta, H. J. Batista and L. D. Carlos, *Chem. Phys.* , 2002, **282**, 21.
29. T. Förster, *Z. Naturforsch. A*, 1949, **49**, 321.
30. N. J. Turro, *Modern Molecular Photochemistry*, University Science Books, Sausalito, 1991.
31. D. L. Dexter, *J. Chem. Phys.*, 1953, **21**, 836.
32. O. L. Malta and F. R. Gonçalves e Silva, *Spectrochim. Acta A*, 1998, **54**, 1593.
33. O. L. Malta, *J. Lumin.*, 1997, **71**, 229.
34. W. M. Faustino, O. L. Malta and G. F. de Sá, *J. Chem. Phys.*, 2005, **112**, 054109.
35. D. B. Judd and G. Wyszecki, *Color in Business, Science and Industry'*, Wiley, 1962.
36. R. W. G. Hunt, *Measuring Colour*, Ellis Horwood, 1991.
37. L. D. Carlos, R. A. S. Ferreira and V. de Zea Bermudez, in *Hybrid Materials*, ed. G. Kickelbic, Wiley-VCH, Weinheim, 2007.
38. C. J. Brinker and G. W. Scherer, in *Sol–Gel Science: the Physics and Chemistry of Sol–Gel Processing*, Academic Press, San Diego, 1990.

Chapter 3 - Energy transfer

3.1 Introduction

One of the most interesting fields for applications of organic/inorganic hybrids, as detailed in the introduction, is photonics, in particular for white light emitters' devices and light-emitting lanthanide-based multi-functional hybrids with potential applications in tunable lasers, amplifiers for optical communications, emitter layers in multilayer light emitting diodes, efficient light conversion molecular devices, UV dosimeters, and light concentrators for photovoltaic devices.[1-3]

Numerous stable and efficient white-light photoluminescent amine- and amide-functionalized hybrids lacking metal activator ions such as those obtained from APTES and GPTES[4-9], urea,[10-15] urethane[16,17] and amide[18] have been introduced, as detailed in the introduction. The photoluminescence (PL) of these amine and amide functionalized hybrids results from a convolution of the emission originated in the NH/C=O groups of the urea, urethane or amide bridges with electron-hole recombination's occurring in the siloxane nanoclusters.[15] Experimental evidence, such as the sublinear dependence of the integrated emission on the excitation intensity, the increase of the lifetimes of the two emissions with the initial time delay and the red-shift of the time-resolved spectra relatively to the steady state one, indicate that the two emissions are related to radiative recombination mechanisms typical of donor-acceptor (*D*-*A*) pairs.[14,15,17,19] While the chemical species involved in the emission related to the siliceous nanodomains were assigned to $^{\bullet}O–O–Si{\equiv}(CO_2)$ oxygen-related defects, detected by electron paramagnetic resonance,[14,15] those responsible for the NH/C=O-related component have not yet unequivocally been addressed.

In an attempt to gain more insight into the origin and mechanisms responsible for the photonic properties of these amine- and amide-functionalized hybrids, this chapter examines selectively the two emissions associated with the organic and inorganic counter-parts. Two model compounds of the di-ureasil framework (composed of poly(oxyethylene) chains grafted to siloxane domains by means of urea cross-linkages, Scheme 3.1) were synthesized and characterized: one reproducing the organic component of the hybrid structure and the other emulating the siliceous inorganic skeleton. Furthermore, time-resolved spectroscopy clearly demonstrates the existence of energy transfer between the

two distinct emissions. The energy transfer rates between the Si- and NH-related states is quantitatively estimated for a di-ureasil hybrid, generalizing the ideas proposed recently for the intramolecular energy transfer between singlet and triplet ligand levels and ligand-to-metal charge transfer (LMCT) states in lanthanide coordination compounds.[20]

A significant part of the research in light-emitting lanthanide-based multi-functional hybrids has involved the encapsulation of lanthanide organic complexes with β-diketonates, aromatic carboxylic acids or heterocyclic ligands into hybrid matrices through: i) simple embedding of the complexes,[21-23] ii) use of ligands covalently grafted to the framework,[23-32] or iii) anchoring the metal centre to specific functional groups of the hybrid matrix.[33-42] Some of these works explicitly quantified the modifications in the emission features of the hybrids, relatively to those of the precursor complex. The improvement in the photostability under UV radiation (one of the drawbacks of lanthanide β-diketonates chelates)[21,43] and the increase in the emission quantum yields (relatively to the values found for the corresponding precursor complexes) are reported examples of improvements due to the immobilization of the complexes.[41,42] Despite the continuous effort related to lanthanide-based organic/inorganic hybrids, the host-to-ligand and the host-to-metal energy transfer mechanisms were not subjected to a comprehensive quantitative discussion. Only in a handful of reports was this problem faintly addressed.[36,38,41] In general, the energy transfer mechanisms between donor and acceptor species have been treated within the framework of the classic Förster[44] and Dexter[45] approaches. Whereas the Dexter model considers short range exchange interactions the Förster model takes multipolar long range interactions into account.[46,47] The two approaches allow the calculation of the spectral overlap integral between the emission of the donor and the absorption of the acceptor. In the case of the Förster model, besides the overlap integral, it is also possible to calculate the critical radius R_0 for energy transfer, corresponding to the distance of separation for which the donor-acceptor (*D-A*) energy transfer rate is equal to the rate of decay of the excited donor in the absence of acceptor.[44,46,47] In the Dexter model, however, the overlap integral is the only quantity that can be calculated directly from empirical spectroscopic data; the energy transfer rate constants require the knowledge of parameters, which are not related to experimentally determinable quantities.[45-47]

In this chapter a quantitative discussion of the energy transfer mechanisms occurring in di-ureasils incorporating Eu^{3+} compounds is also addressed. Host-to-Eu^{3+} energy transfer occurs either via ligand excited states or directly from the hybrid emitting centres. The corresponding energy transfer rates are estimated for di-ureasils incorporating [$Eu(btfa)_3$(4,4'-bpy)(EtOH)] (btfa= benzoyltrifluoroacetonate, 4,4'-bpy=4,4'-bipyridine) generalizing the ideas previously proposed for the intramolecular energy transfer between singlet (S) and triplet (T) ligand levels and Eu^{3+} ions[48,49] and between those ligand levels and LMCT states in lanthanide coordination compounds.[20] The classical Förster and Dexter approaches are applied to di-ureasils incorporating europium triflate, $Eu(CF_3SO_3)_3$,[33,35,36] where the energy transfer rates could not be predicted by the former model due to the higher computational effort necessary for calculating the singlet and triplet excited states in extended structures, such as these di-ureasils.

3.2 Synthesis

The synthesis of the di-ureasil organic/inorganic hybrids studied in this chapter was extensively reported before the beginning of this thesis.[10,12,14,17,41]

d-U(600) hybrid

The preparation of the di-ureasil involves a covalent bond formation between the alkoxysilane precursor (3-isocyanatepropyltriethoxysilane, ICPTES) and the oligopolyoxyethylene segment by reacting the isocyanate group of the former compound with the terminal amine groups of doubly functional amine (α,ω-diaminepoly-(oxyethylene-*co*-oxypropylene)) in tetrahydrofuran, THF (Scheme 3.1).

A urea cross-linked organic-inorganic hybrid precursor, so-called di-ureapropyltriethoxysilane, d-UPTESs was thus obtained. The diamine used in this study is commercially designated as Jeffamine ED-600 (with $a + c = 2.5$ and $b = 8.5$). In the second stage of the synthesis, a mixture of ethanol and water was added to the d-UPTES solution (Scheme 3.1).

The final material has been identified by the designation d-U(600), di-ureasils, where U originates from the word “urea” and 600, indirectly indicates the length of the oligopolyoxyethylene chains.

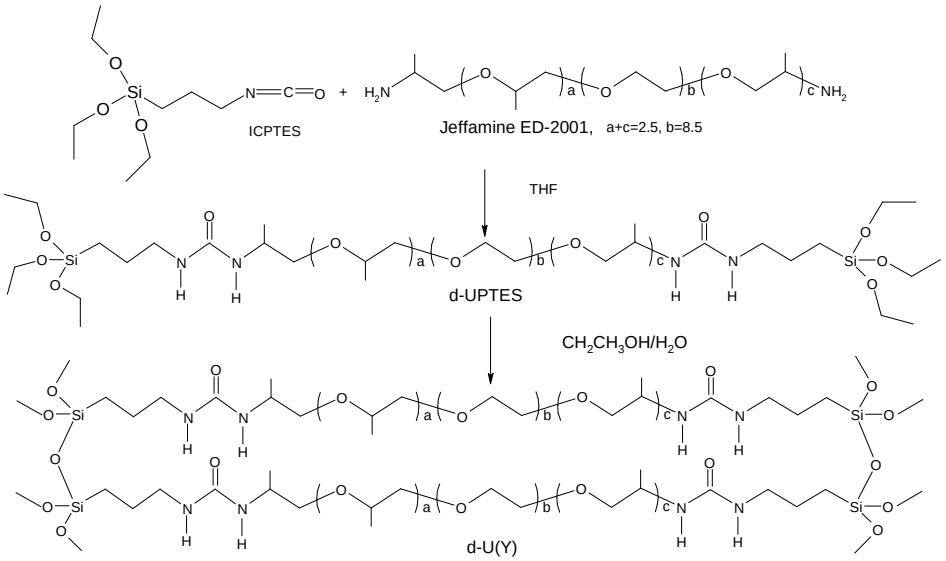

Scheme 3.1 Synthesis of the d-U(600) organic/inorganic hybrid with $a + c = 2.5$ and $b = 8.5$.

Inorganic model compound

A typical synthesis of the inorganic model compound involves the mixture of 2.0 mL (8.78 mmol) of TEOS with 6.32 mL (35.1 mmol) of PTMOS, with a molar ratio TEOS:PTMOS=1:4 in a volume of 10.2 mL of CH_3CH_2OH. Then, 2.53 mL of 0.01 M HCl was added to this solution. The resulting sol was stirred under a nitrogen atmosphere at room temperature for 24 h. The sol was poured into a mould for gelation. Finally, the TEOS/PTMOS gel was dried at *ca.* 50 ^oC for around one week. The reaction is shown in Scheme 3.2.

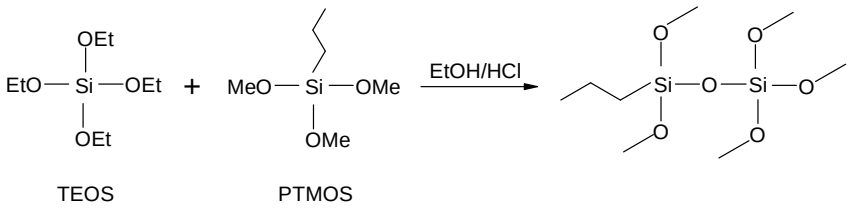

Scheme 3.2 Synthesis of the inorganic model compound.

Organic model compound

The first stage of the synthesis of the organic model compound is the dissolution of 2.0 g (1.0 mmol) of Jeffamine ED-2001 in 10 mL of THF using ultrasonic agitation. Then 0.19 mL (2.0 mmol) of PIC (Propyl IsoCyanate) was added to this solution with a molar ratio of Jeffamine ED-2001:PIC = 1:2. The mixture was stirred under N_2 at room temperature for 24 h. The resulting product was placed at room temperature to evaporate the solvent. Finally a solid product, Jeffamine ED-2001/PIC, was obtained. The reaction equation is described in Scheme 3.3.

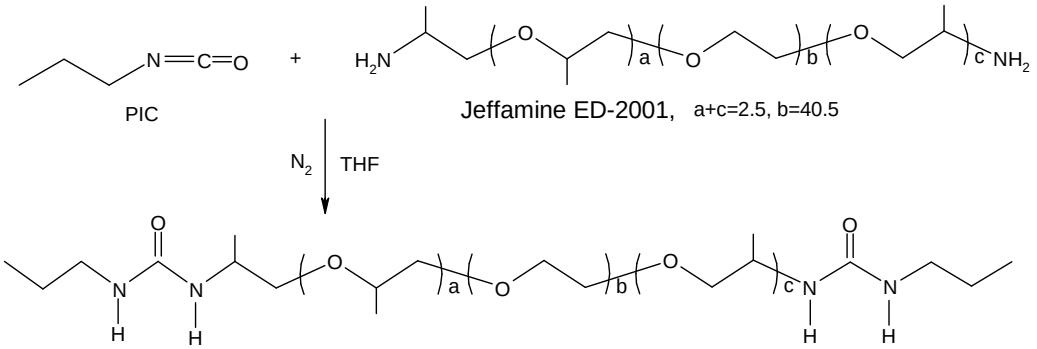

Scheme 3.3 Synthesis of the organic model compound.

3.3 Local structure of the di-ureasil model compounds

The X-ray diffraction patterns of the organic and inorganic model compounds are depicted in Fig. 3.1.

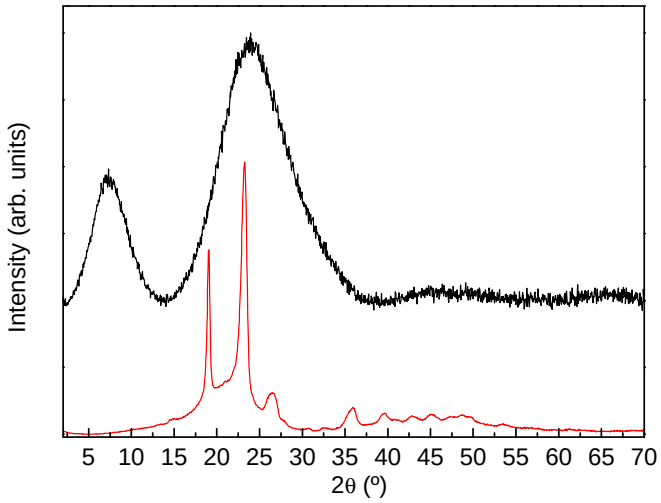

Figure 3.1 XRD patterns of the inorganic (black line) and organic (red line) model compounds.

The diffraction pattern of the inorganic model compound shows two broad peaks, the most intense one centered at 24.22°, associated with the presence of amorphous siliceous domains. Using the Bragg law:

$$2d \sin\theta = n\lambda \tag{3.1}$$

where d represents the structural unit distance, θ is the scattering angle, n the diffraction order and λ is the wavelength of the CuKα radiation (1.54 Å) a value of 3.67 Å was obtained for the structural unit distance.

The coherent length, L, over which the structural unit survives, was estimated fitting the XRD patterns with pseudo-Voigt functions and using the modified Scherrer equation:[17]

$$L = \frac{I\lambda}{A\cos\theta} \tag{3.2}$$

where *A*, in radians, is the integrated area of the peaks, I is its intensity and λ=1.54 Å.

The coherent length obtained was 11±2 Å. The least intense broad peak, centered at 7.49°, was assigned to an interference effect between siliceous domains spatially correlated. Both peaks are deviated about 4° relatively to the hybrids diffraction pattern,[17,50] which can be related with (i) changes in the conformation of the siliceous skeleton upon incorporation into the hybrid, (ii) absence of the urea groups and (iii) presence of new Si local environments. The diffraction patterns of the organic model compound - very similar to those of poly(ethylene glycol), PEG, and d-U(2000) di-ureasil[50] - is composed of a series of well-defined Bragg peaks (the most intense ones at 19.03° and 23.23°) assigned to the diffraction of crystalline oxyethylene, OCH_2CH_2, unities.

The ^{29}Si MAS NMR spectrum of the inorganic model compound, depicted in Fig. 3.2, exhibits broad signals at approximately –90.9, –100.5, and –108.8 ppm assigned to $(\equiv SiO)_2Si(OH)_2$ (Q^2, geminal silanols), $(\equiv SiO)_3SiOH$ (Q^3, single silanol) and $(\equiv SiO)_4Si$ (Q^4, siloxane) local environments, respectively,[51] and three peaks at approximately –50.0,–55.7 and –66.3 ppm, ascribed to organosiloxane atoms $R'Si(OSi)(OR)_2$ (T_1), $R'Si(OSi)_2(OR)$ (T_2) and $R'Si(OSi)_3$ (T_3), respectively.[17]

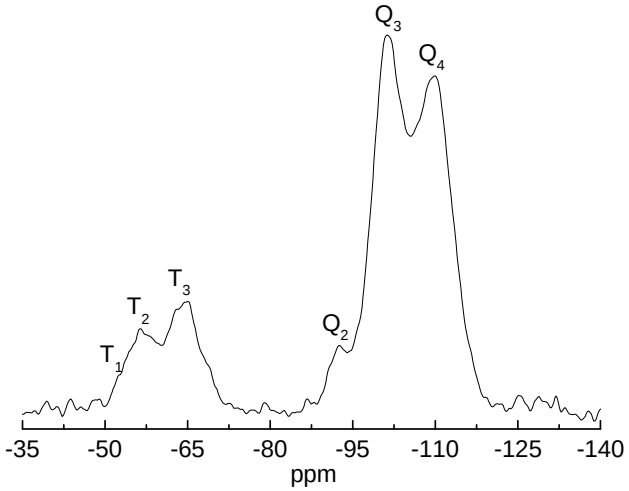

Figure 3.2 ^{29}Si NMR MAS spectrum of the inorganic model compound.

The ^{13}C MAS NMR spectra of the organic model compound and Jeffamine ED-2001®/PIC, are shown in Fig. 3.3 a,b with and without ^{1}H decoupling during the signal acquisition. These spectra were treated by Dr. Luis Mafra from CICECO, University of

Aveiro. The ^{13}C resonance assignments of the Jeffamine ED-2001/PIC sample may be obtained based on the typical chemical shift range of the different chemical species and on a previous assignment study of the ^{13}C spectrum of a di-ureasil based cross-linked hybrid such as d-U(600) containing the Jeffamine ED-2001 unit as the organic part.[17]

The two ^{13}C resonances located at *ca.* 11.2 and 11.7 ppm are assigned to the terminal -CH_3 groups while the peaks at *ca.* 17.5 and 18.5 ppm are attributed to the different branched -CH_3 groups of the molecular chain.[52] The peaks at *ca.* 21.2 and 23.8 ppm are typical of –CH_2- aliphatic carbons. In the range of 40-48 ppm are found the –NCH_2- groups. The peak centered at *ca.* 46 ppm may be assigned to -NCH- groups because it shows a doublet shape instead of a triplet (Fig. 3.3d). The region between 60 and 80 ppm, refers to the different -OCH_n (n=1, 2) groups. On the basis of the assignment proposed by other authors,[53] the strongest peak in this region (*ca.* 70.6 ppm) is attributed to the -(OCH_2CH_2)- groups (Fig. 3.3c). The high frequency shifted peaks at *ca.* 158 and 159 ppm are typical of the urea C=O groups[17] and unequivocally prove the integrity of the organic model.

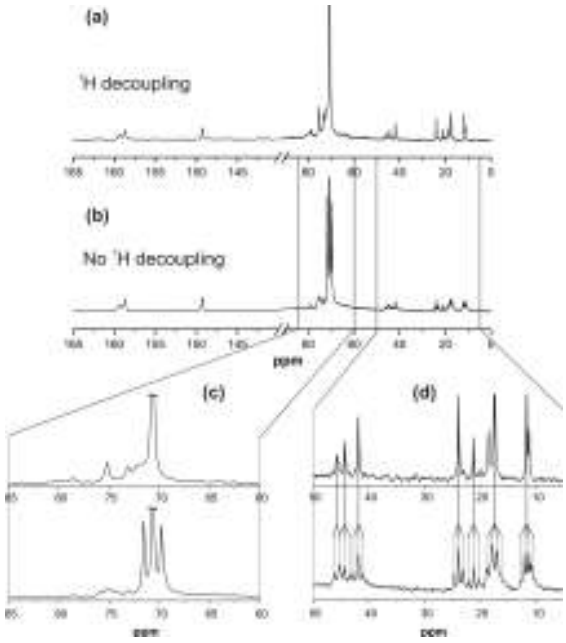

Figure 3.3 ^{13}C MAS NMR spectra of Jeffamine ED-2001/PIC organic model employing (a) ^1H decoupling and (b) without ^1H decoupling. The insets shows the (c) 60 to 85 and the (d) 5 to 50 ppm regions of (a) and (b) to better observe the *J*-multiplets of each carbon resonances. The value of the $^1J_{CH}$ coupling constants ranges from *ca.* 92 Hz (corresponding to the 45.8 ppm peak) to *ca.* 141 Hz (corresponding to the 70.7 ppm peak).

The presence of -NHC(=O)NH- groups in Jeffamine ED-2001/PIC was monitored also through the analysis of the infrared absorption bands in the "amide I" region (1600-1800 cm^{-1}). The "amide I" mode is a highly complex vibration that involves primarily the contribution of the C=O stretching. The "amide I" region of the organic model compound (Fig. 3.4) shows several components involving hydrogen bonding between the NH groups of the urea and the oxygen atoms of ether or carbonyl groups, like it was reported for di-ureasil hybrids.[12,17]

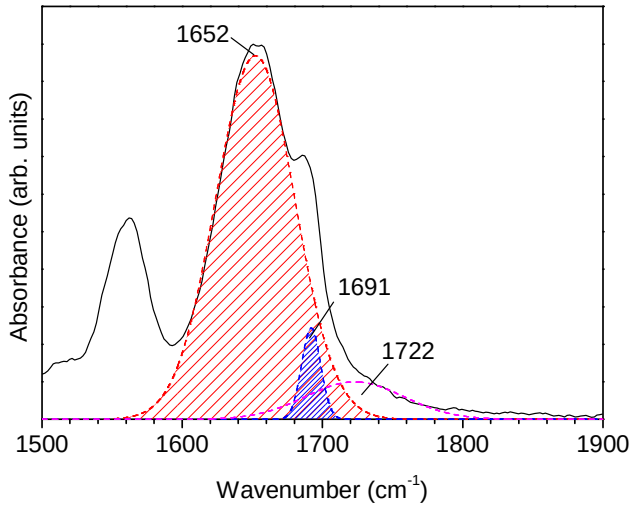

Figure 3.4 FT-IR spectrum of the "amide I" region the organic model compound. The dashed lines represent the curve-fitting.

To access the frequency of the vibrational modes a deconvolution fitting procedure using Gaussian functions (Fig. 3.4) was employed. Three components were isolated for the "amide I" envelope at *ca.* 1652, 1691 and 1722 cm^{-1}. The former peak is ascribed to the formation of strong self-associated hydrogen-bonded urea-urea associations and the remaining ones are attributed to the vibration of NHC(=O)NH groups belonging to urea-polyether chains. The absence of a band at *ca.* 1750 cm^{-1} indicates that neither C=O nor N-H groups were left free.[12,17]

All the structural data of the Jeffamine ED-2001/PIC and TEOS/PTMOS compounds support their use as, respectively, organic and inorganic structural models for the two counterparts of the organic/inorganic di-ureasil hybrid. In the strict sense, the Jeffamine ED-2001/PIC compound models the d-U(2000) organic chains structurally because of its polymer average molecular weight. However, the situation found in this material (*i.e.*, the

presence of larger quantities of urea-urea associations) resembles closely that observed in the di-ureasil with lower molecular weight d-U(600) and, therefore, this compound will be used in the next section as a model to discuss the emission component originated in the NH/C=O groups of the urea, urethane, or amide bridges.

3.4 Photoluminescence

di-ureasil and model compounds

Fig. 3.5 A,B show the room temperature emission spectra of the inorganic and organic model compounds, respectively.

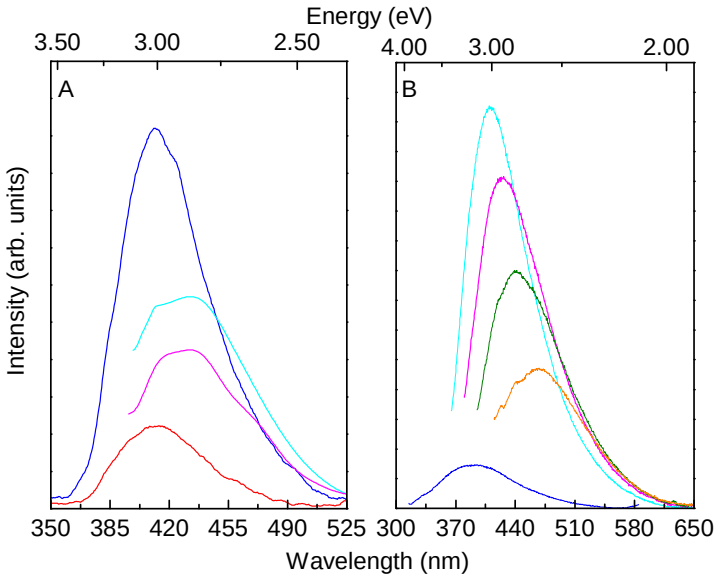

Figure 3.5 Room temperature emission spectra of (A) inorganic and (B) organic model compounds excited at different wavelengths: 280 nm (red), 300 nm (blue), 330 nm (cyan), 350 nm (magenta), 365 nm (olive) and 380 nm (orange).

All the spectra are formed of a large broad band, which peak position deviates to the red as the excitation wavelength increases. This behavior was observed for the di-ureasil hybrids[4,9,13-17,39,50,54,55] and non-hydrolyzed precursors,[14,15,54,55] and it was modeled as radiative recombinations involving thermal relaxation within localized states, in the framework of the extended multiple trapping approach.[56,57] The emission bands of Jeffamine ED-2001/PIC and TEOS/PTMOS compounds are well reproduced by a single

Gaussian function, whose energy peak position varies from 3.17-2.54 eV and 3.00-2.89 eV for the organic and inorganic model compound, respectively, as the excitation wavelength increases from 300-420 nm (4.13-2.95 eV) and 280-365 nm (4.42-3.40 eV). Comparing these values with those observed for the NH/C=O groups and siliceous related emission in the hybrid materials,[50,58] a blue shift of the emission of the Jeffamine ED-2001/PIC compound is observed, whereas the hybrids' siliceous related emission energy is approximately that observed in the TEOS/PTMOS model. Also, the emission spectra of the organic compound are blue-shifted with respect to that of the diamine Jeffamine ED2001.

Fig. 3.6 compares the time resolved emission spectra of the d-U(2000) di-ureasil hybrid and those of the model compounds.

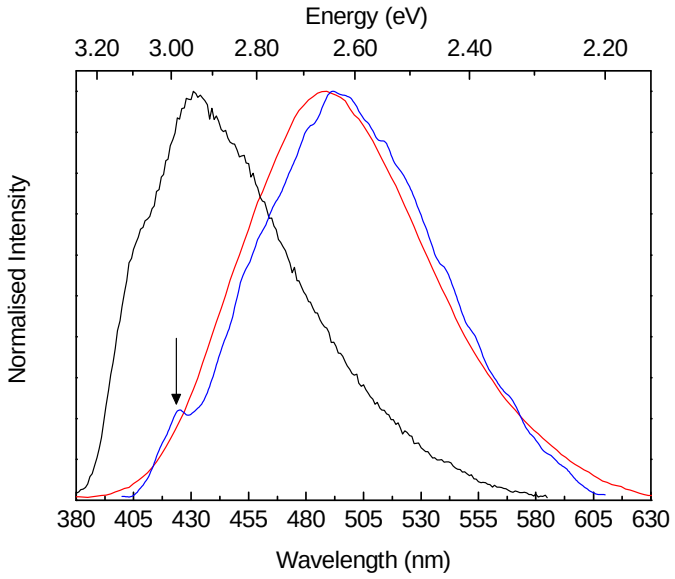

Figure 3.6 Time-resolved emission spectra of inorganic (black), organic (red) model compounds and d-U(2000) (blue) excited at 300 nm, 350 nm and 365 nm, respectively, with an integration window of 20.00 ms. The starting delays were set as 0.05 ms (model compounds) and 20.00 ms (hybrid). The arrow indicates the siliceous related component in the d-U(2000) emission spectrum.

For starting delays below 5.00 ms the hybrids' emission displays two main components at *ca.* 427 nm and *ca.* 500 nm.[14,15,50] The former component were ascribed to the siliceous network and the latter one was assigned to emission arising from the NH/C=O groups within the urea cross linkages.[14,15,50] The emission of the model compounds is formed by a single emission component (similarly to that observed for the steady-state emission, Fig. 3.5 A,B), being that the emission of the inorganic model compound is blue-

shifted with respect to that of the organic model compound like observed in the hybrid material. Moreover, the spectral range observed for the emission of each of the model compounds is in perfect agreement with the emission assignment proposed for the hybrids time resolved spectra.

Additional measurements were carried out in order to compare the physical nature behind the emission features of the model compounds with those of the hybrids, in particular the presence of radiative emission mediated by donor-acceptor pairs. The existence of donor-acceptor pairs can be inferred from the analysis of the behavior of the emission intensity, *I*, as the excitation power, *L*, is varied. The emission intensity depends on the excitation power according to the power-law $I \propto L^k$. Whereas $k \leq 1$ is characteristic of *D-A* pairs, $1 < k < 2$ is typical of exciton-like transitions.[15,59] As shown in Fig. 3.7 the emission integrated intensity depends linearly on the power excitation, revealing a slope *k* of 1.00 and 0.98, for the inorganic and organic model compounds, respectively. These values are similar to those reported for different organic/inorganic hybrids, such as the di-ureasils[15] and the di-amidosils,[19] indicating that the hybrids' and the model compounds' emission is mediated by donor-acceptors pairs.

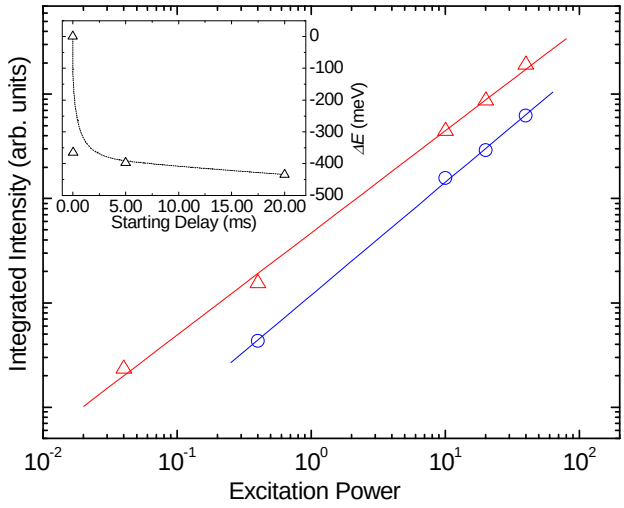

Figure 3.7 Emission integrated intensity of inorganic (open circles) and organic (open triangles) model compounds at different excitation powers. The solid lines correspond to linear fits to the data (R > 0.99). The inset shows the shift (ΔE) of the organic model compound's emission between the energy of the maximum intensity of the time-resolved spectra and the corresponding value measured under continuous excitation. The spectra were measured at 350 nm for a fixed acquisition window of 10.00 ms and for starting delays between 0.05 and 20.00 ms. The dashed line is a guide for the eyes.

Further experimental evidence of donor-acceptor pair transitions can be inferred from time-resolved spectroscopy. The emission energy from a donor-acceptor pair separated by a distance R, $E_{D\text{-}A}$, can be expressed as:[60]

$$E_{D-A} = E_G - E_A - E_D + \frac{e^2}{\varepsilon_0 R} \tag{3.3}$$

where E_G is the energy gap and E_A and E_B are the acceptor and donor ionization energies, respectively. The last term is the D-A pair Coulomb interaction, where e is the electronic charge and ε_0 represents the static dielectric constant. The recombination energy increases as the pair separation R becomes smaller and the radiative recombination probability is known to decrease exponentially with increasing D-A separation. For longer delay times, a red shift in the spectrum is expected because distant pairs have a smaller recombination probability.[60] The respective energy levels have therefore longer lifetimes, a situation that is favored with increasing time delay. As a consequence, the recombination takes place at lower energies. The inset in Fig. 3.7 shows for the organic model compound the energetic shift (ΔE) between the energy of the maximum intensity of the time-resolved spectra, measured for a starting delay between 0.05 and 20.00 ms, and the corresponding value detected under continuous excitation. Increasing the starting delay induces an emission shift towards the red of 430 nm. For di-ureasil and di-amidosil hybrids and for the starting delay interval between 0.05 and 20.00 ms, ΔE is 150 meV.[15,19] For the inorganic compound, ΔE is null for starting delays between 0.00 and 100.00 ms. Although $\Delta E \neq 0$ was expected, this may not controvert a D-A pair recombination mechanism. In fact, a similar behavior was already reported for the emission of silicon nanocrystals mediated by donor-acceptor pairs,[61] and for the siliceous-related component in di-ureasils and di-amidosils.[15,19]

The lifetime values for the two model compounds were monitored at 14 K within the maximum intensity bands in Fig. 3.5 using the same experimental conditions reported for the hybrids, in particular starting delays of 40.00 and 0.08 ms for the NH/C=O- and siliceous-related emissions, respectively. [14]

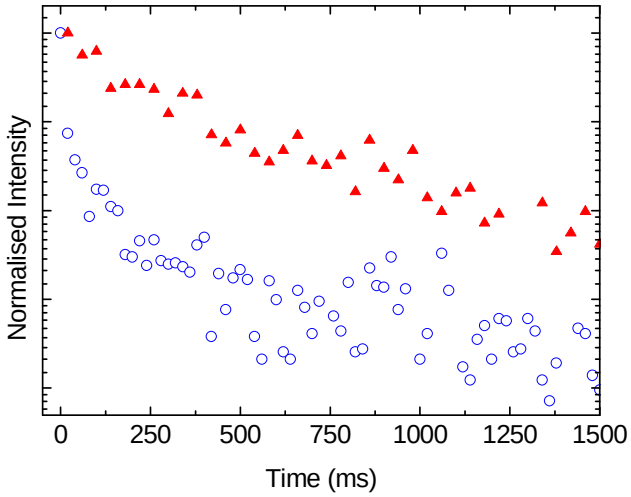

Figure 3.8 Emission decay curves of d-U(2000) di-ureasil acquired at 14 K with a starting delay of 0.08 ms and monitored at 488 nm under (open circles) 365 nm and (solid triangles) 420 nm.

Such decay curves are well reproduced by single exponential functions revealing lifetime values of 211.7 ±11 ms and 161.9 ±10 ms for the inorganic and organic model compound, respectively. At room temperature, the lifetimes of the two model compounds are of the same order of magnitude than those of the two emissions in the hybrids, 10^{-8}-10^{-9} s.[14,15] Comparing the values measured at 14 K with those known for d-U(2000), the lifetime of the organic model compound is the same as the one found for the NH/C=O-related emission in the d-U(2000) di-ureasil, whereas the lifetime value estimated for the inorganic model compound is two orders of magnitudes higher than the value ascribed to the siliceous related emission in the hybrid. This significant increase strongly suggests that non-radiative channels associated with the siliceous network exist in the hybrids that were not present in the isolated inorganic model compound. The *Arrhenius* dependence of the lifetime of the siliceous-related component in the hybrids between 14 and *ca.* 220 K (whereas the lifetime values of the NH/C=O-related emission is constant)[14] points out that such non-radiative channels may be related with the existence of energy transfer between the two emissions. The non-radiative desexcitation probability of the siliceous levels may be approximately described by the Mott-Seitz model, which expresses the temperature dependence of the experimental lifetimes (τ) as:

$$\tau^{-1} = \tau_0^{-1} + k_1 e^{-\frac{\Delta E_1}{k_B T}} \qquad (3.4)$$

where τ_0 is the lifetime at $T = 0\ K$, k_1 is the migration energy rate, ΔE_1 is the activation energy for desexcitation of the siliceous emitting states, and k_B is the Boltzmann's constant. With the Mott-Seitz model to the siliceous lifetime dependence on the temperature (14-220 K) for the d-U(2000) data,[14] the activation energy estimated is 565 cm^{-1}. While the activation energy predicted by the Mott-Seitz model value is known to be underestimated,[62] such a small value is compatible with the above suggestion that the thermally activated non-radiative mechanism associated with the siliceous related component may involve energy transfer from the NH/C=O groups. This point will be further addressed below.

Other evidence of energy transfer from the siliceous-related component to the NH/C=O groups are found by monitoring the lifetime of the latter component under selective excitation wavelength (420 nm) and under excitation wavelengths that simultaneously excite both emissions (350-400 nm).[14,15,50,58] For the hybrids, the NH/C=O related decay curves depend on the starting delay time and excitation wavelength. While the decay curve acquired under 420 nm can be described by a single exponential function, independently of the selected starting delay, the decay curves excited under 350-400 nm display a non-exponential behavior, for starting delays smaller than 40.00 ms. These observations are illustrated in Fig. 3.8, where the decay curves monitored within the NH/C=O groups under 365 and 420 nm are plotted in a logarithmic scale, where the linear behavior can only be applied to the 420 nm decay curve.

Eu^{3+}- containing hybrids

In the following part, the photoluminescence evidence of host-to-Eu^{3+} energy transfer in di-ureasil hybrids incorporating either [Eu(btfa)$_3$(4,4'-bpy)(EtOH)] or Eu(CF_3SO_3)$_3$ synthesized using a procedure described elsewhere is summarized.[33-36,41] The hybrids were designated as d-U(600)-[Eu(btfa)$_3$(4,4'-bpy)] and d-U(2000)$_n$Eu(CF_3SO_3)$_3$, respectively, where *n* represents the number of ether-type oxygen atoms of the poly(ethyleneoxide) chains per Eu^{3+} ion. Attention will be focussed in three particular d-U(2000)$_n$Eu(CF_3SO_3)$_3$ di-ureasils with an Eu^{3+} content of 1.18, 2.75, and 4.96 wt% (n=200, 80 and 40, respectively).

Fig. 3.9 depicts the emission spectra of d-U(600)-[Eu(btfa)$_3$(4,4'-bpy)] and d-U(2000)$_n$Eu(CF$_3$SO$_3$)$_3$ (n=200, 80, 40). The spectra (experimental conditions reported elsewhere[33,35,36,41]) are composed of a series of straight lines assigned to the $^5D_0 \rightarrow {}^7F_{0\text{-}4}$ Eu^{3+} transitions and of a broad band in the blue/green spectral region, much more evident in the d-U(2000)$_n$Eu(CF$_3$SO$_3$)$_3$ hybrids, ascribed to the emitting levels of the hybrid host. This band was already observed in the non doped di-ureasil[14,15] and its origin was discussed above. The relative intensity of the hybrid emitting components depends on the amount of Eu^{3+}, in such a way that the higher the Eu^{3+} concentration the lower the relative intensity of the NH/C=O groups and siliceous related emission. The emission spectrum of d-U(600)-[Eu(btfa)$_3$(4,4'-bpy)] shows essentially the Eu^{3+} lines, presenting only minor hybrid emission intensity.

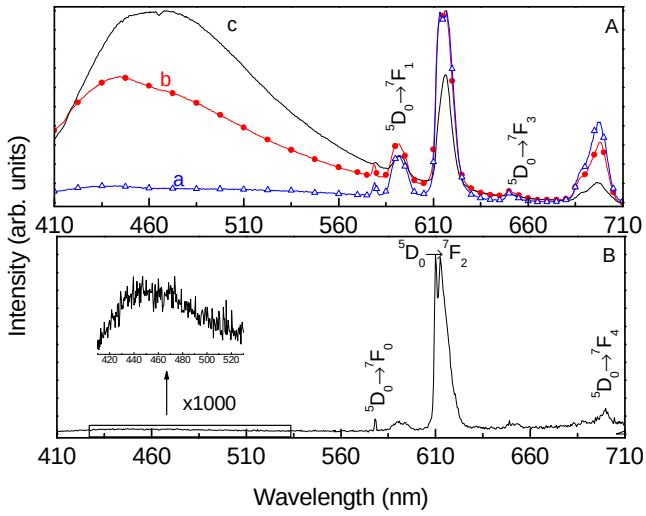

Figure 3.9 Room temperature emission spectra (excited at 365 nm) of (A) d-U(2000)$_n$Eu(CF$_3$SO$_3$)$_3$, (a) *n*= 40, (b) *n*=80, and (c) *n*=200 and (B) d-U(600)-[Eu(btfa)$_3$(4,4'-bpy)]. The asterisk denotes an intra-4f^6 self-absorption $^7F_0 \rightarrow {}^5D_2$.

The relative intensity dependence of the hybrid emission on the concentration of lanthanide centres and the presence of organic ligands, is a strong argument pointing out the existence of host-to-metal energy transfer either via ligand excited states or directly from the hybrid emitting centres. Further qualitative arguments supporting the existence of that energy transfer are the dependence of the emission quantum yield and of the lifetime of the hybrid excited states on the incorporated Eu(CF$_3$SO$_3$)$_3$ amount. The emission quantum yield decreases from 9%, non doped di-ureasil, to 1.4 %, *n*=20.[36] The 14 K

lifetime of the hybrid excited states decreases from *ca.* 160 ms (NH/C=O groups) and *ca.* 3.5 ms (oxygen-related defects)[14] to values below 10^{-5} ms, in the presence of Eu^{3+} ions.[36] Such decreases suggest that the Eu^{3+} ions activate non-radiative decay channels (not present in the non doped di-ureasil) related with energy transfer from the host to the lanthanide levels.[36,39] Further evidence of energy transfer in di-ureasils incorporating Eu^{3+}, was demonstrated by intra-4*f* self-absorption lines superimposed in the hybrid host emission band.[36]

3.5 Energy transfer rates

The calculus of the energy transfer rates requires the determination of the average D-A distance. This determination was obtained by geometry optimization making use of the Sparkle/AM1 model[63] (work performed by Prof. Ricardo Freire, Federal University of Sergipe-Brazil). For the d-U(2000) the high number of involved orbitals impeded accurate calculations, so for the sake of the simplicity, the calculation was done only for the d-U(600) (the di-ureasil host with shorter polymer chains).

Non doped d-U(600)

The Förster[44] and Dexter[45] classical models were the first approaches to the calculation of the energy transfer rates in the di-ureasils. In order to use these models it is necessary to have an overlap of the absorption spectrum of the acceptor specie (organic model compound) with the emission spectrum of the donor specie (inorganic model compound), *cf.* chapter 2. Fig. 3.10A shows the absorbance spectrum of the organic model compound (acceptor) for solvents with different polarities index (P_i) such as water (P_i=10.2), acetronitrile (P_i=5.6), chloroform (P_i=4.1) and toluene (P_i=2.4). Fig. 3.10B displays the emission spectra of the donor (inorganic model compound). There is no overlap between the absorbance spectrum of the organic model compound and the emission spectrum of the inorganic model compound, and, thus, it was not possible to apply the Förster and Dexter models.

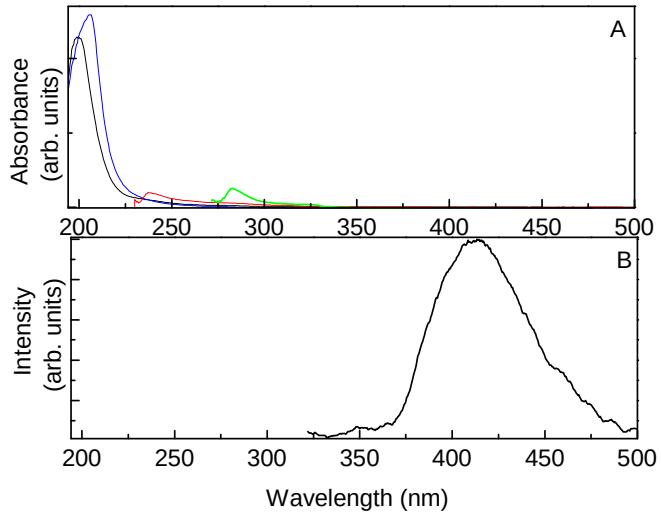

Figure 3.10 (A) Absorbance spectra of organic model compound (10^{-3} mol.L^{-1}) in water (black), acetonitrile (red), chloroform (blue) and toluene (green). (B) Room temperature emission spectrum of the inorganic model compound excited at 280 nm.

Following the theoretical procedure proposed by Malta for the intramolecular energy transfer between singlet and triplet ligand levels and LMCT states in lanthanide coordination compounds[20] (*cf.* chapter 2) the energy transfer between the donor and acceptor centres was estimated considering two-electron determinantal states ($|i\rangle$ and $|f\rangle$) involving the π, π^*, ϕ and ϕ^* molecular orbitals ascribed to the electronic energy levels of the $^{\bullet}$O–O–Si≡(CO_2) oxygen-related defects and the NH/C=O-based ones, respectively (Fig. 3.11).

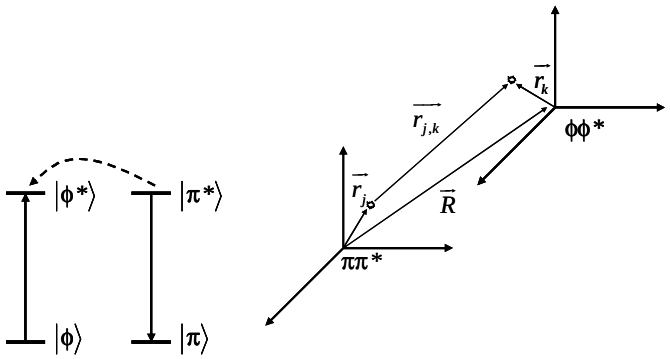

Figure 3.11 Energy level diagram and coordinate systems used to describe the interaction between the electrons involved in the $\pi \rightarrow \pi^*$ and $\phi \rightarrow \phi^*$ transitions. The indexes *j* and *k* indicate the electron that undergoes a transition between molecular orbitals of the •O–O–Si≡(CO_2) oxygen-related defects and NH-based ones, respectively, in coordinate systems placed at the baricenters of the corresponding excited states, and *R* is the average D-A distance (average distance between the •O–O–Si≡(CO_2) oxygen-related defects and NH-based ones).

With this approach, the exchange mechanism is taken into account without the need of using the exchange operator, and the relevant matrix element of the interaction Hamiltonian (the isotropic term) between the two electronic clouds is given by: [20]

$$\langle f|H|i\rangle = \pm\frac{e^2}{R}\langle\phi^*|\pi^*\rangle\langle\phi|\pi\rangle \tag{3.4}$$

where *e* is the electronic charge. According to Fermi's Golden rule the transfer rate between the levels of the •O–O–Si≡(CO_2) oxygen-related defects and NH/C=O-based ones is:

$$W_H^{ex} = \frac{2\pi}{\hbar}\left|\langle f|H|i\rangle\right|^2 F \tag{3.5}$$

where the temperature dependent factor *F* contains a sum over Franck-Condon factors and the appropriate energy mismatch conditions. Substituting Eq. 3.4 into Eq. 3.5 the energy transfer rate has the following form:

$$W_H^{ex} = \frac{2\pi}{\hbar}\frac{e^4}{R^2}\left\langle\phi^*\middle|\pi^*\right\rangle^2\left\langle\phi\middle|\pi\right\rangle^2 F \tag{3.6}$$

Actually, this transfer rate is highly sensitive to the distance *R* through the overlap integrals $\langle \phi^* | \pi^* \rangle$ and $\langle \phi | \pi \rangle$. The form of Eq. 3.5 also reflects the dominance of the exchange mechanism in the isotropic contribution to the transfer rates. As the widths at half-height of the two donor and acceptor bands, $\hbar\gamma_{Si}$ and $\hbar\gamma_{NH}$, respectively, are of the same order, the factor *F* is given by:[20]

$$F = \frac{\ln 2}{\sqrt{\pi}} \frac{1}{\hbar^2 \gamma_{Si} \gamma_{NH}} \left\{ \left[\left(\frac{1}{\hbar \gamma_{NH}} \right)^2 + \left(\frac{1}{\hbar \gamma_{Si}} \right)^2 \right] \ln 2 \right\}^{-\frac{1}{2}}$$

$$\times \exp \left[\frac{1}{4} \frac{\left(\frac{2\Delta}{(\hbar \gamma_{Si})^2} \ln 2 \right)^2}{\left[\left(\frac{1}{\hbar \gamma_{NH}} \right)^2 + \left(\frac{1}{\hbar \gamma_{Si}} \right)^2 \right] \ln 2} - \left(\frac{\Delta}{\hbar \gamma_{Si}} \right)^2 \ln 2 \right] \qquad (3.7)$$

where Δ is the energy difference between the donor and acceptor excited states of the two centres.

The excited state energy of each emitting centre in d-U(600) has been determined from the crossing point between the excitation and emission curves (Fig. 3.12). These transition energies in wavenumbers (σ_{Si} and σ_{NH}) together with the Δ energy difference and the widths at half-height of the two bands ($\hbar\gamma_{Si}$ and $\hbar\gamma_{NH}$) are given in Table 3.1. as mentioned before, the average donor-acceptor distance given in Table 3.1 was obtained from the optimized ground-state geometry of d-U(600) making use of the Sparkle/AM1 model.[64,65] The value obtained is in very good agreement with the mean distance between the siloxane domains and the urea groups determined by single-crystal X-ray diffraction in a non-hydrolyzed lamellar-bridged silsesquioxane precursor,[66] which molecular structure is analogous to that of the amine- and amide-functionalized hybrids discussed in this work.

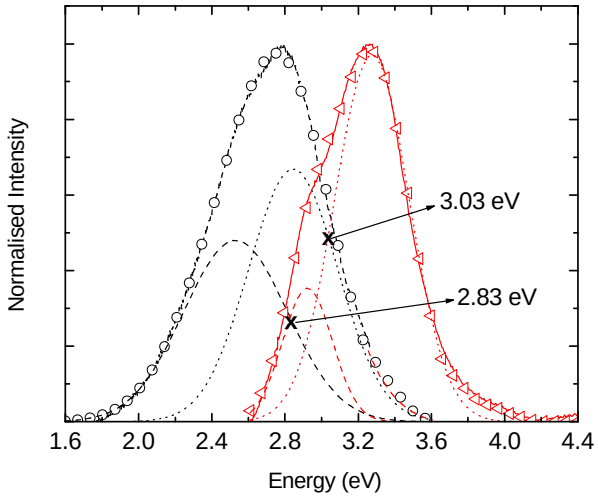

Figure 3.12 Room temperature emission (black, dash line with open circles, excitation wavelength of 300 nm) and excitation spectra (red, full line with open triangles, monitored wavelength of 490 nm) of d-U(600). The $^{\bullet}$O–O–Si≡(CO_2) oxygen-related and NH/C=O-based components are represented by the dot and dash lines, respectively. The crossing points between each excitation and emission curves (black crosses) determine the excited state energy of each emitting centre.

The energy transfer rate between the levels of the oxygen-related defects and those of the NH/C=O-based ones due to the dipole-dipole mechanism (W_H^{dd}) can be given by a Förster-Dexter type expression:

$$W_H^{dd} = \frac{2\pi}{\hbar} \frac{S_{Si}\, S_{NH}}{G_{Si}\, G_{NH}\, R^6} F \tag{3.8}$$

where S_{Si} and S_{NH} are the dipole strengths of the $\pi \rightarrow \pi^*$ and $\phi \rightarrow \phi^*$ transitions, respectively, in units of (e.s.u.)^2 cm^2, which can be given in terms of the radiative lifetimes (τ_{RAD}) and transitions energies in wavenumbers by:

$$S = \frac{3}{4} \frac{\hbar c^3}{(2\pi c \sigma)^3 \tau_{RAD}} \tag{3.9}$$

G_{Si} and G_{NH} in Eq. 3.14 are the degeneracies of the levels of the $^{\bullet}$O–O–Si≡(CO_2) oxygen-related defects and those of the NH/C=O-based ones, respectively. Since the excited state

radiative lifetimes of these centres (τ_{Si} and τ_{NH}) are considerably long (Table 3.1), it is reasonable to assume that these states have a triplet like character, while the respective ground-states are both singlets. Thus, G_{Si}=3 and G_{NH}=1. However, the usual electric dipole selections rules may be considerably relaxed through vibronic-spin-orbit perturbations, particularly if promoting modes become operative at higher temperatures.

Table 3.1 Energy transfer rates between the levels of the oxygen-related defects and those of the NH/C=O-based ones due to the exchange (W_H^{ex}) and dipole-dipole (W_H^{dd}) mechanisms in d-U(600). The parameters used for the estimation of these energy transfer rates are also displayed.

$\hbar\gamma_{Si}$ (cm^{-1})	3915
$\hbar\gamma_{NH}$ (cm^{-1})	4571
σ_{Si} (cm^{-1})	24485
σ_{NH} (cm^{-1})	22809
Δ (cm^{-1})	1676
τ_{Si} (s)	211×10^{-3}
τ_{NH} (s)	160×10^{-3}
R(cm)	5.7×10^{-8}
W_H^{ex} (s^{-1})	3.7×10^{8}
W_H^{dd} (s^{-1})	1.3×10^{9}

The dipole strengths were initially estimated from the experimental lifetimes of the model compounds, *i.e.* donor in the absence of acceptor and *vice-versa*, measured at low temperature (14 *K*) to circumvent the contributions of the thermally-activated non-radiative component. Rough estimates of the overlap integrals $\langle\phi^*|\pi^*\rangle$ and $\langle\phi|\pi\rangle$ indicate that they may assume values between 0.01 and 0.1.[20] For R=5.7×10^{-8} cm, was assumed the rather conservative value of 0.01. Table 3.1 gathers the estimated energy transfer rates, as well as the values of all the parameters required for the calculations.

The dipole-dipole energy transfer rate between the two emitting centres of the d-U(600) di-ureasil is 1.3×10^{9} s^{-1}, larger than the value estimated for the transfer rate mediated by the exchange mechanism, 3.7×10^{8} s^{-1}, indicating that the dipole-dipole mechanism is dominant.

Eu^{3+}-based di-ureasils

d-U(2000)$_n$Eu(CF$_3$SO$_3$)$_3$

As mentioned before, for d-U(2000) hybrid the high number of involved orbitals impeded accurate calculations of the singlet and triplet excited states using the Sparkle/AM1 model and conclusively the application of the already described Malta's model.

The discussion of the energy transfer mechanisms in d-U(2000)$_n$Eu(CF$_3$SO$_3$)$_3$ di-ureasils is made using the classical Förster and Dexter approaches. Furthermore, this strategy provided some insight in how far classical models can lead to reliable predictions regarding energy transfer pathways in lanthanide-doped organic/inorganic hybrid materials.

In the investigated concentration range, the Eu^{3+} ions interact with the hybrid host through the carbonyl-type oxygen atoms of the urea bridges which are located closely to the hybrid emitting centres. Two essential parameters which are commonly used for the characterization of Förster energy transfer processes are: (*i*) the spectral overlap integral J_{FT} of donor emission and acceptor absorption and (*ii*) the critical radius R_0, *cf.* chapter 2. The spectral overlap integral J_{FT}, given by Eq. 2.23, is calculated using the emission spectrum of the donor species (hybrid host) normalized to unity area and the absorption spectrum of the acceptor species (Eu^{3+}). The absorption spectrum of Eu^{3+}-based hybrids was obtained as an approximation by correcting the excitation spectra of d-U(2000)$_n$Eu(CF$_3$SO$_3$)$_3$ for the band corresponding to the host emitting centres, remaining only the 4*f* lines. As can be expected the Eu^{3+} neighborhood is considerably influenced by the coordinated H_2O molecules, the thus obtained spectrum was adapted to the extinction coefficient of the Eu^{3+} ion in aqueous solution (ε_{394} = 1.4 $M^{-1}cm^{-1}$).[67]

The spectral overlap integral J_{FT} has been calculated for different excitation wavelengths because the emission depends on the excitation wavelength.[33,35,36] However, the obtained values are very similar (the difference is in the order of 15%) and thus, we refer here only to 365 nm as excitation wavelength for which the maximal di-ureasil emission was observed.[36] The calculated Förster overlap integral ranges from 1.55×10^{-16} (n=40) to 1.62×10^{-16} cm^6mol^{-1} (n=200). Since Eu^{3+} has a very small extinction coefficient

(see above) and the absorption spectrum is used without normalization,[47] contrary to calculations related to the Dexter mechanism (see below), small spectral overlap integrals result.

The critical radius R_0 (Eq. 2.22) is defined as *D-A* distance, where the energy transfer efficiency yield reaches 50%. In other words, at this distance the rates of the intrinsic deactivation of the excited state donor and energy transfer are equal. The obtained R_0 values range from 3.3 to 3.5 Å, which is similar to the average Eu^{3+}-NH/C=O distance as estimated from the ground state geometry (R_L *ca.* 3.5 Å). Thus, application of the Förster theory for the description of host-to-Eu^{3+} energy transfer would predict an efficiency of *ca.* 50% and a W_{FT} transfer rate of *ca.* 10^6-10^7 s^{-1}, with Eq. 2.21 assuming τ_D *ca.* 10^{-6}-10^{-7} s (as discussed above).

The efficiency of the energy transfer Φ_{exp} can be calculated with:

$$\Phi_{\exp} = 1 - \frac{\phi_{DA}}{\phi_D} \tag{3.10}$$

where ϕ_{DA} is the quantum yield of the Eu^{3+}-based hybrids (6.4 to 1.4%, for *n*=200 to 40, respectively) and ϕ_D the quantum yield of the non doped di-ureasil (9 % at 365 nm excitation).[36] The obtained values range from 28 to 84%, for *n*=200 to 40, respectively. The value for d-$U(2000)_{200}Eu(CF_3SO_3)_3$ is smaller than predicted by the Förster theory, which would be 50% for *D-A* distances in the range of the critical radius. A possible explanation is that at lower Eu^{3+} concentrations a certain number of hybrid donor sites are not occupied with metal ions, therefore leading to an apparently lower energy transfer quantum yield. However, such an argumentation does not apply at higher Eu^{3+} concentrations, where all the hybrid donor sites have metal ions in their proximity (the C=O group of urea entities belongs to the Eu^{3+} coordination shell and the $^{\bullet}O–O–Si{\equiv}(CO_2)$ oxygen-related defects are nearby). The corresponding energy transfer efficiency is higher than expected for the critical radius (84% versus 50%), which strongly suggests that the Förster contribution to the energy transfer mechanism is minor. This is in agreement with the assumption that at small distances (*ca.* 3.0–3.5 Å) orbital overlap of energy donor and acceptor is possible and for such a situation the energy transfer is likely better described as Dexter (exchange) mechanism.

According to the Dexter model the overlap integral (J_{DX}) was estimated using the emission spectrum of the donor normalized to unity area and the absorption spectrum of the acceptor normalized to the unit area, Eq. 2.20. The determined spectral overlap J_{DX} integrals range from 6.67×10^{-5} cm (n=40) to 8.17×10^{-5} cm (n=200), sufficiently large enough to account for the experimentally verified efficient energy transfer. However, contrary to the Förster theory for resonance energy transfer, the Dexter theory relies strongly on quantum-mechanical parameterization, which excludes predictions of energy transfer rates and efficiencies solely based on spectroscopic data. Therefore, based on the comparison of data predicted from the Förster theory and experimental or these from derived values we limit ourselves to the statement that Förster energy transfer is highly unlikely to play a dominant role in the d-U(2000)$_n$Eu(CF$_3$SO$_3$)$_3$ (n=200, 80, 40) di-ureasils and that the observations rather point to a Dexter-type mechanism.

d-U(600)-[Eu(btfa)$_3$(4,4'-bpy)]

For the d-U(600)-[Eu(btfa)$_3$(4,4'-bpy)] hybrid the Malta model was used. Three distinct energy transfer pathways can be figured out for d-U(600)-[Eu(btfa)$_3$(4,4'-bpy)]: i) the energy absorbed by the emitting centres of the hybrids is transferred to the ligand excited states (hybrid-to-ligand energy transfer); ii) energy transfer from excited ligand states to the Eu^{3+} ions (ligand-to-Eu^{3+} energy transfer); and iii) energy transfer occurring directly from the $^{\bullet}$O–O–Si≡(CO$_2$) oxygen- and NH/C=O-related centres to the Eu^{3+} ions (hybrid-to-Eu^{3+} energy transfer). The calculations of the energy transfer rates were performed by Professor Oscar Malta from CCEN, Federal University of Pernambuco, and Professor Luís Carlos, University of Aveiro.

i) *Hybrid-to-Ligand Energy Transfer Rates*: The energy transfer between the donors (hybrid centres) and acceptors (triplet and singlet ligand levels) can be estimated considering two-electron determinantal states, $|i\rangle$ and $|f\rangle$, involving the molecular orbitals ascribed to the electronic energy levels of each hybrid emitting centre and the ligand excited states (triplet and singlet). With this approach, the energy transfer rate is given by Eq 3.12, where now π/π^* stand for molecular orbitals ascribed to the electronic energy levels of the hybrid emitting centres and ϕ/ϕ^* represent the ligand molecular orbitals and

it is the temperature-dependent factor F which contains a sum over Franck-Condon factors and the appropriate energy mismatch conditions. As the width at half-height of the donor ($\hbar\gamma_H = \hbar\gamma_{Si}$=3915 cm^{-1} or $\hbar\gamma_H = \hbar\gamma_{NH}$=4571 cm^{-1}) and acceptor ($\hbar\gamma_L = \hbar\gamma_T$=3250 cm^{-1} or $\hbar\gamma_L = \hbar\gamma_S$=4878 cm^{-1}) levels are of the same order the factor F is given by:

$$F = \frac{\ln 2}{\sqrt{\pi}} \frac{1}{\hbar^2 \gamma_H \gamma_L} \left\{ \left[\left(\frac{1}{\hbar \gamma_L} \right)^2 + \left(\frac{1}{\hbar \gamma_H} \right)^2 \right] \ln 2 \right\}^{-\frac{1}{2}} \times \exp\left[\frac{1}{4} \frac{\left(\frac{2\Delta}{(\hbar \gamma_H)^2} \ln 2 \right)^2}{\left[\left(\frac{1}{\hbar \gamma_L} \right)^2 + \left(\frac{1}{\hbar \gamma_H} \right)^2 \right] \ln 2} - \left(\frac{\Delta}{\hbar \gamma_H} \right)^2 \ln 2 \right] \tag{3.11}$$

where Δ is the difference between the donor and acceptor transition energies involved in the transfer process. For this purpose, the excited state energy of each emitting hybrid centre in d-U(600)-[Eu(btfa)$_3$(4,4'-bpy)] are considered equal to that determined for the d-U(600) host through the crossing point between the excitation and emission curves, as described above.

The energy transfer rates between the levels of the hybrid emitting centres and the ligand states due to the dipole-dipole mechanism (W_{HL}^{dd}) is given by the Förster-Dexter type in Eq. 3.14 by substituting S_{Si} by S_L (S_S or S_T), S_{NH} by S_H (S_{Si} or S_{NH}), G_{si} by G_L (G_S or G_T) and G_{NH} G_H (G_{Si} or G_{NH}). The dipole strengths (S_L and S_H) are calculated using Eq. 3.9. Since the excited state radiative lifetimes of the hybrid levels ($^{\bullet}$O–O–Si≡(CO_2) oxygen-related defects and NH/C=O-based ones) are considerably long at low temperature (as stated above) it is reasonable to assume that these states have a triplet like character, while the respective ground-states are both singlets. Thus, G_{Si}=G_{NH}=3. The usual electric dipole selections rules may be considerably relaxed through vibronic-spin-orbit perturbations, particularly if promoting modes become operative at higher temperatures. The dipole strengths were estimated assuming radiative rates at room temperature of 10^6–10^7 s^{-1} (much higher than the corresponding ones measured from the lifetimes at low temperature, *ca.* 5-10 s^{-1}). Rough estimates of the overlap integrals $\langle \phi^* | \pi^* \rangle$ and $\langle \phi | \pi \rangle$ indicate that

they may assume values between 0.01 and 0.1.[20] For the typical distances between the hybrid centres and the triplet ligand (Table 3.2) a value of 0.01 was assumed. Table 3.2 gathers the estimated hybrid-to-ligand (triplet and singlet) energy transfer rates, as well as the energy difference Δ and distance R through the overlap integrals. We note that since the energy of the excited levels of the hybrid emitting centres is lower than that of the singlet, the hybrid-to-singlet energy transfer rates should be calculated by multiplying the direct transfer rates by the Boltzmann factor, $\exp(-\Delta E / k_B T)$, where ΔE is the energy difference between the levels, k_B the Boltzmann constant and T the room temperature).

ii) Hybrid-to-Eu^{3+} and Ligand-to-Eu^{3+} Energy Transfer Rates. The energy transfer rates from the hybrid emitting centres to the Eu^{3+} ions, directly or through the ligand excited states, are calculated by O. L. Malta and L. D. Carlos using the Eqs 2.26 and 2.27[41] and listed in Table 3.2.

Table 3.2 Energy transfer and back-transfer rates of d-U(600)-[Eu(btfa)$_3$(4,4'-bpy)]. The oxygen atom of the carbonyl group of the hybrid host was considered in the first coordination sphere substituting the ethanol molecule of the precursor complex. The dominant mechanism of each path is included. [b]Back-transfer rates (s^{-1}): 4.51×10^4, [c]Back-transfer rates (s^{-1}): 5.34×10^2, [d]Back-transfer rates (s^{-1}): 1.44, [e]Back-transfer rates (s^{-1}): 3.99×10^5, [f]Back-transfer rates (s^{-1}): 3.95×10^1.

levels	Δ (cm^{-1})	R or R_L (Å)	transfer rate (s^{-1})	Transfer Mechanism
S → $^5D_4$[b]	1318	3.70	2.41×10^7	multipolar
S → $^5G_6$[c]	2166	3.70	1.62×10^7	multipolar
S → $^5L_6$[d]	3593	3.70	3.92×10^7	multipolar
T → $^5D_1$[e]	2403	3.70	3.75×10^{10}	exchange
T → $^5D_0$[f]	4173	3.70	1.71×10^{10}	exchange
Si → $^5D_4$	3115	9.03	5.23×10^{-4}	multipolar
Si → $^5G_6$	2267	9.03	1.29×10^0	multipolar
Si → $^5L_6$	840	9.03	5.76×10^3	multipolar
Si → $^5D_1$	5415	9.03	6.54×10^5	exchange
Si → $^5D_0$	7185	9.03	2.34×10^5	exchange
NH → $^5D_4$	4791	4.44	1.38×10^{-4}	multipolar
NH → $^5G_6$	3943	4.44	2.03×10^{-2}	multipolar
NH → $^5L_6$	2516	4.44	1.02×10^2	multipolar
NH → $^5D_1$	3739	4.44	3.26×10^9	Exchange
NH → $^5D_0$	5509	4.44	1.85×10^9	exchange
Si → S	4433	7.88	9.23×10^{-2}	exchange
Si → S	4433	7.88	4.27×10^1	dipole-dipole
Si → T	3012	7.88	1.88×10^8	exchange
Si → T	3012	7.88	2.12×10^5	dipole-dipole
NH → S	6109	4.32	7.76×10^{-5}	Exchange
NH → S	6109	4.32	4.92×10^{-1}	dipole-dipole
NH → T	1336	4.32	6.95×10^8	exchange
NH → T	1336	4.32	1.07×10^7	dipole-dipole

According to the selection rules of the multipolar and exchange mechanisms presented above, the $^5D_2$, $^5L_6$, $^5G_6$ and $^5D_4$ levels are good candidates to be involved in energy transfer processes through the former mechanism,[48] while through the exchange mechanism the $^5D_1$ manifold is the strongest candidate.[49] Moreover, although direct energy transfer to the $^5D_0$ level is not allowed through both processes this rule is relaxed due to J-mixing effects and thermal population of the $^7F_1$ level. Therefore, here the discussion is focussed on the multipolar contribution for the $^5L_6$, $^5G_6$ and $^5D_4$ levels (for the $^5D_2$ level the

matrix elements of the $U^{(\lambda)}$ operators is too small to be taken into account)[49] and on the exchange ones for the $^5D_1$ and $^5D_0$ levels.

The values of back-transfer rates from the Eu^{3+} ion to the ligand singlet and triplet states were also considered. According to table 3.2, the most efficient luminescence pathway is $(S_0)_{Hybrid} \rightarrow (T)_{Hybrid} \rightarrow (T)_{Ligand} \rightarrow (^5D_1, ^5D_0) \rightarrow {}^7F_{0-6}$, Fig. 3.13.

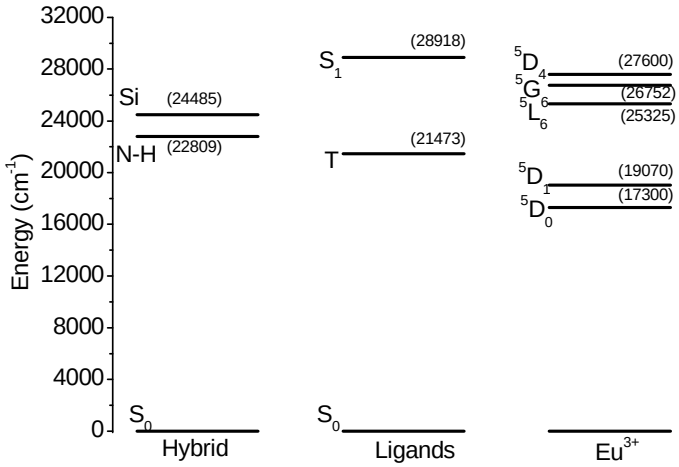

Figure 3.13 Energy level diagram of d-U(600)-[Eu(btfa)$_3$(4,4'-bpy)]. The experimental energies of the singlet and triplet states are depicted. The experimental energy of the singlet (28 918 cm^{-1}) was derived from the absorption spectrum, whereas the energy of the lowest ligand triplet state (21 473 cm^{-1}) corresponds to the maximum peak observed in Gd^{3+}-based di-ureasil emission spectrum.[41]

3.6 Conclusions

In order to understand the origin and mechanisms responsible for the photonic properties of amine- and amide-functionalized organic/inorganic hybrids, in this chapter were examined independently the two emissions associated with their corresponding organic and inorganic counterparts. Two model compounds reproducing respectively the organic (Jeffamine ED-2001/PIC) and inorganic (TEOS/PTMOS) parts of a di-ureasil hybrid were synthesized and characterized in detail by XRD, $^{29}Si/^{1}H/^{13}C$ MAS NMR, FT-IR and PL spectroscopy. XRD, $^{29}Si/^{1}H/^{13}C$ MAS NMR and FT-IR of Jeffamine ED-2001/PIC and TEOS/PTMOS support their use as, respectively, organic and inorganic structural models for the two counterparts of the di-ureasil hybrids.

The emission bands of Jeffamine ED-2001/PIC and TEOS/PTMOS compounds are well reproduced by a single Gaussian, which energy peak changes from 3.17-2.54 eV and 3.00-2.89 eV, for the organic and inorganic model compounds, respectively, as the excitation wavelength increases from 300-420 nm (4.13-2.95 eV) and 280-365 nm (4.42-3.40 eV). Comparing these values with those observed for the NH/C=O- and siliceous-related emissions in the amine- and amide-functionalized hybrids a blue shift of the emission of the Jeffamine ED-2001/PIC compound is observed, whereas the hybrids' siliceous related emission energy is approximately that observed for the TEOS/PTMOS model compound. The linear dependence of the emission integrated intensity of both materials on the power excitation, slopes of *ca.* 1.00 and 0.98, for the inorganic and organic model compounds, respectively, and the energetic shift between the energy of the maximum intensity of each time-resolved spectra, measured for starting delays between 0.05 and 20.00 ms, and the corresponding value detected under continuous excitation, point out that the model compounds' emission is also mediated by donor-acceptors pairs, as it has been reported for the di-ureasils and di-amidosils.

The decays curves of the two materials are well reproduced by single exponential functions revealing lifetime values of 211.7 ±11 ms and 161.9 ±10 ms, for the inorganic and organic model compounds, respectively. Comparison of these values with those for d-U(2000) reveals that the lifetime of Jeffamine ED-2001/PIC is the same as that found for the NH/C=O-related emission, whereas the value estimated for TEOS/PTMOS is two orders of magnitude higher than the value ascribed to the siliceous related emission in the

hybrid. This significant increase suggests the existence of thermally activated non-radiative mechanisms associated with the siliceous related component that may involve energy transfer from the NH/C=O groups. The Arrhenius dependence with temperature of the siliceous related lifetime in the d-U(2000) hybrid (activation energy *ca.* 565 cm^{-1}), as well as the non-exponential behavior of the decay curve of the siliceous-related emission under lower excitation wavelengths (both emissions simultaneously) also support the occurrence of this energy transfer process. The energy transfer rate between the levels of the oxygen-related defects and those of the NH/C=O-based ones is quantitatively estimated for d-U(600) (the di-ureasil host used with smallest number of polymer repeat units) generalizing the ideas proposed recently by Malta and co-workers for the intramolecular energy transfer between singlet and triplet ligand levels and ligand-to-metal charge transfer states in lanthanide coordination compounds. The dipole-dipole energy transfer rate between the two emitting centres of the d-U(600) di-ureasil is 1.3×10^{9} s^{-1}, larger than the value estimated for the transfer rate mediated by the exchange mechanism, 3.7×10^{8} s^{-1}.

In this chapter, the energy transfer mechanisms that occur in sol-gel derived d-U(600)-$[Eu(btfa)_3(4,4'\text{-bpy})]$ and d-$U(2000)_nEu(CF_3SO_3)_3$ (n = 200, 80, and 40) organic/inorganic di-ureasils was also discussed quantitatively. For the former hybrid the energy transfer rates were estimated generalizing ideas previously proposed for the intramolecular energy transfer between excited ligand levels and Eu^{3+} ions and those ligand levels and LMCT transfer states in lanthanide coordination compounds. Host-to-Eu^{3+} energy transfer occurs either via ligand excited states (essentially the triplet) or directly from the hybrid emitting centres through the dipole-dipole, dipole-2^{λ} pole (λ = 2, 4 and 6) and exchange mechanisms. The ligand-to-Eu^{3+} energy transfer rate is typically one order of magnitude larger than the value estimated for the direct transfer from the hybrids emitting centres, 3.75×10^{10} and 3.26×10^{9} s^{-1}, respectively to the $^5D_1$ level. The most efficient luminescence channel is $(S_0)_{Hybrid} \rightarrow (T)_{Hybrid} \rightarrow (T)_{Ligand} \rightarrow (^5D_1, ^5D_0) \rightarrow {}^7F_{0\text{-}6}$.

The Förster and Dexter classic approaches are applied to the d-$U(2000)_nEu(CF_3SO_3)_3$ (n = 200 and 40) di-ureasils where the singlet and triplet excited states of the complex could not be predicted due to a higher computational effort necessary for this type of calculation in big structures. The evidence point out that the exchange (Dexter) mechanism accounted for energy transfer: (i) the critical radius calculated according to the Förster model (3.3-3.5 Å) is in good agreement with the experimental Eu^{3+}/NH-C=O distance (*ca.*

3.5 Å) pointing out that the *D* and *A* species have to come in contact, a pre-condition of Dexter, for which the obtained overlap integral values are compatible, (ii) the calculated values for the energy transfer efficiency taking into account the Förster model are much different than the experimental ones. Therefore, although less efficient, relatively to d-U(600)-[Eu(btfa)$_3$(4,4'-bpy)], the hybrid-to-Eu^{3+} energy transfer is also dominated by the exchange (Dexter) interaction.

The detailed characterization of these energy transfer mechanisms will definitively contribute to the recognition of the paths needed for the development of siloxane-based hybrids characterized by interesting photonic features and high light emission efficiency. Moreover, the procedure reported provides a theoretical scheme that might be useful in guiding the interpretation of experimental data and in the modeling of new organic/inorganic hybrids.

3.7 References

1. P. Gomez-Romero and C. Sanchez, *Eds. Functional Hybrid Materials*, Wiley-Interscience, New York, 2003.
2. G. Kickelbick, *Ed. Hybrid Materials, Synthesis, Characterization, and Applications*, Wiley-Interscience, New York, 2007.
3. C. Sanchez and B. Lebeau, *Mrs. Bull.*, 2001, **26**, 377.
4. W. H. Green, K. P. Le, J. Grey, T. T. Au and M. J. Sailor, *Science*, 1997, **276**, 1826.
5. V. Bekiari and P. Lianos, *Langmuir*, 1998, **14**, 3459.
6. Y. Uchida, Y.-I. Nobu, I. Momiji and H. Matsui, *J. Sol-Gel Sci. Technol.*, 2000, **19**, 705.
7. Y. Han, J. Lin and H. Zhang, *J. Mater. Lett.*, 2002, **54**, 389.
8. E. Cordoncillo, F. J. Guaita, P. Escribano, C. Philippe, B. Viana and C. Sanchez, *Opt. Mater.*, 2001, **18**, 309.
9. T. Brankova, V. Bekiari and P. Lianos, *Chem. Mater.*, 2003, **15**, 1855.
10. V. de Zea Bermudez, L. D. Carlos, M. C. Duarte, M. M. Silva, C. J. R. Silva, M. J. Smith, M. Assunção and L. Alcacér, *J. Alloy Compd.*, 1998, **277**, 21.
11. S. J. L. Ribeiro, K. Dahmouche, C. A. Ribeiro, C. V. Santilli and S. H. Pulcinelli, *J. Sol-Gel Sci. Techn.*, 1998, **13**, 427.
12. V. de Zea Bermudez, L. D. Carlos and L. Alcácer, *Chem. Mater.*, 1999, **11**, 569.
13. E. Stathatos, P. Lianos, U. L. Stangar, B. Orel and P. Judeinstein, *Chem. Mater.*, 2000, **16**, 8672.
14. L. D. Carlos, R. A. S. Ferreira, V. de Zea Bermudez and S. J. L. Ribeiro, *Adv. Funct. Mater.*, 2001, **11**, 111.
15. L. D. Carlos, R. A. S. Ferreira, R. N. Pereira, M. Assunção and V. de Zea Bermudez, *J. Phys. Chem. B*, 2004, **108**, 14924.
16. M. C. Gonçalves, V. de Zea Bermudez, R. A. S. Ferreira, L. D. Carlos, D. Ostrovskii and J. Rocha, *Chem. Mater.*, 2004, **16**, 2530.
17. L. S. Fu, R. A. S. Ferreira, N. J. O. Silva, L. D. Carlos, V. De Zea Bermudez and J. Rocha, *Chem. Mater.*, 2004, **16**, 1507.
18. L. D. Carlos, V. de Zea Bermudez, V. S. Amaral, S. C. Nunes, N. J. O. Silva, R. A. S. Ferreira, J. Rocha, C. V. Santilli and D. Ostrovskii, *Adv. Mater.*, 2007, **19**, 341.

19. S. C. Nunes, V. de Zea Bermudez, J. Cybinska, R. A. S. Ferreira, J. Legendziewicz, L. D. Carlos, M. M. Silva, M. J. Smith, D. Ostrovskii and J. Rocha, *J. Mater. Chem.*, 2005, **15**, 3876.
20. W. M. Faustino, O. L. Malta and G. F. de Sá, *J. Chem. Phys.*, 2005, **112**, 054109.
21. G. Qian and M. Wang, *J. Am. Ceram. Soc.* , 2000, **83**, 703.
22. L. R. Matthews and E. T. Knobbe, *Chem. Mater.*, 1993, **5**, 1697.
23. H. H. Li, S. Inoue, K. Machida and G. Adachi, *Chem. Mater.*, 1999, **11**, 3171.
24. V. Bekiari, P. Lianos and P. Judeinstein, *Chem. Phys. Lett.*, 1999, **307**, 310.
25. A. C. Franville, D. Zambon, R. Mahiou and Y. Troin, *Chem. Mater.*, 2000, **12**, 428.
26. D. Dong, S. Jiang, Y. Men, X. Ji and B. Jiang, *Adv. Mater.*, 2000, **12**, 646.
27. Q. H. Xu, L. S. Fu, L. S. Li, H. J. Zhang and R. R. Xu, *J. Mater. Chem.* , 2000, **10**, 2532.
28. M. Bredol, T. Jüstel and S. Gutzov, *Opt. Mater.* , 2001, **18**, 337.
29. H. R. Li, J. Lin, H. J. Zhang, L. S. Fu, Q. G. Meng and S. B. Wang, *Chem. Mater.*, 2002, **14**, 3651.
30. R. Moleski, E. Stathatos, V. Bekiari and P. Lianos, *Thin Solid Films*, 2002, **416**, 279.
31. K. Binnemans, P. Lenaerts, K. Driesen and Görller-Walrand, *J. Mater. Chem.* , 2004, **14**, 191.
32. L. N. Sun, H. J. Zhang, Q. G. Meng, F. Y. Liu, L. S. Fu, C. Y. Peng, J. B. Yu, G. L. Zheng and S. B. Wang, *J. Phys. Chem. B*, 2005, **109**, 6174.
33. L. D. Carlos, R. A. S. Ferreira, V. de Zea Bermudez, C. Molina, L. A. Bueno and S. J. L. Ribeiro, *Phys. Rev. B*, 1999, **60**, 10042.
34. M. M. Silva, V. de Zea Bermudez, L. D. Carlos, A. P. Almeida and M. J. Smith, *J. Mater. Chem.*, 1999, **9**, 1735.
35. L. D. Carlos, Y. Messaddeq, H. F. Brito, R. A. S. Ferreira, V. de Zea Bermudez and S. J. L. Ribeiro, *Adv. Mater.*, 2000, **12**, 594.
36. R. A. S. Ferreira, L. D. Carlos, R. R. Goncalves, S. J. L. Ribeiro and V. de Zea Bermudez, *Chem. Mater.*, 2001, **13**, 2991.
37. C. Molina, K. Dahmouche, Y. Messaddeq, S. J. L. Ribeiro, M. A. P. Silva, V. De Zea Bermudez and L. D. Carlos, *J. Lumin.*, 2003, **104**, 93.

38. L. S. Fu, R. A. S. Ferreira, N. J. O. Silva, J. A. Fernandes, P. Ribeiro-Claro, I. S. Goncalves, V. De Zea Bermudez and L. D. Carlos, *J. Mater. Chem.*, 2005, **15**, 3117.

39. M. C. Gonçalves, N. J. O. Silva, V. de Zea Bermudez, R. A. S. Ferreira, L. D. Carlos, K. Dahmouche, C. V. Santilli, D. Ostrovskii, I. C. Correia Vilela and A. F. Craievich, *J. Phys. Chem. B*, 2005, **109**, 20093.

40. P. Lenaerts, A. Storms, J. Mullens, J. D'Haen, C. Gorller-Walrand, K. Binnemans and K. Driesen, *Chem. Mater.*, 2005, **17**, 5194.

41. P. P. Lima, R. A. S. Ferreira, R. O. Freire, F. A. A. Paz, L. S. Fu, S. Alves, L. D. Carlos and O. L. Malta, *Chemphyschem*, 2006, **7**, 735.

42. M. Fernandes, V. de Zea Bermudez, R. A. S. Ferreira, L. D. Carlos, A. Charas, J. Morgado, M. M. Silva and M. J. Smith, *Chem. Mater.*, 2007, **19**, 3892.

43. P. Nockemann, E. Beurer, K. Driesen, R. Van Deun, K. Van Hecke, L. Van Meervelt and K. Binnemans, *Chem. Commun.* , 2005, 4354.

44. T. Föerster, *Z. Naturforsch. A*, 1949, **49**, 321.

45. D. L. Dexter, *J. Chem. Phys.*, 1953, **21**, 836.

46. J. R. Lakiwicz, *Principles of Fuorescence Spectroscopy*, Kluwer Academic/Plenum Publishers, New York, 1999.

47. N. J. Turro, *Modern Molecular Photochemistry*, University Science Books, Sausalito, 1991.

48. O. L. Malta, *J. Lumin.*, 1997, **71**, 229.

49. O. L. Malta and F. R. Gonçalves e Silva, *Spectrochim. Acta A*, 1998, **54**, 1593.

50. L. D. Carlos, V. de Zea Bermudez, R. A. S. Ferreira, L. Marques and M. Assunção, *Chem. Mater.*, 1999, **11**, 581.

51. W. Kolodziejsli, A. Corma, M. T. Navarro and J. Perez-Parientte, *Solid State Nucl. Magn. Reson.*, 1993, **2**, 253.

52. J. B. Stothers, *Carbon-13 NMR Spectroscopy*, Academic, New York, 1972.

53. F. Ribot, A. Lafuma, C. Eychenne-Baron and C. Sanchez, *Adv. Mater.*, 2002, **14**, 1496.

54. E. Stathatos, P. Lianos, B. Orel, A. S. Vuk and R. Jese, *Langmuir*, 2003, **19**, 7587.

55. V. Bekiari, E. Stathatos, P. Lianos, U. L. Stangar, B. Orel and P. Judeinstein, *Chem. Mater.*, 2000, **12**, 3095.

56. R. A. S. Ferreira, A. L. Ferreira and L. D. Carlos, *Eur. Phys. J. B*, 2006, **50**, 371.

57. R. A. S. Ferreira, A. L. Ferreira and L. D. Carlos, *J. Non-Cryst. Solids*, 2006, **352**, 1225.

58. R. A. S. Ferreira, L. D. Carlos and V. de Zea Bermudez, *Thin Solid Films*, 1999, **343**, 476.

59. T. Schmidt, K. Lischka and W. Zulehener, *Phys. Rev. B*, 1992, **45**, 8989.

60. H. Koyama, T. Ozaki and N. Koshida, *Phys. Rev. B*, 1995, **52**, 11561.

61. K. S. Zhuravlev, A. M. Gilinsky and A. Y. Kobitsky, *Appl. Phys. Lett.*, 1998, **73**, 2962.

62. B. Canny and D. Curie, in *Advances in Nonradiative Processes in Solids*, ed. B. Dibartolo, Plenum Press, New York, 1991.

63. R. O. Freire, G. B. Rocha and A. M. Simas, *J. Mol. Model.*, 2006, **12**, 373.

64. M. J. S. Dewar, E. G. Zoebisch, E. F. Healy and J. J. P. Stewart, *J. Am. Chem. Soc.*, 1985, **107**, 3902.

65. J. J. P. Stewart, *MOPAC 2002*, Fujitsu Limited, Tokyo, 1999.

66. J. J. E. Moreau, B. P. Pichon, M. Wong Chi Man, C. Bied, H. Pritzkow, J. L. Bantignies, P. Dieudonne and J. L. Sauvajol, *Angew. Chem. Int. Edit.*, 2004, **43**, 203.

67. R. A. W. Dryfe, Z. Ding, R. G. Wellington, P. F. Brevet, A. M. Kuznetzov and H. H. Girault, *J. Phys. Chem. A*, 1997, **101**, 2519.

Chapter 4 - Photoluminescent bridged silsesquioxanes with different morphologies

4.1 Introduction

Functional organic/inorganic hybrid materials with improved or unusual features have received considerable attention in the last few years. Their rational design through bottom-up approaches, especially soft inorganic chemistry routes such as the sol–gel method,[1-3] relying on the appropriate choice of hybrid nano-objects (*i.e.* nanobuilding blocks, NBBs), permits to tailor the properties over broad length scales (from the atomic to the mesoscopic and macroscopic levels) with the consequent impact in diverse fields (*e.g.* photonics, microelectronics and micro-optics, catalysis, smart coatings, cosmetics, energy and biomedicine).[4-7]

In the last few years the combination of sol-gel reactions with self-assembly strategies[8-12] or molecular recognition principles[13] have been successfully explored to produce sophisticated and complex hierarchically structured organic/inorganic hybrid systems. Highly organized hybrids with well defined morphologies on the macroscopic scale and controlled nanostructures were synthesized from di-urea[12,14-18] and mono-amide[19] cross-linked alkylsilanes. The challenging underlying concept relies essentially on the establishment of weak hydrophobic interactions between the alkyl chains and on the ability of adjacent amide/urea groups to self-assemble through strong/very strong hydrogen bonding interactions which give rise to the creation of a hydrogen-bonded array that plays the role of internal template thus directing the growth of the supramolecular architecture.

The organization of hybrid silicas depends critically on the synthetic procedure. In the case of the di-urea cross-linked alkylsilane precursor including a dodecyl chain (**P12**) the use of an acid catalyst (hydrochloric acid, HCl) and a large excess of water (R ($molmol^{-1}$) = H_2O/Si = 300) induced the formation of a crystalline lamellar structure (**L12**).[12] In contrast, when ammonium fluoride (NH_4F) catalyst was employed in ethanol (EtOH) medium under stoichiometric conditions (R = 3) an amorphous material (**A12**) was obtained.[16] Combining the interest in structured hybrids with the interesting photophysical properties of lanthanide (Ln^{3+})-based organic/inorganic hybrids (discussed in chapter) we adopted the supramolecular self-assembly for design lamellar optically-active lanthanide-doped hybrids **Eu@L12**. Seeking at establishing a relationship between the long range organization of hybrid materials and their physical properties we looked forward to

comparing the photoluminescence features of **L12** and **Eu@L12** with those of the corresponding amorphous hybrids (**A12** and **Eu@A12**, respectively).

This study is of the outmost interest in the context of nanoengineering and has become a challenging topic of the field of sol-gel derived hybrid materials. It implies the fine control of the synthetic conditions (often bottom-up approaches) and the rational choice of NBBs that enable the formation of hierarchically structured architectures exhibiting the required properties. In many occasions changing a single synthetic parameter may have the deepest consequences on the morphology and physico-chemical behavior of the same hybrid sample.

Here is presented the unique role played by the Eu^{3+} ions in the modulation of the morphology and size of the **Eu@A12** hybrids (Scheme 4.1) *via* inhibition of the growth of the siloxane network formed through sol-gel reactions and urea-mediated supramolecular self-assembly. This process results in the formation of primary *ca.* 200 nm-long plates which first pile up in a brick-like fashion that mimics the nacre structure,[20,21] and then form fibers that ultimately self-assemble on the micrometer scale. Bundle to dumbbell shapes are produced under increasing Eu^{3+} amount. The voids between the fibers act as percolation channels for the release of ethanol.

This work represents a unique opportunity to address the effect of the morphology on the photoluminescence features of hybrids as we have been able to, starting from the same precursor, synthesize two systems with approximately the same Eu^{3+} concentration (1 %) but displaying completely different morphologies.

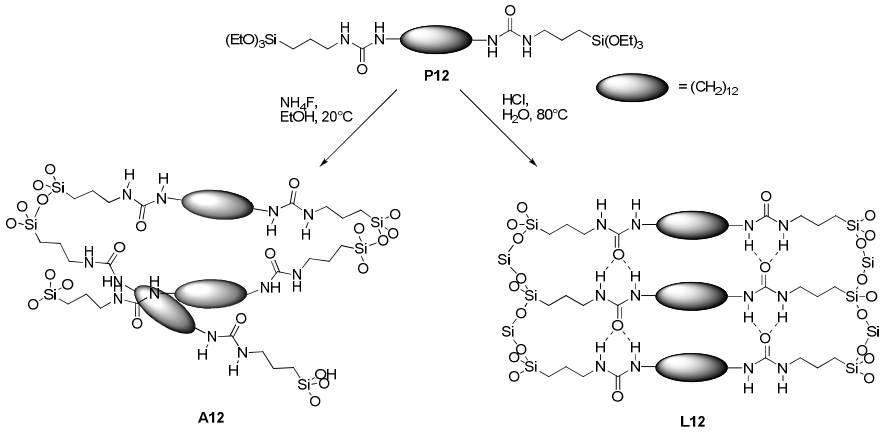

Scheme 4.1 Schematic representation of the synthesis of **A12** and **L12**.

4.2 Synthesis

P12

Freshly distilled 1,12-diaminododecane (Fluka,1.6 g, 8.0 mmol) was dissolved in dry dichloromethane (40 mL) under a nitrogen atmosphere in a Schlenk tube. *γ*-isocyanatopropyltriethoxysilane (4.0 g, 16.1 mmol) was slowly added by syringe at room temperature. The mixture was stirred for 12 h then the solvent was removed in vacuum to give a white powder that was washed three times with dry *n*-pentane and finally dried in vacuum.[8]

L12 and Eu@L12 hybrids

The **P12** precursor (0.3 g, 0.4 mmol) was placed in a 20 mL round bottom flask together with a mixture of water (4.4 mL, 244 mmol), hydrochloric acid (0.1 M, 80 µL, 0.008 mmol) and europium chloride hexahydrate, $EuCl_3 \cdot 6H_2O$ (Aldrich, 7.7 mg, 0.02 mmol; 0.15 g, 0.41 mmol and 0.45 g, 1.2 mmol for **Eu@L12-1, Eu@L12-2** and **Eu@A12-3** respectively). The molar ratio of the reactants is the following: **P12**/H_2O/HCl/$EuCl_3 \cdot 6H_2O$ 1:600:0.2:y (y = 0, 0.05, 0.95, 2.9 corresponds to the **L12**, **Eu@L12-1**, **Eu@L12-2** and **Eu@L12-3** hybrids respectively. The mixture was vigorously stirred, at 80 ^{0}C for 1 h then allowed to stand for 48 h at 80 ^{0}C. After this period of time the hybrid material was recovered by filtration and was successively washed with water, ethanol and acetone. Finally, the hybrids were dried at 110 ^{0}C during 6 h. White powders were obtained in all cases. Elemental analyses revealed Europium content versus the total hybrid's mass (w/w) of 1.01, 1.83 and 15.04 % in the **Eu@L12-1**, **Eu@L12-2** and **Eu@L12-3** hybrids, respectively, Table 4.1.

A12 and Eu@A12 hybrids

The **P12** precursor (1.0 g, 1.4 mmol) was placed in a 20 mL round bottom flask and dissolved in ethanol (5.0 mL, 86 mmol). A mixture of water (155 µL, 8.6 mmol), ammonium fluoride (Fluka, 0.5 mg, 0.014 mmol) and $EuCl_3 \cdot 6H_2O$ (Aldrich, 0.38 g, 1 mmol or 0.75 g, 2.0 mmol for **Eu@A12-1** and **Eu@A12-2** respectively) was added to the **P12** solution. The molar ratio of the reactants is the following: **P12**/EtOH/H_2O/NH_4F/$EuCl_3 \cdot 6H_2O$: 1:60:6:0.01:y (y=0, 0.73 and 1.42 for **A12**, **Eu@A12-**

1 and **Eu@A12-2** hybrids respectively). The initially clear solution was stirred for 30 min and was left standing for 3 days. Gelation occurred within 24 hours. The gel was successively washed with water, ethanol, acetone and was freeze-dried overnight. White powders were obtained in all cases. Another hybrid was also prepared under nucleophilic catalysis, under the experimental conditions previously described but dried at 110 ^{0}C during 6 h, which was designated as **A12$_{T}$**. Elemental analyses revealed a content of 0.74 and 1.31 % (w/w) of Eu in the **Eu@A12-1**, **Eu@A12-2** hybrids, respectively, Table 4.1.

Table 4.1. % Europium (w/w) obtained from elemental analysis of the hybrids.

	Eu@L12-1	**Eu@L12-2**	**Eu@L12-3**	**Eu@A12-1**	**Eu@A12-2**
% Eu (w/w)	1.01	1.83	15.04	0.74	1.31

4.3 Local Structure

The Scanning Electron Microscopy (SEM) images of the **L12**, **Eu@L12-1**, **Eu@L12-2** and **Eu@L12-3** hybrids depicted in Fig. 4.1 show well-defined thin plates 1-2 µm large, 3-5 μm long, and 50-100 nm thick.

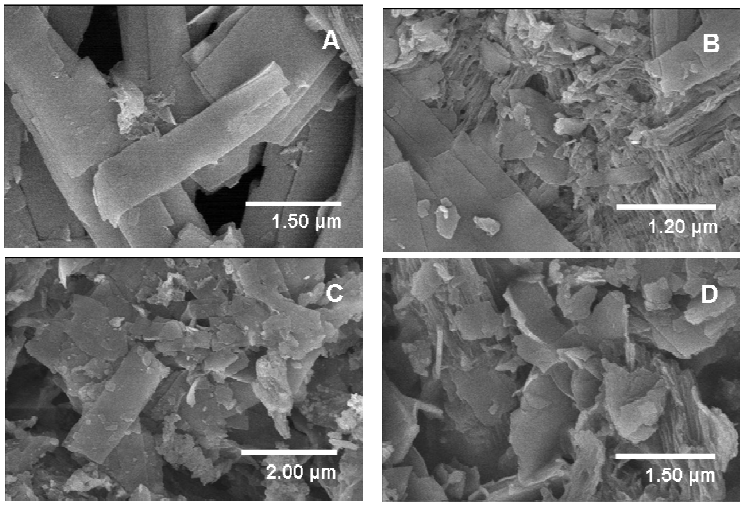

Figure 4.1 SEM images of (A) **L12**, (B) **Eu@L12-1**, (C) **Eu@L12-2** and (D) **Eu@L12-3**.

The SEM images of the **A12**, **Eu@A12-1** and **Eu@A12-2** hybrids are depicted in Fig. 4.2 and display different morphologies relatively to those of **L12** hybrids. The SEM images of **A12** reveal an irregular round shape morphology (3.0 to 10.0 µm in diameter) with a rough surface composed of plates (Fig. 4.2A). We note that this morphology differs from that previously reported due to the lack of thermal treatments in the current study.[16] In the case of the Eu^{3+}-containing hybrids, 3.0-4.0 µm long and 0.5-1.0 µm width, bundles of twisted fibres or ribbons are observed for **Eu@A12-1** (Fig. 4.2B). In the case of **Eu@A12-2** (Fig. 4.2C), these bundles grow thicker (1.0-3.0 µm width) on increasing the amount of Eu^{3+}, although their length remains unaffected. The resulting dumbbell structure exhibits a hollow substructure at the tips composed of channels of *ca* 0.1 µm in diameter (Fig. 4.2C). These observations demonstrate that the Eu^{3+} content plays a key factor in the structuring of these systems. It is noteworthy that the Eu^{3+} ions and Si atoms are homogeneously distributed at the surface of these objects, in regions with an average size of *ca.* 200 nm as evidenced by the X-ray mapping of the relative Si and Eu contents performed on

Eu@A12-2 (Fig. 4.2D and 4.2E, respectively). Whereas for **L12** hybrids the Eu^{3+} ions have a passive role (all the materials display a similar lamellar morphology) for **A12** hybrids the addition of Eu^{3+} salts plays a key role in the structuring (the morphology depends on the concentration of Eu^{3+}).

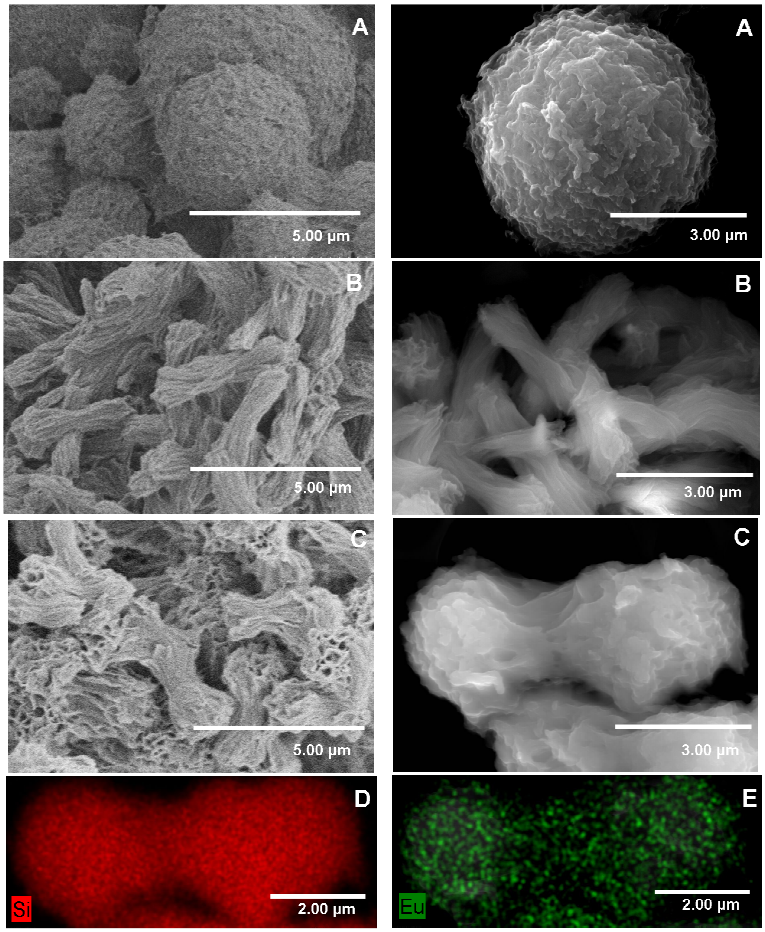

Figure 4.2 SEM images of (A) **A12**, (B) **Eu@A12-1** and (C) **Eu@A12-2** and EDX of **Eu@A12-2** for (D) Si and (E) Eu.

A more detailed view of the surface of these hybrids was obtained using Atomic Force Microscopy (AFM). The lamellar morphology observed in the AFM images of the **L12** hybrid host (Fig. 4.3) is consistent with the SEM results (Fig. 4.1).

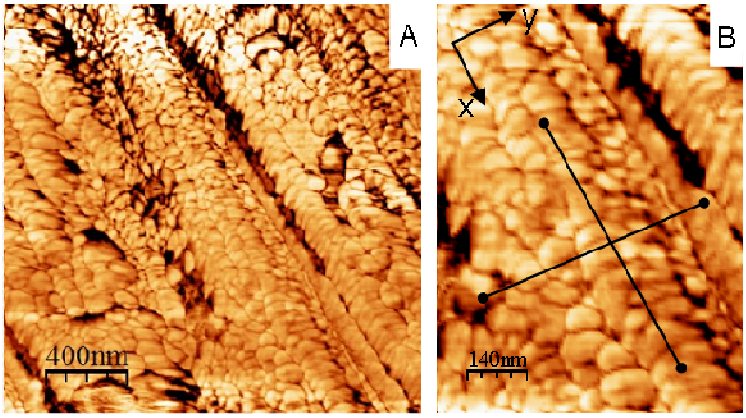

Figure 4.3 (A) AFM image (scanned area = 2 x 2 μm^2) of **L12**; (B) detailed amplification of a region of figure 4.3A.

The characteristic dimensions of the lamellar morphology were estimated taking several cross-section profiles in different planes of the image of Fig. 4.3A, as presented in Fig. 4.4. Average size values of 63±10 and 108±15 nm were deduced along the yy' and xx' directions, respectively.

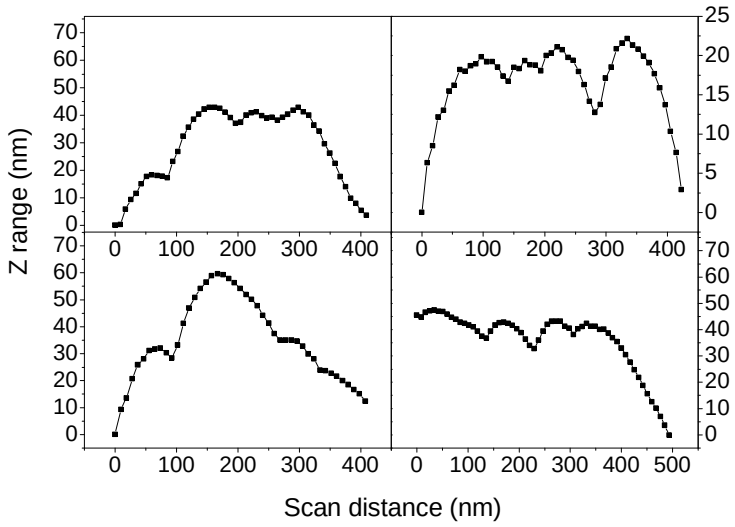

Figure 4.4 Representative cross sections of the AFM profile of **L12**.

According to the AFM image, the surface of **A12** consists of long and irregular plates aligned along the same axis (Fig. 4.5A). In the case of **Eu@A12-1** (Fig.4.5B), the image shows two microfibers separated by a grain boundary and evidences the presence of regular thin flakes (166 ± 30 nm × 353 ± 90 nm) that tend to pile up and to align along the micro-fibres axis, in a brick-to-brick like arrangement. Such organization is less obvious

on the surface of the dumbbell shape of **Eu@A12-2** (Fig. 4.5C), with slightly bigger flakes (195 ± 15 nm × 410 ± 25 nm).

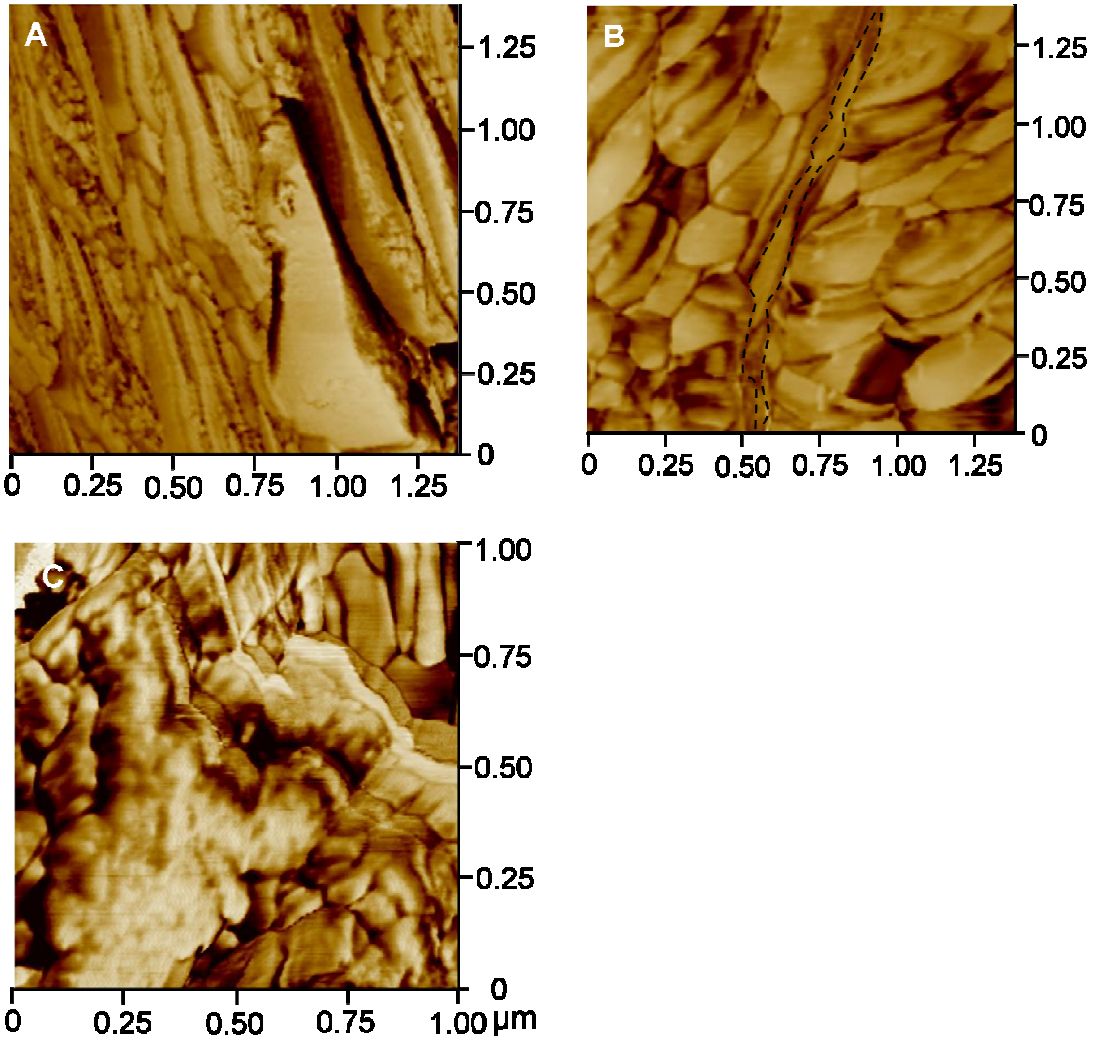

Figure 4.5 AFM image of (A) **A12**, (B) **Eu@A12-1** and (C) **Eu@A12-2**. The dashed line indicates the grain boundaries between two microfibers.

The ^{13}C CP-MAS NMR spectra of the lamellar hybrids (**L12**, **Eu@L12-1**, **Eu@L12-2** and **Eu@L12-3**) are reproduced in Fig. 4.6A and those of the amorphous hybrids (**A12**, **Eu@A12-1** and **Eu@A12-2**) in Fig. 4.6B.

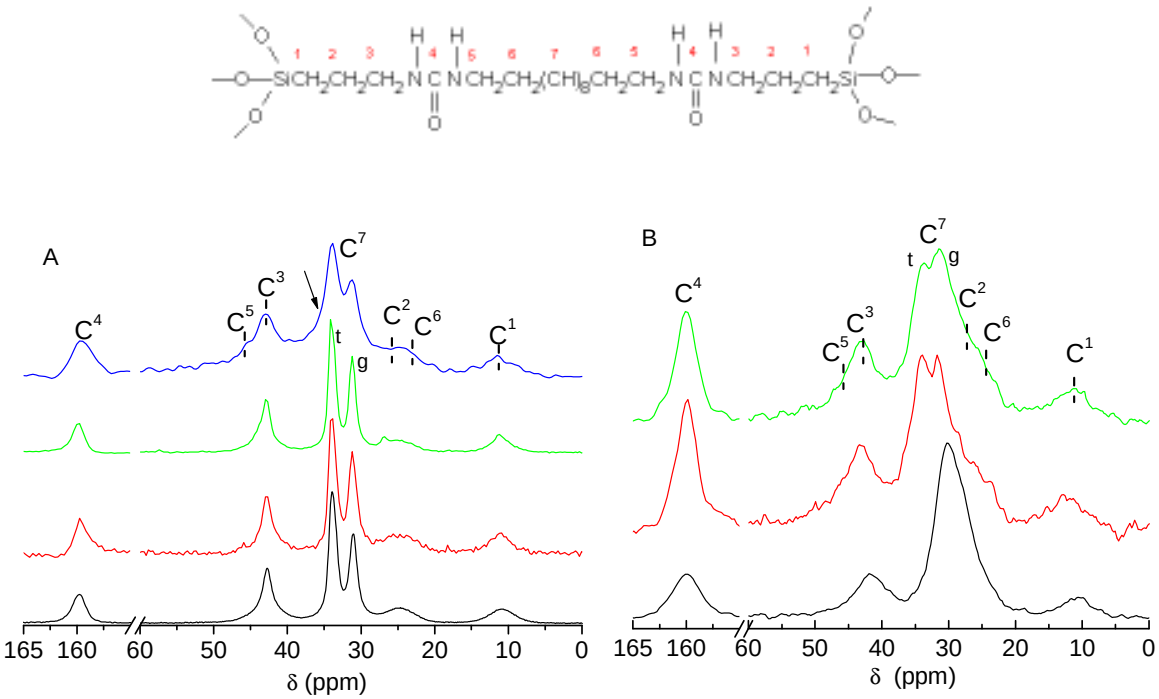

Figure 4.6 ^{13}C CP-MAS NMR spectra of (A) **L12** (black line), **Eu@L12-1** (red line), **Eu@L12-2** (green line), and **Eu@L12-3** (blue line). (B) **A12** (black line), **Eu@A12-1** (red line) and **Eu@A12-2** (green line).

All the hybrids present signals at 10.0-12.0 ppm ascribed to the ***C***H_2-Si carbon (C^1), thus confirming the covalent bonding of the organic fragment with the siloxane network. The presence of the urea groups is evidenced by the low field signal at 159.9 ppm (C^4). The propyl and alkyl chains also remain unaffected in the final materials as demonstrated by the presence of the carbons resonances at 41.9-43.0 ppm (**C**H_2-N) (C^3, C^5), and 30.3-31.5 ppm (CH_2-(**C**H_6)-CH_2) (C^7) (alkyl chain).[22-24]

The ^{13}C CP-MAS spectra of the **L12**, **Eu@L12-1**, **Eu@L12-2** and **Eu@L12-3** are dominated by the resonances centred at 33.8 and 31.2 ppm which are assigned to the C^7 carbon atoms of the alkyl chains in crystalline (densely packed all-*trans* chains) and amorphous regions (essentially *gauche* conformations), respectively.[22-24] For the **Eu@L12-1** and **Eu@L12-2** the integrated intensity and fwhm of the resonances (obtained by fitting the ^{13}C CP/MAS spectra of Fig. 4.6A with Lorentzian-Gaussian functions) are similar to those of the pristine **L12** framework, but marked changes are detected in the most concentrated sample: i) a new resonance (shoulder) observed at *ca.* 37.0 ppm (arrow in Fig. 4.6A) is assigned to crystalline alkyl chains with lower conformational order,[22] ii)

despite the *trans/gauche* conformational ratio (estimated through their relative integrated areas) remains unchanged the fwhm of the C^7 *trans* and C^7 *gauche* resonances increases considerably, from 1.2 to 2.3 and 1.3 to 2.4 ppm, respectively (the other resonances also broaden *ca.* 1.5 times). This evidence suggests that the Eu^{3+} incorporation induces polymer chain disorder in the lamellar host. The presence of paramagnetic Eu^{3+} ions may, in principle, also broaden the NMR lines. However, this interaction would also introduce into the ^{13}C CP/MAS NMR spectra relatively intense spinning sidebands. Because these bands are not intense in the spectrum of **Eu@L12-3**, the paramagnetism of the Eu^{3+} ions should have only a small contribution to the broadening of the all-*trans* and *gauche* resonances.

While in the case of **A12** the methylene groups of mostly resonate at 30.0 ppm, with no contribution at 34.0 ppm, the spectra of the **Eu@A12-1** and **Eu@A12-2** are dominated by two resonances centred at 31.3 and 33.9 ppm, evidencing the presence of highly ordered *all-trans* chains together with chains that adopt *gauche* conformations. This ordering of the structure of the doped hybrids can also be evidenced by the narrowing of the urea signal at 159.9 ppm. The fwhm of the corresponding resonance decreases from 3.2 ppm for **A12** to 2.4 ppm for **Eu@A12-2**, indicating a smaller dispersion of environments around the non coordinated urea groups.

The ^{29}Si CP-MAS NMR spectra of all the hybrids lamellar and amorphous are shown in Figs. 4.7A and 4.7B. The solid state ^{29}Si NMR spectra of all the hybrids exhibit resonances centred at –47.9, –57.1 and –67.0 ppm, respectively, ascribed to $R'Si(OSi)_1(OH)_2$ (T_1), $R'Si(OSi)_2(OH)$ (T_2) and $R'Si(OSi)_3$ (T_3) silicon environments. The absence of signals attributable to *Q* types of silicon atoms evidences the total conservation of the linkage between the organic and inorganic counterparts. The condensation degree (*c*) was calculated using the expression:

$$c=1/3(\%T_1+2\%T_2+3\%T_3) \quad (4.1)$$

For the **L12** and **Eu@L12** hybrids, the condensation degrees have similar values, between 64 to 67%. The condensation degree determined for **A12** (91 %) indicates that the material is almost fully condensed, whereas for **Eu@A12-1** and **Eu@A12-2** this value decreases to 65 and 63 %, respectively, indicating the occurrence of a dominant T_2

environment, as already observed for other organic/inorganic hybrids synthesized in the presence of Eu^{3+} complexes.[25]

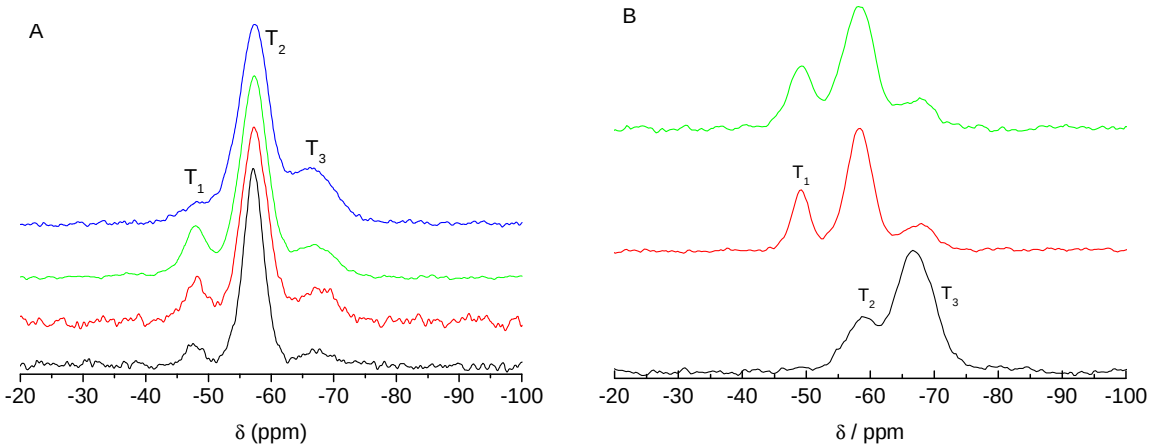

Figure 4.7 ^{29}Si CP-NMR spectra of (A) **L12** (black line), **Eu@L12-1** (red line), **Eu@L12-2** (green line), and **Eu@L12-3** (blue line). (B) **A12** (black line), **Eu@A12-1** (red line) and **Eu@A12-2** (green line).

Fig. 4.8 displays the XRD patterns of the **L12, Eu@L12-1**, **Eu@L12-2** and **Eu@L12-3** hybrids. The patterns display narrow peaks, typical of medium- to long-range ordered structures, which relative intensity (and signal-to-noise ratio) decreases as the amount of Eu^{3+} incorporated increases from 1 to 15%, indicating that the Eu^{3+} incorporation induces chain disorder. The k^{th} order reflections (k between 2 and 8) of a lamellar structure are discerned. The low intensity of the 2nd harmonic is probably due to a zero of the structure factor which accidently occurs for a value of the scattering vector q ($q = \frac{4\pi}{\lambda}\sin\theta$) close to 4.34 nm.[26]

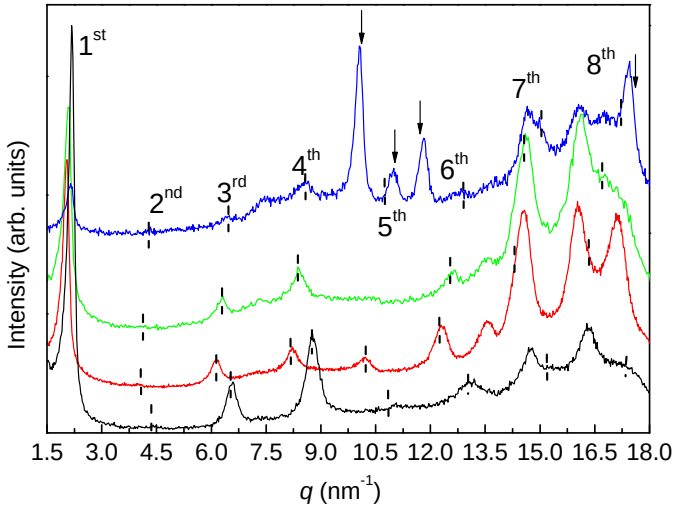

Figure 4.8 XRD patterns of **L12** (black line), **Eu@L12-1** (red line), **Eu@L12-2** (green line), and **Eu@L12-3** (blue line). The dashed lines assign the n^{th} order reflections in each pattern and the arrows denote reflections originated from $EuCl(OH)_2$ (Reference code: 04-006-9702).

The characteristic interlamellar spacing *d* was calculated using the SAXS data (Fig. 4.9), using $d=2\pi/q$, where *q* is the magnitude of the scattering vector. The characteristic interlamellar spacing gave values of 2.92±0.01 nm,[15,16,26] for **L12**, 3.01±0.01 nm, for both **Eu@L12-1** and **Eu@L12-2**, and 2.85±0.01 nm, for **Eu@L12-3**. This interlamellar distance corresponds to the separation between siliceous domains governed by the alkyl chain length[15,16,26] and is compatible with the length of the organic spacer in these hybrids (estimated average distance of 2.99 nm assuming average C–C,C–N, and C(=O)–N distances of 0.13 nm). The increase of the interlamellar distance for **Eu@L12-1** and **Eu@L12-2** is essentially associated with the breakdown of the hydrogen bonded urea-urea array caused by the entrance of Eu^{3+} and Cl^- ions into the lamelar **L12** structure, as it will be further addressed in more detail. In fact, for these low Eu^{3+} contents the *trans/gauche* conformational ratio remains essentially unchanged (*cf.* Fig. 4.6A) and thus the incorporation of the Eu^{3+} and Cl^- ions into the ordered **L12** hydrogen bonded template is the main responsible for the increase of the interdomain distance. In contrast, the subsequent decrease of the interlamellar distance as the Eu^{3+} amount increases from *ca.* 2 (**Eu@L12-2**) to 15% (**Eu@L12-3**) is ascribed to an increase in the degree of disorder of the polymer chains, as suggested by XRD and ^{13}C CP-MAS NMR data.

For assessment of the average coherence length of the lamellar order, the integral breadths of the 1^{st} order diffraction peaks observed in the SAXS patterns (Fig. 4.9) were

corrected from the instrumental broadening by using a well crystalline sample as a standard reference of experimental aberrations. The corrected integral breadth was estimated from $\beta^2 = B^2-b^2$, where B is the integral breadth of the first order diffraction peak and b the instrumental broadening. Assuming that the corrected integral breadths are essentially due to the size effects, the coherence length of this lamellar order, estimated by the modified Scherrer equation, $L=I\lambda/A\ cos\theta$, where A, in radians, is the integrated area of the peaks and I is its intensity.[27] The obtained values were 90.1±4.5 nm, for **L12**, 119.5±6.0 nm, for **Eu@L12-1**, 116.3±5.8 nm, for **Eu@L12-2**, and 102.2±5.1 nm, for **Eu@L12-3**. It should be noted that the average coherence length of the lamellar order in the **L12** hybrid calculated by SAXS agrees well with the average size estimated from AFM data along to the xx' direction (Fig. 4.3) (108±15 nm), illustrating that this hybrid represents one of the first examples of a lamellar organized structure that may be really seen by AFM.

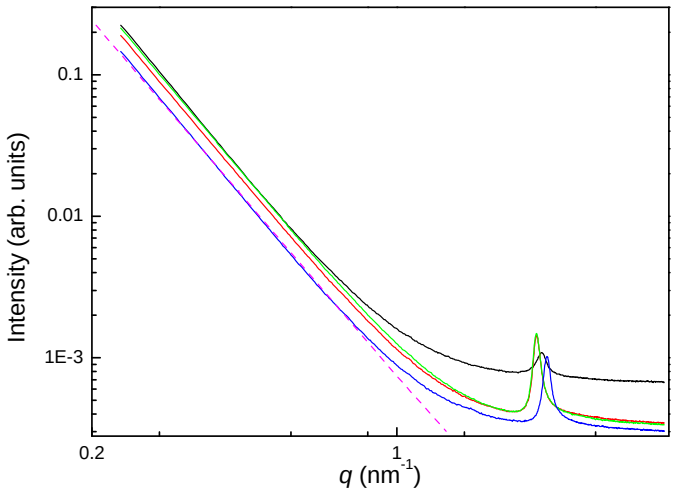

Figure 4.9 SAXS patterns of **L12** (black line), **Eu@L12-1** (red line), **Eu@L12-2** (green line), and **Eu@L12-3** (blue line). The magenta dashed line represents the linear fit to the scattered intensity of the Eu@L12-3 hybrid (r=0.9997).

The intensity of the SAXS patterns at low q values (q<1 nm^{-1}) depends on the geometric structure of the scattering entities. For a large number of sol-gel derived materials this geometry has been described using the concept of fractal geometry.[28-30] For surface fractals (uniform objects that scatter radition only from the surface) the scattered

intensity obeys to a power law in the magnitude of q, $I(q) \sim q^{D-6}$, where D is the surface fractal dimension relating surface area to length. For smooth surfaces D=2 and the scattered intensity decays as q^{-4} (Porod's law). For fractal surfaces, $2<D<3$, Porod slopes between –3 and –4 are expected.[28]

For all the **L12**-based hybrids the obtained slope is *ca.* –3.7 meaning that the boundaries of the scattering particles are quite well defined. Moreover, the Eu^{3+} incorporation enlarges the q range for which the SAXS curves follow that slope (q_{min} *ca.* 0.56 nm^{-1} and *ca.*1.10 nm^{-1} for **L12** and doped hybrids, respectively, Fig 4.9) indicating that the differences in the structures induced by the Eu^{3+} incorporation occur in a length scale lower than *ca.*11 nm. Between this value and *ca.* 27 nm (corresponding to the lower angle measured) the structure of all the samples is identical.

The XRD patterns in the high q region (Fig. 4.8) exhibit four peaks between 13.5 and 17.5 nm^{-1}, better resolved in the XRD patterns of **Eu@L12-1** and **Eu@L12-2**. Despite the overlap between these peaks and the 7th and 8th orders, (007) and (008) planes, which causes a broadening effect (Fig. 4.8) it was possible to rationalize their shifts as a function of the Eu^{3+} amount incorporated into the **L12** hybrid host. The ill-defined peak at 14.01 nm^{-1} (corresponding to a distance of 0.448 nm) in the **L12** XRD pattern shifts to 13.55 nm^{-1} (0.463 nm) in the XRD patterns of **Eu@L12-1** and **Eu@L12-2**. This peak can be attributed to the separation between two neighbouring urea groups in the self-associated urea-urea hydrogen-bonded array[14,16,31] (Scheme 4.1). The shift reported is therefore in accordance with the Eu^{3+} coordination to some carbonyl groups with the concomitant increase of the mean distance between adjacent urea moieties. The peak at 14.75 nm^{-1} (0.426 nm) in the **L12** XRD pattern can be attributed to ordering within the siloxane domains, as previously reported for amorphous organic/inorganic hybrids.[27,32] This peak remains essentially unchanged for all the **Eu@L12** hybrids suggesting that the Eu^{3+}/Cl^- incorporation does not significantly affect the siloxane domains. The pair of peaks at 16.31 and 17.20 nm^{-1} in the **L12** diffractogram of Fig. 4.8 (with d-spacings of 0.385 and 0.365 nm, respectively), previously reported for similar hybrids with shorter hydrocarbon chains[16] and for other ordered hybrids as a large broad single band,[10,23,33] is attributed to chain-chain spacings (Scheme 4.1). The peak at 16.31 nm^{-1} shifts to 16.07 nm^{-1} (0.390 nm) as the Eu^{3+} concentration increases (XRD patterns of **Eu@L12-1**, **Eu@L12-2**, and **Eu@L12-3**, Fig. 4.8). This increase of the mean distance between the alkyl chains is in

agreement with the incorporation of Eu^{3+} and Cl^{-} ions into the lamellar **L12** structure, despite the fact that the ill-defined peak at 17.20 nm^{-1} also seems to shift towards lower *q* values in the XRD patterns of the doped samples (Fig. 4.8). The overlapping with the 8th order, in the XRD patterns of **L12**, **Eu@L12-2** and **Eu@L12-3**, and with a $EuCl(OH)_2$ reflection, in the latter diffractogram, prevents a definite conclusion.

It is worth noting that in the XRD pattern of the **Eu@L12-3** hybrids several peaks appear between 10 and 20 nm^{-1} (Fig. 4.8), these reflections are indexed to $EuCl(OH)_2$ (ICD 04-006-9702). Presumably, the high amount of Eu^{3+} ions added during the synthesis could not be totally incorporated within the hybrid's framework, and precipitated out as a $EuCl(OH)_2$ salt that was not washed out during the treatments and remained mixed with the hybrid silica ($EuCl_3 + 2\ H_2O \rightarrow EuCl(OH)_2 + 2H^+ + 2Cl^-$).

Fig. 4.10 displays the XRD patterns of the **A12**, **Eu@A12-1** and **Eu@A12-2** hybrids.

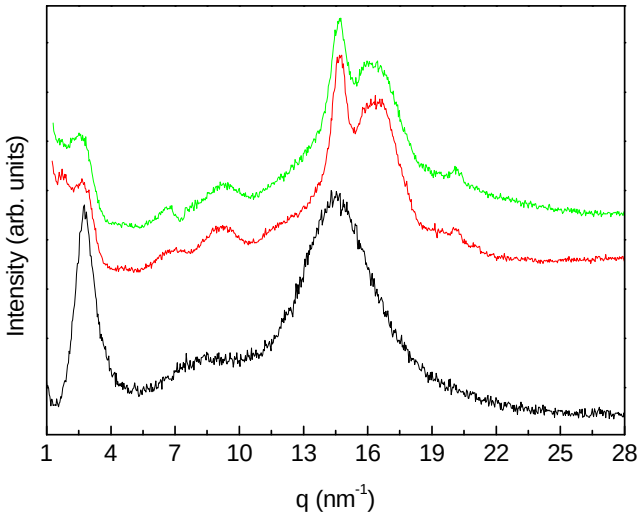

Figure 4.10 XRD patterns of **A12** (black line), **Eu@A12-1** (red line) and **Eu@A12-2** (green line).

The diffractogram of **A12** is dominated by a peak centred at 2.97 nm^{-1} and a hump centred at 14.70 nm^{-1} (Fig. 4.10). When the sol-gel synthesis is performed in the presence of europium chloride, the peak at lower *q* values, corresponding to the separation between siliceous domains governed by the alkyl chains length,[16,25,26] shifts to 2.65 nm^{-1} and 2.51 nm^{-1} for **Eu@A12-1** and **Eu@A12-2**, respectively, indicating an increase of the mean chain length. The characteristic interlamellar spacing *d* was calculated giving values of 2.25 ± 0.01 nm (**A12**) 2.37 ± 0.01 nm (**Eu@A12-1**) and 2.50 ± 0.01 nm (**Eu@A12-2**). This

is in good agreement with the increase in the proportion of *all-trans* conformations observed by in NMR data. Unfortunately these peaks are located in the beam-stop and appear as shoulders of the latter and hence do not allow the calculation of coherence lengths and the subsequent comparison with that of the **A12** hybrid. The broad peak of **A12** at 14.53 nm^{-1} results from the overlap of: (i) the separation between two neighbouring urea groups in the self-associated urea-urea hydrogen-bonded array,[14,16,19,31] (ii) the ordering within the siloxane domains and (iii) the chain-chain spacing. Upon Eu^{3+} incorporation the broad band at high *q* values is split into two shoulders indicating a better structuring in the resulting hybrids. It was possible to identify, after a deconvolution with Gaussian functions, three components at 13.08 nm^{-1} (separation between two neighbouring urea groups, 0.480 nm), 14.64 nm^{-1} (ordering within the siloxane domains, 0.426 nm) and 16.41 nm^{-1} (chain-chain spacing of 0.383 nm). In the case of the corresponding Eu^{3+}-doped lamellar hybrid **L12** it was observed (for the lower Eu^{3+} concentrations) that the separation between two neighbouring urea groups was 0.463 nm, the ordering within the siloxane domains was 0.426 nm and the chain-chain spacing was 0.385 nm. Taking in account the experimental error (0.01 nm), the values obtained for these three distances are the same in the two systems. Finally, the **Eu@A12** hybrids also exhibit three diffraction peaks at 6.77, 9.29 and 20.41 nm^{-1}, which have not yet been assigned.

The FT-IR spectra of the lamellar hybrids and amorphous hybrids are reproduced in Fig. 4.11A and Fig. 4.11B, respectively.

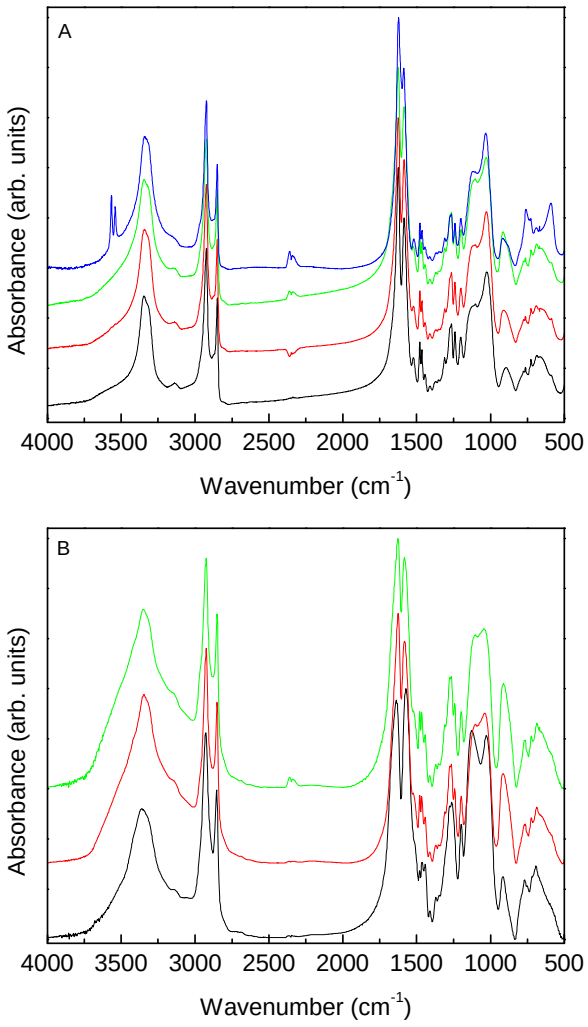

Figure 4.11 FT-IR spectra of (A) **L12** (black line), **Eu@L12-1** (red line), **Eu@L12-2** (green line), and **Eu@L12-3** (blue line). (B) **A12** (black line), **Eu@A12-1** (red line) and **Eu@A12-2** (green line).

Table 4.2 presents the characteristic bands of the **L12** and **A12** hybrids. The main purpose of the FT-IR analysis was to elucidate the Eu^{3+} coordination and to get in parallel reliable information regarding hydrogen bonding interactions.[17,26,34,35] The "amide I" and "amide II" regions of the FT-IR spectra of the hybrids were analyzed in detail (Fig. 4.12). Because of the presence of one hydrogen acceptor moiety (C=O) and two hydrogen donor moieties (NH) per urea group, the hydrogen bonds established between adjacent urea groups are typically arranged along a planar bifurcated geometry[31] that results in the occurrence of highly ordered (*i.e.* very strong) urea-urea aggregates.[36]

Table 4.2 Characteristic FT-IR bands of the **L12** and **A12** hybrids.

Vibration (cm^{-1})	**Attribution**
3690	νSiO-H free
3400-3200	νSiO-H bonded by H bonding
~3340	Amide A (νNH)
2936-2916	ν_{as} (CH_2)
2863-2843	ν_{s} (CH_2)
1800-1600	Amide I (νCO)
1600-1500	Amide II (δNH+νCN)
1475-1450	δCH_2
1130-1000	ν_{as} Si-O (Si-O-Si)
830-950	ν Si-O

The "amide I" region of the hybrids corresponds to the amide I region (1800-1600 cm^{-1}) of polyamides.[37,38] The "amide I" mode (or carbonyl stretching mode) is a very complex vibration that receives a major contribution from the C=O stretching vibration.[38] Owing to the fact that this vibration mode is sensitive to the specificity and magnitude of hydrogen bonding, the "amide I" band consists of several distinct components which correspond to different C=O environments, usually known as aggregates. As the absorption coefficients of C=O groups involved in different aggregates can be different, it is not possible to compare intensity values of different spectral components and thus only the changes undergone by each mode are an adequate reflection of the concentration variation of a certain type of association.[17,34,38,39] The "amide II" mode of the hybrids corresponds to the amide II band (1600-1500 cm^{-1}) of polyamides.[38] It is a mixed mode containing a major contribution from the N-H in-plane bending vibration, sensitive to both chain conformation and intermolecular hydrogen bonding and gives valuable information about the distribution of hydrogen bond strengths.[17,34,38]

The results of the curve-fitting performed in the "amide I" and "amide II" regions of the FT-IR spectra of the **L12**, **Eu@L12-3, A12** and **Eu@A12-1** hybrids using Voigt functions are represented in Fig. 4.12.

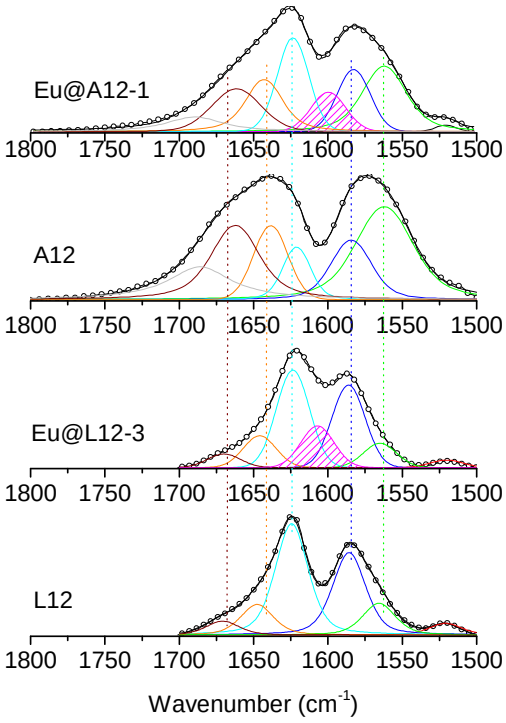

Figure 4.12 FT-IR spectra in the "amide I" and "amide II" regions of **L12**, **Eu@L12-3**, **A12** and **Eu@A12-1**. The multi Voigt fit components are also shown.

The "amide I" band of **L12** was decomposed into two components situated at approximately 1624 cm^{-1}, 1645 cm^{-1} and a very weak event centred around 1668 cm^{-1}. These components are assigned to the absorption of C=O groups included in ordered hydrogen-bonded urea-urea associations of decreasing strength. As the area of the 1620 cm^{-1} peak largely exceeds those of the 1668 and 1645 cm^{-1} components, we are led to conclude that the great majority of hydrogen-bonded aggregates formed in **L12** are highly ordered. The component associated with the absorption of "free" urea groups (*i.e.*, urea groups in which the N-H or C=O groups are free from any hydrogen bonding interactions and in which the C=O groups do not coordinate to Eu^{3+} ions), expected at 1751 cm^{-1},[34] is not seen in the "amide I" region of the **L12** sample.

These findings provide evidence that in the **L12** network all the urea groups present are involved in the formation of an array of strong urea-urea hydrogen-bonded aggregates extended throughout the material. Thus, to coordinate to the C=O groups the Eu^{3+} ions need to disrupt this urea-urea hydrogen-bonded network. The examination of the "amide I" and "amide II" regions of the Eu^{3+}-doped **L12** hybrids demonstrated that for **Eu@L12-1**

and **Eu@L12-2** the levels of doping are too low to give rise to detectable spectral modifications. However, in the case of **Eu@L12-3**, a new "amide I" component appears at 1606 cm^{-1}. It is attributed to the vibration of carbonyl groups strongly coordinated to Eu^{3+} ions, indicating an effective interaction between the hybrid host and the lanthanide metal centre. The "amide II" band was deconvoluted into two major bands centred at 1562 and 1584 cm^{-1}, suggesting that hydrogen bonded aggregates with two hydrogen bond strengths exist in the hybrids.

The "amide I" band of **A12** was decomposed into four components situated at approximately 1686, 1662, 1638 and 1622 cm^{-1} (Fig. 4.12). The component associated with the absorption of "free" urea groups is also absent in the amide I region of the **A12** sample. When the synthesis is performed with Eu^{3+} ions, a new component centred at 1600 cm^{-1} and ascribable to the vibration of carbonyl groups strongly coordinated to Eu^{3+} ions arises, as in the case of the **Eu@L12** hybrids, indicating an effective interaction between the hybrid host and the lanthanide metal centres. The "amide II" band, was deconvoluted into two major bands centred at 1562 and 1584 cm^{-1}, as in the case of the **L12** hybrids, suggesting that hydrogen bonded aggregates with two hydrogen bond strengths exist in both materials.

4.3.1 Mechanistic interpretation of the formation of the Eu^{3+}-based hybrids

The reaction conditions are a crucial factor in structuring the hybrids. Organised lamellar hybrids were obtained in water, whereas the use of only few equivalents of water in ethanol afforded solids with different morphologies. This is probably related to more favourable development of hydrophobic interactions in water than in the less polar ethanol. The nature of the catalyst also plays an important role, the catalysis by the nucleophilic fluoride ion which allows fast condensation, results in an amorphous material. Conversely, acid catalysis, which allows fast hydrolysis and slower condensation than under nucleophilic catalysis conditions, provides organised lamellar solids.[16]

Highly ordered lamellar **L12** and **L12@Eu** hybrids were obtained from the **P12** precursor using HCl as catalyst and a large excess of water (R = H_2O/Si = 300) in the absence or presence of Eu^{3+} ions. No significant change of morphology that presents analogous spectroscopic features, see below, were detected between the Eu^{3+}-doped and non doped **L12** hybrids. The slower condensation allowed to form a flexible siloxane network favoured by the arrangement of the organic fragments, which self-assembled through a combination of hydrogen-bonding interactions between urea groups and hydrophobic interactions between the alkylene chains. The precursors, which hydrolyse to Si-OH-containing molecules, behave as amphiphilic molecules capable of self-assembly (Sheme 4.2).[16]

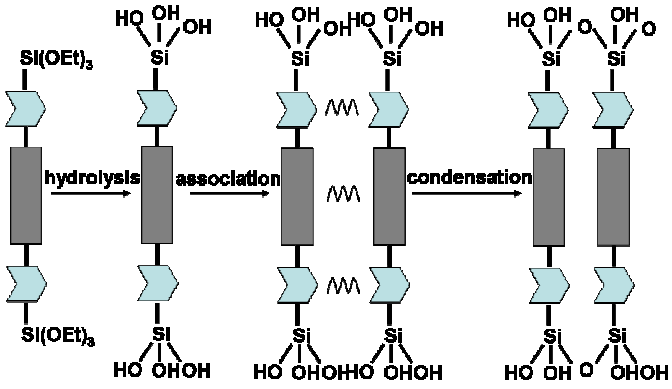

Scheme 4.2 Schematic representation of the hydrolysis-condensation process effording lamellar hybrids.[16]

On the basis on the SEM, ^{13}C CP-MAS and ^{29}Si CP-MAS NMR, XRD/SAXS and FT-IR results, scheme 4.3 depicts a tentative representation of the structure of the hybrids network for **Eu@L12-1** and **Eu@L12-3**.

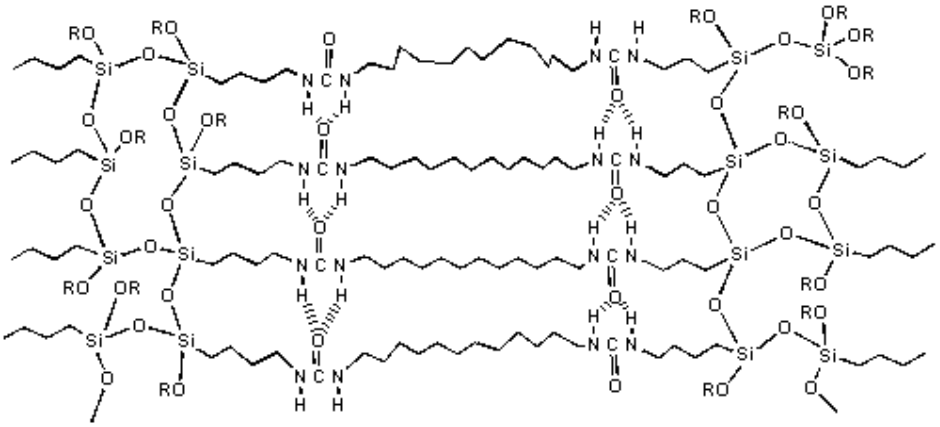

A

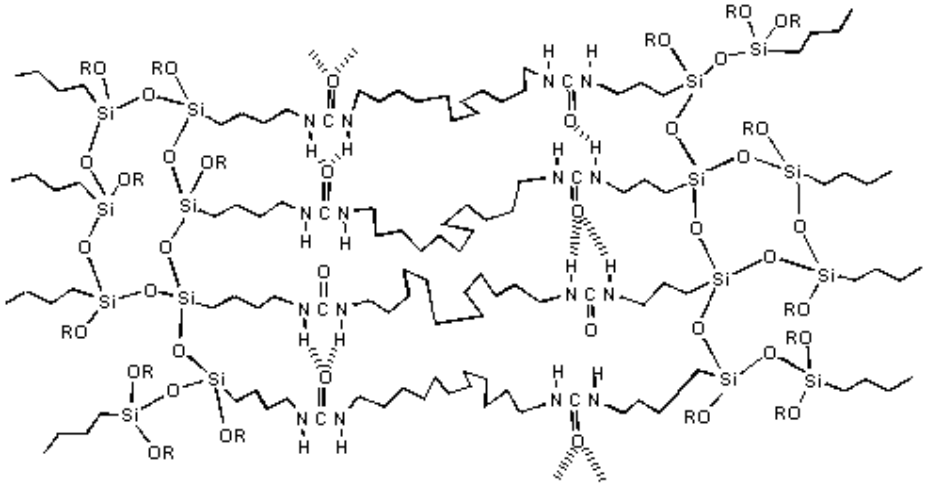

B

Scheme 4.3 Schematic representation of the structure of **Eu@L12-1** (A) and **Eu@L12-3** (B). The relative *trans*/*gauche* conformation ratio is only a tentive representation.The Eu^{3+} ions have been omitted for clarity and since they are randomly coordinated to the oxygen from urea groups.

A marked ordering of the structure of the hybrid is observed when the NH_4F-catalyzed synthesis is carried out in the presence of $EuCl_3 \cdot 6H_2O$. But in contrast to the related lamellar **Eu@L12** hybrids, the **Eu@A12** obtained in the present work exhibit neither sharp XRD peaks at low *q* values, non lamellar features. Indeed, the main changes

observed when the synthesis of the **A12** hybrids is performed in the presence of Eu^{3+} ions are related to short distance ordering of the organics resulting in a more regular stacking of the alkyl chains. This is evidenced both by XRD studies with the appearance of a well defined peak at 16.41 nm^{-1} and by the ^{13}C NMR investigations, with the enhancement of the signal at 34.0 ppm, typically attributable to an *all-trans* arrangement of the methylene groups. Consequently, the single peak at low *q* values shifts to lower values in the case of the Eu^{3+}-doped samples, evidencing an increase of the chain length (2.25 to 2.37 and 2.50 nm for **A12**, **Eu@A12-1** and **Eu@A12-2**, respectively) that results from the more regular *trans* arrangement of the methylene units. These values are, however, far from the interlamellar distances of 2.92 and 3.01 nm reported for the long-range ordered lamellar **Eu@L12** hybrids. The shorter distance of **Eu@A12-1** and **Eu@A12-2** surely arises from their less ordered character relatively to that of **Eu@L12** hybrids. Compared to **A12**, the better organization of the chains found in **Eu@A12-1** and **Eu@A12-2** is mainly explained by a reinforcement of the hydrogen bonds between the urea groups: in parallel to the smaller dispersion of the urea groups environment evidenced by the sharp peak at 159.9 ppm (Fig. 4.6B), the deconvolutions of the "amide I" region of the infrared spectra of **A12** and **Eu@A12-1** show that Eu^{3+} incorporation during the synthesis results in a higher contribution of the most strongly hydrogen-bonded associations at the expense of the destruction of the weaker ones, a situation already observed for di-ureasil hybrids.[40] Hence it clearly appears that the Eu^{3+} ions play a crucial dual role in the doped materials acting, not only as active emitting species, but also as templates, being responsible for the short-range structuring of these materials. Palladium salts have already been reported to assist the fast formation of sol-gel hybrids through a Pd-complexed alkene system.[41]

We believe that the structure directing effect of the Eu^{3+} ions is intimately associated with the presence of two available types of coordinating sites provided by the reacting **P12** precursor molecule itself. One of the sites is the oxygen atom of the silanol group which is generated during the fluoride (F^-)-based catalyzed hydrolysis. The other site, inherent to the starting **P12** molecule, is the carbonyl oxygen atom of the urea cross-linkage.

Under neutral conditions the mechanism of the F^- ion in sol-gel processes is thought to occur *via* an S_N2 mechanism similar to the base-catalyzed one – in which anionic intermediates precede the condensation steps – with the F^- ion acting as nucleophile.[42-44]

Penta- and hexavalent negatively charged silicon intermediates are formed and a water molecule can induce a nucleophilic substitution of the OR group.[45]

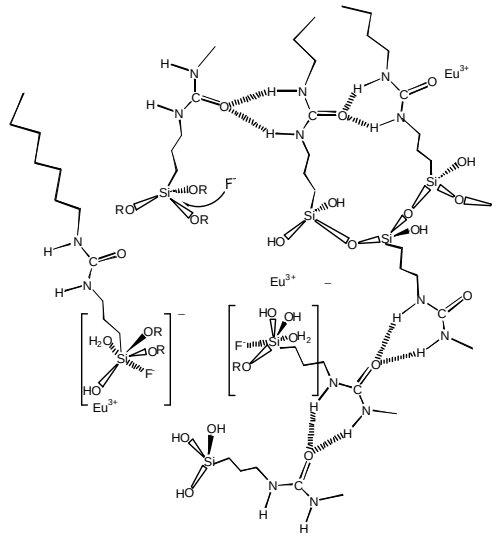

A

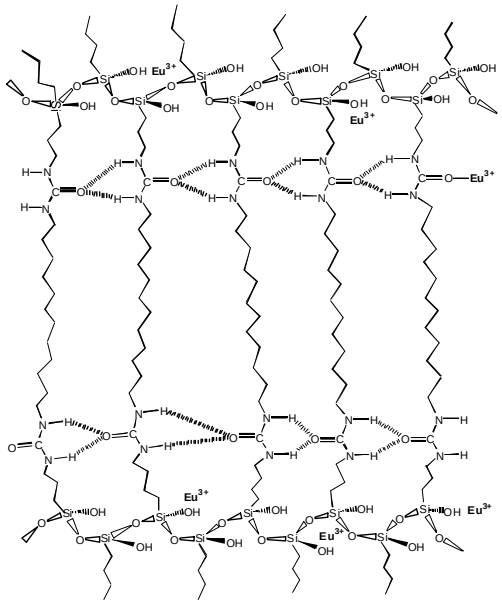

B

Scheme 4.4 Tentative representation of the mechanism of formation of **Eu@A12** in the (A) early and (B) late stages. In these schemes the other ligands of the Eu^{3+} ion coordination sphere (e.g., chloride ions, water molecules and other carbonyl groups) have been omitted for the sake of clarity.

We suggest here that in the case of the **Eu@A12** hybrids the negative charge of the intermediate species will attract the Eu^{3+} ions due to electrostatic interactions (Scheme

4.4A). These cations will remain bonded to the oxygen atoms of the silanol groups even after elimination of the ROH alcohol and F^- ion in the last step of the mechanism. In parallel to this anchoring process undergone by a fraction of the incorporated emitting species, the remaining Eu^{3+} ions will prefer to bind to the carbonyl oxygen atoms of the urea groups. This interaction will induce a more positive charge over the NH proton, thus promoting the formation of additional hydrogen-bonds with neighboring urea groups over the whole reaction medium. A strong and ordered hydrogen-bonded array will eventually build up. The direct consequence of the formation of these bifurcated hydrogen-bonded aggregates will the stacking of the hydrophobic alkyl chains into tapes (Scheme 4.4B). These tapes will assemble with other close, readily formed tapes and the survival of the process will be entirely dictated by the inhibitor role played by the silanol-bonded Eu^{3+} ions located at the surface of the growing siloxane network which prevent further condensation of the latter. At this point of supramolecular self-assembly regular nanometer-size, thin plates (150-400 nm long) will be produced. As shown in Fig. 4.2E the Eu^{3+} ions are homogeneous distributed in regions with size dimensions (>200 nm) compatible to the length range of these plates, supporting therefore the condensation inhibitor role played by the silanol-bonded Eu^{3+} ions. Owing to their regular size, these anisotropic plates will easily pile up along one dimension to form micrometric assemblies along a brick-to-brick like arrangement (Fig. 4.13) similarly to nature-existing aragonite in a much higher dimension (10.0-20.0 μm wide and 0.5 μm thick)[20,46], thus explaining the axial symmetry of the resulting uniform micron-size fibres (up to 4 μm). Finally, the fibres become bundles as a result of microscopic self-assembly (Fig. 4.2B and 4.2C).

Hence, the inhibitor effect of silanol-bonded Eu^{3+} ions aided by Eu^{3+}–mediated hydrogen bonding combined with supramolecular and micrometer self-assembly processes account for the different morphologies observed: twisted fibres in dumbbell shapes in the case of the **Eu@A12-2** hybrids and spherical forms (resulting from the assembly of non-uniform size flakes (0.3-1.0 μm)) in the case of the non doped **A12**. In the latter case, ramdom stacking of the irregular flakes formed and isotropic growth yields a spherical final shape (Fig. 4.2A).[47,48]

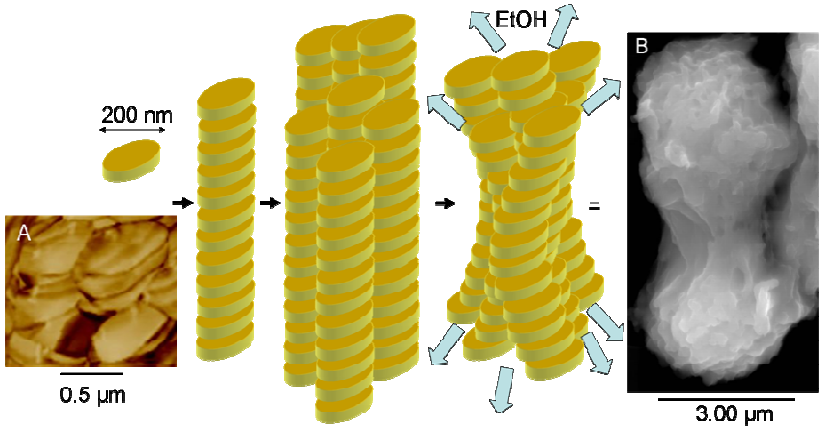

Figure 4.13 Schematic representation of the proposed mechanism for the formation of the bow-tie shaped **Eu@A12-2**. (A) AFM and (B) SEM images of **Eu@A12-2**.

We believe that the dumbbell shape of the **Eu@A12-2** bundles may result from a concerted template effect governed both by the ethanol released during the hydrolysis-condensation reactions and the Eu^{3+}-based inter-fibre cross-links. Indeed the flow of the ethanol formed during the sol-gel reactions is likely to increase on going from the centre to the tips of the assembled fibres (Fig. 4.13). At high salt concentration, the Eu^{3+} ions coordinate to adjacent fibres (as discussed below), thus constraining the ethanol flow pathways and inducing the formation of the dumbbell morphology. In the SEM pictures of Fig. 4.4C the hollow channels (up to 0.5 µm diameter) sculpted by the solvent release are clearly observed at the far end of the fibre-made dumbbell structures.

4.4 Photoluminescence

Fig. 4.14 shows the low temperature emission spectra of the pristine **L12** hybrid under different excitation wavelengths. All the spectra are composed of a large Gaussian-shaped broad band between 320 and 600 nm, whose maximum intensity deviates to the red as the excitation wavelength increases. This behavior was observed for the di-ureasil hybrids,[27,32,49-55] the di-urethanesils,[27] the mono[19]- and di-amidosils[56] and it was modeled as radiative recombinations involving thermal relaxation within localized states, in the framework of the extended multiple trapping approach.[57,58] The origin of the broad band, discussed in detail in chapter 2, has been ascribed to the overlap of two distinct emissions mediated by donor-acceptor pair transitions that occur within the urea, urethane or amide, respectively, cross-linkages and within the siliceous skeleton, due to the presence of oxygen related defects, •O-O-Si≡(CO_2). [55]

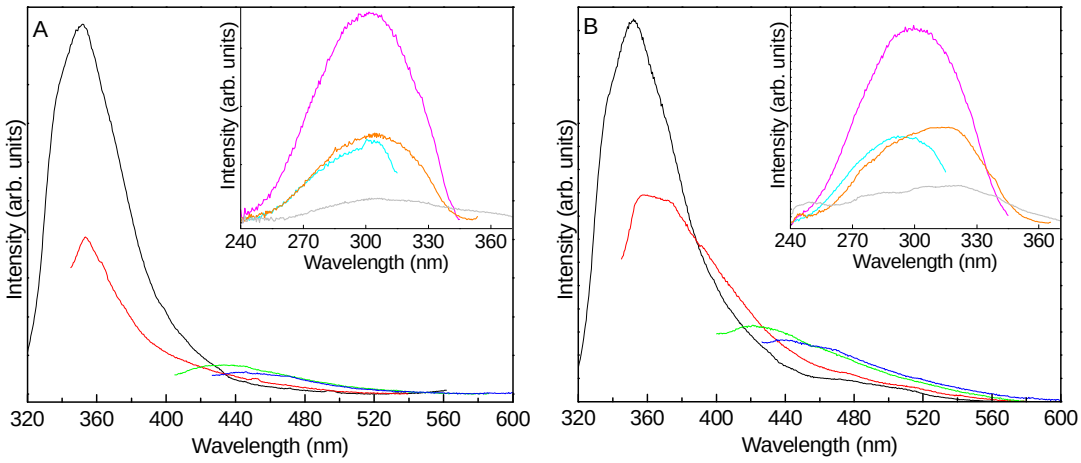

Figure 4.14 Emission spectra (A) 14 K and (B) 300K of **L12** excited at 300 nm (black line), 330 nm (red line), 360 nm (green line) and 380 nm (blue line). The inset shows the excitation spectra (14 K) monitored at 330 nm (cyan line), 360 nm (magenta line), 390 nm (orange line) and 420 nm (gray line).

The 14 K excitation spectra of **L12** hybrid were monitored along the hybrid host emission (inset of Fig. 4.14). The excitation spectra consist of a broad band between 240 to 380 nm, which maximum intensity shifts to the red and which fwhm increases approximately from 5750 to 8650 cm^{-1}, as the monitoring wavelength increases from 320 to 430 nm. Similarly to the situation observed for the emission features, the high- and low-

wavelength side can be ascribed to the preferential excitation of the urea- and siliceous-related emission, respectively. At room temperature the photoluminescence features are essentially the same as those observed at 14 K (Fig. 4.14). The absolute emission quantum yields of the **L12** hybrid were measured for excitation wavelengths ranging from 290-330 nm, yielding to a maximum value of 0.14 ± 0.02 (310 nm). Although this value is similar to those reported for analogous amorphous hybrids, it is four times higher than that measured for ordered mono-amide cross-linked alkyl/siloxanes.

Fig. 4.15 shows the room temperature emission spectra of the **A12** (freeze dried) and of the **A12$_T$** (oven dried) hybrids under different excitation wavelengths.

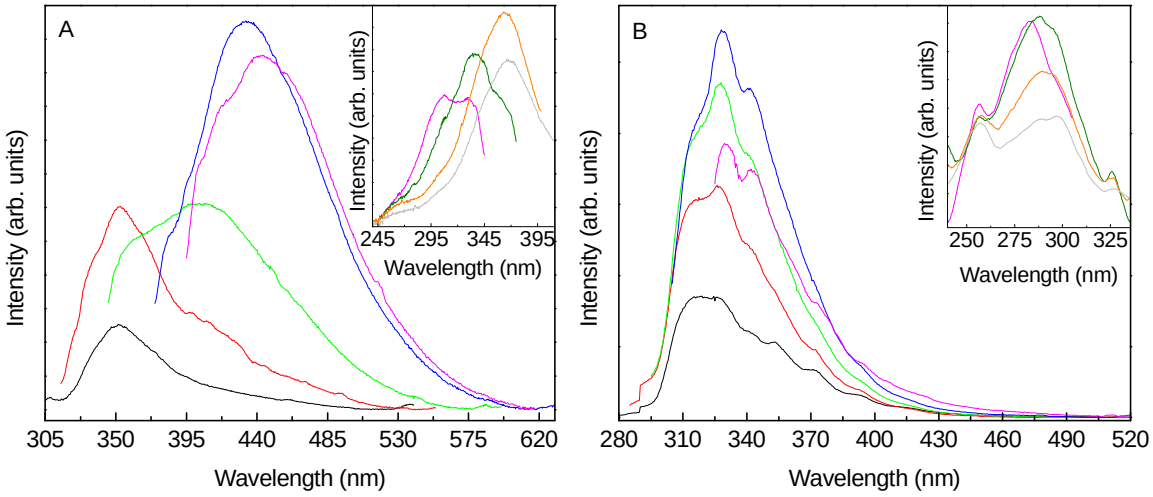

Figure 4.15 Emission spectra of: (A) **A12$_T$** excited at 280 nm (black line), 300 nm (red line), 330 nm (green line), 360 nm (blue line) and 380 nm (magenta line). The inset shows the excitation spectra monitored at 360 nm (magenta line), 390 nm (olive line), 440 nm (orange line) and 460 nm (grey line); (B) **A12** excited at 260 nm (black line), 270 nm (red line), 280 nm (green line), 290 nm (blue line) and 310 nm (cyan line), respectively. The inset shows the excitation spectra monitored at 320 nm (magenta line), 350 nm (olive line), 360 nm (orange line) and 370 nm (grey line).

The emission spectra of **A12$_T$** (Fig. 4.15A) are composed of a large Gaussian-shaped broad band between 320 and 600 nm, whose maximum intensity deviates to the red as the excitation wavelength increases, similarly to what was observed of the pristine **L12** hybrid and ascribed to the same emitting centres. The excitation spectra (inset of Fig. 4.15A) consist of a broad band between 240 to 395 nm, whose maximum intensity shifts to the red

and whose fwhm increases approximately from 6932 to 5799 cm^{-1}, as the monitoring wavelength increases from 360 to 460 nm.

The emission spectra of the **A12** (Fig. 4.15B) are composed of a large Gaussian-shaped structured broad band between 280 and 420 nm, with three main shoulders at 315, 330 and 340 nm. The excitation spectra (inset of Fig. 4.15B) consist of a broad band between 240 to 350 nm with a shoulder at 256 nm, as the monitoring wavelength increases from 320 to 370 nm the maximum intensity (at higher wavelengths) of the band shifts to the red and the shoulder at 256 nm remains constant. The absolute emission quantum yields values were measured for the **A12** hybrid under distinct excitation wavelengths (260-310 nm), a maximum value of 0.24 ± 0.02 was attained under 290 nm excitation.

Fig. 4.16 displays the excitation spectra (14 K) of the **Eu@L12** hybrids monitored at 612 nm, showing a large broad band peaking at 345 nm (**Eu@L12-1** and **Eu@L12-3**) and 335 nm (**Eu@L12-2**) overlapping a series of narrow lines ascribed to the Eu^{3+} intra- $4f^6$ transitions between the $^7F_0$ and the $^5L_6$, $^5D_{4\text{-}2}$ levels. The origin of the large broad band may be ascribed to the convolution of the hybrid host excited states (inset of Fig. 4.14) and to a ligand-to-metal charge transfer (LMCT) transition resulting from the interaction between the Eu^{3+} ions and the oxygen atoms of the carbonyl groups.[59,60]

Increasing the temperature up to 300 K results in marked changes in the excitation spectra, as exemplified for the **Eu@L12-2** hybrid in the inset of Fig. 4.16. At room temperature the excitation spectra are formed by two distinct components, peaking at 330 and 430 nm, and no sign of excitation components around 350-380 nm is discerned. The disappearance of such excitation component suggests a thermally deactivated mechanism, in accordance with the presence of an LMCT band. Moreover, LMCT states have been identified around 360 nm for analogous organic/inorganic hybrids where the Eu^{3+} ions local environment also involves the oxygen atoms of the carbonyl groups.[60] The lower wavelength broad band in Fig. 4.16 may be ascribed to the hybrid's excited states (inset of Fig. 4.16) that transfer energy to the Eu^{3+} levels. The band detected at higher wavelengths (430 nm) is attributed to excited states of the hybrid's emitting centres. The relative higher contribution of this component in the excitation spectrum of **Eu@L12-1** (Fig. 4.16) is due to the higher overlap between the hybrid host emission and the Eu^{3+} lines as it will detailed below.

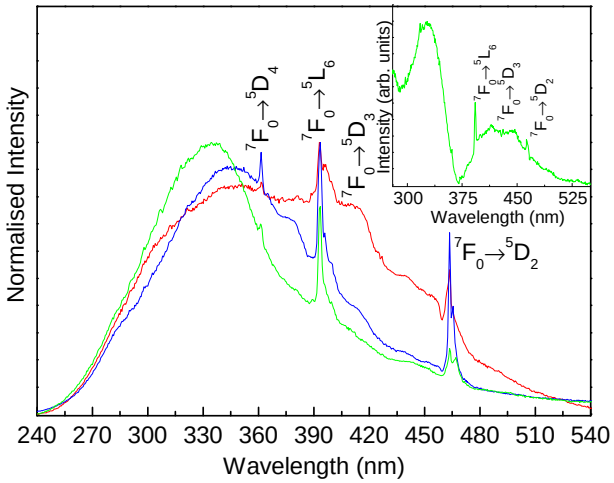

Figure 4.16 Excitation spectra (14 K) of **Eu@L12-1** (red line), **Eu@L12-2** (green line) and **Eu@L12-3** (blue line) monitored at 612 nm. The inset shows the room temperature excitation spectrum of **Eu@L12-2** monitored at 612 nm.

Fig. 4.17A displays the 14 K emission spectra for **Eu@L12-1**, **Eu@L12-2** and **Eu@L12-3** excited at 360 nm.

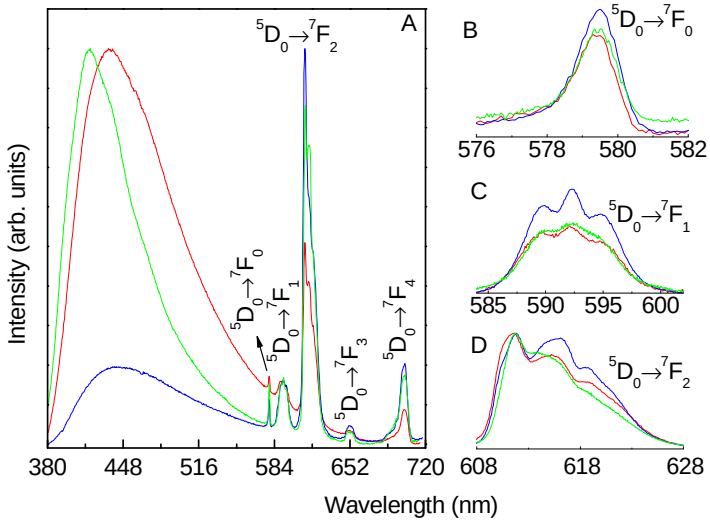

Figure 4.17 (A) Emission spectra (14 K) of **Eu@L12-1** (red line), **Eu@L12-2** (green line) and **Eu@L12-3** (blue line) excited at 360 nm; (B), (C), and (D) show a magnification of the $^5D_0 \rightarrow {}^7F_{0\text{-}2}$ transitions excited at 335 nm **Eu@L12-2** and at 340 nm **Eu@L12-1** and **Eu@L12-3**.

The large broad band, already observed in the non doped host (Fig 4.14), is deviated towards the red comparing with the non doped host, pointing out an effective interaction

between the Eu^{3+} ions and the hybrid host's emitting centres. Upon increasing the excitation wavelength, the hybrid host emission shifts towards the red (Fig 4.18) as already reported for the **L12** framework.

The hybrids' band relative intensity strongly depends on the amount of Eu^{3+} incorporated, in such a way that for higher Eu^{3+} concentrations it is observed a decrease in the intensity of the hybrids' host emission induced by energy transfer between the hybrid host emitting centres and the Eu^{3+} excited levels. As suggested previously for amorphous hybrids, as the ion concentration increases more ions are located near the hybrid's emitting centres, which means that there is a higher number of emitting centres transferring energy to the Eu^{3+} ions, thus contributing to a continuous decrease of the broad band emission with respect to the Eu^{3+} lines.[60]

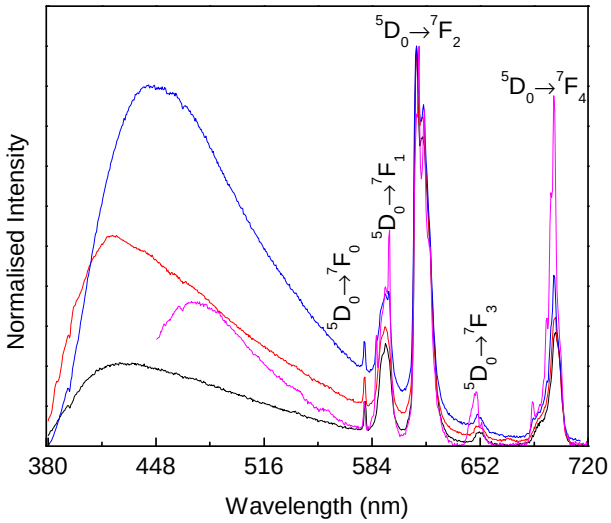

Figure 4.18 Emission spectra (300K) of **Eu@L12-3** excited at 310 nm (black line), 335 nm (red line), 360 nm (blue line) and 393 nm (magenta line).

In order to get further insight into the Eu^{3+}-local coordination the $4f^6$ emission lines were scanned with high resolution (Fig. 4.17 B-D). The detection of a single $^5D_0 \rightarrow {}^7F_0$ line, the J-degeneracy splitting of the $^7F_{1,2}$ levels into 3 and 4 Stark components, respectively, the observation of the same number of local-field split components over the entire range of excitation wavelength used, indicate that the Eu^{3+} cations in each of the hybrids occupy a single low symmetry site. This site do not have an inversion centre in accordance with the higher intensity of the electric-dipole $^5D_0 \rightarrow {}^7F_2$ transition, relatively

to that of the magnetic-dipole $^5D_0 \rightarrow {}^7F_1$ one. The $^5D_0 \rightarrow {}^7F_0$ transition was fitted using a single Gaussian function and fwhm values of 37±2 cm^{-1} were obtained independently of the Eu^{3+} content (larger than those reported for analogous amorphous hybrids, 19-31 cm^{-1})[59], point out that the Eu^{3+} cations are accommodated in a continuous distribution of similar **Eu@L12** framework sites. With the increase of Eu^{3+} content the $^5D_0 \rightarrow {}^7F_0$ energy and the relative intensity between the $^5D_0 \rightarrow {}^7F_2$ and the $^5D_0 \rightarrow {}^7F_1$ transitions slightly change (Fig. 4.17 B-D) indicating that, although similar in the three hybrids, the Eu^{3+} first coordination shell should present minor variations.

Upon changing the excitation wavelength to intra-$4f^6$ excitation ($^5L_6$, 395 nm), the emission spectrum of the more Eu^{3+} concentrated hybrid (**Eu@L12-3**) also displays sharp lines (Fig. 4.18) assigned to the presence of $EuCl(OH)_2$, consistent with the data obtained by XRD.

The emission of the hybrids appears to be white to the naked eyes as exemplified in Fig. 4.19, where the *Commission Internationale d'Eclairage* (CIE) chromaticity diagram depicts the room temperature (x,y) colour coordinates for **L12**, **Eu@L12-2** and **Eu@L12-3**.

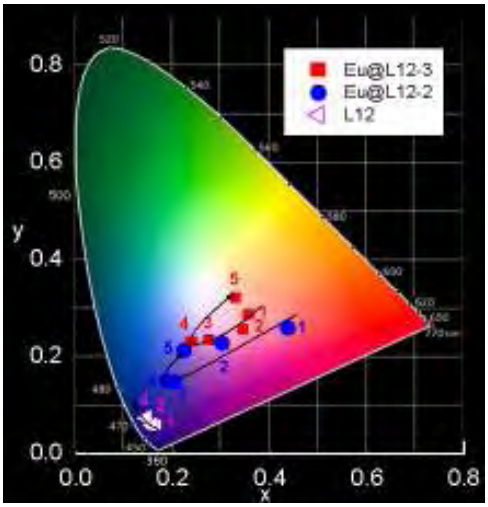

Figure 4.19 Chromaticity diagram (CIE, 1931) showing the (x,y) emission colour coordinates of **L12**, **Eu@L12-2** and **Eu@L12-3** under different excitation wavelengths. The arrow indicates the excitation wavelength variation: (1) 290, (2) 310, (3) 335, (4) 360, and (5) 394 nm.

The emission colour of the non doped **L12** varies from the purplish-blue (0.16,0.04) to the blue spectral region (0.16,0.07), by changing the excitation

wavelength from 330 to 380 nm. The incorporation of Eu^{3+} ions induces a deviation of the emission colour towards the centre of the diagram. Whereas for **Eu@L12-1** and **Eu@L12-3** the colour coordinates change from the purplish-pink region (0.44,0.26) to the white area (0.24,0.24), for **Eu@L12-3** the colour can be tuned within the same regions, from (0.36,0.28) to (0.34,0.34), as the excitation wavelength is varied from 330 to 395 nm. This latter colour coordinates correspond to the white colour, since the centre of the diagram has (0.33,0.33) coordinates.

The $^5D_0$ emission decay curves were monitored between 14 K and room temperature, Fig. 4.20, within the $^5D_0 \rightarrow {}^7F_4$ transition to avoid spectral overlap with the hybrid host's intrinsic emission (Fig. 4.18), and excited at 335-350 nm, and 310 nm respectively. It should be noted that such excitation wavelengths do not directly excite $EuCl(OH)_2$.

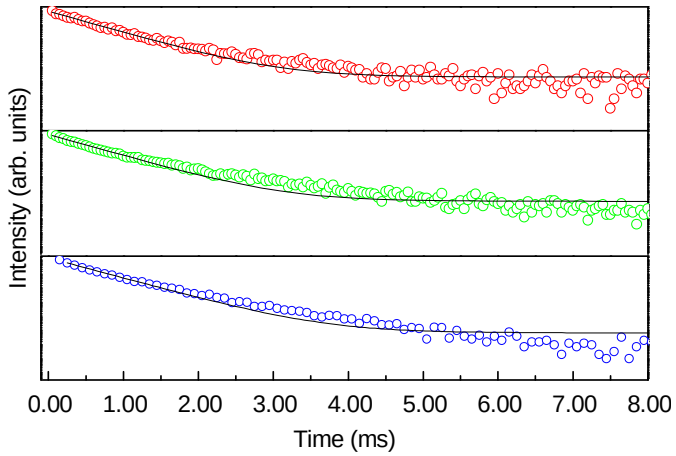

Figure 4.20 Emission decay curves of **Eu@L12** (14K) monitored at 612 nm and excited at 335-340 nm for **Eu@L12-1** (red), **Eu@L12-2** (green) and **Eu@L12-3** (blue). The solid lines correspond to the data best fit using an exponential function.

For all the hybrids, the emission decay curves display a single exponential behavior with lifetime values (τ) listed in Table 4.3. At 14K and 300K the $^5D_0$ lifetime faintly (< 5%) depends on the increase of the Eu^{3+} concentration, in accordance with a quite similar Eu^{3+}-local coordination site in all the hybrids. The decrease in the $^5D_0$ lifetime values as the temperature increases, points out the presence of thermally activated nonradiative mechanisms, as mentioned before.

Fig. 4.21 shows the excitation spectrum monitored within the $^5D_0 \rightarrow {}^7F_2$ transition (614 nm) for **Eu@A12-1**. The inset of the figure displays the excitation spectra monitored along the hybrid host emission (430-470 nm). These spectra resemble that of the non doped **A12** host (inset in Fig. 4.15B) displaying a large broad band whose peak position depends on the monitoring wavelength. The excitation spectrum monitored within the Eu^{3+} lines reveals a large broad band peaking at 340 nm and a high-wavelength component between 360 and 540 nm superimposed on a series of Eu^{3+} transitions between the $^7F_{0,1}$ levels and the $^5L_6$ and $^5D_{3,2}$ excited states. The main component may be ascribed to the hybrid host excited states that are transferring energy to the Eu^{3+} ions as it overlaps the excitation spectra monitored within the hybrid host excited states (inset in Fig. 4.15B). The excitation spectra of **Eu@A12-2** resemble that of **Eu@A12-1**.

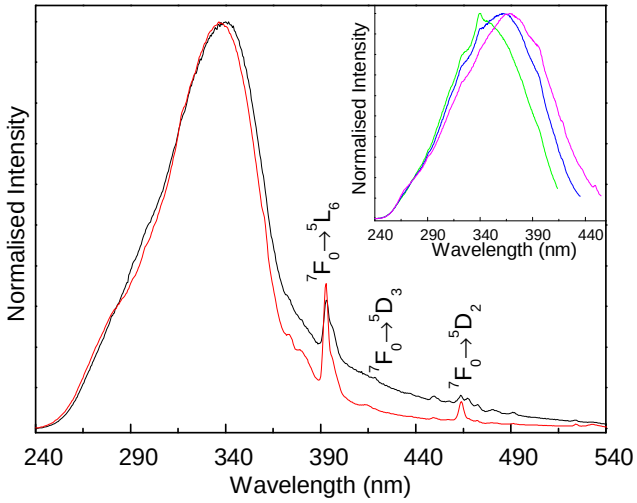

Figure 4.21 Excitation spectra of **Eu@A12-1** (black line) and **Eu@A12-2** (red line) monitored at 614 nm. The inset shows the excitation spectra of the **Eu@A12-1** monitored at 430 nm (green line), 450 nm (blue line) and 470 nm (magenta line).

Fig. 4.22 displays the emission spectra for **Eu@A12-1** and **Eu@A12-2** excited at 360 and 393 nm. Both spectra are composed of a series of straight lines ascribed to the intra-$4f^6$ $^5D_0 \rightarrow {}^7F_{0-4}$ transitions superimposed on a large broad band, whose energy deviates towards the red as the excitation wavelength increases (280-393 nm). A similar broad band emission was also detected for the non doped **A12** host (Fig. 4.14B). The relative intensity of the hybrids' emission band depends on the amount of Eu^{3+} incorporated, in such a way that for the higher Eu^{3+} concentration a decrease in the intensity of the hybrids' host

emission is observed which suggests the presence of host-to-Eu^{3+} energy transfer, as previously observed in analogous amorphous hybrids.[60]

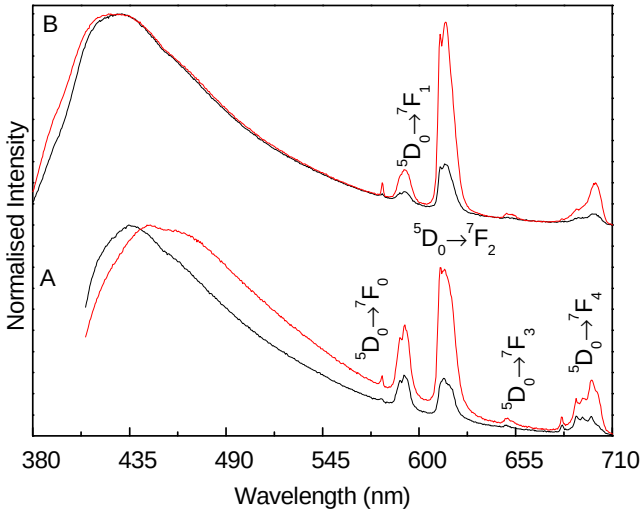

Figure 4.22 Emission spectra of **Eu@A12-1** (black line) and **Eu@A12-2** (red line) excited at (A) 360 nm and (B) 393 nm.

The incorporation of Eu^{3+} into the **A12** hybrid induces a decrease in the absolute emission quantum yield values. As stated above, the **A12** hybrid has a maximum value of 0.24 ± 0.02 under the 290 nm excitation wavelength. A maximum value of 0.06 ± 0.01 was found for **Eu@A12-1** and **Eu@A12-2** under excitation via the hybrid host excited states (340-360 nm). The decrease in the quantum yield value (relatively to that measured for the non doped **A12** hybrid) is in good agreement with the existence of hybrid-to-Eu^{3+} energy transfer. Under direct intra-$4f^6$ excitation, the quantum yield values lie below the detection limits of our equipment (< 0.01) reinforcing the active role of the hybrid host in the Eu^{3+} sensitization. Comparing these values with those of analogous organic/inorganic hybrids containing lanthanide-based salts, the quantum yield values reported here although smaller than that reported for Eu^{3+}-contaning di-ureasils (0.13 ± 0.02)[60], are substantially higher than those observed for the Eu^{3+}-containing **L12** lamellar hybrids (< 0.01).

The photoluminescence measurements reported here were all carried out within two months after preparing fresh samples. When the samples are kept in ambient atmosphere the quantum yield values decrease (approximately 2.5 times in one year) and the relative intensity of the intra-$4f^6$ lines in **Eu@A12-1** and **Eu@A12-2** increases with aging time.

However, both the overall broad emission of the hybrid host and the energies of the Eu^{3+} lines remain unaltered. That dependence of the quantum yield values and relative intra-$4f^6$ intensities on the aging time needs further investigation.

In order to get further insight into the Eu^{3+}-local coordination the intra-$4f^6$ emission lines were scanned with higher resolution. Fig. 4.23 A shows the $^5D_0 \rightarrow {}^7F_{0\text{-}4}$ transitions under excitation via the hybrid host' excited states (340 nm) and directly into the $^5L_6$ level (393 nm).

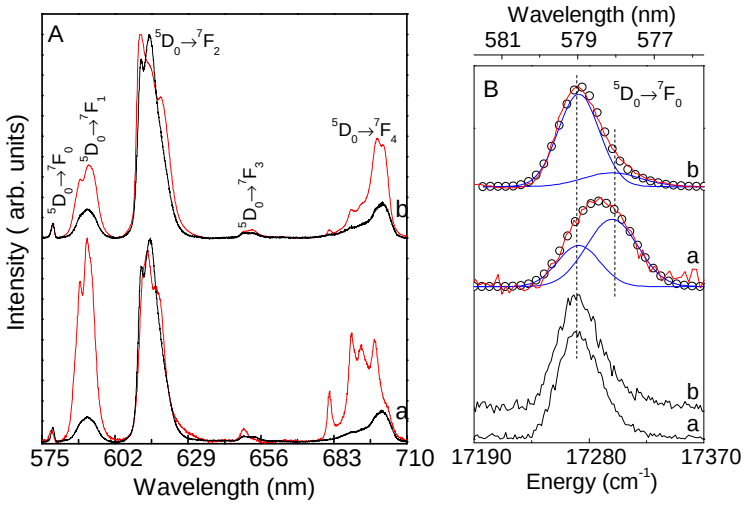

Figure 4.23 (A) High resolution emission spectra of (a) **Eu@A12-1** and (b) **Eu@A12-2** hybrids excited at 340 nm (black line) and 393 nm (red line). (B) Magnification of the $^5D_0 \rightarrow {}^7F_0$ transition for **Eu@A12-2** and **Eu@A12-1**. For 393 nm excitation the curve fit (represented by open circles) was performed using two Gaussian functions (blue lines).

Under 340 nm excitation the Eu^{3+} emission spectra display a single $^5D_0 \rightarrow {}^7F_0$ line and a *J*-degeneracy splitting of the $^7F_{1,2}$ levels into 3 and 4 Stark components, respectively. No changes in the energy and Stark splitting are observed by changing the Eu^{3+} concentration (Fig. 4.23 A), indicating that the Eu^{3+} ions occupy the same average local environment in **Eu@A12-1** and **Eu@A12-2** (labelled site A), involving Eu^{3+} coordination to oxygen atoms of the carbonyl groups (as the above mentioned structural results indicate), besides chloride anions and water molecules. Under 393 nm excitation the spectra drastically change (Fig. 4.23) indicating the existence of a second Eu^{3+} local environment (labelled site B). Particularly a series of narrower Stark components become much more evident in the overall envelope of the $^5D_0 \rightarrow {}^7F_{1\text{-}4}$ transitions and the $^5D_0 \rightarrow$

$^7F_2/^5D_0 \rightarrow {}^7F_1$ intensity ratio significantly decreases (indicating the presence of a centre of inversion in Eu^{3+} site B).

To further elucidate the origin of this Eu^{3+} local site B, selectively excited under 393 nm, the energy and fwhm of the $^5D_0 \rightarrow {}^7F_0$ line were estimated both as function of the excitation wavelength (340 and 393 nm) and Eu^{3+} concentration, using the following fit procedure. The $^5D_0 \rightarrow {}^7F_0$ transition was fitted using a single and a sum of two Gaussian functions for the emission obtained under 340 and 393 nm excitation, respectively. Under 340 nm the energy and fwhm of the $^5D_0 \rightarrow {}^7F_0$ transition are the same for the two Eu^{3+} concentrations, namely 17272.4 ± 0.3 cm^{-1} and 34.0 ± 0.6 cm^{-1}, respectively (Fig. 4.23 B). Under 393 nm, the energy of the $^5D_0 \rightarrow {}^7F_0$ transition is well modelled assuming the sum of one component with the same features (energy and fwhm) of the one measured under 340 nm with another component at high energies, peaking at 17298.0 ± 2.5 cm^{-1} with a fwhm of 45.0 ± 5.5 cm^{-1}. The fact that the E_{00} value for site B is blue-shifted when compared with the energy of the $^5D_0 \rightarrow {}^7F_0$ transition assigned to Eu^{3+} ions in site A points out a less covalent degree of the Eu-O bonds in Eu^{3+} site B local environment. Site B corresponds to silanol-bonded Eu^{3+} ions with a higher number of OH groups, relatively to the typical number in site A. Comparing the relative intensity of the two $^5D_0 \rightarrow {}^7F_0$ transitions, we may unequivocally visualise a higher relative contribution of the Eu^{3+} ions located at site B for the less concentrated hybrid, **Eu@A12-1** (Fig. 4.23 B), in strong agreement with the mechanistic interpretation of the formation of the fibres-type structures described above. We may rationalize that the increase of the Eu^{3+} content will promote the contiguity of fibers leading to the formation of dumbbell structures. In this way, distinct fibers will be linked via Eu^{3+} ions coordinated to oxygen atoms of the carbonyl groups belonging to distinct fibers.

Additional arguments supporting the assignment of the two distinct Eu^{3+}-local coordination groups, in particular the presence of silanol groups, may be found by the analysis of the $^5D_0$ emission decay curves monitored under 340 and 393 nm excitation, Fig. 4.23. Under 340 nm excitation all the curves are well described by a single exponential function, yielding to lifetime values of $0.673 \pm 0.017 \times 10^{-3}$ s and $0.536 \pm 0.016 \times 10^{-3}$ s, for **Eu@A12-1** and **Eu@A12-2**, respectively. The smaller value found for the highest concentrated hybrid suggests a higher nonradiative transition probability, as we will detail next. Under 393 nm, the emission decay curves are well modelled by a bi-exponential

function. Considering that one of the lifetime values coincides with that determined under 340 nm excitation, the curve fitting yields a second value of 0.115 ± 0.011 and 0.060 ± 0.006 ms for **Eu@A12-1** and **Eu@A12-2**, respectively. The lower $^5D_0$ lifetime value obtained for Eu^{3+} ions located in site B (when compared with that measured for site A excited at 340 nm excitation) supports the above suggestion that this local environment involves metal coordination to a larger number of OH groups belonging to the silanol groups, leading to an increase in the nonradiative transition probability.

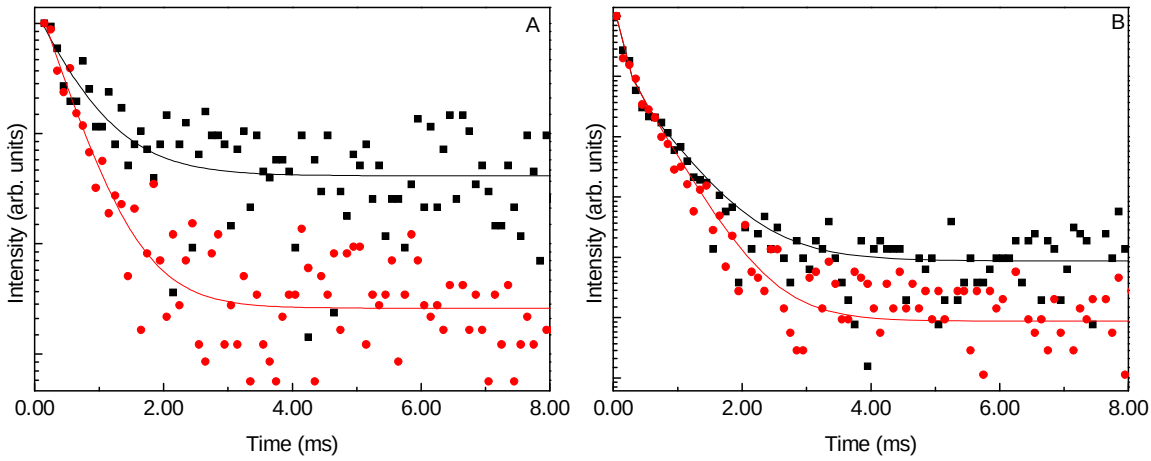

Figure 4.24 Emission decay curves of (A) **Eu@A12-1** (squares) and **Eu@A12-2** (circles) monitored at 579 nm and excited at 340 nm, (B) **Eu@A12-1** (squares) and **Eu@A12-2** (circles) monitored at 579 nm and excited at 393 nm. The solid lines correspond to the data best fit using an exponential function.

Attending to the fact that only under intra-$4f^6$ excitation the presence of Eu^{3+} ions in site B it is detected, we will further use the selective excitation wavelength of 340 nm. The decrease in the $^5D_0$ lifetime value with the increase of the Eu^{3+} concentration suggests an increase in the nonradiative paths, as we will detail next.

4.4.1 Intensity Parameters, Radiative and Nonradiative Transition Rates, Quantum Efficiency and Number of Coordinated Water Molecules

The estimation of the $^5D_0$ radiative (A_{RAD}) and nonradiative (A_{NRAD}) transition probabilities, and the $^5D_0$ quantum efficiency (η), were made based on the emission spectrum and $^5D_0$ lifetime, using Eqs. 2.14 and 2.17 of chapter 2. The radiative

contribution is calculated from the relative intensities of the $^5D_0 \rightarrow {}^7F_{0\text{-}4}$ transitions (the $^5D_0 \rightarrow {}^7F_{5,6}$ branching ratios are neglected due to their poor relative intensity with respect to that of the remaining $^5D_0 \rightarrow {}^7F_{0\text{-}4}$ lines), using Eq. 2.16. The experimental intensity parameters, Ω_2 and Ω_4, were determined by using the $^5D_0 \rightarrow {}^7F_2$ and $^5D_0 \rightarrow {}^7F_4$ electronic transitions in the emission spectra, respectively, using Eq. 218. The calculated values are gathered in Table 4.3 for the **Eu@L12** and **Eu@A12** hybrids. The room temperature emission spectra used was the one for which the Eu^{3+} ions coordinated to the hybrid host are selectively excited thus avoiding $EuCl(OH)_2$ contributions in the case of the **Eu@L12-3** (340 nm) and the Eu^{3+} ions located at the surface of the fibres or dumbbell structures in the case of the **Eu@A12** (340 nm).

The calculated values show a decrease in the η value as the concentration increases for both the **Eu@L12** (from 0.19 to 0.16) and **Eu@A12** (from 0.37 to 0.26) and that this decreases is essentially related with an increase of the A_{NRAD} (from 1.625 to 1.808 to the **Eu@L12** and from 0.937 to 1.384 to the **Eu@A12**).

The variations in η and A_{NRAD} values may be rationalised in terms of number of water molecules coordinated to the Eu^{3+} ions ($n_w \pm 0.1$), Eq. 2.19. Although the number of water molecules estimated for the three **Eu@L12** hybrids is around 2, and for the two **Eu@A12** is around 1, the small increase in n_w with the increase of the Eu^{3+} amount is in agreement with the arguments figured out previously concerning the minor variation of the Eu^{3+} first coordination shell both in the **Eu@L12** and **Eu@A12** hybrids.

The relative high values of Ω_2, similar to those previously found in amorphous organic/inorganic hybrids, might be interpreted as a consequence of the hypersensitive behaviour of the $^5D_0 \rightarrow {}^7F_2$ transition, suggesting that the dynamic coupling mechanism is quite operative and that the chemical environment is highly polarizable. In particular, a correlation has been noticed in the sense that compounds expected to have a higher degree of covalency tend to present higher values of Ω_2. As shown in Table 4.3, the Ω_2 values decreases slightly as the Eu^{3+} concentration increases, pointing out a small decrease in the average degree of covalency of the Eu-O bonds, in agreement with the conclusions mentioned above regarding the minor variation of the Eu^{3+} first coordination shell in the three hybrids studied here. In particular, values for the **Eu@A12** are higher than the ones for the **Eu@L12** indicating a higher degree of covalency for the amorphous hybrids.

Table 4.3 Room temperature $^5D_0$ lifetime values (τ_{EXP}), radiative (A_{RAD}) and nonradiative (A_{NRAD}) transition probabilities, quantum efficiency (η), number of water molecules coordinated to the Eu^{3+} ion (n_w) and Ω_λ=2,4 intensity parameters (10^{-20}) for **Eu@L12-1**, **Eu@L12-1**, **Eu@L12-3**, **Eu@A12-1** and **Eu@L12-2** hybrids. The lifetime values presented between parentheses were acquired at 14 K.

	Eu@L12-1	**Eu@L12-2**	**Eu@L12-3**	**Eu@A12-1**	**Eu@A12-2**
τ_{EXP} / ms	0.497 ±0.039 (0.657 ±0.006)	0.477 ±0.019 (0.664 ±0.007)	0.463 ±0.032 (0.692 ±0.009)	0.673 ±0.017	0.536 ±0.016
A_{RAD} / ms^{-1}	0.387	0.381	0.352	0.549	0.482
A_{NRAD} / ms^{-1}	1.625	1.715	1.808	0.937	1.384
η	0.19	0.18	0.16	0.37	0.26
n_w	1.7 ±0.1	1.8 ±0.1	2.0 ±0.1	0.7±0.1	1.2±0.1
Ω_2/cm^2	10.1	9.6	8.9	15.4	13.3
Ω_4/cm^2	3.3	3.5	3.4	3.8	3.6

The photoluminescence features of the **L12@Eu-1** and **A12@Eu-1** hybrids (containing approximately the same Eu^{3+} concentration, 1 %) were compared to address the effect of the morphology in these features. The changes on the $^7F_0 \rightarrow {}^5D_0$ energy (17272.5 ± 0.2 cm^{-1}, site A in **Eu@A12-1**, and 17254.6 ± 0.3 cm^{-1}, **Eu@L12-1**), $^5D_0$ lifetime, $^5D_0$ quantum efficiency, number of coordinated water molecules, Ω_2 values (Table 4.3) and on the $^5D_0 \rightarrow {}^7F_2/{}^5D_0 \rightarrow {}^7F_1$ intensity ratio, clearly indicate that the Eu^{3+} local enviroment considerably depends on the overall morphology of the samples.

4.6 Conclusions

For the first time a short range distance ordering yielding hierarchically structured bridged polysilsesquioxanes by means of an unprecedent Eu^{3+}-assisted process has been presented and characterized.

In the case of the **L12** the lanthanide has a passive role, as the same lamellar morphology is maintained after the Eu^{3+} incorporation.

The presence of the lanthanide ions induces different morphologies (bundles of fibers and dumbbells) that contrast with the spherical arrangement of small platelets found in the **A12** pristine material. The fibers consist of nanometer-size plates which pile up together along a tile-like arrangement. The latter stacking arrangement is only possible due to the regular size of the plates. Their anisotropic shape is a direct consequence of the inhibitor effect played by some of the Eu^{3+} ions which bond to surface siloxane silanol groups (Eu^{3+} sites B) thus suppressing the condensation of the inorganic network. Interestingly, the synthesis of the Eu^{3+}-doped hybrids involves the combination of classical F^--catalyzed sol-gel reactions with self-assembly processes that span several length scales. Supramolecular self-assembly, aided by strong urea-urea hydrogen-bonding interactions, will be active in the early steps of the formation of the hybrids. Micro-scale self-assembly alone or aided by urea carbonyl-bonded Eu^{3+} ions (Eu^{3+} sites A) that act as fiber cross-linkers, will be activated in the late steps of the synthesis giving rise to bundles at low Eu^{3+} concentration or dumbbell shapes at high Eu^{3+} concentration, respectively.

The Eu^{3+}-containing hybrids are room temperature multi-wavelength emitters due to the convolution of the hybrids' emitting centre and the intra-$4f^6$ transitions. The **Eu@L12** hybrids just display one local site for Eu^{3+}. The **Eu@A12** present two distinct Eu^{3+} local sites (named A and B) are clearly discerned in the emission spectra. The Eu^{3+} first coordination shell in site A is very similar in the two hybrid structures, incorporating oxygen atoms of the carbonyl group, chloride atoms and water molecules, despite the minor variations found in the $^5D_0$ quantum efficiency (0.26-0.37), number of coordinated water molecules (0.7-1.2) and experimental intensity Ω_2 parameter (15.4-13.3 × 10^{-20} cm^2) with the increase of Eu^{3+} content. Furthermore, the Eu^{3+} ions located in site B are characterized by: i) a series of narrower Stark components, ii) a low $^5D_0 \rightarrow {}^7F_2/{}^5D_0 \rightarrow {}^7F_1$ intensity ratio (indicating the presence of a centre of inversion), iii) a blue-shifted E_{00} value

(when compared with that associated with the Eu^{3+} ions in site A) that points out a less covalent degree of the Eu-O bonds and iv) a lower $^5D_0$ lifetime value. All these evidence support the suggestion that the Eu^{3+} ions in site B are coordinated to silanol groups (with therefore a higher number of OH oscillators, relatively to the typical number in site A). The relative contribution of the Eu^{3+} ions located in site B decreases as Eu^{3+} concentration increases reflecting the establishment of Eu^{3+} ionic inter-fibers cross-links leading to the formation of dumbbell structures.

Furthermore, as hybrids with approximately the same Eu^{3+} concentration (~1 %) but with completely different morphologies (**L12@Eu-1** and **A12@Eu-1**) were synthesized starting from the same precursor, this family of hierarchical structured bridged polysilsesquioxanes represents a unique example in which the effect of the morphology in the photoluminescence features could be addressed in great detail. The results point out that the Eu^{3+} local neighborhood considerably depends on the overall morphology of the samples, sensing therefore the structural changes induced by the acid- or fluoride-base catalyst used.

4.7 References

1. L. L. Hench and J. K. West, *Chem. Rev.*, 1990, **90**, 33.
2. C. Sanchez and F. Ribot, *New. J. Chem.*, 1994, **18**, 1007.
3. H. Schmidt, *J. Sol-Gel Sci. Techn.*, 2006, **40**, 115.
4. C. Sanchez, B. Julian, P. Belleville and M. Popall, *J. Mater. Chem.*, 2005, **15**, 3559.
5. G. Schottner, *Chem. Mater.*, 2001, **13**, 3422.
6. C. Sanchez and B. Lebeau, *Mrs. Bull.*, 2001, **26**, 377.
7. C. Sanchez, B. Lebeau, F. Chaput and J. P. Boilot, *Adv. Mater.*, 2003, **15**, 1969.
8. N. G. Liu, K. Yu, B. Smarsly, D. R. Dunphy, Y. B. Jiang and C. J. Brinker, *J. Am. Chem. Soc.*, 2002, **124**, 14540.
9. Y. G. Yang, M. Nakazawa, M. Suzuki, M. Kimura, H. Shirai and K. Hanabusa, *Chem. Mater.*, 2004, **16**, 3791.
10. J. Alauzun, A. Mehdi, C. Reye and R. J. P. Corriu, *J. Mater. Chem.*, 2005, **15**, 841.
11. A. Shimojima, R. Goto, N. Atsumi and K. Kuroda, *Chem. Eur. J.*, 2008, **14**, 8500.
12. J. J. E. Moreau, L. Vellutini, M. Wong Chi Man, C. Bied, J. L. Bantignies, P. Dieudonne and J. L. Sauvajol, *J. Am. Chem. Soc.*, 2001, **123**, 7957.
13. G. Arrachart, G. Creff, H. Wadepohl, C. Blanc, C. Bonhomme, F. Babonneau, B. Alonso, J.-L. Bantignies, C. Carcel, J. J. E. Moreau, P. Dieudonné, J.-L. Sauvajol, D. Massiot and M. Wong Chi Man, *Chem. Eur. J*, 2009, **15**, 5002.
14. J. J. E. Moreau, B. P. Pichon, M. Wong Chi Man, C. Bied, H. Pritzkow, J. L. Bantignies, P. Dieudonne and J. L. Sauvajol, *Angew. Chem. Int. Edit.*, 2004, **43**, 203.
15. J. J. E. Moreau, L. Vellutini, P. Dieudonne, M. Wong Chi Man, J. L. Bantignies, J. L. Sauvajol and C. Bied, *J. Mater. Chem.*, 2005, **15**, 4943.
16. J. J. E. Moreau, L. Vellutini, M. Wong Chi Man, C. Bied, P. Dieudonne, J. L. Bantignies and J. L. Sauvajol, *Chem. Eur. J.*, 2005, **11**, 1527.
17. J. L. Bantignies, L. Vellutini, D. Maurin, P. Hermet, P. Dieudonne, M. Wong Chi Man, J. R. Bartlett, C. Bied, J. L. Sauvajol and J. J. E. Moreau, *J. Phys. Chem. B*, 2006, **110**, 15797.

18. P. Dieudonne, M. Wong Chi Man, B. P. Pichon, L. Vellutini, J. L. Bantignies, C. Blanc, G. Creff, S. Finet, J. L. Sauvajol, C. Bied and J. J. E. Moreau, *Small*, 2009, **5**, 503.
19. L. D. Carlos, V. de Zea Bermudez, V. S. Amaral, S. C. Nunes, N. J. O. Silva, R. A. S. Ferreira, J. Rocha, C. V. Santilli and D. Ostrovskii, *Adv. Mater.*, 2007, **19**, 341.
20. A. Lin and M. A. Meyers, *Materials Science and Engineering A*, 2005, **390**, 27.
21. G. M. Luz and J. F. Mano, *Phil. Trans. R. Soc. A*, 2009, **367**, 1587.
22. J. Clauss, K. Schmidtrohr, A. Adam, C. Boeffel and H. W. Spiess, *Macromolecules*, 1992, **25**, 5208.
23. A. N. Parikh, M. A. Schivley, E. Koo, K. Seshadri, D. Aurentz, K. Mueller and D. L. Allara, *J. Am. Chem. Soc.*, 1997, **119**, 3135.
24. L. Q. Wang, J. Liu, G. J. Exarhos, K. Y. Flanigan and R. Bordia, *J. Phys. Chem. B*, 2000, **104**, 2810.
25. L. S. Fu, R. A. S. Ferreira, N. J. O. Silva, J. A. Fernandes, P. Ribeiro-Claro, I. S. Goncalves, V. De Zea Bermudez and L. D. Carlos, *J. Mater. Chem.*, 2005, **15**, 3117.
26. J. L. Bantignies, L. Vellutini, J. L. Sauvajol, D. Maurin, M. Wong Chi Man, P. Dieudonne and J. J. E. Moreau, *J. Non. Cryst. Solids*, 2004, **345-46**, 605.
27. L. S. Fu, R. A. S. Ferreira, N. J. O. Silva, L. D. Carlos, V. De Zea Bermudez and J. Rocha, *Chem. Mater.*, 2004, **16**, 1507.
28. K. D. Keefer and D. W. Schaefer, *Phys. Rev. Lett.*, 1986, **56**, 2376.
29. K. Dahmouche, C. V. Santilli, J. A. Chaker, S. H. Pulcinelli and A. F. Craievich, *Jpn J. Appl. Phys. 1*, 1999, **38**, 172.
30. P. Judeinstein, J. Titman, M. Stamm and H. Schmidt, *Chem. Mater.*, 1994, **6**, 127.
31. L. Born and H. Hespe, *Colloid Polym. Sci.*, 1985, **263**, 335.
32. L. D. Carlos, V. de Zea Bermudez, R. A. S. Ferreira, L. Marques and M. Assunção, *Chem. Mater.*, 1999, **11**, 581.
33. Y. Kaneko, N. Iyi, T. Matsumoto, K. Fujii, K. Kurashima and T. Fujita, *J. Mater. Chem.*, 2003, **13**, 2058.
34. V. de Zea Bermudez, L. D. Carlos and L. Alcácer, *Chem. Mater.*, 1999, **11**, 569.
35. S. C. Nunes, V. de Zea Bermudez, D. Ostrovskii and L. D. Carlos, *J. Mol. Sctruct.*, 2004, **702**, 39.

36. J. vanEsch, R. M. Kellogg and B. L. Feringa, *Tetrahedron Lett.*, 1997, **38**, 281.
37. T. Miyazawa, T. Shimanouchi and S. I. Mizushima, *J. Chem. Phys.*, 1956, **24**, 408.
38. D. J. Skrovanek, S. E. Howe, P. C. Painter and M. M. Coleman, *Macromolecules*, 1985, **18**, 1676.
39. M. M. Coleman, K. H. Lee, D. J. Skrovanek and P. C. Painter, *Macromolecules*, 1986, **19**, 2149.
40. V. de Zea Bermudez, D. Ostrovskii, A. C. Gonçalves, S. Lavoryk, L. D. Carlos and R. A. S. Ferreira, *J. Phys. Chem. B*, 2005, **109**, 7110.
41. R. J. P. Corriu, J. J. E. Moreau, P. Thepot and M. Wong Chi Man, *J. Mater. Chem.*, 1994, **4**, 987.
42. I. C. Tilgner, P. Fischer, F. M. Bohnen, H. Rehage and W. F. Maier, *Micropor. Mesopor. Mat.*, 1995, **5**, 77.
43. J. MrowiecBialon, L. Pajak, A. B. Jarzebski, A. I. Lachowski and J. J. Malinowski, *Langmuir*, 1997, **13**, 6310.
44. R. J. P. Corriu, C. Guerin and J. J. E. Moreau, *Stereochemistry at Silicon. Top Stereochem*, 1984, **15**, 43.
45. J. L. Brefort, R. J. P. Corriu, C. Guerin, B. J. L. Henner and M. Wong Chi Man, *Organometallics*, 1990, **9**, 2080.
46. B. J. F. Bruet, H. J. Qi, M. C. Boyce, R. Panas, K. Tai, L. Frick and C. Ortiz, *J. Mater. Res.*, 2005, **20**, 2400.
47. J. J. E. Moreau, L. Vellutini, M. Wong Chi Man and C. Bied, *Chem. Eur. J.*, 2003, **9**, 1594.
48. B. P. Pichon, M. Wong Chi Man, P. Dieudonne, J. L. Bantignies, C. Bied, J. L. Sauvajol and J. J. E. Moreau, *Adv. Funct. Mater.*, 2007, **17**, 2349.
49. W. H. Green, K. P. Le, J. Grey, T. T. Au and M. J. Sailor, *Science*, 1997, **276**, 1826.
50. T. Brankova, V. Bekiari and P. Lianos, *Chem. Mater.*, 2003, **15**, 1855.
51. E. Stathatos, P. Lianos, B. Orel, A. S. Vuk and R. Jese, *Langmuir*, 2003, **19**, 7587.
52. E. Stathatos, P. Lianos, U. L. Stangar, B. Orel and P. Judeinstein, *Chem. Mater.*, 2000, **16**, 8672.
53. V. Bekiari, E. Stathatos, P. Lianos, U. L. Stangar, B. Orel and P. Judeinstein, *Chem. Mater.*, 2000, **12**, 3095.

54. L. D. Carlos, R. A. S. Ferreira, V. de Zea Bermudez and S. J. L. Ribeiro, *Adv. Funct. Mater.*, 2001, **11**, 111.
55. L. D. Carlos, R. A. S. Ferreira, R. N. Pereira, M. Assunção and V. de Zea Bermudez, *J. Phys. Chem. B*, 2004, **108**, 14924.
56. S. C. Nunes, V. de Zea Bermudez, J. Cybinska, R. A. S. Ferreira, J. Legendziewicz, L. D. Carlos, M. M. Silva, M. J. Smith, D. Ostrovskii and J. Rocha, *J. Mater. Chem.*, 2005, **15**, 3876.
57. R. A. S. Ferreira, A. L. Ferreira and L. D. Carlos, *Eur. Phys. J. B*, 2006, **50**, 371.
58. R. A. S. Ferreira, A. L. Ferreira and L. D. Carlos, *J. Non-Cryst. Solids*, 2006, **352**, 1225.
59. L. D. Carlos, R. A. S. Ferreira, V. de Zea Bermudez, C. Molina, L. A. Bueno and S. J. L. Ribeiro, *Phys. Rev. B*, 1999, **60**, 10042.
60. R. A. S. Ferreira, L. D. Carlos, R. R. Goncalves, S. J. L. Ribeiro and V. de Zea Bermudez, *Chem. Mater.*, 2001, **13**, 2991.

Chapter 5 - Bipyridine based bridged silsesquioxanes

5.1 Introduction

In chapter 3 and chapter 4 organic/inorganic hybrid hosts which possess two emitting centres' (assigned to $^{\bullet}O–O–Si\equiv(CO_2)$ oxygen-related and NH/C=O-related defects) were discussed. Here a hybrid (Scheme 5.1) in which the organic fragment, 2,2'-bipyridine (bpy) unit will also contribute (along with the other two centres common to the precious hybrids studied) to the luminescence features is introduced. Moreover bpy will act as light harvesting moiety.

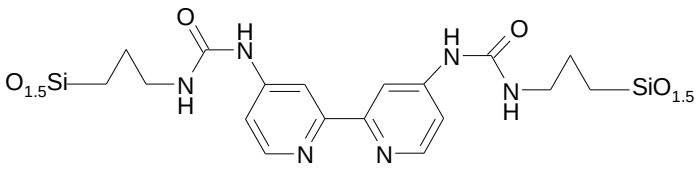

Scheme 5.1. Bpy-based bridged silsesquioxane **H**.

For applications in photonics and solid state lighting it is necessary to develop organic/inorganic hybrids featuring i) high quantum yield, ii) high brightness, iii) stability in time and under irradiation, iv) ability to be excited with cheap light sources, *eg.* long-wavelength UV (360-400 nm) and blue commercial light emitting diodes (LEDs). The development of new metal-free phosphors for long UV-to-visible conversion will contribute to trim down the use of Hg vapor plasma fluorescent lights (dropping the corresponding environmental contamination risks during disposal)[1-3] and is crucial to improve the efficiency and light quality of LED-based solid-state lighting devices (composed by commercial UV LEDs plus appropriate phosphors).[4]

To these purposes, class II hybrid materials, mainly bridged silsesquioxanes, with stable Si-C bonds to ensure the organic loading, are good candidates to achieve such metal-free phosphors. Thus appropriately conceived organic fragments can be incorporated to introduce targeted properties to these functional materials. In chapter 3, it was shown that an amorphous bridged silsesquioxane bearing urea groups and a long alkyl chain exhibits a relatively high emission quantum yield (up to 0.24), whereas its corresponding lamellar hybrid has much lower performances. However, the amorphous hybrid exhibits a low brightness and its quantum yield decreases with time. According to these observations, we thus focus on a system favoring an amorphous morphology and possessing light harvesting

chromophores. Recently a bpy-based material (**H**, Scheme 5.1) was reported for applications in catalysis[5] (the same hybrid host incorporating Eu^{3+} and Tb^{3+} ions has been almost simultaneously reported).[6] The non linear geometry of the organic moiety prevents a good packing of the motifs during the sol-gel synthesis and favors the formation of an amorphous material.

Bpy is one of the most commonly used ligands in the design of highly luminescent Ln^{3+}-containing materials because of its intense absorption band in the near-UV and its ability to efficiently transfer energy onto the Ln^{3+} excited states (antenna effect)[7]. Since the pioneering work of Zambon[8] on pyridyl-amide based hybrids, a handful of studies were reported on bpy-based Ln^{3+}-containing materials either obtained by co-gelification with a silica source (*e.g.*, tetramethylorthosilicate (TMOS) or tetraethylorthosilicate (TEOS)),[9-11] or directly from a single precursor.[6] The main advantages of the latter method are: i) materials with an homogeneous distribution of organics within the silica network are obtained; ii) a controlled and higher loading of organics and Ln^{3+} ions can be incorporated; iii) self-structuring may be envisaged in the presence of self-assembling groups in the organic fragments.[12]

This chapter describes the photoluminescent properties of a bpy-based amorphous bridged silsesquioxane exhibiting the highest emission quantum yield reported so far for excitation in the deep UV/blue regions (0.22±0.02) in hybrid materials, stability over time, and that can be excited at 395 nm with commercial LEDs. Moreover, the photoluminescence features of these urea/bpy-based hybrid incorporating Gd^{3+}, Eu^{3+}, and/or Tb^{3+} ions are also presented. For the first time, in this particular family of hybrids, the key role played by the light emitted by the hybrid host in the luminescence of the corresponding Ln^{3+}-based hybrids is demonstrated and we will show that the fine tuning of the emission colour along the *Commission Internationale d'Éclairage* (CIE) chromaticity diagram can be achieved either through the variation of the type of Ln^{3+} ion and changes in the excitation wavelength.

5.2 Synthesis

Precursor P

Precursor **P** was obtained from the reaction of the 4,4'-diamino-2,2'-bipyridine isomer with 3-isocyanatopropyltriethoxysilane (Scheme 5.2). This precursor was prepared by Dr. Sofia Benyahya and the detailed description of the synthetic procedure has already been reported.[5]

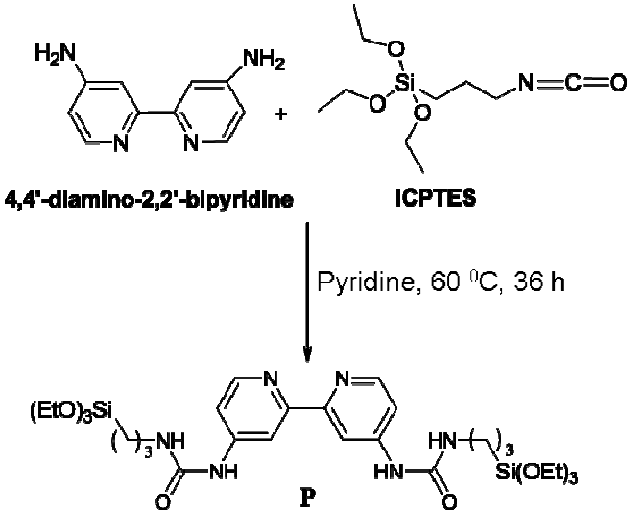

Scheme 5.2 Schematic representation of the synthesis of precursor **P**.

The sol-gel synthesis of the hybrids was realized under nucleophilic catalysis either using ammonium fluoride (NH_4F) or tetrabutylammonium fluoride (TBAF) at room temperature (Scheme 5.3).

TBAF catalysis

The sol-gel synthesis of the hybrid was realized under nucleophilic catalysis (TBAF) at room temperature from an homogeneous mixture of **P**, water, TBAF of 1:12:0.01 at 0.1 mol.L^{-1} in dimethyl sulfoxide (DMSO). After 3 hours, the mixture gelified and was aged for 3 days, yielding a white powder, in quantitative yield, designated as **H**.

NH_4F catalysis

The preparation of the Ln^{3+}-doped hybrids (Ln = Eu, Gd, Tb or 1:1 mixture of Eu and Tb) consisted of stirring, at 45 °C, for 5 minutes, an homogeneous mixture of **P**, water (H_2O), ammonium fluoride (NH_4F) and lanthanide chloride hexahydrate ($LnCl_3{\cdot}6H_2O$), (molar ratio **P**/($LnCl_3.6H_2O$)/H_2O/NH_4F: 1/0.33/30/0.01) at 0.1 mol.L^{-1} in methanol (freshly dried over magnesium and distilled). After 3 hours, the resulting gel was aged for 3 days at room temperature to yield a white monolith. The Ln^{3+}-containing hybrids were designated by **M-Ln** (Ln=Eu, Gd, and Tb) or **M-EuTb** (Eu^{3+}/Tb^{3+} mixture). The synthesis of the non-doped hybrid, abbreviated as **M**, was performed in a similar fashion. Elemental analyses for the Si, N and Ln elements were performed and the obtained values, in % (w/w), were: **M** (Si, 8.54; N, 16.27), **M-Eu** (Si, 8.29; N, 14.10; Eu 4.98), **M-Gd** (Si, 7.27; N, 12.61; Gd, 7.44), **M-Tb** (Si, 8.22; N, 13.29; Tb, 6.34) and **M-EuTb** (Si, 6.10; N, 13.70; Eu, 2.68; Tb, 3.37). The calculated bpy/Ln ratios were 5.1, 3.2, 4.0 and 4.2, for **M-Eu**, **M-Gd**, **M-Tb** and **M-EuTb**, respectively. Previously, Li *et al.* made the assumption that a bpy/Ln 2/1 ratio was formed in similar materials.[6] Nevertheless, in the **M-Ln** hybrids reported here the formation of a 3/1 ratio cannot be discarded. In any case, it appears that free and Ln^{3+}-complexed ligands co-exist in all the samples.

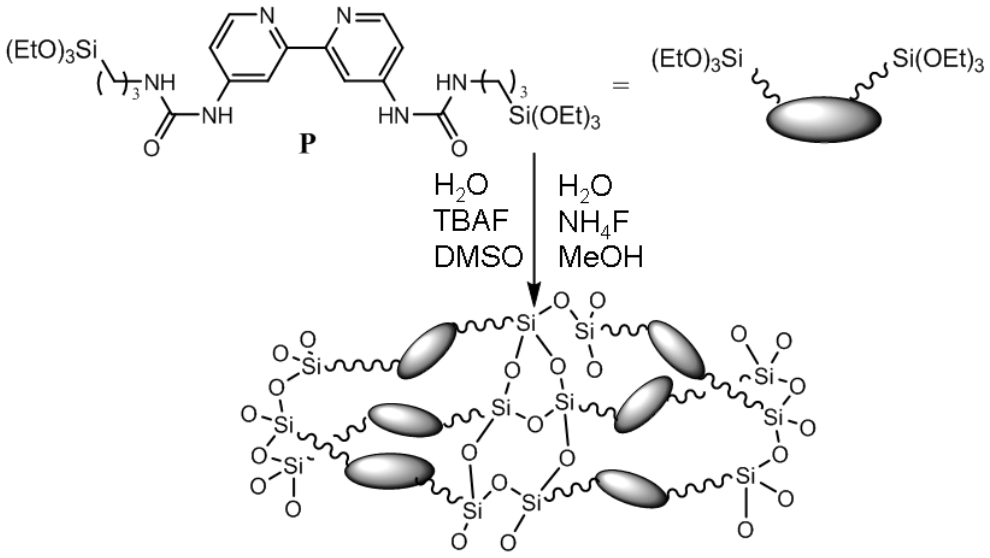

Scheme 5.3 Schematic representation of **H** and **M** synthesis.

5.3 Local structure

The SEM images of **H**, **M** and **M-Eu** hybrids are depicted in Fig. 5.1 A, B and C, respectively. The **H** hybrid displays plate morphology as the **M** and **M-Eu** display an amorphous morphology.

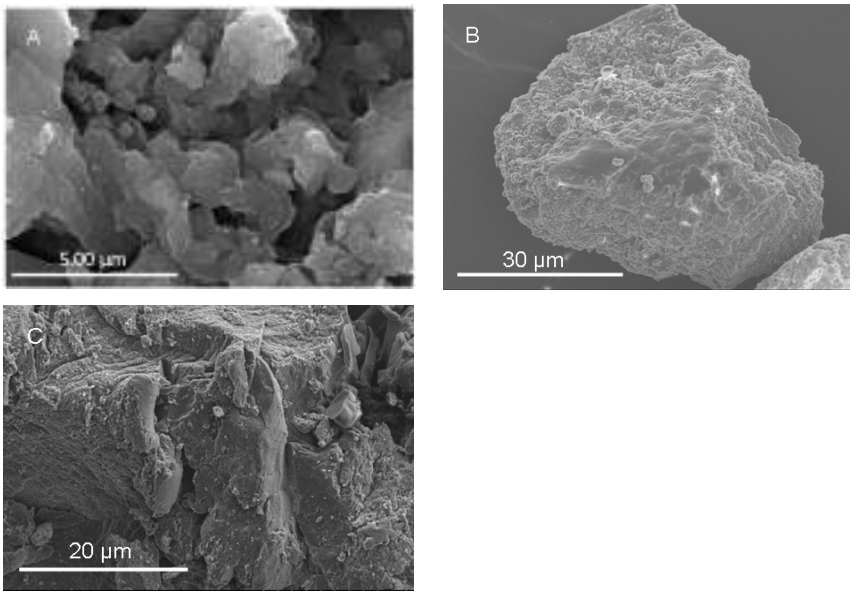

Figure 5.1 SEM images of (A) **H,** (B) **M** and (C) **M-Eu**.

The ^{29}Si MAS NMR studies were performed only for **H** and **M**, because for the Ln^{3+}-containing hybrids the paramagnetism of the Ln^{3+} ions inhibits such measurements. The spectrum of **M** displays broad signals at -44.9, -57.1 and -67.0 ppm, Fig. 5.2, ascribed to the $R'Si(OSi)(OH)_2$ (T_1), $R'Si(OSi)_2(OH)$ (T_2) and $R'Si(OSi)_3$ (T_3) silicon environments, respectively. The **H** hybrid displays signals at -57.1 and -67.0 ppm.

The condensation degree (*c*) was calculated using the Eq. 4.1, yielding to 86% for **H** and 87 % for **M**. The high degree of condensation is in agreement with the values already reported for organic/inorganic hybrids prepared by fluoride (F^-) ion-catalysed hydrolysis.[13,14]

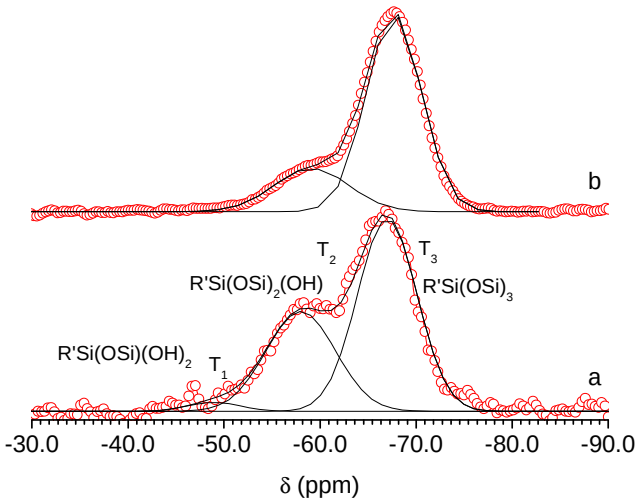

Figure 5.2 ^{29}Si NMR spectra of (a) **M** and (b) **H**. The solid lines represent the best fit using a sum of three and two Gaussian function, respectively.

It is noteworthy that no *Q* environment is observed in the ^{29}Si NMR spectra of both hybrids, evidencing no Si-C bond cleavage during the synthesis. This result was confirmed by the ^{13}C NMR spectrum of **M** and **H** (Fig. 5.3), which exhibits a signal at 10.7 ppm assignable to the propyl carbon atoms directly bonded to the silicon atoms, together with the other signals from the alkyl chain (23.3 ppm, $SiCH_2$-CH_2 and 42.8 ppm, CH_2-N), and from the bipyridine and urea groups (110-160 ppm). The presence of the sharp peak at 18.3 ppm attributed to ethoxy groups in the spectrum of the **H** hybrid has been observed for materials obtained under nucleophilic catalysis due to the fast condensation process, in the case of the **M** hybrids the absence of signals at 18.3 and 58.7 ppm (ethoxy groups) point out a complete hydrolysis of the Si-OEt groups under the reaction conditions. The ^{13}C CP/MAS NMR spectrum of **M-Eu** resembles closely that of **M** (Fig. 5.3). Due to the larger broadening induced by the higher paramagnetism of Tb^{3+}, the spectra of **M-Tb** and **M-EuTb** could not be recorded.

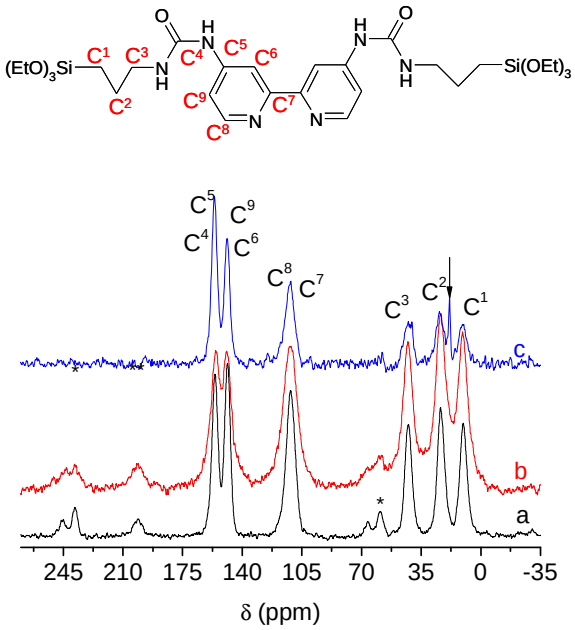

Figure 5.3 ^{13}C CP/MAS NMR spectra of (a) **M,** (b) **M-Eu** and (c) **H** (the peak at 18.3 ppm (marked with an arrow) is attributed to C atoms of the CH_3CH_2O groups). The asterisks correspond to the side spin bands of the peaks at 155.6, 148.6 and 111.7 ppm.

The XRD patterns of **H**, **M** and the corresponding Ln^{3+}-containing hybrids are shown in Fig. 5.4. All diffractograms are characteristic of amorphous materials. The diffractogram of **H** evidences an amorphous local structure with very broad peaks centred at 6.2 and 15.5 nm^{-1}. The diffractogram of **M** is dominated by a broad band centred at *ca.* 18.5 nm^{-1} indicative of the amorphous nature of the material. The shift of this peak to low *q* values after the incorporation of the Ln salt (*ca.* 16.9 nm^{-1}) is ascribed to the coordination of Eu^{3+} ions to some bpy groups with the concomitant increase of the mean distance between the organic moieties.[12]

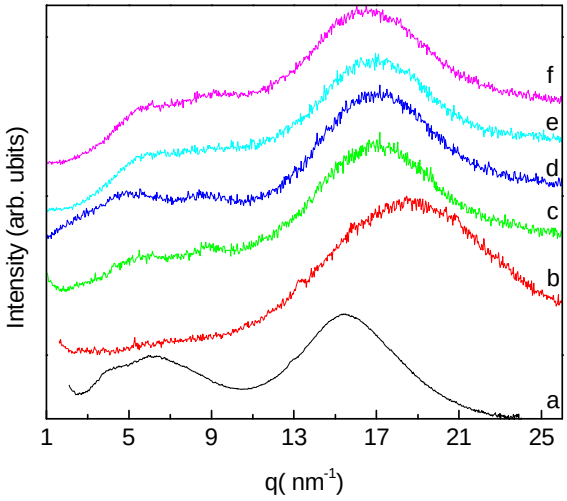

Figure 5.4 XRD patterns of (a) **H**, (b) **M**, (c) **M-Eu**, (d) **M-Tb**, (e) **M-Gd** and (f) **M-EuTb** hybrids.

To add some insight into the Ln^{3+} local coordination, the FT-IR spectra was recorded for the non-doped hybrid matrix **M** and the doped **M-Eu**, **M-Tb** and **M-EuTb**. Infrared spectroscopy is particularly useful to elucidate ligand-Lewis acid interactions in the case of bpy-based complexes, since the vibration modes of this ligand in the free and complexed states have been widely investigated and their attribution is well established.[6,15-21]

We have examined three spectral intervals of the infrared spectrum of bpy that are known to be sensitive to coordination effects: (i) 1480-1420 cm^{-1} interval. It is characteristic of ring stretching (ν_{ring}) modes[18,21] (*i.e.*, $\nu_{C=C}$ and/or $\nu_{C=N}$) and, according to some authors,[15,17,20] also CH deformation (δCH) modes. (ii) 1175-945 cm^{-1} interval. While most of the authors agree that it includes ring breathing modes and coupled ring deformation (δ_{ring}) and δCH modes,[15,17,18,20] some suggest that it also[15,17] or only[21] comprises in-plane δCH ($\delta_{i.p.}$CH) modes. (iii) 850-600 cm^{-1} interval. Typically in this region out-of-plane δCH ($\delta_{o.p.}$CH) modes and in-plane δ_{ring} ($\delta_{i.p.}$ring) modes absorb.[15,17,18,20,21]

Fig. 5.5A reproduces the spectral signature of the four samples under study in the 1480-1420 cm^{-1} interval. These spectra demonstrate that the addition of Eu^{3+} and Tb^{3+} ions, alone or mixed, to the **M** framework leads to the emergence of a new feature at 1434 cm^{-1}. Another change resulting from the presence of the lanthanide ions is the shift of the band centered at about 1467 cm^{-1} to 1471 cm^{-1}. Fig. 5.5B shows that the 996 cm^{-1} mode of free bpy undergoes an upshift to 1003 cm^{-1} upon coordination. Another effect detected in this

region is the shift of the intensity maximum at 1026 cm^{-1} to 1032 cm^{-1}. The third region examined, depicted in Fig. 5.5C, reveals that the addition of the lanthanide salt(s) to the **M** matrix leads to the growth of new features at 778, 734 and 654 cm^{-1}.

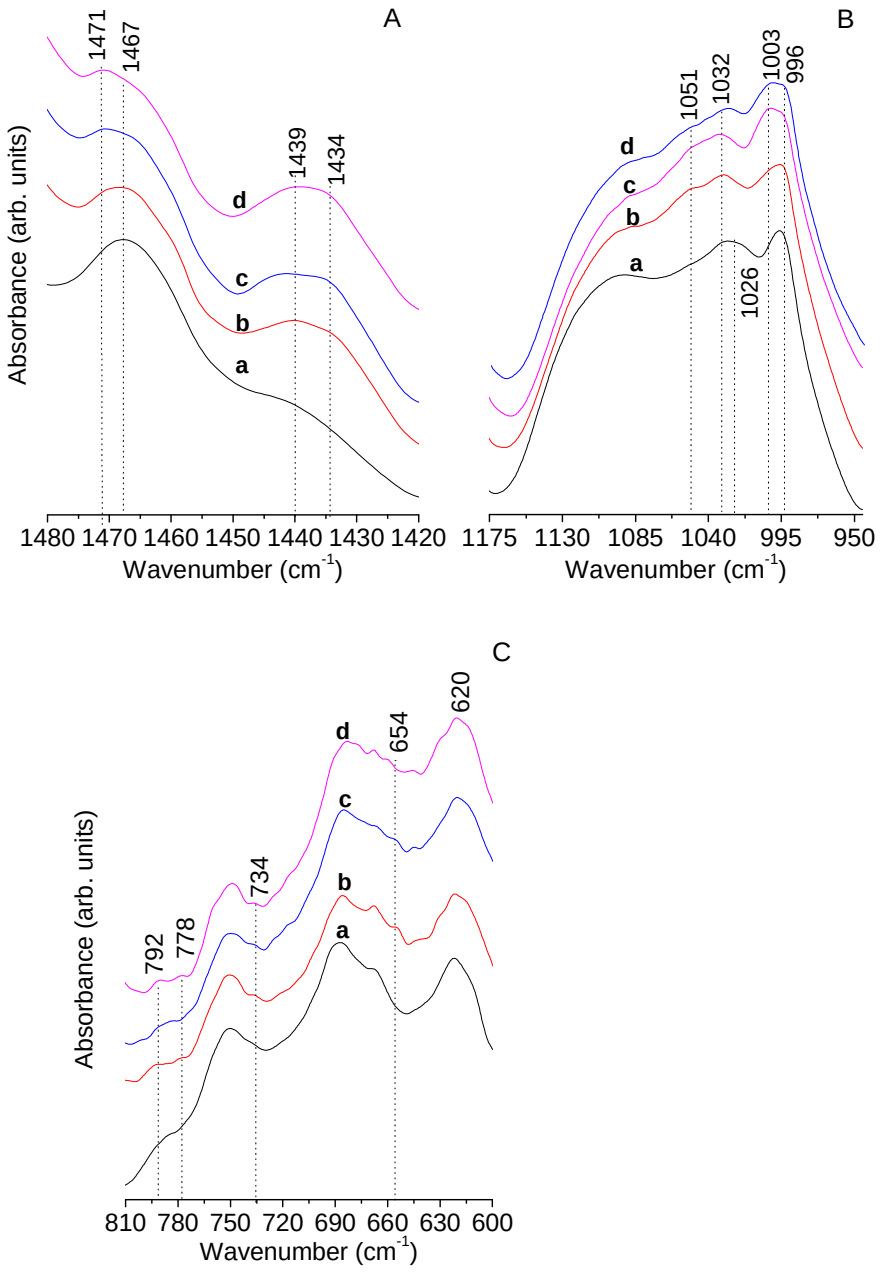

Figure 5.5 Three distinct (A), (B), (C) mid-FT-IR spectra regions (a) **M**, (b) **M-Eu**, (c) **M-Tb** and (d) **M-EuTb**.

Many of the spectral modifications (band shifts and/or growth of new bands) referred above for the M-based doped hybrid materials have been reported previously for Ru(II),[18,20] Ir(III),[20] Cr(VI),[21] Mo(VI),[21] W(VI),[21] and Ln-based complexes[6,15,19], as well as, for intercalation compounds,[16,17] providing evidence that the bpy ligands of **M** framework bond to the Eu^{3+} and Tb^{3+} ions in all the doped samples. In all the cases, in spite of the growth of new bands attributed to Ln-bpy complex formation, the bands due to the free ligand do not vanish, indicating that non-coordinated (free) bpy ligands remain in the matrix. This is an expected result, considering the low concentration of guest salt(s) in the xerogel samples.

It is of interest to emphasize that one of the most solid proofs of the formation of the Ln-bpy adduct in the hybrids studied is the emergence of the 1434 cm^{-1} event in the FT-IR spectra of **M-Eu**, **M-Tb** and **M-EuTb** (Fig. 5.5A). It is worth noting that Álvaro et al.[19] and Tsaryuk *et al.*[15] also detected this feature in the infrared spectra of bipy-based complexes of Eu^{3+}. Finally, a comment is necessary concerning the possibility of bonding of the carbonyl (C=O) oxygen atoms of the urea cross-linkages to the Ln^{3+} ions. Although this hypothesis cannot be discarded, we may speculate simply from the standpoint of steric considerations that the approach of the C=O groups to the emitting centres is rather difficult. Inspection of the "amide I" and "amide II" bands (essentially associated with the C=O stretching and N–H in-plane bending modes, respectively) in the 1800-1600 and 1600-1500 cm^{-1} band envelopes, respectively, is complex, since both spectral intervals are superimposed with several bpy characteristic ν_{ring} modes.[6,15,17,18,20,21]

5.4 Photoluminescence

Non-doped hybrids H and M

Fig. 5.6 A shows the emission spectra of **H** and **M** hybrids under different excitation wavelengths. The emission features of both hybrids are very similar. For excitation wavelengths between 320 and 380 nm, the emission is composed of a large Gaussian-shaped broad band (380-660 nm) peaking around 455 nm, ascribed to the bpy-related triplet state. Increasing the excitation wavelength (380-440 nm), an energy dependent band whose peak position deviates towards the red is detected. This is the typical behaviour ascribed to the intrinsic emission, attributed to the convolution of electron-hole recombinations originated in the NH/C=O groups of the urea cross-linkages and within the siliceous nanoclusters. Decreasing the temperature from 300 to 14 K, no significant changes are detected in the photoluminescence features, Figs. 5.6 C, D.

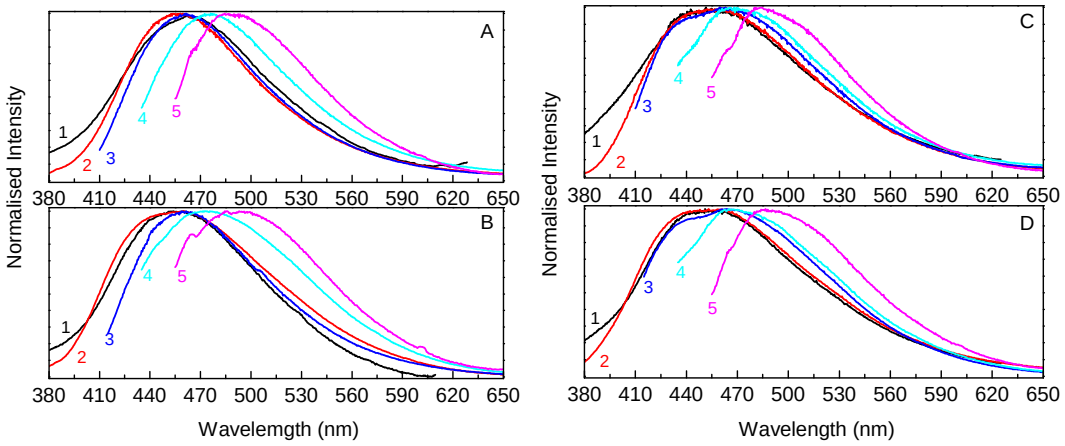

Figure 5.6 Room temperature emission spectra of (A) **M** and (B) **H** and 14K (C) **M** and (D) **H** excited at (1) 320 nm (2) 360 nm, (3) 390 nm, (4) 420 nm and (5) 440 nm.

The excitation spectra monitored between 420 and 480 nm are presented for the **H** and **M** hybrids in Fig. 5.7. All the spectra are formed of a broad band (320-465 nm) with two components at 375 and 400 nm. The increase in the monitoring wavelength induces a broadening of the high-wavelength component. Similarly to the above mentioned interpretation, the low and high wavelength components can be ascribed to the bpy- and

hybrid-host excited states, respectively. Decreasing the temperature from 300 to 14 K, no significant changes are detected in the photoluminescence features, Figs 5.7 C and D.

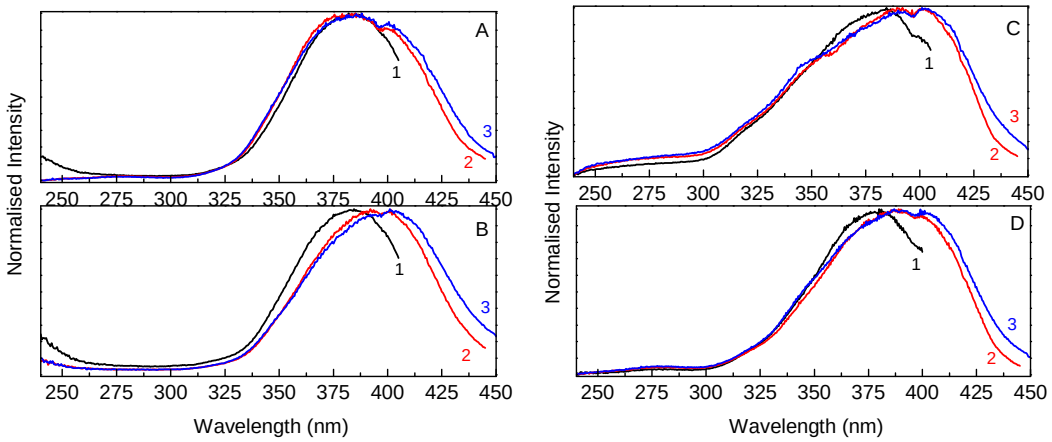

Figure 5.7 Room temperature excitation spectra of (A) **M** and (B) **H** and 14K (C) **M** and (D) **H** monitored at (1) 420 nm, (2) 460 nm and (3) 480 nm.

To ascertain the origin of this blue light, the emission spectra were acquired in time-resolved mode at 14 and 300 K (Fig. 5.8) Fig. 5.8A shows the room temperature time-resolved emission spectrum of material **H** under 390 nm excitation wavelength for a starting delay (SD) of 0.05 ms, showing a large broad band peaking at 455 nm. Comparing this spectrum with the one acquired in steady-state regime (Fig. 5.6B), a decrease (around 20 %) of the fwhm is observed, so that only the low-wavelength region overlaps in both spectra. This observation strongly suggests that the emission mechanisms behind the high-wavelength components detected in steady-state mode are characterised by a shorter time scale. The lifetime of this component was estimated through the measurement of the emission decay curve monitored at 455 nm, Fig 5.9. The emission decay curve displays a non-exponential behaviour with an average lifetime value (for which the maximum emission intensity is reduced to 1/*e* of its maximum intensity) of 0.063 ± 0.003 ms.

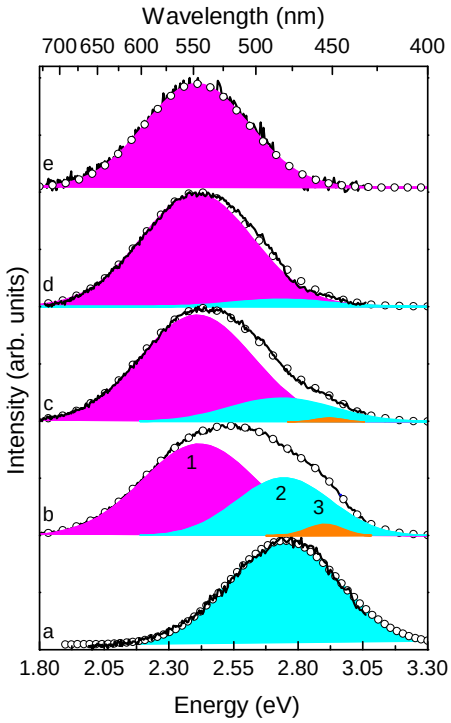

Figure 5.8 Time-resolved emission spectra of **H** excited at 390 nm and acquired at 300K with SD values of (a) 0.05 ms and at 14 K with SD values of (b) 0.05 ms, (c) 0.06 ms, (d) 0.07 ms and (e) 100.00 ms. The multi-Gaussian envelope fit (open circles) and the corresponding Gaussian components (1), (2), and (3), ascribed to the NH-related emission, bpy triplet sate and siliceous-related emission, respectively, are also shown.

This emission observed in the room temperature time resolved spectrum can unequivocally be attributed to the triplet states of the bpy groups since the respective lifetime (0.063 ± 0.003 ms) is four orders of magnitude higher than those already measured for the emission originated in the urea and amide cross-linkages and siliceous nanodomains (10^{-6} ms).[22] Moreover, the triplet band energy is both independent of the excitation wavelength and of the SD values, which are not features typical of the siliceous and urea cross-linkages-related emission, which are known to red-shift either with the increasing in the excitation wavelength and in the SD values.[23-25]

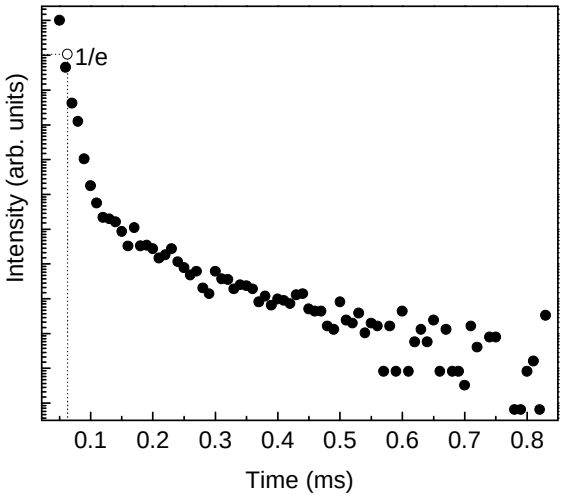

Figure 5.9 Emission decay curve of **H** acquired at 300 K, excited at 400 nm and monitored at 452 nm.

For the same SD value of 0.05 ms, decreasing the temperature to 14 K induces a significant broadening of the spectrum (Fig. 5.8b), with a maximum now located at around 515 nm and two overlapping bands at 452 nm and 467 nm. Increasing the SD value to 0.06 and 0.07 ms strongly decreases their intensity and for SD values higher than 100 ms only the long-lived component at 550 nm remains.

In order to get further knowledge on the energy and fwhm of the three components a deconvolutiom fitting procedure using a sum of three Gaussian functions for SD values between 0.05 ms and 100.00 ms was performed. Attending to the high number of fitting parameters, the following procedure was used to fit the experimental time-resolved emission spectra to the Gaussian parameters (peak energy, integrated intensity, and fwhm). First, one Gaussian function was adjusted to fit the urea-related long-lived emission selectively detected for a SD value of 100.00 ms yielding to an energy peak position and fwhm of 2.41 ± 0.01 eV and 0.40 ± 0.01 eV, respectively (Fig. 5.8e). Then, the bpy-triplet state energy and fwhm were determined from the single Gaussian fit to the room temperature emission spectrum measured for a SD value of 0.05 ms revealing energy and fwhm of 2.74 ± 0.01 eV and 0.40 ± 0.01 eV, respectively (Fig. 5.8a). These values were used as input values to fit the spectra acquired at 14 K with SD values between 0.05 ms and 0.07 ms, which shows a multi-Gaussian profile. This procedure is based on the fact that for a triplet state nature the energy is almost independent of the temperature and SD values, and for the urea-related emission a minor variation of the energy is expected with

variations in the SD. In both cases, the fwhm was kept as constant and independent of the temperature and SD values. As shown in Fig. 5.8, to get a correct fit for the spectra acquired with SD values of 0.05 and 0.06 ms a third component should be considered, with an energy and fwhm of 2.91 ± 0.01 eV and 0.11 ± 0.01 eV, based on the previous results observed with analogous urea-functionalized hybrids, we attributed this component to the electron-hole recombinations occurring within the siloxane nanoclusters.[23-25]

Fig. 5.10 shows the 300 K and 14 K time-resolved emission spectra under SD values of 0.05 ms, 0.08 ms and 20.00 ms for the **M**, excited at 400 nm. The emission acquired for SD of 0.05 ms shows a broad band peaking at 445 nm, resembling the byp-related emission acquired in steady-state mode (Fig. 5.6C). Increasing the SD to 0.08 ms, such broad emission band is resolved into two components, namely, a short lived one at 445 nm and a longer-lived component at 540 nm. For higher SD values, only the latter component could be detected, as exemplified in Fig. 5.10C for SD of 20.00 ms. The energy of the low-wavelength component (445 nm) is independent of excitation wavelength and displays a time scale of the order of 10^{-1} ms, which are in good agreement with a triplet nature associated with the byp ligands. On other hand, the high-wavelength component (540 nm) is red-shift relatively to the steady state emission and displays a longer time scale mechanism (10^{2} ms), resembling the emission features of the emission associated to the urea cross-linkages as previously studied in detail.[24] We should note that in the present case the intrinsic Si-related emission observed in analogous organic/inorganic hybrids was not detected in the time resolved mode because its typical energy is higher than that of the triplet and urea-cross-linkages and, therefore, it is not excited at the selected excitation wavelength (400 nm). Nevertheless, the steady state emission red-shift with increasing excitation wavelength is a finger print of the presence of oxygen-related defects in the siliceous nanodomains.

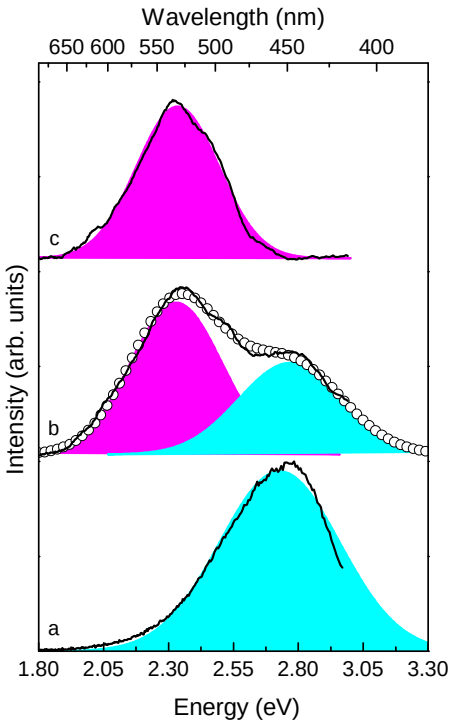

Figure 5.10 Time-resolved emission spectra of **M** excited at 400 nm and acquired at 300K with SD values of (a) 0.05 ms and at 14 K with SD values of (b) 0.08 ms, (c) 20.00 ms.

The emission decay curves of the three components for the **H** were acquired at 14 K (Fig. 5.11).

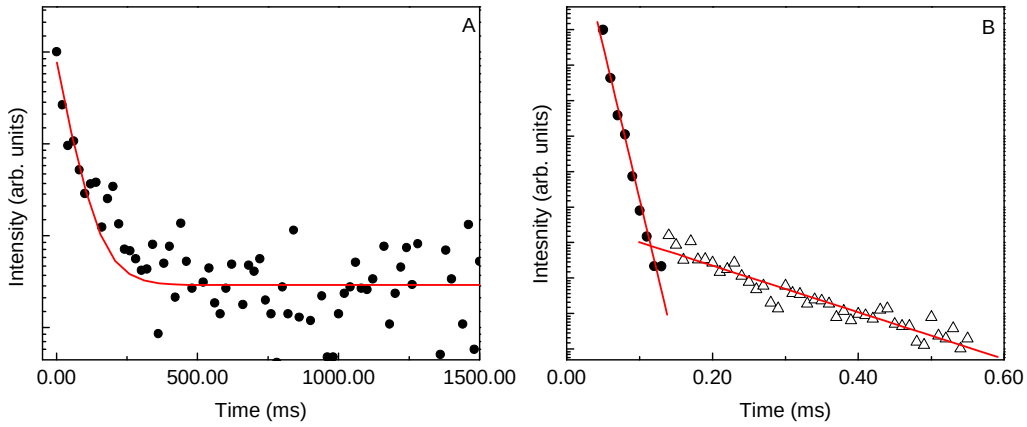

Figure 5.11 Emission decay curves of **H** acquired at 14 K, excited at 390 nm and monitored at (A) 540 nm and (B) 460 nm. The solid lines correspond to the best fit using (A) single exponential and (B) bi-exponential functions.

The emission decay curve associated with the urea-related emission was selectively monitored at 550 nm, revealing an exponential behaviour (Fig. 5.12 A). Attending to the high spectral overlap, the lifetime values of the triplet state and siliceous related emission were simultaneously estimated by monitoring the emission decay curve at 460 nm (Fig. 5.12B). The corresponding lifetimes of the urea-, bpy- and siliceous-related emissions were estimated at 14 K as 58.9 ± 0.004, 0.152 ± 0.007 and 0.012 ± 0.001 ms, respectively.

The **H** emission can be easily excited by a commercial LED (395 nm), being blue to the naked eye (Figs. 5.12 B, C). The emission color is simply tuned from the blue spectral region to the green one changing the excitation wavelength from 390 to 440 nm; (x,y) Commission Internationale d'Éclairage (CIE) coordinates vary from (0.18,0.22) to (0.20,0.30) (Fig. 5.11 A).

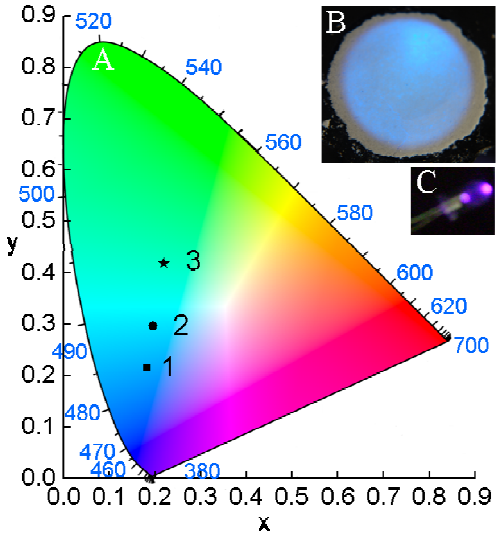

Figure 5.12 (A) CIE chromaticity diagram showing the (x,y) emission color coordinates of **H** excited at (1) 390 nm, (2) 420 nm and (3) 440 nm. (B) Photograph of a pellet of **H** under 395 nm LED excitation operating at 2.4 V. (C) LED (ROITHNER LASERTECHNIK) used to excite the pellet.

The emission features were further quantified through the estimation of the absolute emission quantum yield under distinct excitation wavelengths (360-440 nm). A maximum value of 0.22 ± 0.02 for **H** and 0.18 ± 0.02 for **M** were attained under excitation in the long-wavelength UV and blue spectral regions (360-420 nm). These are the highest quantum yield values reported so far for silsesquioxanes exciting in the long UV/blue

regions; the 3-aminopropyltriethoxysilane-formic acid hybrid exhibits 0.35 ± 0.1 but measured under UV excitation (365 nm).[2]

Ln^{3+}-M hybrids

The Ln^{3+}-doped hybrids are multi-wavelength emitters under UV excitation. Fig. 5.13 illustrates the emission features of **M-Eu** and **M-Tb** under distinct excitation wavelengths showing a series of peaks, attributed to the Eu^{3+} $^5D_0 \rightarrow {}^7F_{0\text{-}4}$ (**M-Eu**) and Tb^{3+} $^5D_4 \rightarrow {}^7F_{6\text{-}0}$ (**M-Tb**) transitions, superimposed on a large broad band. Whereas the energy and full width at half maximum (fwhm) of the intra-4f transitions are almost independent of the excitation wavelength, suggesting that the Ln^{3+} ions occupy the same average local environment (see below), the broad band energy and fwhm strongly depend on the excitation wavelength. In particular, for excitation wavelengths between 270 and 360 nm the broad band energy remains essentially unaltered, peaking at *ca.* 450 nm. The increase of the excitation wavelength (360-460 nm) leads to the decrease of the emission energy. A similar broad band displaying an analogous dependence on the excitation wavelength was already observed in the non-doped **M** host (Fig.5.6A).

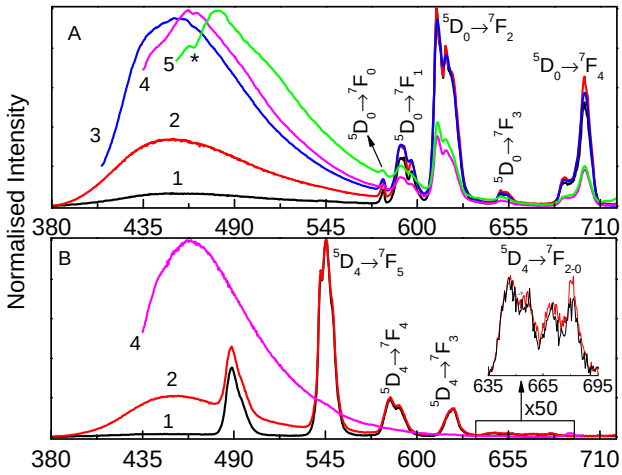

Figure 5.13 Room temperature emission spectra of (A) **M-Eu** and (B) **M-Tb** excited at (1) 270 nm, (2) 360 nm, (3) 393 nm, (4) 420 nm and (5) 460 nm. The asterisk denotes the $^7F_{0,1} \rightarrow {}^5D_2$ self-absorptions.

Fig. 5.14 shows the excitation spectra of **M-Eu** and **M-Tb** monitored within the Eu^{3+} $^5D_0 \rightarrow {}^7F_2$ and Tb^{3+} $^5D_4 \rightarrow {}^7F_5$ transitions, respectively. The spectra are composed of a broad

band with two main components (260-280 nm and 320-340 nm) overlapped with the intra-$4f^6$ $^7F_0 \rightarrow {}^5L_6, {}^5D_2$, $^7F_{0,1} \rightarrow {}^5D_1$ and intra-$4f^8$ $^7F_6 \rightarrow {}^5D_4$ transitions, for **M-Eu** and **M-Tb**, respectively. A low-relative intensity band between 360 and 450 nm (more evident in the excitation spectrum of **M-Eu**) is also discerned. While the low–wavelength region (240-360 nm) is related to the excited states of the bpy-ligands,[15,26] the high–wavelength one (360-450 nm) is associated with the excited states of the NH/C=O groups and of the siliceous nanoclusters,[23,24] as shown in the excitation spectra monitored within the hybrid emission (Fig. 5.14). The presence of either the bpy and hybrid host excited states in the excitation spectra monitored within the Eu^{3+} and Tb^{3+} excited states points out the presence of bpy/hybrid-to-Ln^{3+} energy transfer. Moreover, the negligible relative intensity of the intra-4f lines, points out that the Ln^{3+} ions sensitization is more efficient than direct intra-4f excitation.

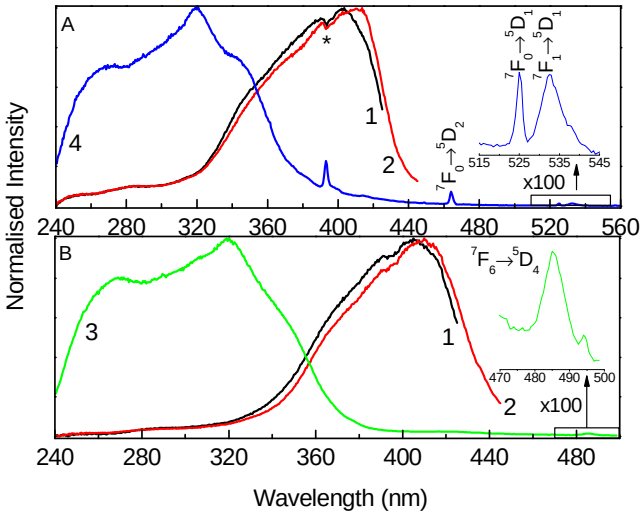

Figure 5.14 Room temperature excitation spectra of (A) **M-Eu** and (B) **M-Tb** monitored at (1) 440 nm, (2) 460 nm, (3) 544 nm, and (4) 612 nm. The asterisk denotes the $^7F_0 \rightarrow {}^5L_6$ self-absorption. The insets show a magnification of the $^7F_6 \rightarrow {}^5D_4$ (A) and $^7F_{0,1} \rightarrow {}^5D_1$ transitions.

The lifetime values of the Eu^{3+} and Tb^{3+} excited states ($^5D_0$ and $^5D_4$, respectively) were monitored at 700 and 544 nm and excited at 464 and 330 nm, respectively, at 14 and 300 K. All the emission decay curves are well reproduced by a single exponential function yielding $\tau(^5D_0)=0.456 \pm 0.005$ and $\tau(^5D_4)=0.913 \pm 0.004$ ms, at 14 K, and $\tau(^5D_0)=0.384 \pm 0.016$ and $\tau(^5D_4)=0.868 \pm 0.007$ ms, at 300 K, Fig. 5.15.

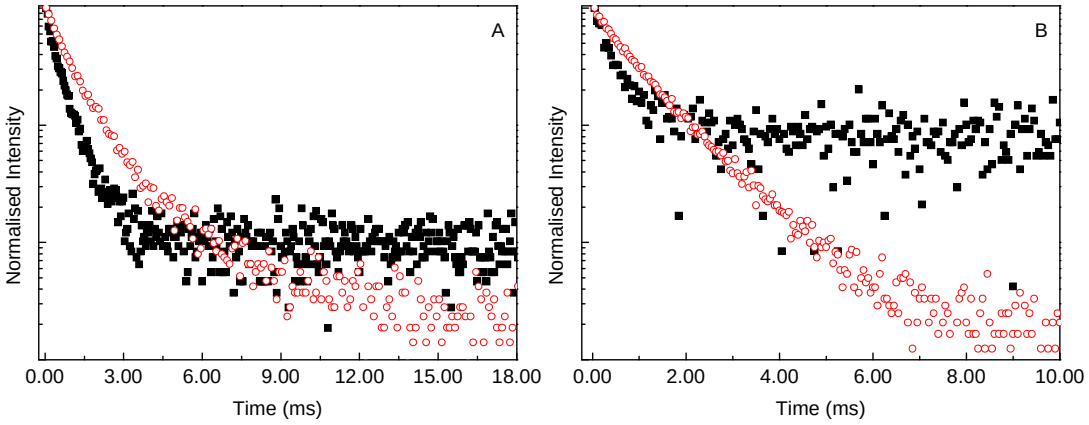

Figure 5.15 Emission decay curves of Eu^{3+} and Tb^{3+} excited states ($^5D_0$ and $^5D_4$, respectively), monitored at 700 and 544 nm and excited at 464 and 330 nm, for **M-Eu** (squares) and **M-Tb** (circles), respectively, at (A) 14K and (B) 300 K.

Fig. 5.16 shows the room temperature emission spectra of **M-EuTb** which is strongly dependent on the excitation wavelength. For excitation wavelengths between 270 and 340 nm, the emission features are essentially attributed to the overlap of the Eu^{3+} and Tb^{3+} $^5D_0 \rightarrow {}^7F_{0\text{-}4}$ and the $^5D_4 \rightarrow {}^7F_{6,5}$ transitions, respectively. At higher excitation wavelengths (340-393 nm), besides the intra-4f transitions the above mentioned hybrid's host emission is observed.

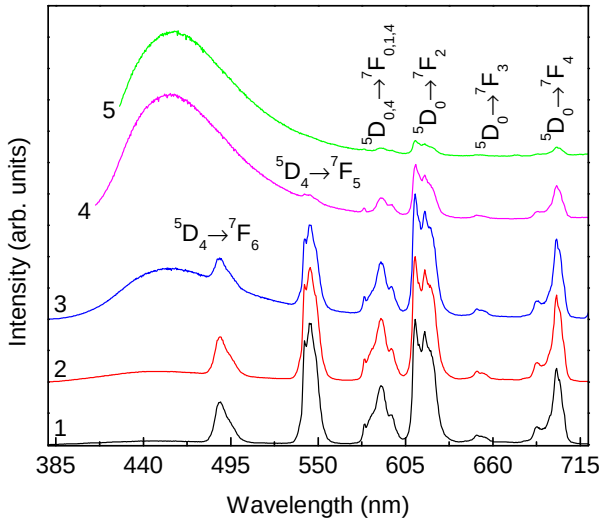

Figure 5.16 Room temperature emission spectra of **M-EuTb** excited at (1) 270 nm, (2) 340 nm, (3) 364 nm, (4) 393 nm and (5) 410 nm.

Accordingly, the emission colour is fine-tuned across the *Commission Internationale d'Éclairage* (CIE) chromaticity diagram (Fig. 5.17) from the red (**M-Eu**), orange (**M-EuTb**) or green (**M-Tb**) regions to the blue one, by changing the excitation wavelength. Interestingly, upon excitation at 360 nm, the (x,y) color coordinates of **M-EuTb** (0.32,0.29) get close to the white point (0.33, 0.33) making it white light emitter.

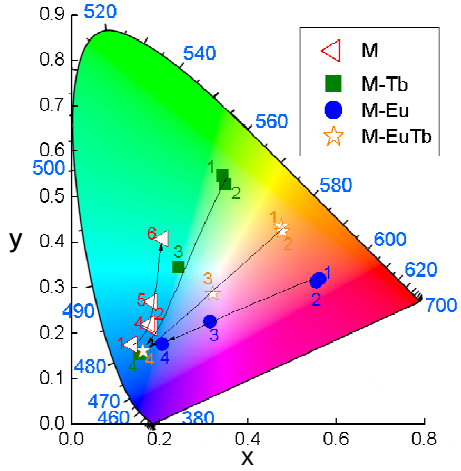

Figure 5.17 Chromaticity diagram (CIE, 1931) showing the (x,y) emission colour coordinates of **M**, **M-Eu**, **M-Tb** and **M-EuTb** under different excitation wavelengths. The arrow indicates the excitation wavelength variation: (1) 270 nm, (2) 320 nm, (3) 360 nm, (4) 400 nm, (5) 420 nm and (6) 440 nm.

The excitation spectra were selectively monitored within the Eu^{3+} and Tb^{3+} $^5D_0 \rightarrow {}^7F_4$ (700 nm) and $^5D_4 \rightarrow {}^7F_5$ (544 nm) transitions, respectively (Fig. 5.18). Both spectra are similar, consisting of a large broad band with two main components peaking at 270 and 340 nm and of a shoulder at 410 nm, resembling the spectrum acquired for **M** (in Fig. 5.7A) and for **M-Ln** (Fig. 5.14). Therefore, the high- and low-wavelength regions can be attributed to the preferential excitation of the bpy and NH/C=O groups and siliceous nanoclusters, respectively. The spectrum selectively monitored within the Eu^{3+} lines displays low relative intensity intra-4f transitions ($^7F_0 \rightarrow {}^5L_6, {}^5D_{3\text{-}1}$, $^7F_1 \rightarrow {}^5D_1$, Eu^{3+}, and $^7F_6 \rightarrow {}^5D_4$, Tb^{3+}). The observation of the Tb^{3+}-related transition is a clear evidence of the occurrence of Tb^{3+}-to-Eu^{3+} energy transfer at room temperature. The spectra acquired at 14 K (not shown) are similar to those measured at room temperature.

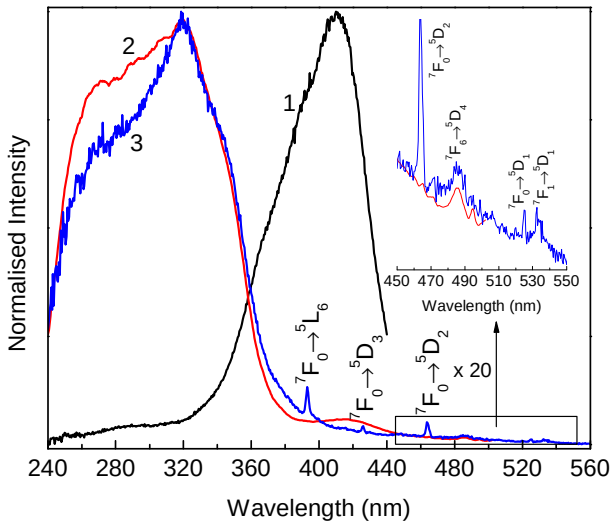

Figure 5.18 Room temperature excitation spectra of **M-EuTb** monitored at 1) 460 nm, 2) 544 nm and 3) 700 nm.

The $^5D_0$ and $^5D_4$ decay curves are non-exponential (Fig. 5.19) illustrating the multiple and complex energy transfer scheme (bpy → hybrid → Tb^{3+} → Eu^{3+}, bpy → hybrid → Ln^{3+} and hybrid → Ln^{3+}) of **M-EuTb**. The analysis of these mechanisms lies outside the scope of the present work.

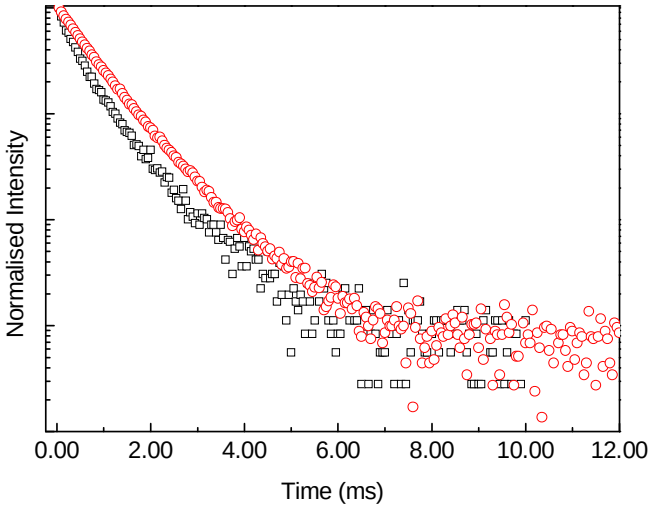

Figure 5.19 Emission decay curves of **M-EuTb** aquired at 300K monitored at 700 nm and excited at 464 (squares) and monitored at 544 nm and excited at 330 nm (circles).

The energy levels of the hybrid host emitting centres (Fig. 5.20) were determined from the emission spectra of **M-Gd** (Fig. 5.21), since Gd^{3+} excited levels have energies

much higher than those of the hybrid host excited states, thus disabling host-to-Ln^{3+} energy transfer.

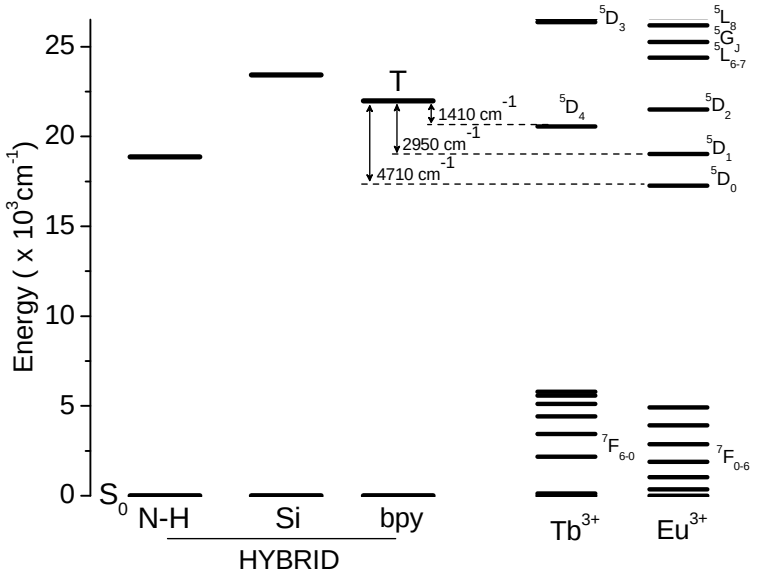

Figure 5.20 Schematic illustration of the partial energy diagram level showing the Tb^{3+} and Eu^{3+} intra-4*f* levels and the energy peak position of the hybrid host emitting centres, urea-(N-H), siliceous-related (Si) components and bpy-triplet state. For the sake of clarity, the first excited Gd^{3+} level ($^6P_{7/2}$) at *ca.* 32.000 cm^{-1} is omitted.

A fitting procedure assuming a sum of multi-Gaussian functions was used (Fig. 5.21). The emission spectra excited at 420 nm is well modelled by a sum of two Gaussian functions peaking at 530 nm (18867 cm^{-1}) and 455 nm (21978 cm^{-1}) ascribed, respectively, to the NH-related emission[23-25] and to the triplet state of the bpy. At lower excitation wavelengths a third Gaussian component, whose peak position deviates towards the red as the excitation wavelength increases, is discerned and can be attributed to the siliceous nanodomains.[23-25] Owing to the emission dependence on the excitation wavelength an average peak position at 427 nm (24414 cm^{-1}) was used in the diagram of Fig. 5.20.

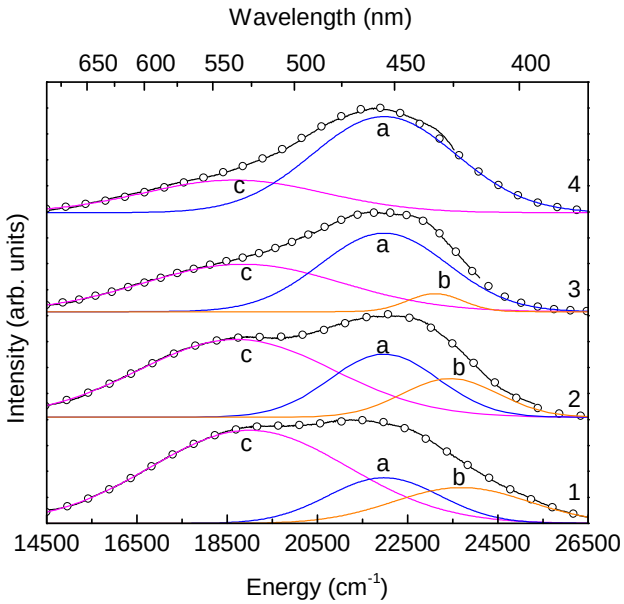

Figure 5.21 Emission spectra (14 K) of **M-Gd** excited at (1) 360 nm, (2) 380 nm, (3) 400 nm and (4) 420 nm. The fit components are also presented: (a) bpy-triplet state, electron-hole recombinations occurring in the (b) siliceous domains and (c) urea cross-linkages. The open circles represent the fit envelope.

The detection of a single $^5D_0 \rightarrow {}^7F_0$ line, the J-degeneracy splitting of the $^7F_{1,2}$ levels into 3 and 4 Stark components, respectively, indicate that the Eu^{3+} ions in **M-Eu** and **M-TbEu** occupy the same average local environment with a low symmetry site, without an inversion centre, in accordance with the higher intensity of the electric-dipole $^5D_0 \rightarrow {}^7F_2$ transition, Fig. 5.22.[27] The energy and fwhm of the $^5D_0 \rightarrow {}^7F_0$ line were estimated using a single Gaussian fit, yielding to 17270.8 ± 0.4 cm^{-1} and 41.6 ± 0.9 cm^{-1}, for **M-Eu**, and 17263.2 ± 0.5 cm^{-1} and 50.4 ± 1.5 cm^{-1}, for **M-EuTb**. The higher energy of the $^5D_0 \rightarrow {}^7F_0$ transition found for the former hybrid indicates that the Eu-ligand bonds have (in average) a less covalent character relative to the situation found in the latter.[27-31] This observation suggests variations in the number and/or type of Eu^{3+}-first neighbours (as it will be further discussed below), which could be caused by the different relative Eu^{3+} content in **M-Eu** and **M-EuTb** (4.98 and 2.68 % w/w, respectively). Moreover, the large values found for the fwhm (higher than those reported for analogous amorphous hybrids, 19-37 cm^{-1}),[32] point out that the Eu^{3+} cations are accommodated in a continuous distribution of similar local sites.

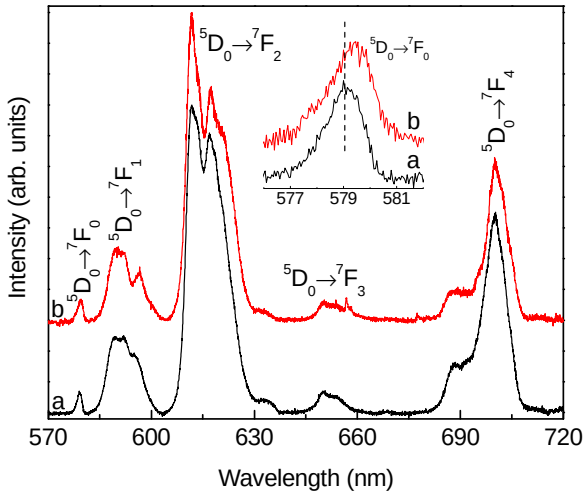

Figure 5.22 Room temperature high resolution emission spectra excited at 464 nm of (a) **M-Eu** and (b) **M-EuTb**. The inset shows a magnification of the $^5D_0 \rightarrow ^7F_0$ transitions.

5.5 Eu^{3+}-M hybrids: $^5D_0$ Quantum Efficiency and Quantum Yields

From the emission spectra shown in Fig. 5.22 we have determined the experimental intensity parameters, Ω_2 and Ω_4, of **M-Eu** and **M-EuTb** by using the $^5D_0 \rightarrow {}^7F_2$ and $^5D_0 \rightarrow {}^7F_4$ electronic transitions, respectively, and using Eq. 2.18.

The values of the Ω_2 and Ω_4 experimental intensity parameters are, respectively, 6.7×10^{-20} and 4.3×10^{-20} cm^2, for **M-Eu**, and 7.9×10^{-20} and 5.1×10^{-20} cm^2, for **M-EuTb**. The relative high values of Ω_2 might be interpreted as a consequence of the hypersensitive behaviour of the $^5D_0 \rightarrow {}^7F_2$ transition, suggesting that the dynamic coupling mechanism is quite operative and that the chemical environment is highly polarisable. In particular, a correlation has been noticed in the sense that compounds expected to have a higher degree of covalence tend to present higher values of Ω_2.[6,28,33,34] The Ω_2 values estimated for **M-Eu** are smaller than those calculated for **M-EuTb**, pointing out a decrease in the average degree of covalence of the Eu-first bonds in **M-Eu**, in agreement with the above mentioned conclusions derived from the analysis of the energy of $^5D_0 \rightarrow {}^7F_0$ transition the in the two hybrids. Furthermore, the Ω_2 values are similar to those previously found for amorphous amine-functionalised organic/inorganic hybrids incorporating europium triflate salt[28,31], for analogous lamellar hybrids incorporating europium chloride[12,31] and mesostructured silica doped with aquo-Eu^{3+}β-diketonate complex,[31,35] despite the distinct morphologies and Eu^{3+}-local coordination sites found in all these hybrids. It is also interesting to note that in these hybrids (except for the mesostructured silica-based hybrid) and in **M-Eu** and **M-EuTb** the Ω_2 and Ω_4 values are of the same order of magnitude, regardless of the fact that in a larger number of Eu^{3+}-containing hybrids the Ω_4 values are substantially smaller than those of Ω_2.[31]

The non-radiative rate A_{NRAD} of **M-Eu** was obtained from the calculated A_{RAD} rate and the experimental $^5D_0$ lifetime by using Eq. 2.14. The $^5D_0$ quantum efficiency (η) was evaluated from the ratio between A_{RAD} and A_T, yielding A_{RAD}=362 s^{-1}, A_{NRAD}=2245 s^{-1} and η=0.14. The A_{NRAD} value may be rationalised in terms of the number of water molecules coordinated to Eu^{3+} (n_w) as determined from Eq. 21.9.[36] For **M-Eu** n_w=2.1±0.1. We note that similarly to the situation found for the intensity parameters, the η and n_w values

estimated for **M-Eu** are very close to those reported for the above mentioned di-ureasils[28,31], L12[12,31] and SBA-15[31,35] Eu^{3+}-based hybrids.

For the Eu^{3+}- and Tb^{3+}-containing hybrids the maximum quantum yield values were attained under excitation *via* the bpy-triplet (320 nm), 0.08 (**M-Eu**) and 0.12 (**M-Tb** and **M-EuTb**). The higher quantum yield values obtained for the Tb^{3+}-containing hybrids can be accounted for the higher resonance between the bpy-triplet state with the $^5D_4$ level of Tb^{3+} ions (1410 cm^{-1}), relatively to that found for the $^5D_1$ level of Eu^{3+} ions (2950 cm^{-1}), Fig. 5.20. Under excitation via the urea cross-linkages and siliceous domains excited states (380-420 nm) the quantum yield values are lower, independently of the selected excitation wavelength, 0.06 (**M-Eu**) and 0.08 (**M-Tb** and **M-EuTb**), pointing out the active role of bpy in the enhancement of the emission quantum yield values of Ln^{3+}-based hybrids.

5.6 Conclusions

Metal-free bpy-bridged silsesquioxanes displaying a tunable blue-to-green emission (emission quantum yields between 0.18 ± 0.02 to 0.22 ± 0.02) were presented. A bpy-bridged silsesquioxane easily excited by commercial long UV/blue LEDs was obtained bringing organic/inorganic hybrids on the way to applications as metal-free phosphors for LED-based lighting and LED-addressed displays.

Bpy-bridged silsesquioxanes incorporating different lanthanides ions (Eu^{3+}, Gd^{3+} and Tb^{3+}, ca. 5-7 % w/w) were obtained by the sol–gel process. The hybrids are room temperature multi-wavelength emitters due to the convolution of the emission arising from the hybrid's emitting centres (urea cross-linkages, siliceous domains and bpy triplet) and the Eu^{3+} and/or Tb^{3+} intra-4*f* transitions. The emission colour is easily tuned across the CIE diagram from the blue to the red, orange or green areas, depending on the Ln^{3+} ions and the excitation wavelength. Bpy-to-Ln^{3+} and Tb^{3+}-to-Eu^{3+} energy transfer mechanisms are demonstrated in the different hybrids. Due to the different bpy/Ln^{3+} ratios, the Eu^{3+}-local coordination in the Eu^{3+} and Eu^{3+}/Tb^{3+} co-doped samples slightly differ, as shown by the $^5D_0 \rightarrow {}^7F_{0\text{-}4}$ transition energies, $^5D_0$ lifetimes and intensity parameters. Although it could not be determined precisely, the Ln^{3+} coordination sphere was shown to comprise bpy fragments, chloride anions and water molecules (1 to 2). Improvement of the hybrids' performances playing with the organic fragments will potentially allow applications as layers for active photonic devices.

5.7 References

1. V. Bekiari and P. Lianos, *Chem. Mater.*, 1998, **10**, 3777.
2. W. H. Green, K. P. Le, J. Grey, T. T. Au and M. J. Sailor, *Science*, 1997, **276**, 1826.
3. M. L. Gomez, D. P. Fasce, R. J. J. Williams, C. M. Previtali, L. Matejka, J. Plestil and J. Brus, 2008, **209**, 634.
4. R. Le Toquin and A. K. Cheetham, *Chem. Phys. Lett.*, 2006, **423**, 352.
5. S. Benyahya, F. Monnier, M. Taillefer, M. Wong Chi Man, C. Bied and F. Ouazzani, *Adv. Synth. Cat.*, 2008, **350**, 2205.
6. H. Li, N. Lin, Y. Wang, Y. Feng, Q. Gan, H. Zhang, Q. Dong and Y. Chen, *Eur. J. Inorg. Chem.*, 2009, **4**, 519.
7. C. Kaes, A. Katz and M. W. Hosseini, *Chem. Rev.*, 2000, **100**, 3553.
8. A. C. Franville, D. Zambon, R. Mahiou and Y. Troin, *Chem. Mater.*, 2000, **12**, 428.
9. H. R. Li, J. Lin, H. J. Zhang, H. C. Li, L. S. Fu and Q. G. Meng, *Chem. Commun.*, 2001, **13**, 1212.
10. H. Li, J. Yu, F. Liu, H.Zhang, L. Fu, Q. Meng, C. Peng and J. Lin, *New J. Chem.*, 2004, **28**, 1137.
11. S. Cousinie, M. Gressier, P. Alphonse and M. J. Menu, *Chem. Mater.*, 2007, **19**, 6492.
12. S. S. Nobre, C. D. S. Brites, R. A. S. Ferreira, V. de Zea Bermudez, C. Carcel, J. J. E. Moreau, J. Rocha, M. Wong Chi Man and L. D. Carlos, *J. Mater. Chem.*, 2008, **18**, 4172.
13. J. J. E. Moreau, L. Vellutini, P. Dieudonne, M. Wong Chi Man, J. L. Bantignies, J. L. Sauvajol and C. Bied, *J. Mater. Chem.*, 2005, **15**, 4943.
14. L. S. Fu, R. A. S. Ferreira, N. J. O. Silva, L. D. Carlos, V. De Zea Bermudez and J. Rocha, *Chem. Mater.*, 2004, **16**, 1507.
15. V. Tsaryuk, V. Zolin, J. Legendziewicz, R. Szostak and P. Gawryszewska, *J. Alloy Compd.*, 2004, **380**, 418.
16. J. G. Qin, C. L. Yang, K. Yakushi, Y. Nakazawa and K. Ichimura, *Solid State Commum.*, 1996, **100**, 427.
17. N. Preda, L. Mihut, M. Baibarac, I. Baltog, M. Husanu, C. Bucur and T. Velula, *Rom. Journ. Phys.*, 2008, **54**, 667.
18. Q. Pozat and C. Sourisseau, *J. Phys. Chem.*, 1984, **88**, 3007.

19. M. Álvaro, V. Fornés, S. García, H. García and J. C. Scaiano, *J. Phys. Chem. B*, 1998, **102**, 8744.
20. B. F. Minaev, V. A. Minaeva, G. V. Baryshnikov, M. A. Girtu and H. Agren, *Russ. J. Appl. Chem.*, 2009, **82**, 1211.
21. B. Soptrajanov, M. Trpkosvska and L. Pejov, *Croatica Chem. Acta*, 1999, **72**, 663.
22. L. S. Fu, R. A. S. Ferreira, M. Fernandes, S. C. Nunes, V. D. Bermudez, G. Hungerford, J. Rocha and L. D. Carlos, *Opt. Mater.*, 2008, **30**, 1058.
23. L. D. Carlos, R. A. S. Ferreira, V. de Zea Bermudez and S. J. L. Ribeiro, *Adv. Funct. Mater.*, 2001, **11**, 111.
24. L. D. Carlos, R. A. S. Ferreira, R. N. Pereira, M. Assunção and V. de Zea Bermudez, *J. Phys. Chem. B*, 2004, **108**, 14924.
25. S. S. Nobre, P. P. Lima, L. Mafra, R. A. S. Ferreira, R. Freire, L. Fu, U. Pischel, V. de Zea Bermudez and L. D. Carlos, *J. Phys. Chem. C*, 2007, **111**, 3275.
26. X. Q. Song, H. R. Zheng, W. S. Liu and Z. H. Ju, *Spectrochimica Acta Part A*, 2008, **69**, 49.
27. L. D. Carlos, R. A. S. Ferreira, V. de Zea Bermudez, C. Molina, L. A. Bueno and S. J. L. Ribeiro, *Phys. Rev. B*, 1999, **60**, 10042.
28. L. D. Carlos, Y. Messaddeq, H. F. Brito, R. A. S. Ferreira, V. de Zea Bermudez and S. J. L. Ribeiro, *Adv. Mater.*, 2000, **12**, 594.
29. O. L. Malta, H. J. Batista and L. D. Carlos, *Chem. Phys.* , 2002, **282**, 21.
30. L. D. Carlos, O. L. Malta and R. Q. Albuquerque, *Chem. Phys. Lett.*, 2005, **416**, 238.
31. L. D. Carlos, R. A. S. Ferreira, V. de Zea Bermudez and S. J. L. Ribeiro, *Adv. Mater.*, 2009, **21**, 509.
32. L. S. Fu, R. A. S. Ferreira, N. J. O. Silva, J. A. Fernandes, P. Ribeiro-Claro, I. S. Goncalves, V. De Zea Bermudez and L. D. Carlos, *J. Mater. Chem.*, 2005, **15**, 3117.
33. O. L. Malta, *J. Lumin.*, 1997, **71**, 229.
34. P. P. Lima, R. A. S. Ferreira, R. O. Freire, F. A. A. Paz, L. S. Fu, S. Alves, L. D. Carlos and O. L. Malta, *Chemphyschem*, 2006, **7**, 735.
35. C. Y. Peng, H. J. Zhang, J. B. Yu, Q. G. Meng, L. S. Fu, H. R. Li, L. N. Sun and X. M. Guo, *J. Phys. Chem. B*, 2005, **109**, 15278.
36. R. M. Supkowski and W. D. Horrocks, *Inorg. Chim. Acta*, 2002, **340**, 44.

Chapter 6 – General conclusions

6.1 Final conclusions and perspectives

6.1 Final conclusions and perspectives

The major objective of this thesis has been the development of functional organic/inorganic hybrids hierarchically ordered with potential applications in photonics. It has also been addressed more fundamental aspects of these hybrid materials, such as the mechanism of self-organization, the relationship between the ordered nanostructures and the corresponding photoluminescence properties and the energy transfer (within the hybrid host and, in Ln^{3+}-doped materials, between the hybrid host and the Ln^{3+} ions). In this thesis two types of hybrids, with possible and different applications in photonics, has been studied: white-light emitting hybrids lacking metal activators and Ln^{3+}- containing hybrids. The main conclusions of this work are listed bellow.

- *Quantitative discussion of energy transfer process*

In chapter 3, particular attention has been paid to understanding the photophysical and chemical origin behind the white-light photoluminescent features known for several amine- and amide-functionalized hybrids lacking metal activators (*e.g.* di-ureasils). In an attempt to shed more light in this issue, two model compounds selectively reproducing the organic and inorganic counterpart parts of a di-ureasil hybrid were synthesized and characterized in detail by XRD, $^{29}Si/^{1}H/^{13}C$ MAS NMR, diffuse reflectance and FT-IR, supporting their use as structural models. The photoluminescence features of both model compounds pointed out that their emissions are mediated by *D-A* pairs, as it has been reported for the di-ureasils. From these data, the ideas previously proposed indicating that the white light features are related to radiative recombination mechanisms typical of *D-A* pairs occurring in the siliceous nanodomains (•O-O-Si≡(CO_2) oxygen-related defects) an in the NH/C=O-cross-linkages were unequivocally reinforced.

For the first time, attempts have been made to model and quantify the energy transfer rates between the siliceous-related component to the NH/C=O groups of di-ureasils (Chapter 3). This energy transfer rate was quantitatively estimated for d-U(600) (the di-ureasil host used with smallest number of polymer repeat units) generalizing the ideas proposed by Malta for the intramolecular energy transfer between singlet and triplet ligand levels and ligand-to-metal charge transfer states in Ln^{3+} coordination compounds. The D-A

energy transfer has been estimated considering two-electron determinantal states ($|i\rangle$ and $|f\rangle$) involving the π, π^*, ϕ and ϕ^* molecular orbitals ascribed to the electronic energy levels of the $^{\bullet}$O–O–Si≡(CO_2) oxygen-related defects and the NH/C=O-based one. The energy-transfer rates due to the exchange and dipole–dipole mechanisms have been quantitatively estimated calculating the average donor–acceptor distance, the difference between the donor and acceptor transition energies involved in the transfer process, the width at half-height of the donor and acceptor emissions, the radiative lifetimes, the transition energies, and the overlap integrals (Chapter 3). The dipole-dipole energy transfer rate between the two emitting centres is 1.3×10^{9} s^{-1}, larger than the value estimated for the transfer rate mediated by the exchange mechanism, 3.7×10^{8} s^{-1}, showing that the former is the dominant mechanism.

Prior to this thesis, only a handful of reports deal with host-to-ligand and host-to-metal energy transfer mechanisms in Ln^{3+}-based organic-inorganic hybrids (essentially providing a qualitative discussion). In general, *D-A* energy transfer mechanisms have been treated within the framework of the classic Förster and Dexter approaches. In the case of the Förster model (Columbic interaction), besides the overlap integral it is also possible to calculate the critical radius R_0 for energy transfer, corresponding to the separation distance for which the *D-A* energy transfer rate is equal to the rate of decay of the excited donor in the absence of acceptor. In the Dexter model (exchange mechanism), the overlap integral is the only quantity that can be calculated directly from empirical spectroscopic data. The Malta model, however, as detailed in Chapter 3, quantifies the ligands-to-Eu^{3+} and LMCT-to-ligands and LMCT-to-Eu^{3+} energy transfer rates.

Three distinct energy transfer pathways have been figured out for di-ureasils (with shorter polymer chains) incorporating [Eu(btfa)$_3$(4,4'-bpy)]: (i) hybrid-to-ligand, (ii) ligand-to-Eu^{3+}, and (iii) hybrid-to-Eu^{3+}. The corresponding energy transfer rates have been estimated using Malta model, generalizing ideas previously proposed for the intramolecular energy transfer between singlet and triplet ligand levels and Eu^{3+} ions and between those ligand levels and LMCT states in Ln^{3+} coordination compounds. The numerical evaluation of those energy-transfer rates have been achieved measuring the transitions energies, the radiative lifetimes, the width at half-height of the hybrids emitting centres emission, singlet and triplet ligand levels and Eu^{3+} intra-4*f* states, and the average

Eu^{3+}-ligands and Eu^{3+}-hybrids emitting-centres distances. The ligand-to-Eu^{3+} energy transfer rate is one order of magnitude larger than the value estimated for the direct transfer from the hybrids emitting centres, 3.75×10^{10} and 3.26×10^{9} s^{-1}, respectively to the $^5D_1$ level. The most efficient luminescence channel is $(S_0)_{Hybrid} \rightarrow (T)_{Hybrid} \rightarrow (T)_{Ligand} \rightarrow (^5D_1, ^5D_0) \rightarrow {}^7F_{0\text{-}6}$.

The Förster and Dexter classic approaches have been applied to di-ureasils with longer polymer chains incorporating $Eu(CF_3SO_3)_3$ showing that the hybrid-to-Eu^{3+} energy transfer was also dominated by the exchange (Dexter) interaction (Chapter 3).

The detailed characterization of these energy transfer mechanisms through a quantitative assessment is expected to contribute to the development of novel siloxane-based hybrids characterized by interesting photonic features and high light emission efficiencies. Moreover, the reported procedure provides a theoretical scheme that might be useful in guiding the interpretation of experimental data and in the modelling of new organic-inorganic hybrids. The calculations of the energy transfer rates using this model may be extended to other organic-inorganic hybrids, particularly organized ones.

- *The key role played by Eu^{3+} in the modulation of hybrids' morphology and size*

Up to now ordered Ln^{3+}-doped organic/inorganic hybrids have been scarcely reported, despite their potential attraction as innovative photonic materials. The majority of the research has been indeed mainly focused on amorphous organic/inorganic hybrids incorporating either Ln^{3+} ionic salts or organic complexes, often including organic ligands, such as β-diketonates.

The organization of hybrid silicas depends critically on the synthetic procedure. In the case of the di-urea cross-linked alkylsilane precursor presented in Chapter 4 (Scheme 4.1) the use of HCl and a large excess of water induced the formation of a crystalline lamellar structure (**L12**). In contrast, when NH_4F catalyst was employed in EtOH medium under stoichiometric conditions an amorphous material (**A12**) has been obtained. The unique role played by the Eu^{3+} ions in the modulation of the morphology and size of the **Eu@A12** hybrids has been for the first time demonstrated *via* inhibition of the growth of the siloxane network formed through sol-gel reactions and urea-mediated supramolecular self-assembly (chapter 4). This process results in the formation of primary *ca.* 200 nm-long

plates which first tile up in a brick-like fashion that mimics the nacre structure, and then form fibres that ultimately self-assemble at the micrometer scale. Bundle to dumbbell shapes are produced under increasing Eu^{3+} amount. The voids between the fibres act as percolation channels for the release of ethanol.

Seeking at establishing a relationship between the long range organisation of hybrid materials and their physical properties, the photoluminescence features of lamellar **L12 and Eu@L12** with those of the corresponding amorphous hybrids, **A12** and **Eu@A12**, respectively, have been compared. This represented a unique opportunity to address the effect of the morphology on the hybrids' photoluminescence features as two systems with approximately the same Eu^{3+} concentration (1 %) but displaying completely different morphologies have been synthesise, based on the same precursor. Therefore, the Eu^{3+} photoluminescence has been used as local probe to sense morphological changes that were themselves induced by the cations incorporation into the hybrid framework.

The Eu^{3+}-containing hybrids are room temperature multi-wavelength emitters due to the convolution of the hybrids' emitting centres and the intra-$4f^6$ transitions. The incorporation of Eu^{3+} into the **L12** and **A12** hybrids induces a decrease in the absolute emission quantum yield values, 0.24±0.02 (**A12**) and 0.06±0.01 (**Eu@A12**), 0.14±0.01 (**L12**) and <0.01 (**Eu@L12**), supporting the existence of hybrid-to-Eu^{3+} energy transfer.

Despite the minor variations found in the $^5D_0$ quantum efficiency (16.3-19.2), number of water molecules (1.7-2.0) and experimental intensity Ω_2 parameter (8.9-10.1 × 10^{-20} cm^2) with the increase of the Eu^{3+} amount, the Eu^{3+} first coordination shell in the **Eu@L12** hybrids is very similar, including the oxygen atoms of the carbonyl group, the Cl atoms and water molecules (chapter 4).

For **Eu@A12** hybrids two distinct Eu^{3+} local sites (A and B) has been clearly discerned (chapter 4). Site A encompasses oxygen atoms of the carbonyl group, chloride atoms and water molecules and site B involves coordination to silanol groups. The relative contribution of the Eu^{3+} ions located in site B decreases as Eu^{3+} concentration increases reflecting the higher surface-to-volume ratio of the fibres-type morphology, relatively to that of the dumbbell structures. The increase of Eu^{3+} content will promote the approach of the fibres leading to the formation of dumbbell structures.

The next step of this work would be to extend this study to other organized/disorganized systems using different lanthanides in order clarify the mechanism

responsible for the formation of the new structures. It would be also interesting to study a wider range of Ln^{3+} concentrations (the intermediate ones between the structures and the effect of higher concentrations).

- *Efficient tunable blue and green light emission of bipyridine-based bridged silsesquioxanes for solid-state lighting*

For applications in photonics and solid state lighting it is necessary to develop hybrids featuring i) high quantum yield, ii) high brightness, iii) stability in time and under irradiation, iv) ability to be excited with cheap light sources, *eg.* long-wavelength UV (360-400 nm) and blue commercial light emitting diodes (LEDs). The development of new metal-free phosphors for long UV-to-visible conversion will contribute to trim down the use of Hg vapor plasma fluorescent lights (dropping the corresponding environmental contamination risks during disposal) and is crucial to improve the efficiency and light quality of LED-based solid-state lighting devices (composed by commercial UV LEDs plus appropriate phosphors).

In Chapter 5, two bpy-based hybrids derive from the same precursor has been prepared under slightly different synthetic conditions, namely sol-gel synthesis under nucleophilic catalysis by TBAF and NH_4F (termed as **H** and **M**, respectively). Their emission spectra consist of a broad band (380-660 nm) unequivocally ascribed (though photoluminescence spectroscopy in steady state and time resolved modes) to a superposition of three distinct components: i) bpy triplet state (*ca.* 2.74 eV), ii) electron-hole recombinations originated in the NH/C=O groups of the urea cross-linkages (*ca.* 2.41 eV) and iii) siliceous nanoclusters (*ca.* 2.91 eV). A maximum quantum yield value of 0.22±0.02 (**H**) and 0.18±0.02 (**M**) has been measured under excitation in the long-wavelength UV and blue spectral regions (360-440 nm). These quantum yield values are the highest ones reported so far for silsesquioxanes exciting in the long UV/blue spectral regions.

It has been demonstrated that **H** displays an easy tuneable blue-to-green emission (CIE colour coordinates from (0.18,0.22) to (0.20,0.30), respectively) by changing the excitation wavelength from 390 to 440 nm. Moreover, **H** can be efficiently excited using a commercial LED operating at 395 nm, placing bpy-bridged silsesquioxane as promising materials for photonics and solid state lighting.

The next step would be structuring these hybrids in order to obtain organized bpy-based bridged silsesquioxanes for solid-state lighting. Advantages of these emission features may also reflect on the design of smart lighting with appropriate colour balance to mimic the daylight, inducing, therefore, the appropriate circadian rhythm.

- *Lanthanide-containing bipyridine-based bridged silsesquioxanes*

Bpy is one of the most commonly used ligands in the design of highly luminescent Ln^{3+}-containing materials because of its intense absorption band in the near-UV and its ability to efficiently transfer energy onto the Ln^{3+} excited states (chapter 5). In this thesis, the photoluminescence of urea/bpy-based hybrids incorporating Eu^{3+}, Gd^{3+}, Tb^{3+}, and Eu^{3+}/Tb^{3+} (obtained under nucleophilic catalysis) has been detailed described. Prior to this thesis, M. Wong Chi Man and H. Li have been discussed (almost simultaneously) the catalytic (non-doped host) and photoluminescence (Eu^{3+}- and Tb^{3+}-containing hybrids) applications (chapter 5).

The hybrids are room temperature multi-wavelength emitters due to the convolution of the emission arising from the hybrid's emitting centres (urea cross-linkages, siliceous domains and bpy triplet) and the Eu^{3+} and/or Tb^{3+} intra-4f transitions. The emission colour is easily tuned across the CIE diagram from the blue to the red, orange or green areas, depending on the Ln^{3+} ions and the excitation wavelength. Upon 360 nm excitation, the (x,y) color coordinates of **M-EuTb** (0.32,0.29) have been estimated close to the white point (0.33, 0.33) making it, therefore, pure white light emitters. Bpy-to-Ln^{3+} and Tb^{3+}-to-Eu^{3+} energy transfer mechanisms have been qualitatively discussed. Due to the different bpy/Ln^{3+} ratios, the Eu^{3+}-local coordination in the Eu^{3+} and Eu^{3+}/Tb^{3+} co-doped samples slightly differ, as shown by the $^5D_0 \rightarrow {}^7F_{0\text{-}4}$ transition energies, $^5D_0$ lifetimes and intensity parameters, probably due to the different relative Eu^{3+} content in **M-Eu** and **M-EuTb** (4.98 and 2.68 % w/w, respectively). Although it could not be determined precisely, the Ln^{3+} coordination sphere has been figured out comprising bpy fragments, chloride anions and two water molecules.

The higher quantum yield values obtained for the Tb^{3+}-containing hybrids can be accounted for the higher resonance between the bpy-triplet state with the $^5D_4$ level of Tb^{3+} ions (1410 cm^{-1}), relatively to that found for the $^5D_1$ level of Eu^{3+} ions (2950 cm^{-1}). Under excitation via the urea cross-linkages and siliceous domains excited states (380-420 nm)

the quantum yield values are lower, independently of the selected excitation wavelength, 0.06 (**M-Eu**) and 0.08 (**M-Tb** and **M-EuTb**), pointing out the active role of bpy in the enhancement of the emission quantum yield values of Ln^{3+}-based hybrids.

Improvement of the hybrids' performances playing with the organic fragments will potentially allow applications as layers for active photonic devices. Work is underway along these lines.

As a final conclusion, this work contributed to a better understanding of the fundamental mechanisms behind energy transfer in organic/inorganic hybrids and of the unprecedent role of Eu^{3+} (acting simultaneously as a structuring agent and a local probe) in the modulation of the morphology and size of organized hybrids at different length scales. The better knowledge of these two aspects will certainly contribute to improve the performance of these materials in photonic devices (particularly in smart lighting) and to optimize their rational shaping, opening up, therefore, exciting new directions in the engineering of the attractive functionalities of organic/inorganic hybrids.

Appendix A - Experimental techniques

A.1 Photoluminescence

Luminescence is a general term which describes any non thermal processes in which energy is emitted from a material at a different wavelength from that at which it is absorbed.[1,2] The term broadly includes the commonly-used categories of fluorescence and phosphorescence. Fluorescence occurs where emission ceases almost immediately after withdrawal of the exciting source, whereas in phosphorescence the emission persists for some time after removal of that excitation.[1,2] The distinction between the so-called types of luminescence is somewhat arbitrary and confusing. Confusion is avoided by using the term luminescence, and specifying the activating energy as a descriptive prefix. For instance, bioluminescence is related with light emission from lived animals and plants, cathodoluminescence results from excitation by electrons, chemicaluminescence is the emission occurring during a chemical reaction, roentgenoluminescence is produced by X-rays, triboluminescence is ascribed to rubbing, mechanical action, and fracture, electroluminescence is the conversion of electrical energy into light, and photoluminescence results from excitation by photons.[1,2]

Photoluminescence requires the absorption of photons, the interaction mechanisms between the photon and the matter depend on the photon energy. When the photon energy of the incident radiation is lower than the energy difference between two electronic states, the photons are not really absorbed and the material is transparent to such radiation energy. For higher photons energy, absorption occurs and the valence electrons will make a transition between two electronic energy levels. The excess of energy will be dissipated through vibrational processes that occur throughout the near infrared (NIR) spectral region. Then, the excited atoms may return to the original level through radiative (with the spontaneous emission of a photon) and nonradiative transitions.[2]

Examples of radiative and nonradiative processes will be given considering the typical distribution of electronic levels in a molecule with two electrons (Fig. A.1). In the fundamental level the electrons in the same orbital have opposite spins ($s_1 = +1/2$ and $s_2 = -1/2$); so that the total spin ($S = s_1 + s_2$) is equal to zero. Thus, the fundamental state multiplicity ($M = 2S + 1$) is one, and the ground state is designated as singlet (S_0). After optical absorption, the electrons will be excited. If this transition does not involve spin inversion, the excited state is also a singlet (S_1), *i.e.* it has the same state multiplicity as the

ground level. However, if there is spin inversion, the two electrons have the same spin, S = 1 and 2S + 1 = 3, and the excited state is called triplet (T_1). It should be noted that such absorption involving a triplet state is forbidden by the spin selection rule: allowed transitions must involve the promotion of electrons without a change in their spin ($\Delta S = 0$). The relaxation of the spin selection rule can occur though strong spin-orbit coupling, which is for instance the case of rare earth ions. Fig. A.1 summarizes the typical radiative and nonradiative transitions within a molecule.[2]

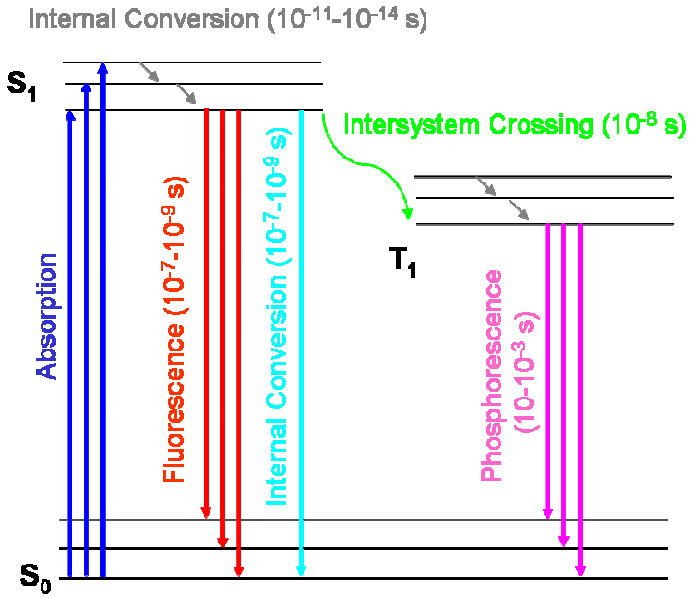

Figure A.1 Scheme of possible radiative and non-radiative transitions within a molecule. The S and T denote Singlet and Triplet states, respectively. The time-scale characteristic of each transition type is indicated in parenthesis.[2]

The internal conversion (an electron close to a vibrational energy level, relaxes to the ground state via transitions between vibrational energy levels giving off the excess energy to other molecules as heat, vibrational energy) and the intersystem crossing (the electron transition in an upper S_1 excited state to a lower energy level, such as T_1) are examples of nonradiative processes.[2]

The fluorescence (emission of a photon from S_1 to the vibrational states of S_0 occurring in a time scale of 10^{-10} to 10^{-7} s) and phosphorescence (emission of a photon from T_1 to the vibrational sates of S_0 and this process is much slower than fluorescence

because it involves two states of different multiplicity) are examples of radiative processes.[2]

The key elements for photoluminescence measurements are the excitation source, the monochromators and the detection device. Fig. A.2 schematizes a possible photoluminescence experimental set-up.[2,3]

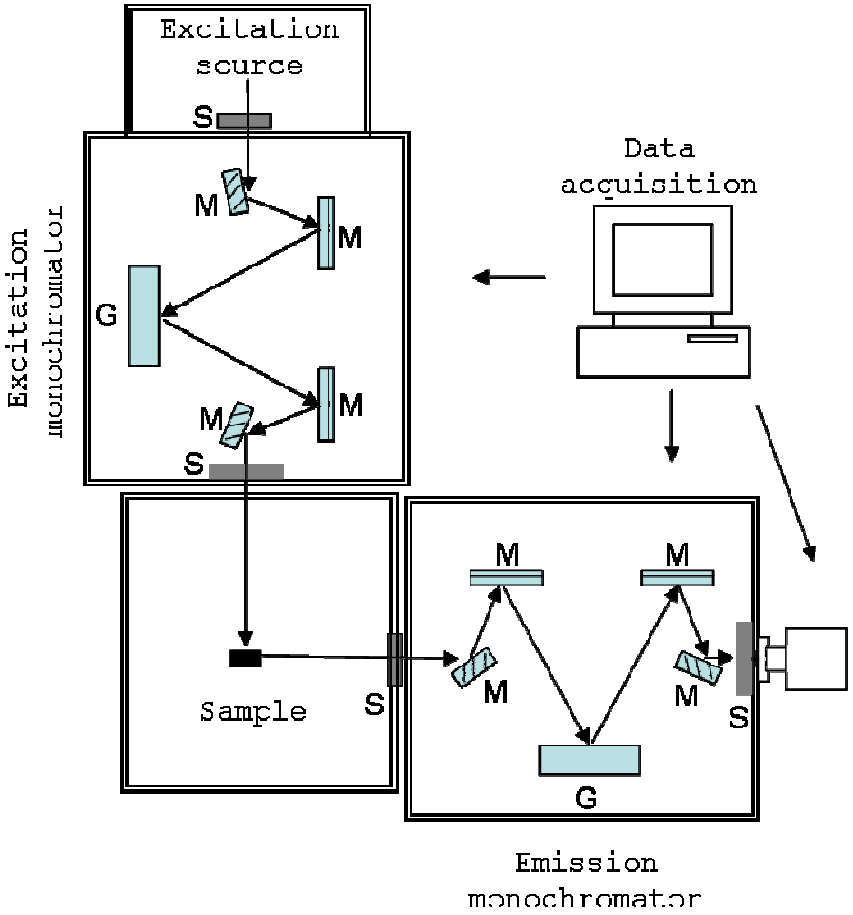

Figure A.2 Experimental layout for photoluminescence measurements. M, G, S and D stand for mirror, diffraction grating, slits and detector, respectively. The arrows indicate the light path. The layout presented for the mirrors and gratings inside each monochromator is called as Czerny–Turner configuration.[2]

Excitation source

Xenon arc lamp: This lamp provide a continuous light output from 250 to 700 nm and a number of sharp lines occurring near 450 nm and above 800 nm. Xenon arc lamps emit a continuum of light as a result of the recombination of electrons with ionized Xe atoms. These ions are generated by collisions of Xe atoms with the electrons which flow across the arc. Complete separation of the electrons from the atoms yields the continuous emission. Xe atoms which are in excited states but not ionized yield lines rather than broad emission bands. The peaks near 450 nm are due to these excited states. The output intensity drops rapidly below 280 nm. Furthermore, many Xe lamps are classified as being ozone free, meaning that their operation does not generate ozone in the surrounding air. The quartz envelope used in such ozone free lamps does not transmit light with wavelengths shorter than 250 nm, and the output of such lamps decreases rapidly with decreasing wavelength. [3]

Monochromators

Monochromators are used to disperse polychromatic light into the various wavelengths. This dispersion can be accomplished using diffraction gratings. The performance specifications of a monochromator include the dispersion, the efficiency, and the stray light levels. The dispersion is usually given in nanometres per millimetre, where the slit width is expressed in millimetres. In selecting a monochromator for fluorescence spectroscopy, one looks for low stray light levels to avoid problems due to scattered stray light. By stray light we mean light transmitted by the monochromator at wavelengths outside of the chosen wavelength and bandpass. In addition, monochromators are chosen for high efficiency to maximize the ability to detect low light levels. The slit widths are generally variable, and a typical monochromator will have both an entrance and an exit slit. The light intensity which passes through a monochromator is approximately proportional to the square of the slit width. Larger slit widths yield increased signal levels, and therefore higher signal-to-noise ratios. Smaller slit widths yield higher resolution, but at the expense of light intensity.[4] However, if the entrance slit of the excitation monochromator is already wide enough to accept the focused image of the arc, then the intensity will not be increased

significantly with wider slit widths. Monochromators may have planar or concave gratings. Planar gratings are usually produced mechanically and may contain imperfections in some of the grooves. Concave gratings are usually produced by holographic and photoresist methods and imperfections are rare. Imperfections of the gratings are the major source of stray light transmission by the monochromators and of ghost images from the grating.[3,4]

The most common arrangement for the monochromator is known as Czerny-Turner monochromator. This design involves a plane grating illuminated by collimated light. The incident light is usually diverging from a source or slit, and collimated by a concave mirror, and the diffracted light is focused by a second concave mirror, Fig. A.3.[4]

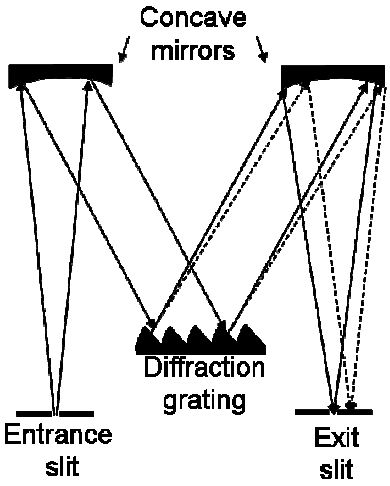

Figure A.3 The Czerny-Turner monochromator scheme.

The spectrum is scanned by rotating the grating; this moves the grating normal relative to the incident and diffracted beams, which changes the wavelength diffracted toward the second mirror. Since the light incident on and diffracted by the grating is collimated, the spectrum remains at focus at the exit slit for each wavelength, since only the grating can introduce wavelength-dependent focusing properties.

A diffraction grating consists of a large number of evenly spaced parallel lines ruled on a reflecting surface. The number of lines varies from 300 to 3600 lines/mm. The monochromatic parallel beams 1 and 2 are incident on the surface of the diffraction grating with an angle *i* relatively to the normal of the surface, Fig. A.4. The maximum for constructive interference occurs for an angle of reflection *r*. The beam 2 travels a bigger

distance than the beam 1 and the difference between the two paths is equal to *(CB+BD)*. For constructive interference to occur this difference must be equal to $n\lambda$, where *n* is a integer and designates the diffraction order. Taking into account that the angle *CAB* is equal to the angle *i* and that the angle *DAB* is equal to the angle *r* and also the trigonometric relations, the following relation is obtained:

$$n\lambda = d(\sin I + \sin r), \text{ with } n = 0, \pm 1, \pm 2, \ldots \quad \text{(A.1)}$$

where *d* is the distance between two consecutive lines.

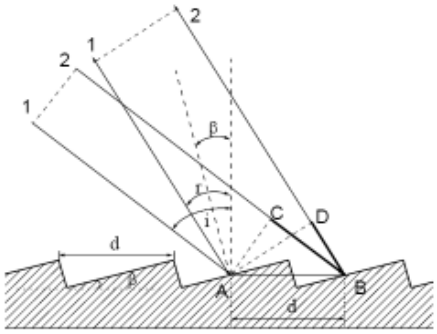

Figure A.4 Section of a grating surface showing the optical paths between the incident and diffracted beam.

The angular dispersion of the diffraction grating can be obtained by differentiating the equation 2.1 with the incident angle i fixed:

$$\frac{dr}{d\lambda} = \frac{n}{d\cos r}(rad/nm) \quad \text{(A.2)}$$

The linear dispersion is the product of the equation 2.2 with the focal length *f*:

$$D = f\frac{dr}{d\lambda}(mm/nm) \quad \text{(A.3)}$$

The resolvance or "chromatic resolving power" for a device used to separate the wavelengths of light is defined as:

$$R = \frac{\lambda}{\Delta\lambda} \tag{A.4}$$

The limit of resolution is determined by the Rayleigh criterion as applied to the diffraction maxima, i.e., two wavelengths are just resolved when the maximum of one lies at the first minimum of the other. Since the space between maxima for *M* slits is broken up into *M*-2 subsidiary maxima, the distance to the first minimum is essentially 1/*M* times the separation of the main maxima. This leads to a resolving power for a grating of:[4]

$$R = \frac{\lambda}{\Delta\lambda} = mM \tag{A.5}$$

where *M* is the total number of slits illuminated and *m* is the order of the diffraction. In experiments where very weak signals are detected, the efficiency (the light throughput becomes very important. To obtain high efficiency in a selected wavelength range, gratings are ruled with the grooves at a specific angle with the grating surface, θ_b, known as the blaze angle. The intensity of the diffracted light is the highest in the direction for which the groove acts as a mirror (angle of reflection from the groove surface). The blaze angle is related to the blaze wavelength by:

$$n\lambda_b = 2d \sin\theta_b \tag{A.6}$$

Detectors

Photomultiplier tube (PMT): is a single channel detector with extremely high sensitivity. A photomultiplier tube is a vacuum tube consisting of an input window, a photocathode, focussing electrodes, an electron multiplier and an anode usually sealed into an evacuated glass tube, in Fig. A.5 is presented a schematic construction of a photomultiplier tube.[5]

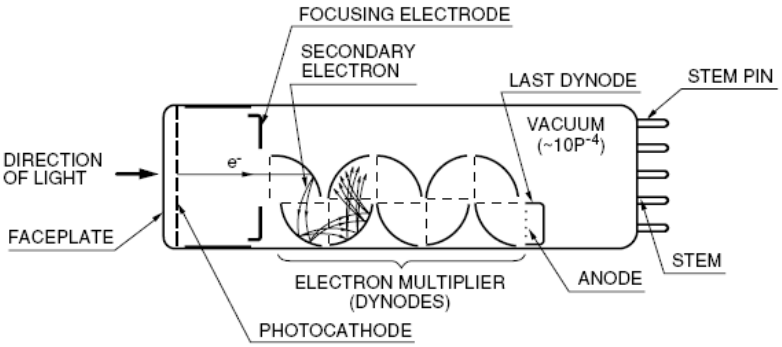

Figure A.5 General scheme of a photomultiplier tube.[5]

An incident photon hits the photocathode and creates an electron (photoelectric effect). The high voltage inside the PMT (typically 2000 V) accelerates this first electron until it hits the first dynode. Due to the high kinetic energy of the first electron, several electrons are emitted from the first dynode and are accelerated towards the second dynode. In this way, the cascade of dynodes enhances the cascade of electrons by creating an electron avalanche. The final electronic signal can be directly detected. Depending on the different required spectral ranges, photomultipliers with different photocathode's can be used. Multi-alkali compounds are widely used. Another choice is semiconductors like GaAs or InGaAs. PMTs for infrared, visible or the UV range of light are available. [5]

Photodiode: Photodiodes are typically semiconducting devices. They are usually operated in a reverse-biased mode where the change of a small reverse current due to light-induced carrier generation is measured. The incident light is absorbed in the depletion layer of a p-n junction (p-i-n diode), where it creates an electron hole pair. Depending on the spectral range of the experiment, different photodiodes for the infrared, visible, or UV range of light can be used. A photodiode is a single channel detector. By combining several (*ca.* 1000) diodes in one array (photodiode-array), photodiodes can be used as a multichannel detector.

Quantum yields

The most common way of measuring the quantum yield is by using an integrating sphere or alternative methods involving the use of white reflecting standards or phosphor standards.

Integrating sphere: The used system encompasses an excitation source, a monochromator, a integrating sphere and a detector. The inside of the sphere is coated with a highly reflective material (e.g. BaSO4). The quantum yield can be determined with a experimental set-up such as the one represented in Fig. A.6 by measuring the emission spectra of a sample and of a reference, where the reference is an empty container, and the sample is a container including a target sample. If the sample absorbs the excitation light and radiates, the excitation light intensity for the sample decreases compared with that for the reference. Since the difference in the excitation light intensity between the reference and the sample corresponds to the number of photons absorbed by the sample, and the photoluminescence intensity corresponds to the number of photons emitted from the sample, the quantum yield is calculated by the reason on both.

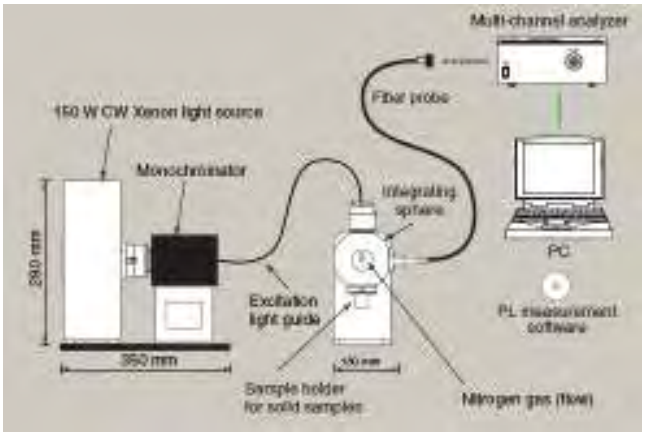

Figure A.6 General scheme of an integrating sphere.[6]

A.2.1 Experimental conditions used in this thesis

Emission, excitation, time-resolved emission, emission decay curves

Steady-state emission and excitation spectra, time-resolved emission, emission spectra decay curves were measured at temperatures between 14 and 300 K on a Fluorolog-3 Model FL3-2T spectrometer. The double grating excitation monochromator (Triax 320) is fitted with 1200 grooves mm^{-1} gratings blazed at 330 nm (reciprocal linear dispersion = 2.1 nm/mm). The single grating emission monochromator is fitted with a 1200 grooves mm^{-1} emission grating blazed at 500 nm (reciprocal linear dispersion = 2.64 nm/mm). The photomultiplier tube is a R928 model from Hamamatsu. The source is either a 450 W xenon arc lamp (steady state) or a pulsed Xe-Hg lamp with 6 ms pulse at half width and 20–30 μs tail. The set-up used for the measurements is displayed in Fig. A8. Low temperature measurements were made using a helium closed-cycle cryostat (model APD *Cryogenics*-HC2).

The emission spectrum is acquired by exciting the sample with an absorbed wavelength, usually the maximum intensity absorption (or excitation) peak, and the emission monochromator scans the luminescence within a wavelength interval. The most important parameters are i) the excitation wavelength and ii) the slits width (must be a compromised between resolution and signal, as explained previously). Emission spectra were also corrected for the spectral response of the monochromators and the detector using typical correction spectra provided by the manufacturer.

The excitation spectrum is measured by setting the emission monochromator fixed in a given emission wavelength (for instance the one corresponding to the maximum of the emission spectrum). The excitation monochromator is then scanned in a given wavelength interval and the luminescence intensity corresponding to the monitored emission wavelength is measured. The most important parameters are i) the monitoring wavelength and the ii) slits width. Excitation spectra were corrected from 240 to 600 nm for the spectral distribution of the lamp intensity using a silicon photodiode reference detector.

The lifetime measurement is made by exciting the sample with a pulse excitation source and for a certain emission wavelength (for instance, the maximum intensity of the emission time-resolved spectrum) the detection is made after successive increasing delay times. For the lifetime the most important experimental parameters are: i) the initial detector delay relative to the excitation pulse (*ID*); ii) the maximum delay, which allows the emission intensity to decay to the baseline (*MD*); iii) the detection time window (*W*) and iv) the number of, and time between, excitation flashes (*TBF*). The initial delay was set at the minimum value of 0.05 ms. The maximum delay was determined by estimating the time required for the intensity, *I*, to reach ~0.1 % of the initial emission intensity, I_0 from: $I/I_0 = 0.001 = e^{-t/\tau}$, where τ is the lifetime and *t* is the maximum delay. The number of flashes was adjusted to achieve emission intensity, of at least 2 or 3 orders of magnitude more than the level of noise. The time between flashes (*TBF*) was governed by the relationship $TBF = ID + MD + W + 20.00$ ms and has a minimum value of 40.00 ms. The sample window was adjusted in accordance with the observed sample lifetime. Lifetime measurements were performed using fixed excitation and emission wavelengths, specific for the sample under study.

The time resolved measurement is made by exciting the sample with a pulse excitation source and recording the emission after a certain time (initial delay). For time resolved emission the most important experimental parameters are: i) the initial detector delay relative to the excitation pulse (*ID*); ii) the excitation wavelength; iii) the detection time window (*W*) and iv) the number of, and time between, excitation flashes (*TBF*).

Quantum yields

The quantum yield measurements were measured at room temperature using a Quantum Yield Measurement System C9920-02 from Hamamatsu with a 150 W Xenon lamp coupled to a monochromator for wavelength discrimination, an integrating sphere as sample chamber and a multi channel analyzer for signal detection and the setup presented in Fig. A.7. The experimental error is 10%.Three measurements were carried out for each sample, so that the presented quantum yield value corresponds to the arithmetic mean value.

CIE *xy* colour coordinates

The *XYZ* tristimulus values were calculated from corrected emission spectra at 5 nm intervals using expression 2.30. The *XYZ* values were converted to corresponding *xy* colour coordinates using expression 2.31.

A.2 Fourier Transform infrared (FT-IR)

Fourier Transform infrared (FT-IR) spectra of powdered samples suspended in KBr pallets were acquired at room temperature between 400 and 4000 cm^{-1} using a Mattson Mod 7000 spectrometer. The solid samples (2 mg) were finely ground, mixed with approximately 175 mg of dried potassium bromide (Merck, spectroscopic grade) and pressed into pellets. Prior to recording the spectra, the pellets were first dried under vacuum at 50–60 ^{0}C in order to reduce the levels of adsorbed water. To evaluate FT-IR band envelopes the iterative least squares curve-fitting procedure of the PeakFit® software was used extensively. The best fit of the experimental data was sought by employing Voigt band shapes and a linear baseline correction was employed. The standard errors of the curve fitting procedure were less then 0.03.

A.3 Nuclear Magnetic resonance

^{29}Si magic-angle spinning (MAS) nuclear magnetic resonance (NMR) and ^{13}C cross-polarization (CP) MAS NMR spectra were collected by Dr. Isabel Martins (Chemistry Department, University of Aveiro, Portugal) recorded on a Bruker Avance 400 (9.4 T) spectrometer at 79.49 and 100.62 MHz, respectively. ^{29}Si MAS NMR spectra were recorded with 2 μs (θ~30º) rf pulses, a recycle delay of 60 s and at a 5.0 kHz spinning rate. ^{13}C CP/MAS NMR spectra were recorded with 4 μs 1H 90º pulse, 2 ms contact time, a recycle delay of 4 s and at a spinning rate of 8 kHz. For both ^{13}C and ^{29}Si, chemical shifts are quoted in ppm from tetramethylsilane (TMS).

A.4 X-ray Diffraction (XRD) and Small Angle X-ray Sctarering (SAXS)

The XRD diffraction patterns of the di-ureasil model compounds (chapter 3), **Eu@L12** and **Eu@A12** hybrids (chapter 4) were collected by Dr. Rosário Soares (CICECO, University of Aveiro, Portugal) using a Philips X'Pert MPD powder X-ray diffractometer. The samples were exposed to the CuK_α radiation (1.54 Å) in a 2θ range between 1 and 60º with a step of 0.05 and resolution of 40 s per step.

The XRD diffraction of the bipyridine based hybrids (chapter 5) were collected by Dr. Philippe Dieudonné (Laboratoire des Colloïdes, Verres et Nanomatériaux, Université de Montpellier II, France) and were carried out in glass capillaries (1.5 mm in diameter) with a transmission configuration. A copper rotating anode X-ray source (4 kW) with a multilayer focusing "Osmic" monochromator giving high flux (10^8 photons s^{-1}) and punctual colimation was employed. $\lambda_{k\alpha}$= 1.542 Å. An "Image plate" 2D detector was used. The diffraction curves were obtained, giving diffracted intensity as a function of the wave vector q. The diffracted intensity was corrected by exposition time, transmission and intensity background coming from diffusion by an empty capillary.

The low *q* region (for the **L12** and **Eu@L12** hybrids) was recorded at the National Synchrotron Light Laboratory (LNLS), Campinas (Brazil), using a SAXS beam line which provides a monochromatic (λ=0.1488 nm) and horizontally focused beam. The parasitic scattering intensity from air, slits, and windows was subtracted from the total intensity. The scattering intensity was also normalized by taking into account the varying intensity of the direct X-ray beam and sample absorption. The integral breadth of the first order diffraction peak (*B*) observed in the SAXS pattern was corrected from the instrumental broadening (*b*) by using a well crystalline sample as a standard reference of experimental aberrations. The corrected integral breadth was estimated from $\beta^2 = B^2 - b^2$.

A.5 Scanning Electron Microscopy (SEM)

The SEM images were obtained with a JEOL 6300F microscope after carbon metallization by Dr. Didier Cot (Institut Européen des Membranes, Montpellier France) and a Hitachi S-4500 apparatus after platinum metallization by Dr. Marta Ferro (CICECO, University of Aveiro, Portugal). X-ray microanalysis was performed for studying the

distribution of chemical composition (elemental maps) using a Bruker AXS Quantax 400 energy dispersive X-ray spectrometry system (EDS) connected to a Hitachi SU-70 FEG-SEM apparatus.

A.6 Elemental analysis

The Eu and Si content was obtained by ICP-OES (inductively coupled plasma optical emission spectroscopy) analysis on an Jobin Yvon Activa instrument with a glass concentric nebulizer. For the Eu analysis the samples were digested under microwaves with 6 mL of HCl, 2 mL of HNO_3 and 1 mL of HF at 150 ^{0}C and dried. The F- ion was removed by two successive auditions of 5 mL of HCl after the evaporation. The solution was recovered in 10 mL of HNO_3 20% and diluted. For the Si analysis the samples were digested under microwaves with 6 mL of HCl, 2 mL of HNO_3 and 1 mL of HF and diluted. The method is accurate within 10 %. The measurements were perfomed by Dr Lina Carvalho (CICECO, University of Aveiro, Portugal).

Elemental analysis for C, H and N were performed with a CHNS-932 Elemental analyser with standard combustion conditions and handling of the samples at air at the Microanalysis Laboratory of the University of Aveiro (Department of Chemistry).

A.7 Atomic Force Microscopy (AFM)

The AFM images were collected by Andreia Macedo (CICECO, University of Aveiro, Portugal) and recorded in a Nanoscope IIIA equipment, in tapping mode using a super sharp silicon tip, curvature radius 10 nm, and frequency resonance equals to 350 kHz. The images were deconvoluted considering the probe's shape using the *WSXM* software assuming a normalised tip with a radius of 10 nm. In order to improve the images quality, flattening and elimination of line noise tools and a Gaussian filter were used.

A.8 References

1. J.-C. G. Bünnzli, in *Lanthanide Probes in Life, Chemical and Earth Sciences, Theory and Practice*, eds. G. R. Choppin and J.-C. G. Bünnzli, Elsevier, Amsterdam, Netherlands, 1989.
2. L. D. Carlos, R. A. S. Ferreira and V. de Zea Bermudez, in *Hybrid Materials*, ed. G. Kickelbic, Wiley-VCH, Weinheim, 2007.
3. J. R. Lakiwicz, *Principles of Fuorescence Spectroscopy*, Kluwer Academic/Plenum Publishers, New York, 1999.
4. *Diffraction Grating Handbook*, Richardson Grating Laboratory, New York, 2002.
5. *Photomultiplier Tubes, Basics and Applications*, Hamamatsu Photonics K.K., 2006.
6. *Absolute PL Quantum Yield Measurement System (with Monochromatic Light Source) Instruction Manual (C9920-02)*, Hamamatsu Photonics, K.K, 2007.

Appendix B - Résumé en français

Le terme ‘matériaux hybrides’ est utilisé pour désigner différents systèmes combinant des unités organiques et inorganiques, que ce soient des composés de coordination hautement ordonnés, ou bien des composés amorphes, et qu’il y ait ou non des interactions fortes entre les unités organiques et inorganiques.[1] La définition la plus large est la suivante : Un matériau hybride organique/inorganique comporte des entités des deux types, mélangées à l’échelle moléculaire. Une définition plus précise fait la distinction entre deux classes de matériaux selon les interactions entre les fragments organiques et inorganiques. Les hybrides de type I (Classe I) sont ceux qui ont les plus faibles interactions entre les deux phases, comme les forces de Van der Waals, les liaisons hydrogène, ou des interactions électrostatiques faibles. Les composés de type II (Classe II) sont ceux où l’on a des interactions chimiques fortes entre les deux composants, comme les liaisons covalentes.[2]

Le choix de l’unité organique de ces polymères est habituellement guidé principalement par leurs comportements mécaniques ou thermiques. Cependant, d’autres propriétés comme l’équilibre entre les comportements hydrophiles ou hydrophobe, la stabilité chimique, la bio-compatibilité, les propriétés optiques et/ou électroniques et les fonctionalités chimiques (par exemple la solvatation, la mouillabilité, les effets templates) sont aussi considérées. La contrepartie inorganique permet dans beaucoup de cas une mise en forme facile des matériaux, et un meilleur procédé de fabrication. Les composants inorganiques (comme la silice, les oxydes de métaux de transition, les phosphates métalliques, certaines argiles, les nano-métaux, et les chalcogénures de métaux) confèrent des stabilités thermique et mécanique, mais aussi des propriétés nouvelles, qui dépendent de la nature chimique, de la structure, de la taille et de la cristallinité de la phase inorganique. Ainsi, le composant inorganique peut transférer ou améliorer les propriétés magnétiques, électroniques ou d’oxydo-réduction, la densité, l’indice de réfraction.[2-5]

Le procédé sol-gel, qui est principalement basé sur des réactions de polymérisation inorganique est une voie de synthèse qui était initialement utilisée pour la préparation de matériaux inorganiques comme les verres ou les céramiques.[6] Son avantage principale réside dans sa mise en œuvre à basse température, compatibles avec les fragments organiques, donnant ainsi des opportunités uniques pour créer des matériaux hybrides organiques-inorganiques purs, de composition bien définie grâce à l’incorporation de molécules organiques de faible masse, ou de polymères ou oligomères organiques au sein

de réseaux inorganiques. Il s'est ainsi avéré comme une méthode prometteuse et douce pour concevoir des hybrides organiques-inorganiques aux propriétés contrôlables.[4,6,7]

Le procédé sol-gel est basé sur deux réactions distinctes : l'hydrolyse et la condensation. La première réaction est appelée hydrolyse car un groupe hydroxyle remplace un fragment alcoxy, comme indiqué dans l'équation suivante :

$$Si(OR)_4 + H_2O \rightarrow HO\text{-}Si(OR)_3 + ROH$$

Selon le catalyseur et la quantité d'eau ajoutés, l'hydrolyse peut être complète (tous les fragments alcoxy OR sont remplacés par des hydroxy OH) :

$$Si(OR)_4 + 4H_2O \rightarrow Si(OH)_4 + 4ROH$$

Cette réaction peut aussi s'arrêter avec un groupe silylé partiellement hydrolysé, $Si(OR)_{4-n}(OH)_n$. Au cours d'une réaction de condensation, deux molécules partiellement hydrolysées peuvent ensuite se lier selon l'équation suivante:

$$(RO)_3Si\text{-}OH + HO\text{-}Si(OR)_3 \rightarrow (RO)_3Si\text{-}O\text{-}Si(OR)_3 + H_2O$$

Ou bien

$$(RO)_3Si\text{-}OR + HO\text{-}Si(OR)_3 \rightarrow (RO)_3Si\text{-}O\text{-}Si(OR)_3 + ROH$$

Par définition, l'étape de condensation libère une petite molécule, comme de l'eau ou un alcool. La poursuite de ce type de réaction permet de créer des molécules silylées de plus en plus grandes par un processus de polymérisation. Un polymère (textuellement 'plusieurs parties') est une macromolécule formée par des centaines d'unités appelées monomères, et qui sont capables de former chacun au moins deux liaisons.[6]

Si un monomère peut former plus de deux liaisons, alors il n'y a plus de limite dans la taille de la macromolécule qui peut être formée. Si une molécule atteint des dimensions macroscopiques telles qu'elle s'étend sur l'ensemble de la solution, cette substance peut alors former un gel avec le solvant. Le point de gélification est le temps (ou degré de

réaction) au bout duquel les liaisons qui permettent de relier ensemble des parties dans tout l'espace du sol sont formées. Ainsi, un gel est une substance qui contient un squelette solide continu qui renferme une phase liquide. Le processus de gélification commence avec la formation d'agrégats fractaux qui grossissent jusqu'à se rencontrer, puis ces clusters se lient à leur tour comme décrit par la théorie de percolation. C'est-à-dire que près du point de gélification, des liaisons se forment aléatoirement entre les clusters presque stationnaires (polymères ou agrégats de particules), les liant ensemble pour former un réseau. Le point de gel correspond à un seuil de percolation, quand un seul cluster (appelé le spanning cluster) s'étendant sur l'ensemble du sol est constitué. Ce spanning cluster coexiste avec une phase stationnaire qui contient de nombreux petits clusters qui graduellement s'attachent au réseau principal. La gélification peut avoir lieu après que le sol soit moulé dans un cadre, auquel cas il est possible de faire des objets de forme contrôlée. De plus, la formation de liaisons ne s'arrête pas au point de gélification: dans un premier temps, le réseau n'est pas figé, aussi des petits clusters peuvent toujours bouger et se rencontrer, permettant ainsi la poursuite de la condensation. De plus, il y a toujours un sol au sein du réseau du gel, et ces polymères ou particules plus petits continuent à se lier au réseau principal. Le terme de vieillissement s'applique au processus de modification de la structure et des propriétés après la gélification.

L'eau est nécessaire pour les réactions d'hydrolyse des alcoxydes de silicium. Cependant, comme ces composés ne sont pas miscibles avec l'eau, il est nécessaire d'ajouter un solvant (généralement l'éthanol, le méthanol, le THF ou le N,N-diméthylformamide) pour obtenir une solution initialement homogène. L'alcool agit non seulement comme solvant, mais participe aussi dans les réactions. L'eau est non seulement un réactif pour les réactions d'hydrolyse mais elle est aussi produite au cours des réactions de condensation. Un ratio molaire de 2 entre l'eau et un tétraalcoxyde de silicium est théoriquement suffisant pour avoir une réaction complète. Cependant, dans la plupart des conditions utilisées l'hydrolyse et la condensation ont lieu simultanément. L'hydrolyse est incomplète même pour des ratios $H_2O/Si(OR)_4$ compris entre 2 et 10. L'hydrolyse peut être catalysée par des acides ou des bases. Les acides minéraux ou l'ammoniaque sont souvent utilisés comme catalyseurs des réactions sol-gel. Aussi, la structure et la morphologie du réseau final dépendent fortement de la nature du catalyseur et en particulier du pH du milieu réactionnel.[4,6]

La nanostructuration et le contrôle de la morphologie dans les hybrides sont d'un grand intérêt dans la conception de matériaux fonctionnels. Au cours des dix dernières années, l'organisation et la texturation des réseaux hybrides ont été réalisées grâce à l'utilisation d'agents structurants, principalement des tensio-actifs.[8-10] Le succès de cette stratégie est clairement à mettre en relation avec la possibilité de contrôler et de modifier les interfaces hybrides.

Des hybrides structurés peuvent aussi être obtenus par synthèse sol-gel directe sans utiliser d'agent structurant externe. L'hydrolyse contrôlée de précurseurs d'hybrides organiques-inorganiques possédant des chaînes alkyle terminales et longues a permis la synthèse de structures poreuses périodiques.[11,12] Dans le cas des hybrides possédant des fragments organiques pontants (silsesquioxanes pontés), les efforts ont principalement porté sur l'amélioration de l'ordre structurel du composite résultant, à l'aide d'interactions intermoléculaires et sous l'effet de la forme et de la structure des fragments organiques pontants.[13,14] Des solides hybrides biréfringents avec une organisation anisotropique et un caractère lamellaire ont été obtenus grâce aux interactions de Van der Waals ou π-π entre les fragments organiques.[15] L'évolution de l'ordre structural a aussi été étudié en fonction de la nature chimique et de la géométrie des unités organiques (unités organiques rigides,[15] coudées,[16] planes,[17] ou tetrahédriques[18]). Des solides hautement cristallins ont été obtenus en utilisant des précurseurs d'hybrides avec des chaînes flexibles de type hexyle ou octyle comme unités organiques pontantes, et où seulement des interactions faibles de type Van der Waals existent entre les chaînes alkyles.[19] Les interactions intermoléculaires entre les fragments organiques comme les liaisons H entre des groupes urée et/ou des interactions entre des chaînes alkyles permettent une voie d'accès élégante pour auto-diriger la structuration des silsesquioxanes pontés.[20] Il semble que la capacité des précurseurs moléculaires à s'auto-assembler grâce à des liaisons Hydrogène entre les fragments urée ou par des liaisons faibles de type Van der Waals au cours du processus d'hydrolyse-polycondensation favorise la structuration des matériaux, conduisant à des structures hélicoïdales[21] ou lamellaires.[22,23]

La grande quantité de combinaisons possibles entre les composants organiques et inorganiques a conduit à envisager un domaine très large d'applications pour les hybrides,[1,2] comme dans l'électronique,[24,25] la catalyse,[26-28] la détection,[29,30] les dispositifs bio-médicaux (relargage contrôlé de principes actifs,[31] développement d'os artificiels[32]),

les membranes[33,34] l'optique[35-43] (matériaux à haut indice de réfraction[44] conception de lentilles ophtalmologiques, de filtres, d'adhésifs optiques, de revêtements hautement réfléchissants ou antiréflection[45]). Au cours des dernières années, l'utilisation des hybrides a été de plus en plus largement adoptée pour le développement de matrices à base de silice et à bas coût possédant des propriétés photoniques (par exemple pour des interrupteurs optiques ou le stockage de données,[46] grande efficacité laser et photostabilité,[47] guides d'onde photogravables pour l'optique intégrée,[48-50] détecteurs pour fibre optiques[51,52]…).
Le silicium, qui est le semiconducteur principalement utilisé dans les circuits intégrés en microélectronique, était considéré comme non applicable en optoélectronique à cause de sa bande interdite électronique indirecte (qui limite de fait son efficacité comme émetteur de lumière). Mais depuis le rapport par Canham[53] en 1990 qui démontrait une émission efficace et contrôlable à température ambiante par du silicium poreux, l'intérêt dans les composants luminescents à base de silicium a connu un essor considérable. Le développement de systèmes optiques efficaces et compatibles avec le silicium, permettant à des éléments optiques ou électroniques d'être complètement intégrés aurait un impact important dans les domaines de l'affichage, de la communication, des ordinateurs et des technologies liées. Les hybrides organiques-inorganiques basés sur les réseaux siloxane pourraient permettre une telle intégration entre l'optique et l'électronique.

Récemment, une série d'articles de revue sur les applications en photonique des hybrides à base de siloxanes a été publiée.[35,36,43] Plusieurs hybrides stables et photoluminescents dans le blanc, contenant des fonctions amine ou amide, et ne contenant pas de centre métallique ont été présentés. Parmi ceux-ci, on trouve ceux obtenus à partir d'aminopropyltriéthoxysilane (APTES), ou de 3-glycidyloxypropyltriméthoxysilane (GPTES),[54-59] ceux obtenus à partir de précurseurs contenant des groupes urée [NHC(=O)NH], uréthane [NHC(=O)O], ou amide [NHC(=O)] appelés respectivement di-ureasils,[39,60-64] di-urethanesils,[65,66] et di-amidosils,[67] et ceux obtenus à partir de structures en couche de type perovskite (APTES-$PbCl_4$).[68] L'hybride à base d'APTES et d'acide formique est un des phosphores les plus efficaces qui soit connu parmi ceux qui ne contiennent pas de centre métallique, avec un rendement quantique externe de photoluminescence de 35 ± 10 %.[54] L'analogue APTES-acide acétique possède deux voies distinctes d'émission, avec des rendements quantiques compris entre 12 et 20 %;[55] des valeurs similaires ont été rapportées pour les di-ureasils, di-urethanesils et di-

amidosils.[63,64,66,67] L'intérêt technologique potentiel de ces hybrides fonctionalisés à base d'amines ou d'amides pour la fabrication de plusieurs types de systèmes nanostructurés comme des émetteurs efficaces de lumière blanche à température ambiante a été démontré.[39,60-65,67,69] Cette photoluminescence très efficace (rendements quantiques supérieurs à ceux rapportés pour le silicium poreux amorphe[70] et similaires à ceux rapportés pour les polymères conjugués les plus efficaces[71]), résulte de la convolution de l'émission provenant des groupes C=O/NH des urées, uréthane ou amide et de celle provenant des recombinaisons électrons/trous qui ont lieu dans les nanoclusters de siloxane.

Les ions lanthanides, et en particulier les trivalents Ln^{3+}, sont très importants en photonique à cause de leurs propriétés photophysiques singulières[72], spécialement en ce qui concerne leurs applications comme phosphores,[72-74] la génération et l'amplification de la lumière dans les lasers (par exemple Nd^{3+} dans les lasers YAG [Yttrium-Aluminium Garnet][75]), et comme amplificateurs optiques (avec, par exemple les fibres optiques dopées à l'erbium Er^{3+} : EDFAs[76,77]). En tant qu'acides de Pearson durs, leur interaction avec le champ de ligand est principalement décrite par des liaisons chimiques de type ionique. Des hautes coordinances et des interactions fortes avec les bases dures de Pearson sont leurs principales caractéristiques chimiques. Les transitions 4*f*-4*f*, interdites par parité et par spin, sont observées avec des coefficients d'extinction molaires ε (ou sections efficaces d'absorption σ_{ABS}) typiquement inférieurs à 10 $L.mol^{-1}.cm^{-1}$ (ou $\sigma_{ABS} < 4.10^{-20}$ cm^2), en comparaison avec les valeurs 10 fois plus élevées dans le cas des transitions 3d-3d ou 100 fois plus intenses pour les transitions de transferts de charge ligands vers métal (LMCT). De hauts rendements quantiques de fluorescence peuvent être observés, avec des bandes d'émissions très fines, des états excités à longue durée de vie et des transitions optiques pouvant se situer dans des régions spectrales comprises entre l'UV et le proche infra-rouge. Des niveaux d'énergie plus hauts peuvent être impliqués dans les processus d'excitation de ceux de plus basse énergie, qui sont alors peuplés par des transitions non-radiatives. Aussi, des déplacements de Stokes importants sont observés. De plus, les transitions 4f-4f sont ultrasensibles, ce qui les rend intéressants à la fois pour des analyses biologiques in-vitro et in-vivo,[73,74,78] et la faible toxicité des ions Ln^{3+} (en comparaison avec celle des métaux lourds), en particulier à l'état de complexes[79] et leur haute densité et susceptibilité magnétique permettent l'utilisation des systèmes à base de lanthanide en imagerie de

résonance multimodale, et thérapie anticancéreuse par les radioisotopes.[80,81] Comme nous l'avons déjà vu, la photoexcitation directe des ions lanthanides n'est pas très efficace, ce qui limite la quantité de lumière émise. Cependant, ce point peut-être amélioré avec une augmentation conséquente de l'intensité de luminescence des lanthanides grâce à la conception de complexes de lanthanides dans lesquels les ligands possèdent des chromophores organiques liés au centre métallique 4f. Ces molécules peuvent aussi protéger l'ion métallique des interactions qui provoqueraient des desexcitations non-radiatives des niveaux excités (par exemple avec l'eau ou des vibrateurs OH). Ces chromophores présentent typiquement des sections efficaces d'absorption 10^4-10^5 fois plus importantes, et sur une région spectrale bien plus large que dans le cas des ions Ln^{3+} correspondants ; l'énergie qu'ils absorbent peut être transférée aux ions Ln^{3+} voisins qui à leur tour subissent un processus radiatif d'emission. Par analogie avec les molécules qui recueillent la lumière que l'on trouve dans les systèmes photosynthétiques naturels, ce processus est appelé sensibilisation de la luminescence des lanthanides, ou effet d'antenne,[82] et de tels complexes peuvent être décrits comme des dispositifs moléculaires efficaces de conversion de la lumière (LCMDs).[83,84] Les ions Ln^{3+} forment des complexes avec divers types de molécules organiques comme les acides carboxyliques aromatiques, les β-dicétones, les calixarenes, les cryptants, les podants, et les ligands hétérocycliques, et emettent de façon efficace dans le proche UV (Ce^{3+} et Gd^{3+}), le visible (bleu, Tm^{3+} ; vert Tb^{3+} et Er^{3+} ; jaune Dy^{3+} ; orange Sm^{3+} ; et rouge, Eu^{3+}) et proche infrarouge (Nd^{3+}, Er^{3+}, Tm^{3+} et Yb^{3+}). Ces matériaux présentent un grand intérêt pour un vaste domaine d'applications en photonique, comme les lasers accordables, les amplificateurs pour la télécommunication optique, les composants des couches emettrices dans les diodes organiques multicouches emettrices de lumière (OLEDs), les étiquettes luminescentes dans les dispositifs d'analyse immunitaire par fluorescence résolue dans le temps, les concentrateurs de lumière pour des dispositifs photovoltaïques, et les antennes dans les composés bioinorganiques photosensibles.[74,80,81,85,86] Les verrous technologiques importants concernent la relativement faible stabilité thermique et photochimique des complexes, qui, combinée avec des mauvaises propriétés mécaniques, représentent des inconvénients importants pour l'applicabilité technologique des complexes de lanthanide, principalement dans les domaines de l'éclairage, de la détection, et de l'affichage. De plus, la plupart de ces complexes sont habituellement isolés sous forme d'hydrates, dans

lesquels deux ou trois molécules d'eau sont incluses dans la première sphère de coordination de l'ion central, et désactivent l'émission à cause de l'activation de voies de désexcitation non-radiative. La dégradation de la plupart des complexes à base de lanthanides (par exemple les chelates de β-dicétones)[87,88], sous irradiation UV (dans certains cas en seulement quelques heures) est souvent attribué au photoblanchiment ou dommage chimique photoinduit, et n'a pas encore été totalement élucidé. Afin de surpasser simultanément ces inconvénients, et d'améliorer leur stabilité chimique, leurs caractéristiques mécaniques et les propriétés d'émission de lumière (par exemple le rendement quantique, le temps de vie des états excités, la photostabilité à l'UV), les complexes de lanthanides ont été encapsulés dans des polymères des cristaux liquides ou des hybrides organiques-inorganiques obtenus par voie sol-gel, principalement ceux à base de silice, tels ceux présentés dans cette thèse.[89]

En plus de l'intérêt que présentent les matériaux contenant des ions Ln^{3+} pour leurs propriétés d'émission de lumière, la sensibilité des transitions 4f peut aussi être utilisée pour obtenir des informations sur l'environnement local autour de ces ions métalliques[36,81]. C'est une autre caractéristique importante principalement dans le cas des ions Eu^{3+}, qui constitue un outil remarquable grâce à quelques propriétés spectroscopiques particulières comme : 1) une grande différence d'énergie entre le premier état excité $^5D_0$ et le plus haut état $^7F_6$ du septuplet fondamental (12 300 cm^{-1}). Plus cet écart énergétique est petit, plus il est facile de désactiver l'état excité par des transitions non-radiatives (par exemple par des vibrations OH) ; 2) un premier état excité $^7F_0$ qui permet une analyse facile de l'effet Stark, avec la correspondance entre la dégénerescence dûe à l'éclatement J et la symétrie locale du site de l'europium ; 3) la présence de la transition dipôle magnétique $^5D_0 \rightarrow {}^7F_1$ indépendante du champ de ligand ; 4) la présence d'un seul pic pour la transition permise $^5D_0 \rightarrow {}^7F_0$ dans le cas des groupes de symétrie ponctuelle C_s, $C_{1,2,3,4,5,6}$ et $C_{2v,4v,6v}$ avec un caractère principalement de type dipôle électrique et qui s'explique par des effets de mélange J.[90-92] L'énergie de cette transition non-dégénérée est directement liée à la covalence des liaisons chimiques de la première sphère de coordination de l'ion Eu^{3+} (effet néphélauxétique)[93]; 5) l'observation de couplages vibroniques dans une région spectrale relativement large de la transition d'excitation $^7F_0 \rightarrow {}^5D_2$ (24 400-21 550 cm^{-1}), permettant, d'une façon singulière, l'identification des modes de vibration jusqu'à environ 3 000 cm^{-1}, et dépendant de l'environnement local de l'ion Eu^{3+}; 6) la présence de bandes

de transfert de charge du ligand vers le métal (LMCT) dans la région UV-visible du spectre d'excitation, et attribué à des groupes de ligands particuliers. Ainsi, des variations dans le nombre de composants Stark de chaque variété de transition intra 4f, des variations des intensités relatives entre celles-ci, des différences entre les énergies de certaines bandes, et l'analyse des courbes de déclin des états excités fournissent des informations importantes sur la coordination locale des ions métalliques, comme l'existence de plus d'un groupe local de symétrie autour de l'europium, le nombre de molécules d'eau coordinées, l'amplitude du champ de ligand, et l'importance de la covalence des liaisons Eu^{3+}-ligand.

L'intérêt dans la photoluminescence des hybrides organiques-inorganiques à base de lanthanides a donc augmenté considérablement au cours des dix dernières années, avec la conception de matériaux aux caractéristiques contrôlables et offrant des propriétés variables, ouvrant de nouvelles voies de recherche en science des matériaux et dans les technologies liées, et avec des implications significatives dans les mises en oeuvre nanotechnologiques des dispositifs (par exemple l'intégration, la miniaturisation et la multifonctionnalisation). Des applications prometteuses sont donc attendues, comme les dispositifs émetteurs de lumière ou les points quantiques, les guides d'ondes actifs dans les régions spectrales infrarouges, les revêtements actifs, et les détecteurs et actionneurs bioanalytiques et biomédicaux.[78]

Le principal objectif de cette thèse a été de développer des hybrides fonctionnels hiérarchiquement ordonnés avec des applications potentielles dans des dispositifs optiques passifs intégrés. Un autre objectif du projet a été d'aborder des aspects comme le mécanisme d'auto-organisation, la relation entre l'ordre des nanostructures et les propriétés d'émission qui correspondent, et les mécanismes de transfert d'énergie au sein des hôtes hybrides et entre ceux-ci et les ions lanthanide Ln^{3+}.

La première partie de cette thèse a consisté en l'étude de l'origine et du mécanisme (le processus de transfert d'énergie) derrière les caractéristiques d'émission d'hybrides organiques-inorganiques qui avaient été étudiés et caractérisés au cours de travaux antérieurs à cette thèse, afin de construire une toile de fond théorique qui sera utile pour guider l'interprétation des résultats expérimentaux et la conception de nouveaux matériaux hybrides organiques-inorganiques avec deux buts différents : étudier l'influence de l'organisation et l'effet du fragment organique sur les propriétés de photoluminescence.

Dans les deux cas, le matériau hybride pur et ceux contenant les ions lanthanide Ln^{3+} ont été étudiés.

1. Transfert d'énergie dans des matériaux hybrides organiques-inorganiques sans activateur métallique.

Jusqu'au début de cette thèse, plusieurs hybrides à base d'amine ou d'amide, photoluminescents et émettant de la lumière blanche et ne possédant pas d'activateur métallique ont été décrits.[39,54-67] Des preuves expérimentales comme la dépendance sous-linéaire de l'intensité intégrée d'émission par rapport à l'intensité d'excitation, l'augmentation des temps de vie des deux émissions avec le délai initial et le déplacement vers le rouge des spectres résolus dans le temps par rapport à ceux obtenus en mode continu, indiquent que les deux émissions sont à mettre en relation avec des mécanismes de recombinaison radiative typiques des couples donneur-accepteur (D-A).[63-65,67] Alors que les espèces chimiques impliquées dans l'émission dûe aux nanodomaines silylés ont été assignés à des défauts de type $^{\bullet}O-O-Si\equiv(CO_2)$ liés aux atomes d'oxygène et détectés par résonnance paramagnétique électronique,[64] celles responsables du composant lié aux NH/C=O n'ont pas encore été totalement élucidées. Les expériences de spectroscopie résolue dans le temps ont démontré l'existence de transferts d'énergie entre ces deux émissions distinctes.[38,63,64]

Dans cette thèse, nous avons essayé d'apporter un nouvel éclairage sur l'origine et les mécanismes responsables des propriétés photoniques des hybrides organiques-inorganiques fonctionnalisés par des amines ou amides, et nous avons apporté une discussion quantitative sur les mécanismes de transfert d'énergie qui ont lieu entre les domaines organiques et inorganiques (Schéma 3.1).

Les deux émissions associées à leurs contreparties organique ou inorganique ont été examinées de façon indépendante. Deux composés modèles reproduisant respectivement les parties organiques (Jeffamine ED-2001®/PIC) et inorganique (TEOS/PTMOS) d'un hybride di-uréasil ont été synthétisés et caractérisés en détail par diffraction des rayons X (XRD), RMN $^{29}Si/^{13}C/^{1}H$ MAS, réflectance diffuse, FT-IR, et spectroscopie de photoluminescence (PL). Les XRD, RMN $^{29}Si/^{13}C/^{1}H$ MAS et FT-IR des Jeffamine ED-

2001®/PIC et TEOS/PTMOS soutiennent leur utilisation en tant que modèles structuraux organiques et inorganiques des deux parties des hybrides di-uréasils.

Les bandes d'émission des composés Jeffamine ED-2001®/PIC et TEOS/PTMOS sont bien simulées par des gaussiennes uniques, dont le maximum d'énergie varie de 3,17 à 2,54 eV et de 3,00 à 2,89 eV, pour les composés modèles organiques et inorganiques respectivement, quand la longueur d'onde d'excitation augmente de 300 à 420 nm (4,13 à 2,95 eV) et de 280 à 365 nm (4,42 à 3,40 eV). En comparant ces valeurs avec celles observées pour les émissions provenant des NH/C=O et des domaines silylés dans les hybrides fonctionnalisés par des amines ou amides, un déplacement vers le bleu a été observé pour l'émission du composé Jeffamine ED-2001®/PIC, alors que l'énergie de l'émission liée aux parties silylées est à peu près la même que celle observée pour le composé modèle TEOS/PTMOS. La dépendance linéaire de l'intégrale de l'intensité d'émission par rapport à la puissance d'excitation pour les deux matériaux (pentes de 1,00 et 0,98 pour les composés modèles inorganiques et organiques respectivement), et le déplacement en énergie entre celles du maximum de chaque spectre résolu dans le temps mesuré pour des délais initiaux entre 0,05 et 20,00 ms, et la valeur correspondante détectée sous excitation continue montrent que l'émission des composés modèle se fait aussi par l'intermédiaire de couples donneur-accepteurs, comme cela a été montré pour les di-uréasils et di-amidosils.[64,67]

Les courbes de déclin pour les deux matériaux sont bien reproduites par des fonctions exponentielles uniques et révèlent des temps de vie de 211,7 ± 11 ms et 161,9 ± 10 ms, pour les composés modèles inorganiques et organiques respectivement. Par comparaison de ces valeurs avec celles obtenues pour les hybrides **d-U(2000)**, on observe un temps de vie de Jeffamine ED-2001®/PIC identique à celui trouvé pour les émissions liées au NH/C=O, alors que la valeur estimée pour TEOS/PTMOS est plus grande par deux ordres de grandeurs que celles trouvées pour l'émission liée aux défauts silylés dans les hybrides. Cette augmentation significative suggère l'existence de mécanismes de désexcitation non-radiatifs activés thermiquement et associés avec le composant lié aux siloxanes qui impliquerait des transferts d'énergie à partir des groupes NH/C=O.

La dépendance en température de type Arrhenius du temps de vie associé aux domaines silylés dans l'hybride **d-U(2000)** (énergie d'activation de ~565 cm^{-1}), ainsi que le comportement non exponentiel de la courbe de déclin de l'émission liée aux domaines

silylés à basse longueur d'onde d'excitation (les deux émissions simultanément) soutient aussi l'occurrence de ce processus de transfert d'énergie.

La vitesse de ce transfert d'énergie est estimée de façon quantitative pour l'hybride **d-U(600)** (l'hôte di-uréasil utilisé avec le plus petit nombre de répétitions de l'unité organique) généralisant les idées proposées récemment pour le transfert d'énergie intramoléculaire entre les niveaux singulet et triplet du ligand et les états de transfert de charge du ligand vers le métal dans les composés de coordination des lanthanides.[94] Le transfert d'énergie entre les centres donneur et accepteur peut être estimé en considérant des états déterminants à deux électrons ($|i\rangle$ et $|f\rangle$) impliquant les orbitales π, π^*, ϕ et ϕ^* attribuées aux niveaux d'énergie électronique des défauts $^{\bullet}$O–O–Si≡(CO_2) liés à l'oxygène et à ceux basés sur les NH/C=O. Ces vitesses de transfert d'énergie ente les donneurs (centres hybrides) par les mécanismes d'échange (W_{HL}^{e}) et dipôle-dipôle (W_{HL}^{DD}) ont pu être estimées quantitativement en calculant les distances moyennes donneur-accepteur, la différence d'énergie de transition entre les donneurs et accepteurs impliqués dans le processus de transfert (à travers le point de croisement entre les courbes d'émission et d'excitation), la largeur à mi-hauteur des émissions des donneurs et accepteurs, les temps de vie radiatifs, les énergies de transition et les intégrales de recouvrement.

La vitesse de transfert d'énergie dipôle-dipôle entre les deux centres émetteurs du di-uréasil **d-U(600)** est de $1{,}3.10^{9}$ s^{-1}, supérieure à celle estimée pour la vitesse de transfert impliquant le mécanisme d'échange, $3{,}7.10^{8}$ s^{-1}, montrant que ce dernier est le mécanisme dominant.

2. Mécanismes de transfert d'énergie dans les hybrides organiques/inorganiques incorporant de l'europium : une estimation quantitative par spectroscopie d'émission de lumière

Jusqu'au début de cette thèse, seulement quelques rapports ont concerné les mécanismes de transfert d'énergie de l'hôte vers le ligand et de l'hôte vers le métal dans les hybrides organiques-inorganiques comportant des ions lanthanides, et ils n'ont pas fourni de discussion quantitative et détaillée.[87,95,96] Un des objectifs de cette thèse a été d'apporter une discussion quantitative sur les mécanismes de transfert d'énergie qui ont lieu dans les di-uréasils organiques-inorganiques incorporant des composés d'europium.

En général, les mécanismes de transfert d'énergie entre les espèces donneurs et accepteurs ont été traités dans le cadre des approches classiques de Förster[97] et Dexter[98]. Alors que le modèle de Dexter se base sur des interactions d'échange à courte distance, celui de Förster tient compte d'interactions multipôlaires à longue distance[99,100]. Les deux approches permettent le calcul de l'intégrale de recouvrement entre l'émission du donneur et l'absorption de l'accepteur. Dans le cas du modèle de Förster, en plus de l'intégrale de recouvrement, il est aussi possible de calculer le rayon critique R_0 pour le transfert d'énergie, correspondant à la distance de séparation pour laquelle la vitesse du transfert d'énergie donneur-accepteur (*D-A*) est égale à la vitesse de déclin de l'état excité du donneur en l'absence d'accepteur.[97,99,100] Dans le modèle de Dexter, cependant, l'intégrale de recouvrement est la seule quantité qui peut être directement calculée à partir de données empiriques spectroscopiques; les constantes de vitesse de transfert d'énergie nécessitent la connaissance de paramètres qui ne sont pas dérivés de valeurs déterminables de façon expérimentale.[98-100]

Les aspects quantitatifs du transfert d'énergie qui a lieu dans les hybrides di-uréasils incorporant soit [Eu(btfa)$_3$(4,4'-bpy)(EtOH)] (btfa=benzoyltrifluoroacetonate, 4,4'-bpy=4,4'-bipyridine) soit Eu(CF_3SO_3)$_3$ (Schémas 3.2 et 3.3) ont été discutés.

La dépendance de l'intensité relative de l'émission de l'hybride à la concentration en centre lanthanides et la présence de ligands organiques constituent un argument fort qui souligne l'existence de tranfert d'énergie de l'hôte vers le métal soit par les niveaux excités du ligand ou directement à partir des centres émetteurs de l'hybride. Des arguments qualitatifs supplémentaires qui soutiennent l'hypothèse de l'existence de ce transfert d'énergie sont la dépendance du rendement quantique d'émission et des temps de vie des états excités à la quantité de triflate d'europium Eu(CF_3SO_3)$_3$ incorporée. Le rendement quantique d'émission décroît de 9% pour le di-uréasil non dopé à 1,4% pour n = 20. Le temps de vie à 14 K pour les états excités de l'hybride décroît de ~160 ms (groupes NH/C=O) et 3,5 ms (défauts liés à l'oxygène[101]) à des valeurs inférieures à 10^{-5} ms, en présence d'ions Eu^{3+}, et à ~100.0-20.0 ms (groupes NH/C=O) et 3,1-0,5 ms (défauts liés à l'oxygène) en présence d'ions Nd^{3+}.[102] De telles diminutions suggèrent que les ions Eu^{3+} et Nd^{3+} activent des voies non-radiatives de déclin (non présents dans les di-uréasils non dopés) liées à des transferts d'énergie de l'hôte vers les niveaux des lanthanides.[95,102] Une autre preuve du transfert d'énergie dans les di-uréasils incorporant des ions Eu^{3+}, Nd^{3+}, et

Tm^{3+} a été démontrée par des lignes d'auto-absorption intra-4f superposées à la bande d'émission de l'hôte hybride.[95,101-103]

Trois voies distinctes de transfert d'énergie peuvent être imaginées pour le **d-U(600)-[Eu(btfa)$_3$(4,4'-bpy)(EtOH)]** : (i) l'énergie absorbée par les centres émetteurs de l'hybride est transférée des états excités du ligand (transfert d'énergie de l'hybride vers le ligand) ; (ii) transfert d'énergie des états excités du ligand aux ions Eu^{3+} (transfert d'énergie ligand vers Eu^{3+}) et (iii) transfert d'énergie ayant lieu directement des centre liés à l'oxygène $^{\bullet}O–O–Si\equiv(CO_2)$ et aux NH/C=O vers les ions Eu^{3+} (hybride vers Eu^{3+}).

L'évaluation numérique de ces vitesses de transfert d'énergie a été réalisée, en mesurant les énergies de transition, les temps de vie radiatifs, la largeur à mi-hauteur des émissions des centres émetteurs des hybrides, les niveaux singulet et triplet des ligands et les états intra 4f de Eu^{3+}, et les distances moyennes Eu^{3+}-ligand et Eu^{3+}-centres émetteurs des hybrides. Ces distances moyennes *D-A* ont pu être prédites de façon satisfaisante en utilisant le modèle Sparkle/AM1.[104]

Les vitesses correspondantes de transfert d'énergie sont estimées pour les di-uréasils incorporant [Eu(btfa)$_3$(4,4'-bpy)(EtOH)], généralisant les idées précédemment proposées pour le transfert d'énergie intramoléculaire entre les niveaux singulet (S) et triplet (T) du ligand, et les ions Eu^{3+}, et entre ces niveaux du ligand et les transfert de charge du ligand vers le métal (LMCT) dans les composés de coordination des lanthanides.[94]

La vitesse de transfert d'énergie du ligand vers Eu^{3+} est typiquement supérieure d'un ordre de grandeur à celle estimée pour le transfert direct à partir des centres émetteurs des hybrides ($3{,}75.10^{10}$ et $3{,}26.10^{9}$ s^{-1} respectivement) pour le niveau $^5D_1$. La voie la plus efficace de luminescence est $(S_0)_{Hybride} \rightarrow (T)_{Hybride} \rightarrow (T)_{Ligand} \rightarrow (^5D_1, ^5D_0) \rightarrow {}^7F_{0\text{-}6}$.

Les approches classiques de Förster et Dexter sont appliquées au di-uréasil **d-U(2000)$_n$Eu(CF$_3$SO$_3$)$_3$** (n = 200, 40) où les états excités singulet et triplet du complexe n'ont pas pu être prédits à cause de l'effort calculatoire trop important nécessaire pour ce type de calculs dans les structures de grande dimension. Les preuves suivantes montrent que le mécanisme d'échange (Dexter) est responsable du transfert d'énergie : (i) le rayon critique calculé selon le modèle de Förster (3,3-3,5 Å) est en bon accord avec la distance expérimentale Eu^{3+}/NH-C=O montrant que les espèces *D* et *A* ont à entrer en contact, une pré-condition de Dexter, pour laquelle les intégrales de recouvrement obtenues sont compatibles, (ii) les valeurs calculées pour l'efficacité du transfert d'énergie en tenant

compte du modèle de Förster sont très différentes des valeurs expérimentales. Aussi, bien que moins efficace par rapport à **d-U(600)-[Eu(btfa)$_3$(4,4'-bpy)(EtOH)]**, le transfert d'énergie hybride vers Eu^{3+} est aussi dominé par une interaction d'échange (Dexter).

La caractérisation détaillée de ces mécanismes de transfert d'énergie en utilisant une évaluation quantitative devrait permettre de contribuer au développement de nouveaux hybrides à base de siloxane caractérisés par des propriétés photoniques intéressantes et une bonne efficacité d'émission de lumière. De plus, la procédure rapportée constitue une bonne toile de fond théorique qui pourrait être utile pour aider à l'interprétation des données expérimentales et pour modéliser de nouveaux hybrides organiques-inorganiques.

3. Relation entre la structure et la photoluminescence dans des hybrides organiques-inorganiques de type polysilsesquioxanes pontés purs ou contenant de ions Ln^{3+}

Jusqu'à cette thèse, les recherches s'étaient principalement focalisées sur des hybrides organiques-inorganiques amorphes comportant soit des sels ioniques de lanthanides,[39,60,95,105-108] soit des complexes de lanthanides à ligands organiques, par exemple à base de β-dicétones.[37,87,88,96,101,107,109-112] Cette dernière stratégie permet de surpasser les très faibles coefficients d'absorption des lanthanides grâce à l'absorption par les ligands suivi d'un transfert d'énergie efficace à l'ion lanthanide émetteur. Bien qu'extrêmement attractifs, les hybrides organiques-inorganiques structurés ont cependant été très rarement exploités. Seules deux familles sont connues à ce jour : les matériaux mésostructurés, dans lesquels les ions lanthanides sont piégés dans des silices mésoporeuses (de type MCM-41, MCM-48 et SBA15)[113-120] modifiées en surface ou des organosilanes fonctionnels[41,121-125] et des structures lamellaires de fines couches d'oxyde de lanthanide espacées de façon égale par des entités benzoate ou biphenolate.[126,127]

En combinant l'intérêt dans les hybrides structurés et les caractéristiques de photoluminescence très attrayantes observées pour les hybrides organiques-inorganiques, nous avons envisagé de déterminer s'il y aurait une relation entre la structure et les propriétés de photoluminescence dans des hybrides particuliers obtenus par hydrolyse-condensation du précurseur ponté disilylé $(EtO)_3Si(CH_2)_3NH(C=O)NH(CH_2)_{12}NH(C=O)NH(CH_2)_3Si(OEt)_3$ (**P12**) qui allie des groupements silylés polymérisables, des fonctions urée capables de s'auto-associer par

liaisons hydrogène, et une chaîne alkyle centrale longue (12 unités méthylène). L'hydrolyse-polycondensation du précurseur, qui conduit à des réseaux hybrides, a été conduite sous deux conditions réactionnelles différentes : par catalyse nucléophile, auquel cas la condensation est la réaction la plus rapide, et par catalyse acide, où c'est cette fois-ci l'hydrolyse qui est l'étape la plus rapide. Les ions Eu^{3+} ont été utilisés comme sonde locale, et les réactions sol-gel ont été réalisées en absence et en présence du sel $EuCl_3.6H_2O$.

Il a déjà été décrit que l'hydrolyse du précurseur **P12** en conditions acides dans l'eau conduit à la formation d'un hybride lamellaire (appelé **L12**) ordonné sur une longue distance, alors que l'hydrolyse réalisée en présence de seulement 6 équivalents d'eau dans l'éthanol par catalyse nucléophile (NH_4F) produit un hybride amorphe (**A12**).[128] Des matériaux hybrides avec des morphologies différentes ont été obtenues à partir de ce précurseur unique **P12** en modifiant les conditions réactionnelles en présence ou en absence d'ions Eu^{3+}.

Des hybrides lamellaires hautement structurés ont été obtenus par hydrolyse acide du précurseur **P12** (quatre hybrides ont été étudiés, le matériau pur **L12** et trois hybrides contenant des sels d'Eu^{3+} (avec un contenu massique de 1,01, 1,83 et 15,04 % d'europium)). La morphologie lamellaire a été mise en évidence par microscopie électronique à balayage (SEM), microscopie à force atomique (AFM) et XRD. La catalyse acide permet une hydrolyse rapide et une condensation plus lente. Cette condensation plus lente permet d'obtenir un réseau siloxane flexible favorisé par un arrangement des fragments organiques qui s'auto-assemblent grâce à une combinaison de liaisons hydrogène entre les groupements urée, et d'interactions hydrophobes entre les chaînes alkylène. Le précurseur, qui s'hydrolyse en molécules contenant des fonctions silanol, se comporte comme une molécule amphiphile capable de s'auto-assembler. L'espacement lamellaire interdomaine caractéristique a été calculé en utilisant des données de SAXS, conduisant à des valeurs de 3,01 ± 0,01 nm pour **Eu@L12-1** ou **Eu@L12-2**, et 2,85 ± 0,01 nm pour **Eu@L12-3**. Les hybrides ont des surfaces fractales avec une pente de Porod de -3,7, ce qui signifie que les fontières des particules qui diffractent sont assez bien définies. L'incorporation d'ions Eu^{3+} fait croître le domaine de q pour lequel la courbe SAXS suit cette pente (q_{min} ~0,56 et 1,10 nm^{-1} respectivement pour les hybrides **L12** et dopés), ce qui

indique que les différences structurales induites par l'incorporation des ions Eu^{3+} a lieu sur une échelle de longueurs inférieure à 11 nm. La faible augmentation de la distance interdomaine lorsque la synthèse est conduite en présence d'ions Eu^{3+} (2,92 ± 0,01 nm pour **L12**) a été associée avec la rupture de l'assemblage des urées par l'intermédiaire des liaisons hydrogène causée par l'incorporation des ions Eu^{3+} et Cl^- à l'intérieur de la structure lamellaire **L12**, alors que la diminution observée lorsque le taux d'europium monte à 15% a été attribuée à une augmentation du degré de désordre des chaînes polymère. L'inclusion des ions Eu^{3+} et Cl^- à l'intérieur de la structure lamellaire **L12** est aussi confirmée par une augmentation de la distance moyenne entre les chaînes, manifestée par le déplacement du pic en DRX attribué aux répétitions des distances interchaînes vers des valeurs de *q* plus basses (de 16,31 nm^{-1} (0,385 nm) pour **L12** à 16,07 nm^{-1} (0,390 nm) dans les hybrides **Eu@L12**). De plus, l'augmentation de la largeur à mi-hauteur des signaux attribués aux carbones C^7 en conformation *trans* et *gauche* dans les spectres RMN ^{13}C CP/MAS de l'hybride **Eu@L12-3** par rapport à ceux des hybrides moins concentrés, l'apparition d'une nouvelle résonnance à ~35 ppm associée à des chaînes alkyle cristallines avec un plus bas degré d'ordre conformationnel et les valeurs obtenues pour la longueur de cohérence moyenne de l'ordre lamellaire estimées par SAXS (90,1 ± 4,5 nm, **L12** ; 119,5 ± 6,0 nm, **Eu @L12-1** ; 116,3 ± 5,8 nm, **Eu@L12-2**, et 102,2 ± 5,1 nm, **Eu@L12-3**) semblent aussi montrer que l'augmentation du taux d'europium favorise un désordre des chaînes. Pour la concentration en ions Eu^{3+} la plus basse, une rupture partielle de l'arrangement des urées par liaisons hydrogène a été observée, dû à l'incorporation des ions Eu^{3+} et Cl^- au sein de la structure lamellaire **L12**, alors que pour la plus haute concentration en ions Eu^{3+}, une augmentation du degré de désordre des chaînes de polymère a lieu, même si la morphologie lamellaire est préservée.

Dans le cas des hybrides préparés par catalyse nucléophile, la présence des ions métalliques induit des morphologies très différentes (assemblages de fibres ou haltères) de l'arrangement sphérique de petites plaques observés dans le cas du matériau pur **A12**. Les principaux changements observés lorsque la synthèse des hybrides **A12** est réalisée en présence d'ions Eu^{3+} sont à mettre en relation avec une organisation à courte distance des fragments organiques qui résulte d'un empilement plus régulier des chaînes alkyle. Ceci est démontré à la fois par des études XRD avec l'apparition d'un pic bien défini à 16,41

nm^{-1} et par les études RMN ^{13}C, avec l'augmentation très forte du signal à 34,0 ppm typiquement attribuable à un arrangement *all-trans* des groupes méthylène. Par conséquence, le pic unique à basse valeur de *q* (XRD) se déplace vers des valeurs plus basses dans le cas des échantillons comportant des ions Eu^{3+}, ce qui met en évidence une augmentation de la longueur de chaîne (2,25 à 2,37 et 2,50 nm pour **A12**, **Eu@A12-1** et **Eu@A12-2** respectivement) qui résulte d'un arrangement *trans* plus régulier des unités méthylène. Ces valeurs sont cependant très éloignées des distances interlamellaires de 2,92 et 3,01 nm dans le cas des hybrides lamellaires organisés à longue distance **Eu@L12**. Cette distance plus faible dans le cas de **Eu@A12-1** ou **Eu@A12-2** provient certainement du caractère moins organisé de ces derniers hybrides. Par rapport à **A12**, la meilleure organisation des chaînes est principalement expliquée par un renforcement des liaisons hydrogène entre les groupements urée; en parallèle à la plus faible dispersion des environnements des groupes urée qui est mise en évidence par un signal plus fin en RMN ^{13}C à 159,9 ppm pour les hybrides **Eu@A12**, les déconvolutions de la région 'amide I' des spectres infrarouge de **A12** et **Eu@A12-1** montrent que l'incorporation de sels d'europium durant la synthèse a pour conséquence de plus importantes contributions des associations aux plus fortes liaisons hydrogène au détriment des plus faibles, une situation déjà observée dans le cas des di-uréasils.[108] Aussi, il apparaît clairement que les ions Eu^{3+} jouent un rôle crucial dans cette structuration à courte distance des matériaux comportant des sels d'europium.

La complexation initiale des groupements urée par les sels d'europium peut provoquer une charge partielle positive plus importante des protons N-H des groupes urée. Ceci pourrait créer des liaisons H plus fortes avec d'autres groupes urée ce qui favoriserait l'empilement des fragments hydrophobes sous forme de films. Ceux-ci pourraient s'assembler avec d'autres films formés à proximité pour générer les plaques nanométriques assez régulières (150 × 400 nm). Grâce à cette régularité, ces plaques peuvent alors facilement s'empiler, avec une direction préférentielle pour former des assemblages micrométriques grâce à un arrangement brique sur brique (schéma 4.4 et Fig. 4.5), de façon similaire à ce qui se produit dans la nature avec les empilements de plaques d'aragonite dans de plus grandes dimensions (10-20 µm de long et 0,5 µm de haut).[129,130] Ceci expliquerait la présence d'une symétrie axiale dans les structures finales pour générer les fibres micrométriques de taille uniforme (jusqu'à 4 µm) qui à leur tour ont tendance à

s'auto-assembler sous forme de fagots. Ainsi, le meilleur agencement des fragments organiques à l'intérieur de la structure, qui résulte à la fois de liaisons H plus fortes entre les groupes urée et d'une plus grande cristallinité donc rigidité de la chaîne alkyle $C_{12}H_{24}$ est responsable de la différence de morphologie observée entre les hybrides **Eu@A12** (assemblage de fibres tordues en forme d'haltères) et l'hybride pur **A12** (forme sphérique résultant de l'assemblage de plaques non uniformes (0,3-1,0 µm)). Dans ce dernier exemple, les plaquettes irrégulières ne peuvent pas s'empiler efficacement et une croissance isotrope a lieu, conduisant à une morphologie sphérique.[131,132] De plus, dans les images SEM, des canaux (jusqu'à 0,5 µm de diamètre) sont observées au bout de la structure en forme d'haltère formée de fibres. Cette forme d'haltère des fagots de fibres résulterait du flux d'éthanol libéré durant le processus d'hydrolyse-condensation et des liens entre les fibres assurés par les ions Eu^{3+}. En effet, le flux d'éthanol, qui est formé durant la phase de vieillissement croît lorsque l'on va du centre des assemblages vers leurs extrémités. Les ions Eu^{3+} sont coordinés entre des fibres adjacentes (ceci est discuté en détail plus bas), contraignant le flux d'éthanol et induisant les évasements de la morphologie d'haltère.

Les spectres d'émission des hybrides contenant des ions Eu^{3+} présentent une bande large entre 380 et 560 nm, ainsi qu'une série de lignes fines attribuées aux transitions intra-$4f^6$ $^5D_0 \rightarrow {}^7F_{0\text{-}4}$ des ions Eu^{3+}. La bande large déjà observée pour les hôtes purs **L12** et **A12**, et attribuée à la superposition de deux composants distincts qui ont lieu au sein des assemblages de groupes urée et au sein des domaines silylés sous l'effet de défauts liés à l'oxygène (•O-O-Si≡(CO2)), est déviée vers le rouge, ce qui met en évidence une interaction effective entre les ions Eu^{3+} et les centres d'émission de l'hôte hybride. L'intensité relative de la bande dûe à l'hybride dépend fortement de la quantité d'europium incorporée, ce qui suggère la présence de transfert d'énergie entre les centres émetteurs de l'hôte et les ions Eu^{3+}. Les rendements quantiques absolus d'émission de l'hybride pur **L12** ont été mesurés pour des longueurs d'onde d'excitation allant de 290 à 330 nm, avec une valeur maximum de 0,14 (310 nm). Les valeurs de rendement quantique absolu d'émission obtenues pour les hybrides **Eu@L12** ont donné des valeurs inférieures à 0,01, ce qui indique la présence de voies non radiatives de désexcitation qui sont absentes dans l'hybride pur **L12**. Pour l'hybride pur **A12**, une valeur maximum de 0,24 ± 0,02 a été atteinte pour une longueur d'onde d'excitation de 290 nm. Cette valeur est plus importante

que dans le cas de l'analogue lamellaire, ce qui montre que la différence de morphologie dûe à la voie de synthèse influe fortement sur la valeur du rendement quantique. En particulier, on observe qu'un plus haut degré d'organisation induit une diminution du rendement quantique d'émission, comme cela avait été démontré pour les hybrides fonctionnels à base d'amide.[67] De plus, le rendement quantique de l'hybride **A12** est supérieur aux valeurs rapportées pour les di-uréasils amorphes analogues (0,06-0,08 ± 0,01)[63,64], di-urethanesils (0.19 ± 0.02)[66], di-amidosils (0.05 ± 0.01)[67] les alkyl/siloxanes croisés ordonnés (0,03 ± 0,01)[133]. L'incorporation d'ions Eu^{3+} au sein de l'hybride **A12** induit une diminution des valeurs du rendement quantique absolu d'émission. En particulier, une valeur maximale de 0,06 ± 0,01 a été trouvée dans le cas de **Eu@A12-1** et **Eu@A12-2** lorsqu'on les excite *via* les états excités de l'hôte hybride (340-360 nm). La diminution du rendement quantique (par rapport à ce qui est mesuré dans le cas de l'hybride pur **A12**) est en bon accord avec l'existence de transferts d'énergie de l'hybride vers les ions Eu^{3+}.[95] Sous excitation directe par les transitions intra $4f^6$, la valeur du rendement quantique est inférieure à la limite de détection de l'appareil (<0,01), ce qui renforce le rôle de actif de l'hôte hybride dans la sensibilisation de l'ion Eu^{3+}. En comparant ces valeurs avec celles des hybrides organiques-inorganiques analogues, et contenant aussi des sels de lanthanide, la valeur de rendement quantique rapportée ici est plus faible que dans le cas des di-ureasils (0,13 ± 0,02)[95], et largement supérieure à celles observées pour les composés hybrides lamellaires **Eu@L12** correspondants.

Afin de mieux connaître l'environnement local des ions Eu^{3+} dans les hybrides **Eu@L12** et **Eu@A12**, les lignes d'émission correspondant aux transitions intra $4f^6$ ont été étudiées à haute résolution.

Dans les hybrides de type **Eu@L12**, la détection d'une ligne unique $^5D_0 \rightarrow {}^7F_0$, l'éclatement de dégénérescence J des niveaux $^7F_{1,2}$ en 3 et 4 composants, respectivement, l'observation du même nombre de composants d'éclatement du champ local sur l'ensemble du domaine d'excitation étudié, et le fait que les courbes de déclin des émissions de l'état $^5D_0$ soient modélisable par une exponentielle indique que les cations Eu^{3+} occupent un seul type d'environnement, et ce pour tous les hybrides **Eu@L12** étudiés; ce site a une faible symétrie locale, et ne comporte pas de centre d'inversion, car l'intensité de la transition électrique-dipôle $^5D_0 \rightarrow {}^7F_0$ est plus forte que celle de la transition magnétique dipôle $^5D_0$

$\rightarrow {}^7F_1$. Malgré quelques variations mineures de l'efficacité quantique du niveau $^5D_0$ (16,3-19,2), du nombre de molécules d'eau (1,7-2,0) et du paramètre d'intensité expérimental Ω_2 (8,9-10,1 $.10^{-20}$ cm^2) qui ont lieu quand le taux d'europium augmente, la première sphère de coordination dans les hybrides **Eu@L12** rapportés ici devrait être très similaire, et comporter des atomes d'oxygène venant des groupes urée, des atomes de chlore et des molécules d'eau. Les caractéristiques spectroscopiques des ions Eu^{3+} dans les hybrides sont en accord avec celles de la structure, c'est-à-dire la même morphologie pour toutes les concentrations, et à peu près le même environnement pour tous les hybrides étudiés.

Dans les hybrides **Eu@A12**, deux sites locaux de coordination (appelés A et B) sont clairement discernés dans les spectres d'émission. Pour le site A, la première sphère de coordination est très similaire dans les deux structures hybrides, et comporte des atomes d'oxygène des groupes urée, des atomes de chlore, et des molécules d'eau, et ce malgré de faibles variations trouvées dans l'efficacité quantique du niveau $^5D_0$ (0,26-0,37), du nombre de molécules d'eau coordinées (0,7-1,2) et du paramètre expérimental d'intensité (15,4-13,3 $.10^{-20}$ cm^2) lorsque la concentration en europium augmente. Les ions localisés dans les sites B, sont caractérisés par i) une série de composants de Stark plus fins, ii) un rapport entre les intensités des transitions $^5D_0 \rightarrow {}^7F_2$ et $^5D_0 \rightarrow {}^7F_1$ important (ce qui indique la présence d'un centre d'inversion), iii) Une valeur de E_{00} plus grande (par comparaison avec celle trouvée pour les ions Eu^{3+} en site A) qui indique un degré de covalence moindre des liaisons Eu-O, iv) une valeur bien plus faible du temps de vie de l'état excité $^5D_0$. Toutes ces preuves suggèrent que les ions Eu^{3+} en site B sont localisés à la surface des fibres des structures haltères, et sont ainsi coordinés à un nombre important de groupes OH, par rapport aux ions situés en site A. La contribution relative des ions localisés en site B décroît quand la concentration en Eu^{3+} augmente, ce qui reflète un rapport surface sur volume plus grand pour la morphologie de type fibres (**Eu@A12-1**) par rapport à celle de type haltère (**Eu@A12-2**). L'augmentation du contenu en ions Eu^{3+} peut promouvoir la contiguité des fibres, ce qui conduit à la formation de structures en haltères. Des fibres distinctes seront liées par des ions Eu^{3+}, dont les ligands OH (dans le cas des cations localisés à la surface des fibres) sont remplacés par des atomes d'oxygène des groupes urée.

De plus, comme des hybrides avec approximativement la même concentration (~ 1 %) mais des morphologies complètement différentes (**Eu@L12-1** et **Eu@A12-1**) ont été synthétisés à partir du même précurseur, cette famille de silsesquioxanes pontés structurés hiérarchiquement est un exemple unique pour lequel l'effet de la morphologie sur les propriétés de photoluminescence a pu être abordé en détail. Ces résultats soulignent que l'environnement local des ions Eu^{3+} dépend considérablement de la morphologie globale des échantillons. La photoluminescence des cations Eu^{3+} a ainsi été utilisée comme sonde locale pour détecter les modifications morphologiques qu'ils ont eux-mêmes induit lors de leur incorporation au sein des réseaux hybrides en formation.

4. Emission contrôlable de lumière bleue ou verte de silsesquioxanes pontés à base de 2,2'-bipyridine pour l'éclairage. Silsesquioxanes pontés à base de 2,2'-bipyridine et contenant des lanthanides.

Pour des applications en photonique et en éclairage à l'état solide, il est nécessaire de développer des hybrides possédant les caractéristiques suivantes : i) un bon rendement quantique, ii) une forte brillance, iii) une bonne stabilité au cours du temps et sous irradiation, iv) la possibilité d'être excités par des sources d'éclairage peu onéreuses, comme les diodes électroluminescentes commerciales UV à grande longueur d'onde (360-400 nm) ou bleues. Le développement de phosphores pour la conversion de lumière proche UV en visible pourra contribuer à diminuer l'utilisation de lampes fluorescentes à plasma de vapeurs de mercure (et diminuant par là-même les risques environnementaux de pollution associés à leur élimination)[54,134,135] et est crucial afin d'augmenter l'efficacité et la qualité lumineuse des dispositifs d'éclairage à l'état solide à base de LEDs (composés en général de LEDs UV commerciales recouvertes d'un phosphore approprié)[136]. A cette fin, les matériaux hybrides de classe II, et principalement les silsesquioxanes pontés, qui possèdent des liaisons Si-C stables pour assurer la présence des fragments organiques au sein de la structure sont de bons candidats pour constituer des phosphores exempt d'activateur métallique. Ainsi, des fragments organiques conçus de façon appropriée peuvent être incorporés pour introduire des propriétés ciblées dans ces matériaux fonctionnels. Dans le chapitre précédent, nous avons vu que des silsesquioxanes pontés amorphes comprenant des groupes urée et une chaîne alkyle longue montrent des rendements quantiques assez bons (jusqu'à 0,24) alors que les hybrides lamellaires

correspondants ont des performances plus faibles. Cependant, l'hybride amorphe a une faible brillance, et son rendement quantique décroît au cours du temps. Au vu de ces observations, nous nous sommes focalisés sur un précurseur qui favorise la formation d'une structure hybride amorphe et qui possède des chromophores afin d'augmenter la brillance.

Récemment, un matériau hybride **H** à base de 2,2'-bipyridine (bpy) à été synthétisé (Scheme 5.1) pour des applications en catalyse[137] (le même hôte hybride incorporant des ions Eu^{3+} ou Tb^{3+} a été rapporté indépendemment et simultanément)[138]. La géométrie non linéaire de la partie organique empêche un empilement efficace des motifs durant la synthèse sol-gel, et favorise la formation d'un matériau amorphe. De plus, la présence des noyaux aromatiques permettra d'augmenter l'absorption des hybrides. Dans ce chapitre, les propriétés de photoluminescence de ce polysilsesquioxane ponté amorphe à base de 2,2'-bipyridine sont présentés : ce matériau possède le plus haut rendement quantique rapporté jusqu'ici pour des excitations dans les régions spectrales du proche UV ou du bleu (0,22 ± 0,02) dans les hybrides, une bonne stabilité au cours du temps, et peut être facilement excité à 395 nm par des LEDs commerciales.

La 2,2'-bipyridine est aussi un des ligands les plus connus dans la conception de matériaux luminescents contenant des ions Ln^{3+} car il possède une bande d'absorption intense dans le proche UV, et a la capacité de transférer de façon efficace de l'énergie sur les états excités des ions Ln^{3+} (effet d'antenne)[139]. Depuis le travail pionnier de Zambon[88] sur des systèmes hybrides à base de pyridyl-amide, quelques études ont été menées sur des matériaux contenant des ions Ln^{3+} et à base de bipyridine, soit obtenus par co-gélification avec une source de silice (par exemple le TEOS, orthosilicate de tétraéthyle ou le TMOS, orthosilicate de tétraméthyle),[140-142] soit directement à partir d'un précurseur unique.[138] Les principaux avantages de cette dernière méthode sont que: i) des matériaux avec une distribution homogène des parties organiques au sein du réseau silicate sont obtenus, ii) une quantité contrôlée et plus importante de fragments organiques, et donc d'ions lanthanides peut être incorporée, iii) l'auto-structuration du matériau peut être envisagée en présence de groupements organiques aux capacités d'auto-association. Dans ce chapitre, la photoluminescence de ces hybrides à base de diuréidobipyridine comportant des ions Eu^{3+}, Gd^{3+} et/ou Tb^{3+} est présentée, et pour la première fois, le rôle clef joué par la lumière émise

par l'hôte hybride dans la luminescence des matériaux correspondants contenant des ions Ln^{3+} est mis en avant.

Tous les hybrides présentés ici dérivent du même précurseur **P1** (schème 5.2) obtenu avec un bon rendement (70%) par l'action de l'isocyanatopropyltriéthoxysilane sur la 4,4'-diaminobipyridine. Deux conditions de synthèse différentes ont été utilisées pour former les hybrides : 1) Synthèse sol-gel par catalyse nucléophile (TBAF) à température ambiante à partir d'un mélange homogène de **P1**, d'eau, et de TBAF (rapport molaire 1 : 12 : 0,01) à 0,1 $mol.L^{-1}$ dans le DMSO. Au bout de trois heures, le mélange gélifie, puis après trois jours de vieillissement, et par des traitements standards, un solide blanc appelé **H** est obtenu avec un rendement quantitatif. 2) Réaction sol-gel par catalyse nucléophile (NH_4F) en mélangeant, à 45°C, pendant 5 minutes un mélange homogène de **P1**, d'eau, NH_4F et $LnCl_3.6\ H_2O$ (rapport molaire 1 : 30 : 0,01 : 0,33) à 0,1 $mol.L^{-1}$ dans le méthanol. Après 3 heures à température ambiante, le mélange gélifie, puis après 3 jours de vieillissement, et par des traitements standards, les solides sont obtenus sous forme de poudres blanches. Les hybrides contenant les ions Ln^{3+} sont désignés par **M-Ln** (Ln = Eu, Tb, Gd) ou **M-EuTb** (mélange 1 : 1 Eu/Tb). La synthèse d'un hybride non dopé (**M**) a été réalisée dans des conditions similaires.

Les spectres d'émission des hybrides non dopés à base de diuréidobipyridine (**H** et **M**) consistent en une bande large (380-660 nm) centrée à environ 455 nm pour des longueurs d'onde d'excitation comprises entre 320 et 380 nm; si l'on augmente la longueur d'onde d'excitation (de 380 à 440 nm) la position du maximum de la bande est déviée vers le rouge. Pour comprendre l'origine de cette lumière bleue, les spectres d'émission ont été acquis par spectroscopie résolue dans le temps à 12 et 300 K. Le spectre résolu dans le temps à température ambiante consiste en une bande large, modélisable par une gaussienne unique dont le maximum (455 nm) et la largeur à mi-hauteur sont indépendants de la longueur d'onde d'excitation ou du délai initial (SD). Cette émission peut-être attribuée sans ambigüité aux états triplets des fragments bipyridine étant donné que le temps de vie correspondant (0,063 ± 0,003 ms) est de 4 ordres de grandeur plus grand que ceux déjà mesurés pour les composantes associées aux émissions des urées ou amides, et celles attribuées aux défauts dans le réseau siloxane (10^{-9} s à 300 K). De plus, ces émissions sont déviées vers le rouge quand on augmente la valeur du SD ou la longueur d'onde

d'excitation. Pour la même valeur de SD de 0,05 ms, une baisse de la température à 12 K induit un élargissement significatif du spectre, avec un maximum maintenant situé à environ 515 nm, et deux bandes qui se superposent à 452 et 467 nm. Si l'on augmente la valeur du SD à 0,06 ou 0,07 ms, l'intensité de ces épaulements décroît fortement, et pour des valeurs de SD plus grandes que 100 ms, le composant à longue durée de vie à 550 nm est le seul qui persiste. Cette émission à longue durée de vie à 12 K est modélisable par une gaussienne unique, et possède la même énergie et échelle de temps que celles associées aux mécanismes de recombinaison au travers des liaisons entre les urées dans les hybrides analogues à base d'urée. L'énergie et la largeur à mi-hauteur de l'émission à longue durée de vie liée aux urées (2,41 ± 0,01 et 0,40 ± 0,01 eV) et au triplet du fragment bipyridine (2,74 ± 0,01 et 0,40 ± 0,01) ont été déterminés en modélisant les spectres à 12 K et 100 ms de SD et 300 K et 0,05 ms de SD respectivement, par des gaussiennes uniques. Comme ces paramètres sont assez peu dépendants de la température ou du SD, ils ont été utilisés comme valeurs de départ pour modéliser les spectres multi-composants acquis à 12 K avec des valeurs de SD comprises entre 0,05 et 0,07 ms. Pour avoir une bonne modélisation, un troisième composant doit être pris en compte, avec une énergie et largeur à mi-hauteur de 2,91 ± 0,01 et 0,11 ± 0,01 eV respectivement. En se basant sur les résultats antérieurs obtenus avec des silices hybrides analogues contenant des groupes urée, nous avons attribué ce composant à des recombinaisons électron-trou qui ont lieu au sein des nanoclusters de siloxane. Les temps de vie correspondant aux émissions liées aux urées, bipyridine, et siloxanes ont été estimées à 12 K, conduisant à des valeurs de 58,9 ± 0,497, 0,152 ± 0,007 et 0,012 ± 0,001 ms respectivement. Ces expériences par spectroscopie résolue dans le temps montrent donc que l'émission de cet hybride provient de la superposition de trois composants distincts : i) état triplet de la bipyridine (à environ 450 nm, temps de vie à 300 K de 10^{-5}-10^{-4} s); recombinaisons électron-trou provenant ii) des groupes NH/C=O des liens urées (environ 530 nm) et iii) des nanoclusters de silicium (à environ 427 nm). Ces deux derniers composants (avec un temps de vie à température ambiante de l'ordre de 10^{-9} s) ont aussi été observés dans les hybrides organiques-inorganiques analogues.

Les matériaux hybrides à base de diuréidobipyridine et comportant des sels de lanthanide Ln^{3+} sont des émetteurs multi-longueurs d'onde sous excitation UV, et montrent une série de pics attribués aux transitions $^5D_0 \rightarrow {}^7F_{0\text{-}4}$ des ions Eu^{3+} (**M-Eu**) et $^5D_4 \rightarrow {}^7F_{6\text{-}0}$

des ions Tb^{3+} (**M-Tb**) superposés à une bande large et qui dépend fortement de la longueur d'onde d'excitation. Aussi, la couleur d'émission est facilement modifiable sur le diagramme de chromaticité de la *Commission Internationale d'Eclairage* depuis les régions spectrales du rouge (**M-Eu**), de l'orange (**M-EuTb**) ou du vert (**M-Tb**) au bleu en changeant la longueur d'onde d'excitation. De façon intéressante, sous une excitation à 360 nm, les coordonnées de couleur de l'hybride **M-EuTb** (0,32,0,29) sont très proches de celles du point blanc (0,33,0,33), ce qui en fait un émetteur de lumière blanche.

Afin de mieux comprendre la coordination locale des ions Ln^{3+}, les caractéristiques de photoluminescence de l'ion Eu^{3+} dans **M-Eu** et **M-Tb** ont été utilisées comme sonde locale (ceci est réalisable dans le cas de **M-EuTb** car l'irradiation à 464 nm excite sélectivement les lignes $^5D_0 \rightarrow {}^7F_{0\text{-}4}$). La détection d'une ligne unique $^5D_0 \rightarrow {}^7F_0$, l'éclatement de dégénérescence J des niveaux $^7F_{1,2}$ en 3 et 4 composants respectivement, indiquent que les ions Eu^{3+} occupent le même environnement local avec un site de faible symétrie, sans centre d'inversion, en accord avec la forte intensité de la transition dipôle électrique $^5F_0 \rightarrow {}^7F_2$. L'énergie et la largeur à mi-hauteur de la transition $^5D_0 \rightarrow {}^7F_0$ ont été estimées en utilisant une modélisation par une gaussienne unique, conduisant à des valeurs de 17 270,8 ± 0,4 et 41,6 ± 0,9 cm^{-1} pour **M-Eu** et 17 263 ± 0,5 et 50,4 ± 1,5 cm^{-1} pour **M-EuTb**. La plus haute énergie trouvée pour cette transition dans **M-Eu** indique que les liaisons Eu-ligand ont un caractère moins covalent (en moyenne) que dans **M-EuTb**. Cette observation suggère qu'il y a des variations dans le nombre et/ou le type de premiers voisins des ions Eu^{3+} (comme nous le décrirons plus bas), qui peuvent être dues à des contenus relatifs en ions Eu^{3+} différents entre les deux hybrides (4,98 et 2,68 % en masse repectivement). De plus, les fortes valeurs trouvées pour la largeur à mi-hauteur (plus importantes que celle rapportées pour les hybrides analogues amorphes, 19 à 37 cm^{-1}) montrent que les cations Eu^{3+} sont situés dans une distribution continue de sites locaux similaires. Les paramètres expérimentaux, Ω_2 et Ω_4 ont été calculés et les valeurs de Ω_2 estimées pour **M-Eu** sont plus faibles que celles calculées pour **M-EuTb**, ce qui souligne une diminution du degré de covalence moyen des premières liaisons de l'europium dans **M-Eu**, en accord avec les conclusions mentionnées ci-dessus et dérivées de l'analyse des énergies des transitions $^5D_0 \rightarrow {}^7F_0$ dans les deux hybrides. Les valeurs de Ω_2 sont similaires à celles trouvées dans les hybrides organiques-inorganiques amorphes analogues

à base d'amines et incorporant des sels $Eu(OTf)_3$, dans les hybrides lamellaires incorporant du chlorure d'europium, et dans les silices mésostructurées dopées avec des complexes aquo-β-dicétone malgré les morphologies et sites locaux de coordination distincts trouvés dans ces hybrides. Il est aussi intéressant de noter que dans ces hybrides (à part pour l'hybride à base de silice mésostructurée) et dans **M-Eu** et **M-EuTb** les valeurs de Ω_2 et Ω_4 sont du même ordre de grandeur malgré le fait que dans un grand nombre d'hybrides contenant des ions Eu^{3+} les valeurs de Ω_4 soient substantiellement plus faibles que celles de Ω_2.

L'efficacité quantique (η) de l'état $^5D_0$ a été évaluée : l'hybride **M-Eu** montre une valeur plus faible de η (0,14). Le nombre de molécules d'eau coordinées à l'europium (n_w) a aussi été déterminée, soit 2,1 ± 0,1 pour **M-Eu**. De façon similaire à ce qui a été trouvé pour les paramètres d'intensité, les valeurs de l'efficacité quantique et du nombre de molécules d'eau calculées pour **M-Eu** sont très proches de celles rapportées pour les di-uréasils mentionnés précédemment, **Eu@L12** et les hybrides dérivés de la silice mésoporeuse SBA-15 contenant des ions Eu^{3+}, ce qui renforce l'hypothèse que bien que la coordination locale soit différente au sein des différentes familles d'hybrides (en général impliquant des atomes d'oxygène pour les di-uréasils et **Eu@L12** ou des atomes d'azote du fragment bipyridine dans **M-Eu**), les valeurs de η et n_w sont similaires.

Le rendement quantique absolu d'émission a été mesuré pour chacun des hybrides. Pour l'hybride non dopé **H**, sous des longueurs d'onde d'excitation comprises entre 330 et 450 nm, une valeur maximale de 0,22 ± 0,02 a été atteinte dans le domaine de longueurs d'onde d'excitation 390-440 nm. Ceci est la plus haute valeur de rendement quantique rapportée à ce jour pour des silsesquioxanes pour des excitations dans les régions du long UV ou du bleu; l'hybride à base de 3-aminopropyltriéthoxysilane et d'acide formique a un rendement quantique de 0,35 ± 0,1, mais sous excitation UV (365 nm). De plus, il a été montré que l'hybride **H** peut être excité dans la région spectrale du bleu par une diode électroluminescente commerciale émettant à 395 nm. Pour l'hybride non dopé **M**, synthétisé dans le méthanol, une valeur maximale de 0,18 ± 0,02 a été atteinte dans le proche UV ou le bleu (360-420 nm).

Pour les hybrides contenant des cations Eu^{3+} ou Tb^{3+}, les valeurs maximales de rendement quantique (0,08 pour **M-Eu**, 0,12 pour **M-Tb** et **M-EuTb**) ont été atteintes par

excitation *via* l'état triplet de la bipyridine (320 nm). La valeur plus haute obtenue pour l'hybride à base de sels de Tb^{3+} provient probablement de la plus forte résonnance entre l'état triplet du fragment bipyridine et le niveau $^5D_4$ des ions Tb^{3+} (1 410 cm^{-1}), par rapport à ce qui est trouvé pour le niveau $^5D_1$ des ions Eu^{3+} (2 950 cm^{-1}). Sous excitation *via* les états excités des liaisons H entre les urées et des domaines siloxane (380-420 nm), le rendement quantique est indépendant de la longueur d'onde sélectionnée (0,06, **M-Eu** ; 0,08, **M-Tb** et **M-EuTb**). Les plus faibles valeurs mesurées pour les excitations via les états excités des liaisons entre urées ou des domaines silylés, par rapport à celles mesurés sous excitation *via* l'état triplet des fragments bipyridine souligne le rôle actif de la bipyridine dans l'augmentation des valeurs du rendement quantique d'émission pour les hybrides contenant des ions Ln^{3+}. De plus, les valeurs maximales de rendement quantique (en excitant à 320 nm) sont plus hautes que celles rapportées pour les polysilsesquioxanes pontés amorphes analogues mais ne possédant pas le fragment bipyridine, et dopés par des ions Eu^{3+} (0,06).

En conclusion, cette thèse s'est principalement intéressée aux mécanismes de photoluminescence dans les matériaux hybrides organiques-iorganiques, comportant ou non des ions lanthanide Ln^{3+} (Ln = Eu, Tb ou Gd).

Dans un premier temps, nous avons mimé les parties inorganique et organique des hybrides de type di-uréasils, et avons pu étudier en détail les mécanismes de transfert d'énergie entre les deux sites émetteurs (groupes urée et siloxane) dans le cas des matériaux purs, et entre ces groupes et les ions Eu^{3+} dans le cas de matériaux dopés. Cette étude constitue une toile de fond théorique, très utile pour mieux comprendre les mécanismes de luminescence des nouveaux matériaux hybrides.

Dans un second temps, nous avons tenté d'établir un lien entre la structuration d'un matériau et ses propriétés de photoluminescence. Ceci a été conduit par hydrolyse du précurseur **P12**, qui a donné, selon les conditions, des matériaux purs lamellaire (catalyse acide) ou amorphe (catalyse nucléophile). Un bien meilleur rendement quantique absolu d'émission a été observé dans le cas de l'hybride amorphe. Dans le cas des hybrides synthétisés en présence d'ions Eu^{3+}, il a été montré que la morphologie variait très peu par rapport au composé pur dans le cas de la catalyse acide, alors qu'une structuration à courte distance a été mise en évidence en cas de catalyse nucléophile. Là encore, les propriétés de

photoluminescence sont bien meilleures dans le cas de la catalyse nucléophile. Ces résultats vont permettre de mieux concevoir les nouveaux modèles de matériaux hybrides en vue d'applications photoniques.

Enfin, dans un troisième temps, des matériaux hybrides amorphes contenant des fragments aromatiques de type bipyridine ont été synthétisés et étudiés. La présence des groupes aromatiques a permis d'augmenter fortement la brillance par rapport aux hybrides précédents. L'hybride pur amorphe peut être excité à 395 nm par des LEDs commerciales, et possède le plus haut rendement quantique (22%) pour un matériau hybride exempt de centre métallique, sous excitation dans le proche UV ou bleu. Les matériaux contenant des ions Eu^{3+} et/ou Tb^{3+} ont des couleurs d'émission variables sur une grande partie du diagramme de chromaticité, selon le lanthanide utilisé et la longueur d'onde d'excitation. En particulier, le rôle clef de l'émission par l'hôte sur la couleur d'émission du matériau a été mis en avant.

A partir de ces études, plusieurs types de perspectives peuvent être envisagées :

- Les propriétés intéressantes en photoluminescence des matériaux hybrides à base de bipyridine nous poussent à approfondir cette étude, en étudiant d'autres isomères de ces composés, et en cherchant à mieux comprendre les mécanismes de transfert d'énergie au sein de ces hybrides.
- Il serait aussi intéressant de pouvoir structurer différemment des matériaux hybrides comportant des fragments aromatiques et provenant d'un même précurseur, afin d'étudier l'influence de la structuration sur l'émission dans le cas de ce type d'hybrides.
- Enfin, la formation de dispositifs d'optique passive intégrée à partir de ces matériaux (à obtenir sous forme de monolithes ou de films) est un défi intéressant à relever pour prouver l'applicabilité de ce type de matériaux hybrides.

Refferences

1. C. Sanchez, *J. Mater. Chem.*, 2005, **15**, 3557.
2. P. Judeinstein and C. Sanchez, *J. Mater. Chem.*, 1996, **6**, 511.
3. U. Schubert, N. Husing and A. Lorenz, *Chem. Mater.*, 1995, **7**, 2010.
4. J. Y. Wen and G. L. Wilkes, *Chem. Mater.*, 1996, **8**, 1667.
5. C. Sanchez, C. Boissiere, D. Grosso, C. Laberty and L. Nicole, *Chem. Mater.*, 2008, **20**, 682.
6. C. J. Brinker and G. W. Scherer, in *Sol–Gel Science: the Physics and Chemistry of Sol–Gel Processing*, Academic Press, San Diego, 1990.
7. L. L. Hench and J. K. West, *Chem. Rev.*, 1990, **90**, 33.
8. H. Yang, N. Coombs and G. A. Ozin, *Nature*, 1997, **386**, 692.
9. S. Inagaki, Y. Fukushima and K. Kuroda, *J. Chem. Soc., Chem. Commun.*, 1993, 680.
10. S. Mann and G. A. Ozin, *Nature*, 1996, **382**, 313.
11. A. Shimojima and K. Kuroda, *Angew. Chem. Int. Edit.*, 2003, **42**, 4057.
12. A. Shimojima, Z. Liu, T. Ohsuna, O. Terasaki and K. Kuroda, *J. Am. Chem. Soc.*, 2005, **127**, 14108.
13. R. J. P. Corriu, J. J. E. Moreau, P. Thepot and M. Wong Chi Man, *Chem. Mater.*, 1992, **4**, 1217.
14. K. Shea, D. Loy and O. W. Webster, *Chem. Mater.*, 1989, **1**, 574.
15. B. Boury, R. J. P. Corriu, V. Le Strat, P. Delord and M. Nobili, *Angew. Chem. Int. Edit.*, 1999, **38**, 3172.
16. G. Cerveau, R. J. P. Corriu, E. Framery and F. Lerouge, *Chem. Mater.*, 2004, **16**, 3794.
17. G. Cerveau, R. J. P. Corriu, E. Framery and F. Lerouge, *J. Mater. Chem.*, 2004, **14**, 3019.
18. F. Lerouge, G. Cerveau and R. J. P. Corriu, *New. J. Chem.*, 2006, **30**, 1364.
19. X. F. Zhou, S. Yang, C. Z. Yu, Z. H. Li, X. Yan, Y. Cao and D. Y. Zhao, *Chem. Eur. J.*, 2006, **12**, 8484.
20. J. J. E. Moreau, L. Vellutini, M. Wong Chi Man, C. Bied, J. L. Bantignies, P. Dieudonné and J. L. Sauvajol, *J. Am. Chem. Soc.*, 2001, **123**, 7957.

21. J. J. E. Moreau, L. Vellutini, M. Wong Chi Man and C. Bied, *J. Am. Chem. Soc.*, 2001, **123**, 1509.
22. J. J. E. Moreau, L. Vellutini, P. Dieudonné, M. Wong Chi Man, J. L. Bantignies, J. L. Sauvajol and C. Bied, *J. Mater. Chem.*, 2005, **15**, 4943.
23. J. J. E. Moreau, B. P. Pichon, G. Arrachart, C. Bied and M. Wong Chi Man, *New. J. Chem.*, 2005, **29**, 653.
24. Y. J. Zhang, Q. X. Tang, H. X. Li and W. P. Hu, *Appl. Phys. Lett.*, 2009, **94**, 203304.
25. M. Lu, B. H. Xie, J. H. Kang, F. C. Chen, Y. Yang and Z. H. Peng, *Chem. Mater.*, 2005, **17**, 402.
26. M. H. Valkenberg and W. F. Holderich, *Catalysis Reviews*, 2002, **44**, 321.
27. A. P. Wight and M. E. Davis, *Chem. Rev.*, 2002, **102**, 3589.
28. A. Brethon, C. Bied, J. J. E. Moreau and M. Wong Chi Man, *J. Sol-Gel Sci. Techn.*, 2009, **50**, 141.
29. J. W. Grate, S. N. Kaganove, S. J. Patrash, R. Craig and M. Bliss, *Chem. Mater.*, 1997, **9**, 1201.
30. A. Walcarius, *Chem. Mater.*, 2001, **13**, 3351.
31. H. Zhang, D. K. Pan, K. Zou, J. He and X. Duan, *J. Mater. Chem.*, 2009, **19**, 3069.
32. D. Arcos, I. Izquierdo-Barba and M. Vallet-Regi, *J. Mater. Sci: Mater. Med.*, 2009, **20**, 447.
33. M. K. Mistry, N. R. Choudhury, N. K. Dutta, R. Knott, Z. Q. Shi and S. Holdcroft, *Chem. Mater.*, 2008, **20**, 6857.
34. B. Q. Wang, B. Li, Q. Deng and S. J. Dong, *Anal. Chem.*, 1998, **70**, 3170.
35. C. Sanchez, B. Lebeau, F. Chaput and J. P. Boilot, *Adv. Mater.*, 2003, **15**, 1969.
36. L. D. Carlos, R. A. S. Ferreira, V. de Zea Bermudez and S. J. L. Ribeiro, *Adv. Mater.*, 2009, **21**, 509.
37. V. Bekiari, P. Lianos and P. Judeinstein, *Chem. Phys. Lett.*, 1999, **307**, 310.
38. L. D. Carlos, V. de Zea Bermudez, R. A. S. Ferreira, L. Marques and M. Assunção, *Chem. Mater.*, 1999, **11**, 581.
39. V. de Zea Bermudez, L. D. Carlos, M. C. Duarte, M. M. Silva, C. J. R. Silva, M. J. Smith, M. Assunção and L. Alcacér, *J. Alloy Compd.*, 1998, **277**, 21.
40. P. Escribano, B. Julian-Lopez, J. Planelles-Arago, E. Cordoncillo, B. Viana and C. Sanchez, *J. Mater. Chem.*, 2008, **18**, 23.

41. A. Quach, V. Escax, L. Nicole, P. Goldner, O. Guillot-Noel, P. Aschehoug, P. Hesemann, J. Moreau, D. Gourier and C. Sanchez, *J. Mater. Chem.*, 2007, **17**, 2552.
42. R. Hernandez, A. C. Franville, P. Minoofar, B. Dunn and J. I. Zink, *J. Am. Chem. Soc.*, 2001, **123**, 1248.
43. C. Sanchez and B. Lebeau, *Mrs. Bull.*, 2001, **26**, 377.
44. C. L. Lu and B. Yang, *J. Mater. Chem.*, 2009, **19**, 2884.
45. Y. F. Li, J. H. Zhang, S. J. Zhu, H. P. Dong, Z. H. Wang, Z. Q. Sun, J. R. Guo and B. Yang, *J. Mater. Chem.*, 2009, **19**, 1806.
46. C. Sanchez, F. Ribot and B. Lebeau, *J. Mater. Chem.*, 1999, **9**, 35.
47. M. Faloss, M. Canva, P. Georges, A. Brun, F. Chaput and J. P. Boilot, *Appl. Opt.*, 1997, **36**, 6760.
48. S. Motakef, J. M. Boulton and D. R. Uhlmann, *Opt. Lett.*, 1994, **19**, 1125.
49. R. Buestrich, F. Kahalenberg, M. Popall, P. Dannberg, R.-M. Fiedler and O. Rösch, *J. Sol-Gel Sci. Technol.*, 2001, **20**, 181.
50. E. J. Assar, R. R. Gonçalves, M. Ferrari, Y. Massaddeq and S. J. L. Ribeiro, *J. Alloys Comp.*, 2002, **344**, 221.
51. C. M. McDonagh, A. M. Shileds, A. K. Mcevoy, B. D. MacCraith and F. F. Gouin, *J. Sol-Gel Sci. Technol.*, 1998, **13**, 207.
52. P. Lavin, C. M. McDonagh and B. D. MacCraith, *J. Sol-Gel Sci. Technol.*, 1998, **13**, 641.
53. L. T. Canham, *Appl. Phys. Lett.*, 1990, **57**, 1046.
54. W. H. Green, K. P. Le, J. Grey, T. T. Au and M. J. Sailor, *Science*, 1997, **276**, 1826.
55. V. Bekiari and P. Lianos, *Langmuir*, 1998, **14**, 3459.
56. Y. Uchida, Y.-I. Nobu, I. Momiji and H. Matsui, *J. Sol-Gel Sci. Technol.*, 2000, **19**, 705.
57. Y. Han, J. Lin and H. Zhang, *J. Mater. Lett.*, 2002, **54**, 389.
58. E. Cordoncillo, F. J. Guaita, P. Escribano, C. Philippe, B. Viana and C. Sanchez, *Opt. Mater.*, 2001, **18**, 309.
59. T. Brankova, V. Bekiari and P. Lianos, *Chem. Mater.*, 2003, **15**, 1855.
60. S. J. L. Ribeiro, K. Dahmouche, C. A. Ribeiro, C. V. Santilli and S. H. Pulcinelli, *J. Sol-Gel Sci. Techn.*, 1998, **13**, 427.

61. V. de Zea Bermudez, L. D. Carlos and L. Alcácer, *Chem. Mater.*, 1999, **11**, 569.
62. E. Stathatos, P. Lianos, U. L. Stangar, B. Orel and P. Judeinstein, *Chem. Mater.*, 2000, **16**, 8672.
63. L. D. Carlos, R. A. S. Ferreira, V. de Zea Bermudez and S. J. L. Ribeiro, *Adv. Funct. Mater.*, 2001, **11**, 111.
64. L. D. Carlos, R. A. S. Ferreira, R. N. Pereira, M. Assunção and V. de Zea Bermudez, *J. Phys. Chem. B*, 2004, **108**, 14924.
65. M. C. Gonçalves, V. de Zea Bermudez, R. A. S. Ferreira, L. D. Carlos, D. Ostrovskii and J. Rocha, *Chem. Mater.*, 2004, **16**, 2530.
66. L. S. Fu, R. A. S. Ferreira, N. J. O. Silva, L. D. Carlos, V. De Zea Bermudez and J. Rocha, *Chem. Mater.*, 2004, **16**, 1507.
67. S. C. Nunes, V. de Zea Bermudez, J. Cybinska, R. A. S. Ferreira, J. Legendziewicz, L. D. Carlos, M. M. Silva, M. J. Smith, D. Ostrovskii and J. Rocha, *J. Mater. Chem.*, 2005, **15**, 3876.
68. Z. Y. Cheng, B. X. Gao, M. L. Pang, S. Y. Wang, Y. C. Han and J. Lin, *Chem. Mater.*, 2003, **15**, 4705.
69. L. S. Fu, R. A. S. Ferreira, M. Fernandes, S. C. Nunes, V. D. Bermudez, G. Hungerford, J. Rocha and L. D. Carlos, *Opt. Mater.*, 2008, **30**, 1058.
70. L. Pavesi, L. Dal Negro, C. Mazzoleni, G. Franzó and F. Priolo, *Nature*, 2000, **408**, 440.
71. N. C. Greenham, I. D. W. Samuel, A. B. Holmes and R. H. Friend, *Chem. Phys. Lett.*, 1995, **241**, 89.
72. G. Blasse and B. C. Grabmaier, *Luminescent Materials*, Berlin, Germany, 1994.
73. T. Justel, H. Nikol and C. Ronda, *Angew. Chem. Int. Ed.*, 1998, **37**, 3085.
74. M. H. V. Werts, N. Nerambourg, D. Pelegry, Y. Le Grand and M. Blanchard-Desce, *Photochem. Photobiol. Sci.*, 2005, **4**, 531.
75. J. Marling, *IEEE J. Sel. Top. Quantum Electron*, 1978, **14**, 56.
76. K. Kuriki, K. Y. and Y. Okamoto, *Chem. Rev.*, 2002, **102**, 2347.
77. A. Polman and F. C. J. M. Van Veggel, *J. Opt. Soc. Am. B*, 2004, **21**, 871.
78. S. Comby and J.-C. G. Bünzli, in *Handbook on the Physics and Chemistry of Rare Earths*, eds. K. A. Gschneider, J.-C. G. Bünnzli and V. K. Pecharsky, Elsevier Science, New York, 2007.

79. L. Thunus and R. Lejeune, *Coord. Chem. Rev*, 1999, **184**, 125.
80. D. Parker, R. S. Dickins, H. Puschmann, C. Crossland and J. A. K. Howard, *Chem. Rev.*, 2002, **102**, 1977.
81. J.-C. G. Bünnzli, in *Lanthanide Probes in Life, Chemical and Earth Sciences, Theory and Practice*, eds. G. R. Choppin and J.-C. G. Bünnzli, Elsevier, Amsterdam, Netherlands, 1989.
82. J.-M. Lehn, *Angew. Chem. Int. Edit.*, 1990, **29**, 1304.
83. N. Sabbatini, M. Guardigli and J.-M. Lehn, *Coord. Chem. Rev.*, 1993, **123**, 201.
84. G. F. de Sá, O. L. Malta, C. D. Donegá, A. M. Simas, R. L. Longo, P. A. Santa-Cruz and E. F. da Silva, *Coord. Chem. Rev.*, 2000, **196**, 165.
85. J. Kido and Y. Okamoto, *Chem. Rev.*, 2002, **102**, 2357.
86. J. C. G. Bunzli and C. Piguet, *Chem. Soc. Rev.*, 2005, **34**, 1048.
87. P. P. Lima, R. A. S. Ferreira, R. O. Freire, F. A. A. Paz, L. S. Fu, S. Alves, L. D. Carlos and O. L. Malta, *Chemphyschem*, 2006, **7**, 735.
88. A. C. Franville, D. Zambon, R. Mahiou and Y. Troin, *Chem. Mater.*, 2000, **12**, 428.
89. K. Binnemans, in *Handbook on the Physics and Chemistry of Rare Eraths*, eds. K. A. Gschenieder, J.-C. G. Bünnzli and V. K. Pecharsky, 2005.
90. P. Porcher and P. Caro, *J. Lumin.*, 1980, **21**, 207.
91. O. L. Malta, W. M. Azevedo, E. A. Gouveia and G. F. Desa, *J. Lumin.*, 1982, **26**, 337.
92. L. D. Carlos and A. L. L. Videira, *Phys. Rev.*, 1994, **49**, 11721.
93. L. D. Carlos, J. A. Fernandes, R. A. S. Ferreira, O. L. Malta, I. S. Goncalves and P. Ribeiro-Claro, *Chem. Phys. Lett.*, 2005, **413**, 22.
94. W. M. Faustino, O. L. Malta and G. F. de Sá, *J. Chem. Phys.*, 2005, **112**, 054109.
95. R. A. S. Ferreira, L. D. Carlos, R. R. Goncalves, S. J. L. Ribeiro and V. de Zea Bermudez, *Chem. Mater.*, 2001, **13**, 2991.
96. L. S. Fu, R. A. S. Ferreira, N. J. O. Silva, J. A. Fernandes, P. Ribeiro-Claro, I. S. Goncalves, V. De Zea Bermudez and L. D. Carlos, *J. Mater. Chem.*, 2005, **15**, 3117.
97. T. Förster, *Z. Naturforsch. A*, 1949, **49**, 321.
98. D. L. Dexter, *J. Chem. Phys.*, 1953, **21**, 836.
99. J. R. Lakiwicz, *Principles of Fuorescence Spectroscopy*, Kluwer Academic/Plenum Publishers, New York, 1999.

100. N. J. Turro, *Modern Molecular Photochemistry*, University Science Books, Sausalito, 1991.
101. L. D. Carlos, R. A. Ferreira, J. P. Rainho and V. de Zea Bermudez, *Adv. Func. Mater.*, 2002, **12**, 819.
102. R. A. S. Ferreira, L. D. Carlos, V. de Zea Bermudez, C. Molina, K. dahmouche, Y. Messaddeq and S. J. L. Ribeiro, *J. Sol-Gel Sci. Technol.*, 2003, **26**.
103. M. C. Gonçalves, N. J. O. Silva, V. de Zea Bermudez, R. A. S. Ferreira, L. D. Carlos, K. Dahmouche, C. V. Santilli, D. Ostrovskii, I. C. Correia Vilela and A. F. Craievich, *J. Phys. Chem. B*, 2005, **109**, 20093.
104. J. J. P. Stewart, *MOPAC 2002*, Fujitsu Limited, Tokyo, 1999.
105. L. D. Carlos, R. A. S. Ferreira, V. de Zea Bermudez, C. Molina, L. A. Bueno and S. J. L. Ribeiro, *Phys. Rev. B*, 1999, **60**, 10042.
106. L. D. Carlos, Y. Messaddeq, H. F. Brito, R. A. S. Ferreira, V. de Zea Bermudez and S. J. L. Ribeiro, *Adv. Mater.*, 2000, **12**, 594.
107. C. Molina, K. Dahmouche, Y. Messaddeq, S. J. L. Ribeiro, M. A. P. Silva, V. De Zea Bermudez and L. D. Carlos, *J. Lumin.*, 2003, **104**, 93.
108. V. de Zea Bermudez, D. Ostrovskii, A. C. Gonçalves, S. Lavoryk, L. D. Carlos and R. A. S. Ferreira, *J. Phys. Chem. B*, 2005, **109**, 7110.
109. H. H. Li, S. Inoue, K. Machida and G. Adachi, *Chem. Mater.*, 1999, **11**, 3171.
110. H. R. Li, J. Lin, H. J. Zhang, L. S. Fu, Q. G. Meng and S. B. Wang, *Chem. Mater.*, 2002, **14**, 3651.
111. R. Moleski, E. Stathatos, V. Bekiari and P. Lianos, *Thin Solid Films*, 2002, **416**, 279.
112. L. N. Sun, H. J. Zhang, Q. G. Meng, F. Y. Liu, L. S. Fu, C. Y. Peng, J. B. Yu, G. L. Zheng and S. B. Wang, *J. Phys. Chem. B*, 2005, **109**, 6174.
113. H. R. Li, J. Lin, L. S. Fu, J. F. Guo, Q. G. Meng, F. Y. Liu and H. J. Zhang, *Micropor. Mesopor. Mat.*, 2002, **55**, 103.
114. M. H. Bartl, B. J. Scott, H. C. Huang, G. Wirnsberger, A. Popitsch, B. F. Chmelka and G. D. Stucky, *Chem. Commun.*, 2002, 2474.
115. Q. G. Meng, P. Boutinaud, A. C. Franville, H. J. Zhang and R. Mahiou, *Micropor. Mesopor. Mat.*, 2003, **65**, 127.
116. P. Lenaerts, A. Storms, J. Mullens, J. D'Haen, C. Gorller-Walrand, K. Binnemans and K. Driesen, *Chem. Mater.*, 2005, **17**, 5194.

117. A. Fernandes, J. Dexpert-Ghys, A. Gleizes, A. Galarneau and D. Brunel, *Micropor. Mesopor. Mat.*, 2005, **83**, 35.
118. S. Gago, M. Pillinger, R. A. S. Ferreira, L. D. Carlos, T. M. Santos and I. S. Goncalves, *Chem. Mater.*, 2005, **17**, 5803.
119. C. Y. Peng, H. J. Zhang, J. B. Yu, Q. G. Meng, L. S. Fu, H. R. Li, L. N. Sun and X. M. Guo, *J. Phys. Chem. B*, 2005, **109**, 15278.
120. L. C. C. da Silva, T. S. Martins, M. S. Filho, E. E. S. Teotonio, P. C. Isolani, H. F. Brito, M. H. Tabacniks, M. C. A. Fantini and J. R. Matos, *Micropor. Mesopor. Mat.*, 2006, **92**, 94.
121. P. N. Minoofar, R. Hernandez, S. Chia, B. Dunn, J. I. Zink and A. C. Franville, *J. Am. Chem. Soc.*, 2002, **124**, 14388.
122. Q. M. Wang and B. Yan, *Cryst. Growth Des.*, 2005, **5**, 1303.
123. S. W. Li, H. W. Song, W. L. Li, X. G. Ren, S. Z. Lu, G. H. Pan, L. B. Fan, H. Q. Yu, H. Zhang, R. F. Qin, Q. L. Dai and T. Wang, *J. Phys. Chem. B*, 2006, **110**, 23164.
124. B. Yan and X. F. Qiao, *J. Phys. Chem. B*, 2007, **111**, 12362.
125. R. J. P. Corriu, F. Embert, Y. Guari, A. Mehdi and C. Reye, *Chem. Commun.*, 2001, 1116.
126. M. Karmaoui, R. A. S. Ferreira, A. T. Mane, L. D. Carlos and N. Pinna, *Chem. Mater.*, 2006, **18**, 4493.
127. M. Karmaoui, L. Mafra, R. A. S. Ferreira, J. Rocha, L. D. Carlos and N. Pinna, *J. Phys. Chem. C*, 2007, **111**, 2539.
128. J. J. E. Moreau, L. Vellutini, M. Wong Chi Man, C. Bied, P. Dieudonne, J. L. Bantignies and J. L. Sauvajol, *Chem. Eur. J.*, 2005, **11**, 1527.
129. A. Lin and M. A. Meyers, *Materials Science and Engineering A*, 2005, **390**, 27.
130. B. J. F. Bruet, H. J. Qi, M. C. Boyce, R. Panas, K. Tai, L. Frick and C. Ortiz, *J. Mater. Res.*, 2005, **20**, 2400.
131. J. J. E. Moreau, L. Vellutini, M. Wong Chi Man and C. Bied, *Chem. Eur. J.*, 2003, **9**, 1594.
132. B. P. Pichon, M. Wong Chi Man, P. Dieudonne, J. L. Bantignies, C. Bied, J. L. Sauvajol and J. J. E. Moreau, *Adv. Funct. Mater.*, 2007, **17**, 2349.
133. L. D. Carlos, V. de Zea Bermudez, V. S. Amaral, S. C. Nunes, N. J. O. Silva, R. A. S. Ferreira, J. Rocha, C. V. Santilli and D. Ostrovskii, *Adv. Mater.*, 2007, **19**, 341.

134. V. Bekiari and P. Lianos, *Chem. Mater.*, 1998, **10**, 3777.
135. M. L. Gomez, D. P. Fasce, R. J. J. Williams, C. M. Previtali, L. Matejka, J. Plestil and J. Brus, *Macromolecular Chemistry and Physics*, 2008, **209**, 634.
136. R. Le Toquin and A. K. Cheetham, *Chem. Phys. Lett.*, 2006, **423**, 352.
137. S. Benyahya, F. Monnier, M. Taillefer, M. Wong Chi Man, C. Bied and F. Ouazzani, *Adv. Synth. Cat.*, 2008, **350**, 2205.
138. H. Li, N. Lin, Y. Wang, Y. Feng, Q. Gan, H. Zhang, Q. Dong and Y. Chen, *Eur. J. Inorg. Chem.*, 2009, **4**, 519.
139. C. Kaes, A. Katz and M. W. Hosseini, *Chem. Rev.*, 2000, **100**, 3553.
140. H. R. Li, J. Lin, H. J. Zhang, H. C. Li, L. S. Fu and Q. G. Meng, *Chem. Commun.*, 2001, **13**, 1212.
141. H. Li, J. Yu, F. Liu, H.Zhang, L. Fu, Q. Meng, C. Peng and J. Lin, *New J. Chem.*, 2004, **28**, 1137.
142. S. Cousinie, M. Gressier, P. Alphonse and M. J. Menu, *Chem. Mater.*, 2007, **19**, 6492.